frontiers | Research Topics

Soil and water loss and environmental effects

Edited by
Xudong Peng, Narsimha Adimalla, Zisheng Xing and Qiang Li

Published in
Frontiers in Environmental Science

ISSN 1664-8714
ISBN 978-2-8325-6737-1
DOI 10.3389/978-2-8325-6737-1

Generative AI statement
Any alternative text (Alt text) provided alongside figures in the articles in this ebook has been generated by Frontiers with the support of artificial intelligence and reasonable efforts have been made to ensure accuracy, including review by the authors wherever possible. If you identify any issues, please contact us.

About Frontiers

Frontiers is more than just an open access publisher of scholarly articles: it is a pioneering approach to the world of academia, radically improving the way scholarly research is managed. The grand vision of Frontiers is a world where all people have an equal opportunity to seek, share and generate knowledge. Frontiers provides immediate and permanent online open access to all its publications, but this alone is not enough to realize our grand goals.

Frontiers journal series

The Frontiers journal series is a multi-tier and interdisciplinary set of open-access, online journals, promising a paradigm shift from the current review, selection and dissemination processes in academic publishing. All Frontiers journals are driven by researchers for researchers; therefore, they constitute a service to the scholarly community. At the same time, the *Frontiers journal series* operates on a revolutionary invention, the tiered publishing system, initially addressing specific communities of scholars, and gradually climbing up to broader public understanding, thus serving the interests of the lay society, too.

Dedication to quality

Each Frontiers article is a landmark of the highest quality, thanks to genuinely collaborative interactions between authors and review editors, who include some of the world's best academicians. Research must be certified by peers before entering a stream of knowledge that may eventually reach the public - and shape society; therefore, Frontiers only applies the most rigorous and unbiased reviews. Frontiers revolutionizes research publishing by freely delivering the most outstanding research, evaluated with no bias from both the academic and social point of view. By applying the most advanced information technologies, Frontiers is catapulting scholarly publishing into a new generation.

What are Frontiers Research Topics?

Frontiers Research Topics are very popular trademarks of the *Frontiers journals series*: they are collections of at least ten articles, all centered on a particular subject. With their unique mix of varied contributions from Original Research to Review Articles, Frontiers Research Topics unify the most influential researchers, the latest key findings and historical advances in a hot research area.

Find out more on how to host your own Frontiers Research Topic or contribute to one as an author by contacting the Frontiers editorial office: frontiersin.org/about/contact

Soil and water loss and environmental effects

Topic editors

Xudong Peng — Guizhou University, China

Narsimha Adimalla — East China University of Technology, China

Zisheng Xing — Agriculture and Agri-Food Canada (AAFC), Canada

Qiang Li — University of Houston–Downtown, United States

Citation

Peng, X., Adimalla, N., Xing, Z., Li, Q., eds. (2025). *Soil and water loss and environmental effects*. Lausanne: Frontiers Media SA.

doi: 10.3389/978-2-8325-6737-1

Table of contents

frontiers | Frontiers in Environmental Science

TYPE Original Research
PUBLISHED 07 June 2024
DOI 10.3389/fenvs.2024.1429684

OPEN ACCESS

EDITED BY
Xudong Peng,
Guizhou University, China

REVIEWED BY
Youjin Yan,
Nanjing Forestry University, China
Yusong Deng,
Guangxi University, China

*CORRESPONDENCE
Le-Xing You,
leoxyou@zjnu.edu.cn
Jin-Shi Lin,
jslin@fafu.edu.cn

RECEIVED 08 May 2024
ACCEPTED 21 May 2024
PUBLISHED 07 June 2024

CITATION
Jiang L, Chen J, You L-X, Jiang F-S, Zhang Y, Lin J-S and Huang Y-H (2024), Free iron oxides modulate the surface properties of Benggang soil on Southern China: insights into erosive mechanisms.
Front. Environ. Sci. 12:1429684.
doi: 10.3389/fenvs.2024.1429684

Free iron oxides modulate the surface properties of Benggang soil on Southern China: insights into erosive mechanisms

Ling Jiang[1], Jie Chen[1], Le-Xing You[2]*, Fang-Shi Jiang[1], Yue Zhang[1], Jin-Shi Lin[1]* and Yan-He Huang[1]

[1]College of Resources and Environment, Fujian Agriculture and Forestry University, Fuzhou, China, [2]College of Geography and Environmental Sciences, Zhejiang Normal University, Jinhua, China

Benggang, an erosional phenomenon located in southern China, exhibits distinctive characteristics that can have profound ecological and agricultural consequences as well as pose risks to human life. Previous investigations have primarily focused on elucidating the relationships between the physical and chemical attributes of soils collected from Benggang. However, the precise role of free iron oxides in the surface properties of Benggang soil and its contribution to the formation of Benggang remains largely unexplored. In this study, we aim to investigate the role of free iron oxides in Benggang soil by removing them and subsequently introducing goethite to evaluate their impact on the soil's surface properties. Our results reveal a decrease in the surface charge density of soil colloidal particles with increasing soil depth. Specifically, the uppermost red soil layer exhibits the highest value, followed by the sandy soil and the lowermost clastic layer. Upon removing free iron oxide, we documented reductions of 44.28% (red soil), 20.62% (sandy soil), and 8.70% (clastic layer) in the surface charge density of colloidal particles. The red soil layer presented an over 18-fold increase compared to the initial linear shrinkage, followed by the sandy soil and clastic layer. Notably, the addition of goethite to the iron oxide-free soil layers resulted in the recovery of approximately 81.93%, 121.13%, and 104.35% of the initial surface charge density, respectively. Moreover, significant changes in volume shrinkage were observed, with approximately 97.54% (red soil), 94.75% (sandy soil), and 89.72% (clastic layer) of the initial values being influenced. These findings underscore the substantial influence of free iron oxide on the physicochemical properties of Benggang soil and contribute to a comprehensive understanding of the erosive mechanisms underlying Benggang formation.

KEYWORDS

Benggang, free iron oxide, shrinkage, surface charge density, surface potential

1 Introduction

Benggang is a unique erosional phenomenon in southern China that forms where sloping soil- and stone-rich horizons become fragmented, collapse, and are further scoured away due to the combined actions of water and gravity (Xu, 1996). Benggang formation can severely impact agricultural production and cause the loss of human life, as well as can hinder the development of the social economy in affected regions (Zhong et al., 2013).

Therefore, it is important to comprehensively understand the occurrence and the development of Benggang over time to prevent their formation in the future and/or control their influence when they occur.

Many studies have focused on the macroscopic erosive driving forces that contribute to Benggang formation, and it is widely believed that this type of collapse is influenced by multiple factors, including geomorphology (Chaplot, 2013), vegetation cover (Gyssels et al., 2005; Wang et al., 2014), water flow (Xu and Zeng, 1992; Jiang et al., 2014; Lin et al., 2017), and soil characteristics (Six et al., 2004). Extensive research has been conducted on the physicochemical properties of soil in Benggang, encompassing dry density, water content, clay mineral composition and content (Chen et al., 2018; Wang et al., 2018; Wei et al., 2018; Xia et al., 2019; 2021; Zhang et al., 2022). During periods of rainfall, soil swelling is induced as a result of a rapid influx of water content. Subsequent to the rainfall event, gradual evaporation of soil moisture occurs, leading to soil shrinkage as the water content diminishes. The repetitive cycles of wet and dry conditions exacerbate the development of cracks initiated by soil swelling and shrinkage, ultimately expediting soil erosion processes (Zhang et al., 2023). However, the specific triggers for Benggang formation remain unclear due to the multitude of influential factors.

Charged soils, which contained particles with negative and/or positive charges, are widespread in nature. Phyllosilicates typically exhibit a net negative surface charge under normal pH conditions, whereas iron oxides carry a net positive surface charge (Yu, 1997; Qafoku et al., 2004). Previous studies have demonstrated that the presence of iron oxide can induce a shift in the zeta potential of soil towards positive values (Hou et al., 2007; Jiang et al., 2010; Wang et al., 2013), resulting in corresponding alterations in physicochemical properties such as the linear shrinkage ratio and cation-exchange capacity (Zhang and Kong, 2014). Importantly, the soil surrounding Benggang contains a substantial amount of iron oxide and kaolinite, distinguishing it from other charged soils like purple soil and loessal soil. When this charged soil is dispersed in water, electrical double layers form on both kaolinite and iron oxides. These oppositely charged particles interact with each other by overlapping diffuse layers of electric double layers (Qafoku and Sumner, 2002; Qafoku et al., 2004), thereby altering the surface charge density and subsequently impacting the stability of the soil aggregates (Gao et al., 2019). However, the influence of iron oxides on the surface properties of Benggang soil and their contribution to the formation of Benggang remains largely unexplored despite extensive research in this area.

Moreover, the soil collected in and around Benggang exhibits a distinct layering pattern based on depth, consisting of red soil, sandy soil, and clastic layers. The presence of varying mineralogical compositions within these horizons can lead to significant modifications in their physicochemical properties (Chen et al., 2018). Furthermore, a comparison between Benggang soil and soil collected prior to its formation reveals a decrease in iron oxide concentrations within the red soil layers following the erosive event, while the opposite trend is observed in the sandy soil and clastic layers (Huang et al., 2019). This raises a pivotal question regarding the role of iron oxide content as the primary factor triggering Benggang formation.

To address this issue, we conducted soil sampling in the vicinity of a Benggang in southern China, removing free iron oxide and subsequently introducing goethite to examine the resulting changes in soil properties. Through the analysis of surface charge density and shrinkage characteristics of the red soil, sandy soil, and clastic layers, we aim to elucidate the role of free iron oxides in influencing the surface properties of each soil type and their impact on Benggang formation.

2 Study area

The undisturbed soil samples used in this study were collected from Benggang located at Yangkeng Village in Longmen Town, Fujian Province, China, (118° 05′E, 24° 57′N), which corresponds to the same site as documented in Huang et al. (2019). A multi-point sampling approach was adopted (Figure 1), wherein three soil samples were collected within a defined area of each layer (approximately 0.5 hm^2) to create a composite sample representative of that particular horizon.

3 Material and methods

3.1 Soil physicochemical properties and pretreatment

The bulk density, pH (using a solution-to-soil ratio of 5:1), cation-exchange capacity, and mineralogical compositions of the red soil (Soil-A_1), sandy soil (Soil-A_2), and clastic layers (Soil-A_3) in the undisturbed soil samples were measured in accordance with the methodology outlined in our previous study (Zhang et al., 2023). Subsequently, the undisturbed soil samples were naturally air-dried and ground to achieve a particle size smaller than 2 mm. Approximately 50 g of each soil sample was mixed with 25 mL of a 30% H_2O_2 solution in a 500-mL beaker, which was then subjected to heating at 75°C while simultaneously being mechanically agitated until no bubbles were observed. This process effectively removed all organic matter present in the soil samples. All reagents utilized in the experiment were of analytical grade, and ultrapure water sourced from a Milli-Q Labo apparatus (Nihon Millipore Ltd.) was used for the preparation of solutions. Unless specifically noted, all experiments in this study were replicated three times and all results are expressed as means ± standard deviation (n = 3).

3.2 Removal and addition of iron

The removal of free iron oxides from the undisturbed soil samples in each layer (labeled as Soil-B_1, Soil-B_2, and Soil-B_3) was conducted through a series of meticulous steps (Wu et al., 2017; Chen et al., 2018). Initially, a beaker containing pretreated soil was subjected to a stepwise addition of 40 mL of a sodium citrate solution (0.3 M), 5 mL of a sodium bicarbonate solution (1 M), and 2 g of sodium dithionite. This process was carried out at a temperature of 80°C and repeated until the color of the soil transitioned from red to gray. Subsequently, the gray soil was subjected to three consecutive rinses with deionized water through centrifugation at 4,000 rpm for 20 min per rinse. The resulting precipitate was then freeze-dried for a duration of 10 h

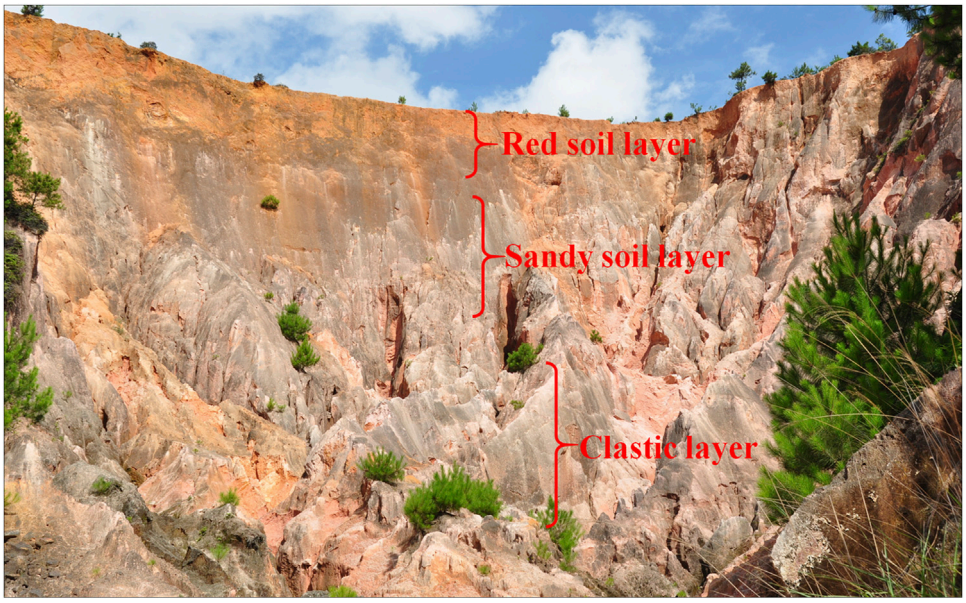

FIGURE 1
Photograph of a typical Benggang at Yangkeng Village in Longmen Town, Fujian Province, China. The layered soil structure and associated sampling sites are labeled.

and subsequently sieved using a 2-mm sieve. The concentration of free iron oxides present in the supernatant was determined using phenanthroline colorimetry.

The introduction of iron into Soil-B was accomplished through the following procedure (Ma et al., 2007). Firstly, the initial moisture content of Soil-B was measured using conventional drying techniques. Subsequently, 53.94 g, 45.75 g, and 35.83 g of goethite was separately added to 1,000 g of the Soil-B_1, Soil-B_2, and Soil-B_3 layers, respectively. These goethite additions were thoroughly mixed with deionized water until homogeneity was achieved, ensuring the absence of any agglomerations. The resulting prepared soils, designated as Soil-C_1, Soil-C_2, and Soil-C_3, were sealed overnight and subsequently placed in an uncovered plastic box to cultivate at room temperature for a period of 1 month. The water content of each soil sample during this process was maintained at 20% ± 1%. Finally, each soil sample was air-dried and passed through a 2-mm sieve.

3.3 Soil shrinkage ratio test

Each pretreated soil sample was diluted with deionized water to achieve a bulk water content of 15% ± 1%. The mixture was thoroughly mixed until homogenized and subsequently sealed, allowing it to sit undisturbed overnight. After that, a ring-knife sample (diameter, 61.8 mm; height, 20 mm) was prepared from this soil using conventional geotechnical test methods. This process was repeated three times for each soil sample to ensure reliability. To determine the linear shrinkage rate, a soil constrictor (TKA-SSY-1, Nanjing Teco Technology Co., LTD, China) equipped with a data acquisition box (TKA-Dai-8D) and data acquisition and processing software V2.1 was employed. After performing these experiments, the height, diameter, and weight of each soil sample was determined to obtain their water content and longitudinal and transverse shrinkage rates.

3.4 Soil surface property

3.4.1 Collection of soil colloidal particles

Each pretreated soil sample (i.e., Soil-A, Soil-B, and Soil-C) was subjected to a sequential addition of approximately 300 mL of deionized water and 10 mL of a 5% sodium metaphosphate solution. The mixture was then placed in a high-speed mixer and stirred for a duration of 10 min at a speed of 500 rpm. The well-stirred soil liquid was subsequently transferred into a 1-L measuring cylinder and further stirred 30 times using a stirring rod. After allowing the suspension to settle for a period of 20 h, the uppermost 7 cm of the suspension within the measuring cylinder was carefully collected. This collected suspension was then subjected to centrifugation and freeze-drying processes to obtain soil colloidal particles with a size of less than 1,000 nm. The crystalline components of all the soil colloidal particles were analyzed using an automated Rigaku Utimal X-ray diffractometer (XRD) equipped with Cu kα radiation. The XRD analysis was performed under the following operating conditions: 40 kV × 40 mA and a 2θ degree angle ranging from 10° to 90° at a scan rate of 4° min^{-1}.

3.4.2 Determination of surface charge density

The surface charge properties of the soil colloids were determined following the combined method of Li et al. (2011), which involved multiple steps. Firstly, 10 g of the colloidal particles from each soil sample (as previously described) were carefully placed in a 500-mL centrifuge bottle, ensuring a soil-to-liquid ratio of 1:5. Subsequently, 50 mL of 0.1 M HCL solution was added to the bottle, and the mixture was subjected to centrifugation for a duration of

12 h. After that, the supernatant was discarded, and this procedure was repeated three times, after which it was finally freeze-dried. Next, 2 g of the freeze-dried soil colloid particles were transferred into another 500-mL centrifuge bottle and were oscillated for 12 h during the addition of 15 mL of 0.02 M $Ca(OH)_2$ solution. Following this, another 24 h period of oscillation was carried out, during which 15 mL of 0.02 M NaOH was added. The pH value of the mixture was adjusted to a range of 6.0–8.0 after the oscillation. This process continued for at least 12 h until the pH reached a neutral value. Finally, the mixed solution was subjected to centrifugation at a speed of 4,000 rpm to obtain the supernatant. The concentrations of Ca^{2+} and Na^+ in the supernatant were measured by atomic absorption spectrometry (PerkinElmer, PinAAcle900F, United States of America) and flame photometry (FP640, Shanghai Precision and Scientific Instrument Co., Ltd., China). The surface charge density (σ_0) and surface potential (φ_0) in the mixed system were calculated as follows (Li et al., 2011):

$$\sigma_0 = \frac{(N_{Na^+} + 2N_{Ca^{2+}}) \times F \times 10^{-5}}{S}$$

$$S = \frac{\kappa N_{Na^+}}{mC^0_{Ca}} e^{\frac{\beta_{Na} F \varphi_0}{2RT}}$$

$$\varphi_0 = \frac{2RT}{(\beta_{Ca} - \beta_{Na})F} ln \frac{C_{Ca^0} N_{Na^+}}{C_{Na^0} N_{Ca^{2+}}}$$

$$\beta_{Ca} = 2 - \beta_{Na} = -0.0213\, ln\, I^{0.5} + 1.2331$$

$$\kappa = \sqrt{\frac{8\pi F^2 C^0}{\varepsilon RT}}$$

Where C_{Na^0}, C_{Ca^0}, N_{Na^+}, and $N_{Ca^{2+}}$ are the bulk concentrations and the adsorbing capacities of Na^+ and Ca^{2+}, respectively. β_{Ca} and β_{Na} are the relative charge coefficients of Na^+ and Ca^{2+}, respectively. $I^{0.5}$ is the square root of the ionic strength in the bulk solution. R, T, F, and S represent the gas constant, absolute temperature (Kelvin), Faraday constant, and the specific surface area of charged soil particles, respectively. κ, m, and ε denote the Debye–Hückel parameter, the modification factor ($m = 0.5259\, ln(\frac{C_{Na^0}}{C_{Ca^0}}) + 1.992$) and the dielectric constant of water, respectively.

3.5 Statistical analysis

Data analysis was conducted using IBM SPSS statistics, employing the least significant difference approach. Specifically, One-way ANOVA with Dunnett's T3 method was utilized for analyzing the shrinkage rate following the removal and subsequent introduction of iron, while the Pearson method was applied to assess the correlation between the soil swelling rate of different soil layers and the shear plane thickness of colloidal particles.

4 Results

4.1 Physical properties of the pretreated soils

The undisturbed soil comprised three distinct types: red soil (Soil-A_1), sandy soil (Soil-A_2), and clastic layers (Soil-A_3). These soils exhibited bulk densities of 1.31, 1.32, and 1.49 g·cm^{-3}, respectively. The pH values of these soils, measured using a solution to soil ratio of 5:1, was determined to be 5.06, 4.82, and 4.65 g·cm^{-3}, respectively. The cation-exchange capacity for Soil-A_1, Soil-A_2, and Soil-A_3 was found to be 8.25, 3.33, and 2.67 cmol·kg^{-1}, respectively. The content of free iron oxide in the red soli was the highest, with a value of 48.57 g·kg^{-1}, followed by the sand soil with 41.19 g·kg^{-1} and debris layers with 32.26 g·kg^{-1}.

Figure 2 displayed the XRD spectra of soil colloidal particles extracted from the pretreated soils. These spectra were carefully compared to relevant references (Chen et al., 2018; Huang et al., 2019) for identification of crystalline types within soil before and after the addition of goethite. The XRD analysis revealed that the red soil and sandy soil layers within Soil-A demonstrated distinct reflection peaks at 6.1°, 8.8°, 12.3°, 18.2°, 24.8°, and 26.6° (Figure 2A), indicating the presence of hydroxy-interlayered vermiculite, illite and kaolinite. Similarly, the clastic layers exhibited characteristic diffraction peaks of illite and kaolinite at 8.8°, 12.3°, 24.8° and 26.6°. These findings align well with previous studies (Huang et al., 2019; Zhang et al., 2023). Notably, the removal of free iron oxide from the undisturbed soil had negligible impact on these XRD reflection peaks, as shown in Figure 2B. Upon the introduction of goethite to Soil-B, the reflection peaks at 8.8°, 12.3°, 18.2°, 24.8°, and 26.6° remained unaltered, while the peak at 6.1° was not observed due to its significantly lower relative intensity (Figure 2C). A new distinct characteristic diffraction peak emerged at 28.4° in Soil-C (Figure 2C). Through a comparative analysis of these spectra with those of Soil-A, Soil-B, and the standard data JCPDS 29-0713 and 54-0489, it was determined that the emergence of this new peak could be attributed to the presence of Fe_2O_3, which originated from the introduction of goethite.

4.2 Shrinkage characteristics

As shown in Figure 3A, it could be observed that the clastic layer of the undisturbed soil exhibited the highest linear shrinkage rate (0.40%) during the 96-h measurement period, while the sandy and red soil layers in the undisturbed soil experienced minimal changes, with linear shrinkage rates of 0.32% and 0.13%, respectively. Upon the removal of free iron oxides (Figure 3B), the red soil layer (Soil-B_1) demonstrated the most pronounced linear shrinkage rate, reaching a magnitude of 2.38%. This value presented an over 18-fold increase compared to the initial linear shrinkage. Subsequently, the sandy soil layer and the clastic layer followed suit with linear shrinkage rates of 1.15% and 0.42%, respectively. Furthermore, upon the addition of goethite (Figure 3C), the corresponding red soil layer (Soil-C_1), sand soil layer (Soil-C_2), and clastic (Soil-C_3) layers experienced a degree of restoration, resulting in linear shrinkage rates of 1.65%, 0.85% and 0.45%, respectively. We also conducted a significance test on the linear shrinkage rate following the removal and subsequent addition of iron. As a result, significant changes ($\rho < 0.05$) were noted in the red soil and sandy soil; however, no statistically significant change ($\rho > 0.05$) was observed in the clastic layer.

To further evaluate the impact of free iron oxide on the soils, we followed the established guidelines outlined by Mishra et al. (2020), wherein we calculated the volume shrinkage of ring-knife samples subsequent to shrinkage. As illustrated in Figure 4, the red soil layer exhibited the most substantial disparity in volume after the removal of free iron oxide, with a magnitude of 14,592.19 mm^3. The sandy

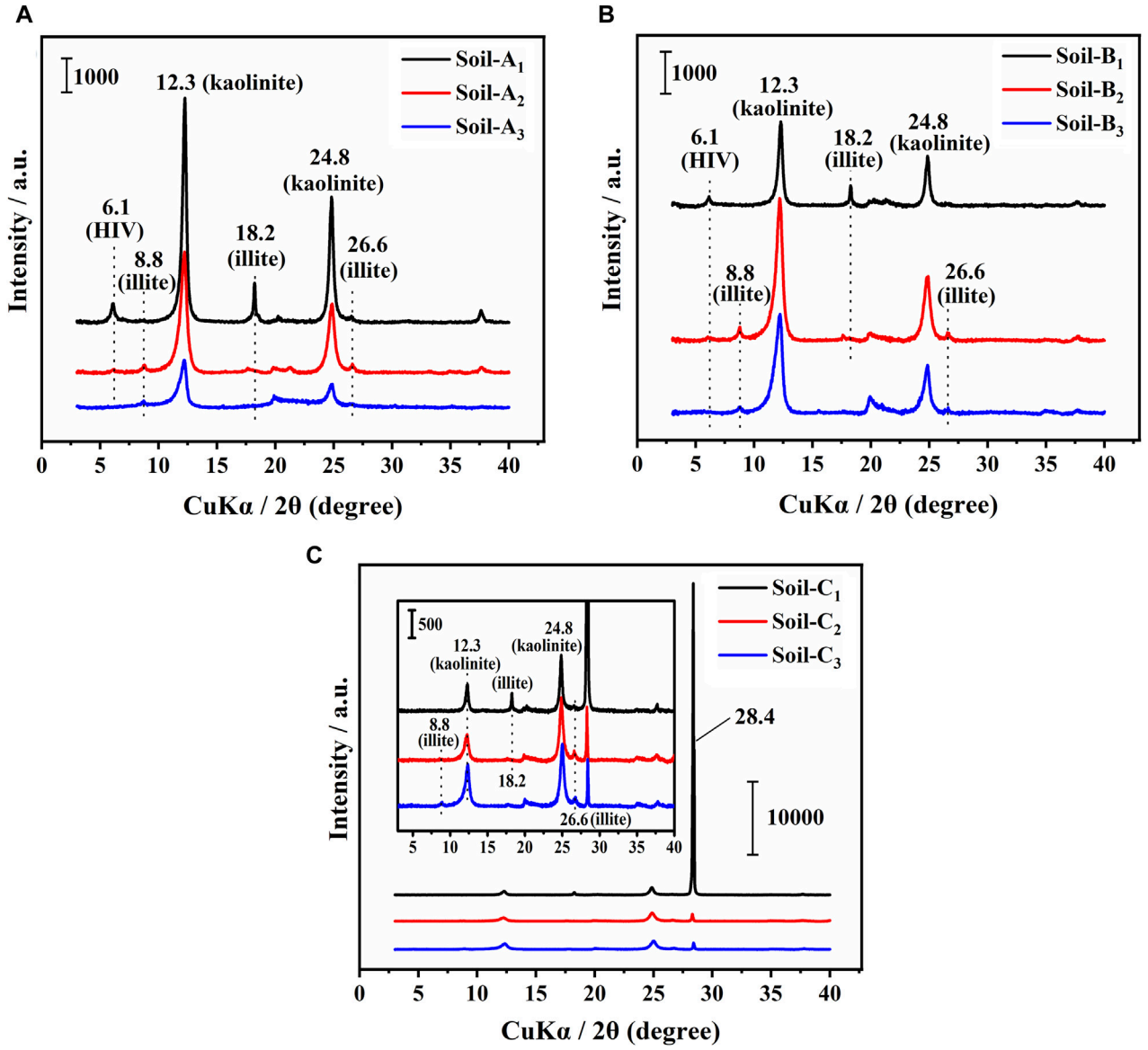

FIGURE 2
XRD spectra of soil colloidal particles collected from **(A)** undisturbed soil (Soil-A), **(B)** undisturbed soil without free iron oxides (Soil-B), and **(C)** Soil-B with the addition of goethite (Soil-C). The inset in part **(C)** shows an enlargement of the spectra. Numbers are as follows: 1, red soil layers; 2, sandy soil layers; 3, clastic soil layers. HIV: hydroxy-interlayered vermiculite.

soil layer followed suit with a volume difference of 9,343.09 mm^3, while the clastic layer displayed a comparatively minor volume difference of 550.14 mm^3. Subsequently, in the case of Soil-B, when subjected to goethite cultivation, the volume shrinkages of Soil-C_1, Soil-C_2, and Soil-C_3 were determined to be approximately 97.54%, 94.75%, and 89.72% of the initial value of the corresponding undisturbed soil layers, respectively.

4.3 Surface charge density of the pretreated soil colloidal particles

Table 1 demonstrated that the surface potential of soil colloidal particles from each soil layer ranged from −67.77 ± 4.73 mV to −82.01 ± 4.88 mV, which correlated with findings reported for purple soil (Ding et al., 2015). For the undisturbed soil (Soil-A), the surface potential of red soil colloidal particles (Soil-A_1) was more negative at −79.78 ± 3.55 mV compared to sandy soil (Soil-A_2) at −76.52 ± 2.03 mV and the clastic (Soil-A_3) layer at −70.94 ± 3.84 mV. Similarly, the calculated surface charge density of the red soil colloidal particles (Soil-A_1, 3.32 ± 0.33 × 10^{-2} C·m^{-2}) was considerably higher than for the sandy soil (Soil-A_2, 1.94 ± 0.04 C·m^{-2}) and the clastic (Soil-A_3, 1.61 ± 0.31 C·m^{-2}) layer. Upon removing free iron oxides from the undisturbed soil, the cation-exchange capacity for the red soil, sandy soil, and clastic layer changed by 6% each. Most importantly, reductions of 44.28%, 20.62%, and 8.70% were observed in the surface charge density of colloidal particles collected from the red soil (Soil-B_1), sandy soil

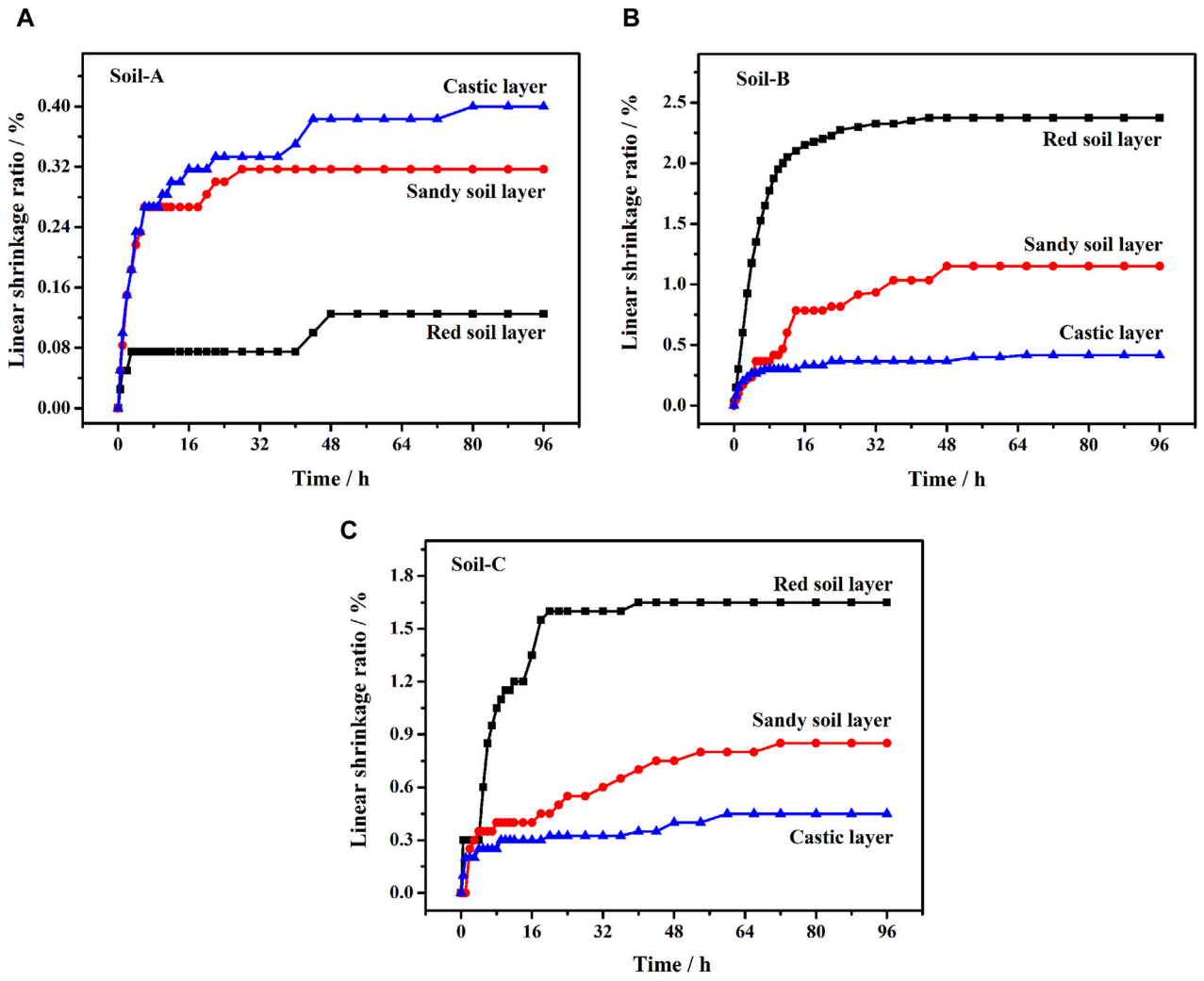

FIGURE 3
Linear shrinkage ratio of **(A)** undisturbed soil (Soil-A), **(B)** undisturbed soil without free iron oxides (Soil-B), and **(C)** Soil-B with the addition of goethite (Soil-C).

(Soil-B_2), and clastic layer (Soil-B_3), respectively. Subsequently, upon the introduction of goethite into Soil-B, the initial surface charge density increased by approximately 81.93% (Soil-C_1), 121.13% (Soil-C_2), and 104.35% (Soil-C_3) in comparison to the corresponding layers in the undisturbed soil. Furthermore, the surface potential of the red soil experienced a reduction after the removal of free iron oxides, which was subsequently reversed by the addition of goethite. In contrast, opposite trend was observed for sandy soil. Notably, the surface potential of the clastic layer did not show significant influence through this process.

4.4 Pearson correlation between the content of free iron oxide and soil properties

Table 2 presented the Pearson correlations between the content of free iron oxide and various soil properties. The analysis revealed that the content of free iron oxide in all soil layer exhibited a consistently low negative correlation with the linear shrinkage rate, and no significant change in this relationship was observed. Furthermore, the analysis indicated the absence of any significant positive correlation between the content of free iron oxide and volume shrinkage. Additionally, no statistically significant correlation was estimated between the content of free iron oxide and surface potential. In contrast, the content of free iron oxide demonstrated moderate and statistically significant negative correlations with the specific surface area of charged soil particles ($\rho < 0.05$), and surface charge density ($\rho < 0.05$).

5 Discussion

Previous studies have extensively documented the profound influence of clay minerals on the physicochemical and surface properties of soil (Hou et al., 2007; Jiang et al., 2010; Wang et al., 2013). In this study, we conducted a designed experiment to investigate the role of free iron oxide in Benggang soil layers, including red, sandy and detritus soil layers. To achieve this, we employed a rigorous

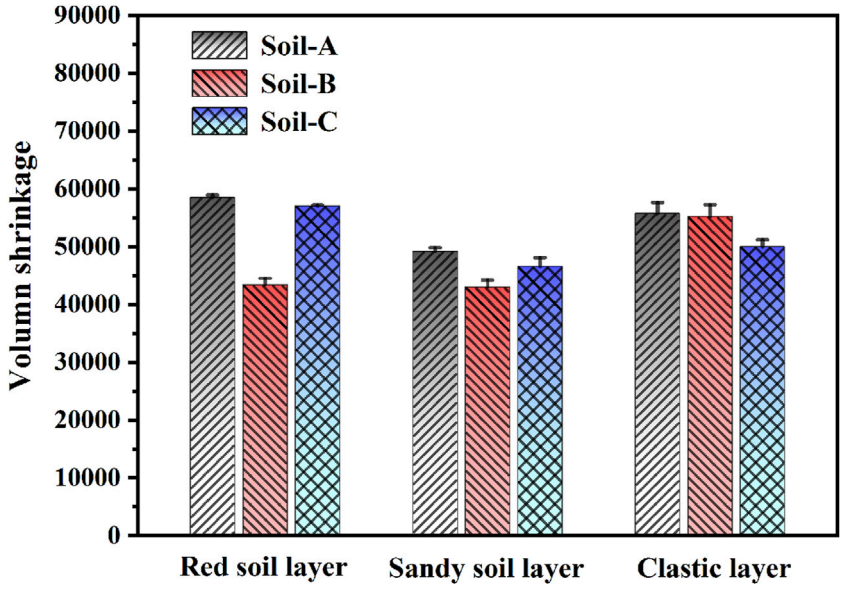

FIGURE 4
Volume shrinkage of undisturbed soil (Soil-A), undisturbed soil without free iron oxides (Soil-B), and Soil-B with the addition of goethite (Soil-C).

TABLE 1 Surface properties of colloidal particles for all pretreated soils.

Soil type	C_{Na+} (10^{-3} M)	C_{Ca2+} (10^{-3} M)	Adsorbing capacity (10^{-2} mol kg^{-1})		S (10^3 m^2 kg^{-1})	φ_0 (mV)	σ_0 (10^{-2} C m^{-2})
			Na^+	Ca^{2+}			
A_1	3.62 ± 0.13	1.28 ± 0.15	3.67 ± 0.01	3.91 ± 0.02	33.33 ± 3.76	−79.78 ± 3.55	3.32 ± 0.33
B_1	1.93 ± 0.21	0.57 ± 0.06	3.84 ± 0.02	3.97 ± 0.01	61.38 ± 15.06	−82.01 ± 4.88	1.85 ± 0.34
C_1	3.14 ± 0.08	1.23 ± 0.09	3.71 ± 0.08	3.90 ± 0.07	41.16 ± 2.94	−76.87 ± 2.33	2.72 ± 0.17
A_2	2.26 ± 0.13	0.87 ± 0.13	3.80 ± 0.01	3.94 ± 0.01	57.88 ± 1.53	−76.52 ± 2.03	1.94 ± 0.04
B_2	1.92 ± 0.07	0.87 ± 0.14	3.84 ± 0.01	3.94 ± 0.01	73.51 ± 8.49	−72.7 ± 4.73	1.54 ± 0.21
C_2	2.57 ± 0.90	0.87 ± 0.10	3.77 ± 0.09	3.94 ± 0.01	47.87 ± 2.29	−79.57 ± 2.76	2.35 ± 0.11
A_3	2.08 ± 0.21	1.02 ± 0.07	3.82 ± 0.02	3.93 ± 0.01	70.01 ± 10.61	−70.94 ± 3.84	1.61 ± 0.31
B_3	2.03 ± 0.07	1.14 ± 0.22	3.83 ± 0.01	3.91 ± 0.02	76.43 ± 10.42	−67.77 ± 4.73	1.47 ± 0.17
C_3	2.28 ± 0.06	1.21 ± 0.10	3.80 ± 0.08	3.91 ± 0.02	65.63 ± 6.82	−69.30 ± 3.97	1.68 ± 0.18

A, undisturbed soil (Soil-A); B, undisturbed soil without free iron oxides (Soil-B); C, Soil-B, with the addition of goethite (Soil-C); 1, red soil layers; 2, sandy soil layers; and 3, clastic soil layers.

TABLE 2 Pearson correlation between the presence of free iron oxide and soil properties.

	Parameter	S (10^3 m^2 kg^{-1})	φ_0 (mV)	σ_0 (10^{-2} C m^{-2})	Linear shrinkage rate (%)	Volume shrinkage
Fe ($g{\cdot}kg^{-1}$)	Pearson correlation	−0.771*	−0.279	−0.702*	−0.34	0.502
	Two-tailed test	0.015	0.468	0.035	0.370	0.168

Asterisk indicates significant values at the 0.05 level (two-tailed).

methodology, which involved the systematic removal of free iron oxide from all soil layers and the subsequent introduction of goethite into the respective soil layers. Our analysis of the XRD spectra revealed that the removal of free iron oxide did not exert a significant influence on the presence of characteristic reflection peaks. However, upon the addition of goethite, a distinct change manifested in the XRD spectra, specifically the emergence of a well-defined diffraction peak at 28.4° (Figure 2). It is crucial to note that this peak was attributed to Fe_2O_3 rather than

goethite. This distinction arises from the fact that goethite in the soil, with the passage of 1 month of cultivation, underwent a process of remodeling after and was ultimately transformed into iron oxide.

The shrinkage characteristic of soil is a fundamental parameter that plays a crucial role in assessing its mechanical properties. Upon removing free iron oxide from Benggang soil, we observed a remarkable increase in the initial linear shrinkage of the red soil and sandy soil layers, with magnitudes exceeding 18-fold and 3.5-fold, respectively. However, no significant change occurred in the clastic layer (Figure 3B). In contrast, upon the introduction of goethite, a substantial decrease in the linear shrinkage rates was observed. Specifically, the red and sandy soil layers exhibited reductions of over 12-fold and 2.6-fold, respectively (Figure 3C). These phenomena could be attributed to the fact that soil physical properties, including soil cohesion, were directly influenced the presence of free iron oxide (Zhang and Kong, 2014). The rapid escalation of soil shrinkage rate directly contributed to the instability of the soil structure, potentially leading to soil erosion. In particular, loose subsoil, such as sandy or detritus soil layer, with low Fe-oxide contents disintegrated first after rainfall, followed by the collapse of the structurally stable red soil with high Fe-oxide contents, ultimately resulting in soil erosion. When goethite was introduced into the corresponding soil layers in the absence of free iron oxide, a significant volume shrinkage of approximately 97.54%, 94.75%, and 89.72% of the initial value was observed in the undisturbed red, sandy and detritus soil layers, respectively. These results clearly established a direct correlation between the presence of free iron oxide content in the soil and the magnitude of shrinkage it underwent.

The removal of free iron oxide and the introduction of goethite possess the inherent capabilities to induce alterations in both the surface charge density and surface potential, which, in turn, have the potential to exert a profound influence on the overall stability of a soil aggregate (Gao et al., 2019). Our measurements of the surface charge density of soil colloidal particles collected from the undisturbed Benggang soil revealed a range of values, ranging from −67.77 ± 4.73 mV to −82.01 ± 4.88 mV (Table 1). These values were consistent with previous findings of −82.8 ± 5.2 mV reported for acidic purple soil with a pH of 4.65 (Ding et al., 2015). However, they slightly differed from the values of −82.79 ± 4.73, −63.45 ± 5.39, and −90.55 ± 13.73 mV obtained in our previous study (Zhang et al., 2023), possibly due to variations in soil physicochemical properties, such as pH value. The removal of free iron oxide (Soil-B) resulted in a decrease in the surface charge density with increasing soil depths, indicating that the presence of free iron oxides had the most significant influence on the surface charge density. Subsequently, upon adding goethite into the corresponding soil layers in the absence of free iron oxide (Soil-C), the surface charge densities reached approximately 81.93%, 121.13%, and 104.35% of the initial surface charge density. Obviously, the impact of free iron oxide varied among soil layers, consistent with the observed variation in soil shrinkage mentioned earlier. The relationships between the content of free iron oxide and soil properties (Table 2), including surface potential, surface charge density and shrinkage, further confirmed the aforementioned results. Nevertheless, the absence of a substantial correlation between shrinkage and free iron oxide content, might be attributed to the fact that alterations in the levels of free iron oxides directly affect soil cohesion, thereby indirectly influencing soil swelling and shrinkage dynamics.

6 Conclusion

Our experimental results show that the surface charge density of undisturbed soil colloidal particles in a Benggang decreases with depth: specifically, the red soil layer has the highest surface charge density, and the debris (clastic) layer has the lowest surface charge density. After the removal of free iron oxide from each layer, this effect did not change, and reductions of 44.28%, 20.62%, and 8.70% were determined for surface charge density of the colloidal particles for red soil, sandy soil, and clastic layers, respectively. After the addition of goethite, the soil colloidal particles recovered approximately 81.93%, 121.13%, and 104.35% of their initial surface charge density, respectively. Furthermore, free iron oxide has an impact on soil shrinkage characteristics, which is especially pronounced for the red soil layer. Approximately 97.54% (red soil), 94.75% (sandy soil), and 89.72% (clastic layer) of the initial volume shrinkage can be achieved by the addition of goethite into the iron oxide-free soil layers, respectively. These results indicate that free iron oxide has the maximum influence on the surface charge density of soil colloidal particles and shrinkage characteristics in red soil layers, followed by sandy soil and clastic layers.

Data availability statement

The raw data supporting the conclusion of this article will be made available by the authors, without undue reservation.

Author contributions

LJ: Investigation, Methodology, Writing–original draft. JC: Investigation, Visualization, Writing–original draft. L-XY: Conceptualization, Data curation, Writing–review and editing. F-SJ: Formal Analysis, Writing–review and editing. YZ: Formal Analysis, Writing–review and editing. J-SL: Conceptualization, Resources, Writing–review and editing. Y-HH: Funding acquisition, Project administration, Supervision, Writing–review and editing.

Funding

The author(s) declare that financial support was received for the research, authorship, and/or publication of this article. This work was supported by the National Natural Science Foundation of China (grant number 41571272), Water Conservancy Science and Technology Project of Fujian Province (KJG21009A), and Modern Agricultural-Industrial Collaborative Innovation Center of Anxi County (KMD18003A).

Conflict of interest

The authors declare that the research was conducted in the absence of any commercial or financial relationships that could be construed as a potential conflict of interest.

Publisher's note

References

Chaplot, V. (2013). Impact of terrain attributes, parent material and soil types on gully erosion. *Geomorphology* 186, 1–11. doi:10.1016/j.geomorph.2012.10.031

Chen, J., Zhou, M., Lin, J., Jiang, F., Huang, B., Xu, T., et al. (2018). Comparison of soil physicochemical properties and mineralogical compositions between noncollapsible soils and collapsed gullies. *Geoderma* 317, 56–66. doi:10.1016/j.geoderma.2017.12.006

Ding, W., Zhu, Q., Wang, L., Luo, Y., Li, Q., Zhu, H., et al. (2015). Calculation of thickness of shear plane in diffuse double layer of constant charge soil colloid in single electrolyte system. *Acta Pedol. Sin.* 52, 859–868. doi:10.11766/trxb201409060453

Gao, X., Li, S., Liu, X., Hu, F., Tian, R., and Li, H. (2019). The effects of NO3- and Cl-on negatively charged clay aggregation. *Soil till. Res.* 186, 242–248. doi:10.1016/j.still.2018.10.025

Gyssels, G., Poesen, J., Bochet, E., and Li, Y. (2005). Impact of plant roots on the resistance of soils to erosion by water: a review. *Prog. Phys. Geog.* 29, 189–217. doi:10.1191/0309133305pp443ra

Hou, T., Xu, R. K., Tiwari, D., and Zhao, A. Z. (2007). Interaction between electrical double layers of soil colloids and Fe/Al oxides in suspensions. *J. Colloid Interf. Sci.* 310, 670–674. doi:10.1016/j.jcis.2007.02.035

Huang, B., Qiu, M., Lin, J., Chen, J., Jiang, F., Wang, M. K., et al. (2019). Correlation between shear strength and soil physicochemical properties of different weathering profiles of the non-eroded and collapsing gully soils in southern China. *J. Soil. Sediment.* 19, 3832–3846. doi:10.1007/s11368-019-02313-7

Jiang, F. S., Huang, Y. H., Wang, M. K., Lin, J. S., Zhao, G., and Ge, H. L. (2014). Effects of rainfall in tensity and slope gradient on steep colluvial deposit erosion in Southeast China. *Soil Sci. Soc. Am. J.* 78, 1741–1752. doi:10.2136/sssaj2014.04.0132

Jiang, J., Xu, R. K., and Zhao, A. Z. (2010). Comparison of the surface chemical properties of four soils derived from Quaternary red earth as related to soil evolution. *Catena* 80, 154–161. doi:10.1016/j.catena.2009.11.002

Li, H., Hou, J., Liu, X. M., Li, R., Zhu, H. L., and Wu, L. S. (2011). Combined determination of specific surface area and surface charge properties of charged particles from a single experiment. *Soil Sci. Soc. Am. J.* 75, 2128–2135. doi:10.2136/sssaj2010.0301

Lin, J., Huang, Y., Zhao, G., Jiang, F., Wang, M. K., and Ge, H. (2017). Flow-driven soil erosion processes and the size selectivity of eroded sediment on steep slopes using colluvial deposits in a permanent gully. *Catena* 157, 47–57. doi:10.1016/j.catena.2017.05.015

Ma, L., Wang, Q., and Yuan, G. H. (2007). Study on the microstructure of cementation function of free iron oxide in red soil. *J. Hebei Univ. Eng.* 24, 28–31. doi:10.3969/j.issn.1673-9469.2007.01.008

Mishra, P. N., Zhang, Y., Bhuyan, M. H., and Scheuermann, A. (2020). Anisotropy in volume change behaviour of soils during shrinkage. *Acta Geotech.* 15, 3399–3414. doi:10.1007/s11440-020-01015-6

Qafoku, N. P., and Sumner, M. E. (2002). Adsorption and desorption of indifferent ions in variable charge subsoils: the possible effect of particle interactions on the counter-ion charge density. *Soil Sci. Soc. Am. J.* 66, 1231–1239. doi:10.2136/sssaj2002.1231

Qafoku, N. P., Van Ranst, E., Noble, A., and Baert, G. (2004). Variable charge soils: their mineralogy, chemistry and management. *Adv. Agron.* 84, 159–215. doi:10.1016/S0065-2113(04)84004-5

Six, J., Bossuyt, H., Degryze, S., and Denef, K. (2004). A history of research on the link between (micro)aggregates, soil biota, and soil organic matter dynamics. *Soil till. Res.* 79, 7–31. doi:10.1016/j.still.2004.03.008

Wang, B., Zhang, G. H., Shi, Y. Y., and Zhang, X. C. (2014). Soil detachment by overland flow under different vegetation restoration models in the Loess Plateau of China. *Catena* 116, 51–59. doi:10.1016/j.catena.2013.12.010

Wang, B., Zhang, G. H., Yang, Y. F., Li, P. P., and Liu, J. X. (2018). The effects of varied soil properties induced by natural grassland succession on the process of soil detachment. *Catena* 166, 192–199. doi:10.1016/j.catena.2018.04.007

Wang, Y. P., Xu, R. K., and Li, J. Y. (2013). Effect of Fe/Al hydroxides on desorption of K+ and NH4+ from two soils and kaolinite. *Pedosphere* 1, 81–87. doi:10.1016/S1002-0160(12)60082-4

Wei, J., Shi, B., Li, J., Li, S., and He, X. (2018). Shear strength of purple soil bunds under different soil water contents and dry densities: a case study in the three gorges reservoir area, China. *Catena* 166, 124–133. doi:10.1016/j.catena.2018.03.021

Wu, X. L., Wei, Y. J., Wang, J. G., Wang, D., She, L., Wang, J., et al. (2017). Effects of soil physicochemical properties on aggregate stability along a weathering gradient. *Catena* 156, 205–215. doi:10.1016/j.catena.2017.04.017

Xia, J., Cai, C., Wei, Y., and Wu, X. (2019). Granite residual soil properties in collapsing gullies of south China: spatial variations and effects on collapsing gully erosion. *Catena* 174, 469–477. doi:10.1016/j.catena.2018.11.015

Xia, J., Cai, C., Wei, Y., Zhou, Y., Gu, J., Xiong, Y., et al. (2021). Variations of soil hydraulic properties along granitic slopes in Benggang erosion areas. *J. Soil. Sediment.* 21, 1177–1189. doi:10.1007/s11368-020-02843-5

Xu, J. X., and Zeng, G. H. (1992). "Benggang erosion in sub-tropical granite weathering crust geo-ecosystems: an example from Guangdong Province," in *Erosion, debris flows and environment in mountain regions*. Editor D. E. Walling, (Wallingford, Oxfordshire, UK: IAHS Publication), 455–463.

Xu, J. X. (1996). Benggang erosion: the influencing factors. *Catena* 27, 249–263. doi:10.1016/0341-8162(96)00014-8

Yu, T. R. (1997) *Chemistry of variable charge soils*. New York: Oxford University Press.

Zhang, X., and Kong, L. (2014). Interaction between iron oxide colloids and clay minerals and its effect on properties of clay. *Chin. J. Geotechnical Eng.* 36, 65–74. doi:10.11779/CJGE201401004

Zhang, Y., Zhao, D. F., Zheng, Q. M., Lin, J. S., Jiang, F. S., Huang, B. F., et al. (2022). Temperature on soil Atterberg limit in soil of collapsing gully wall in the hilly granitic region of south China. *Acta Pedol. Sin.* 59, 119–128. doi:10.11766/trxb20200730087

Zhang, Z., You, L. X., Lin, J. S., Wu, Y. B., Zhong, H. L., Chen, J., et al. (2023). Impact of soil surface properties on soil swelling of different soil layers in collapsing wall of Benggang. *Plos One* 18, e0280729. doi:10.1371/journal.pone.0280729

Zhong, B., Peng, S., Zhang, Q., Ma, H., and Cao, S. (2013). Using an ecological economics approach to support the restoration of collapsing gullies in southern China. *Land Use Policy* 32, 119–124. doi:10.1016/j.landusepol.2012.10.005

frontiers | Frontiers in Environmental Science

TYPE Original Research
PUBLISHED 14 June 2024
DOI 10.3389/fenvs.2024.1410918

OPEN ACCESS

EDITED BY
Narsimha Adimalla,
East China University of Technology, China

REVIEWED BY
Quanhou Dai,
Guizhou University, China
Fengling Gan,
Chongqing Normal University, China

*CORRESPONDENCE
Youcai Kang,
kangyc@nwnu.edu.cn

RECEIVED 03 April 2024
ACCEPTED 28 May 2024
PUBLISHED 14 June 2024

CITATION
Kang Y, Zhang K, Zhang Y and Zhao L (2024), Hydrological response to vegetation restoration and urban sprawl in typical hydrologic years within a semiarid river basin in China.
Front. Environ. Sci. 12:1410918.
doi: 10.3389/fenvs.2024.1410918

Hydrological response to vegetation restoration and urban sprawl in typical hydrologic years within a semiarid river basin in China

Youcai Kang[1]*, Kai Zhang[2], Yuanyuan Zhang[3] and Lianchun Zhao[1]

[1]Key Laboratory of Eco-Function Polymer Materials of Ministry of Education, Key Laboratory of Polymer Materials of Gansu Province, College of Chemistry and Chemical Engineering, Northwest Normal University, Lanzhou, China, [2]Ministry of Education Key Laboratory for Biodiversity Science and Ecological Engineering, Institute of Biodiversity Science, School of Life Sciences, Fudan University, Shanghai, China, [3]Department of Tourism Management, Xinzhou Teachers University, Xinzhou, China

Semiarid regions play a pivotal role in global ecosystem and environmental governance. Changing environment (climate and land use variation) has led to the disruption of hydrology in semi-arid regions and ecological degradation in some area. Understanding their hydrological response to changing environments is crucial for ecological rehabilitation and optimal water resource allocation. This research, conducted in a Chinese semiarid watershed, integrates multi-field models about hydrology, meteorology and geography to investigate hydrological processes in typical hydrological years. The results indicate that the climate in this region is drying, and the likelihood of extreme weather events is increasing with global warming. Projecting changes from 2010 to 2060, 9.21% of grassland converting to 5.63% of forest and 3.58% of gully built-up land. As a result, the flood peak increases by 22.99% in typical drought years, while it decreases by 36.77% in normal years. Based on our analysis of the rainfall-runoff process in typical drought and normal years, we identify two distinct effects: the "local rainfall-runoff effect" and the "global rainfall-runoff effect", respectively. However, in typical wet years, the streamflow state is primarily controlled by intense and concentrated precipitation. This research provides insights into the effect of ecological restoration and typical climate variations on hydrological cycle in semiarid regions, thus contributing to more informed decision-making in environmental management and water resource planning.

KEYWORDS

hydrological processes, land use variation, climate change, SWAT model, the Loess Plateau

1 Introduction

The semiarid regions, as transition zones between wet and dry, are vital regions for ecological management (Zeng et al., 1999; Rotenberg and Yakir, 2010), covering 15% of the world's territory (Li et al., 2015). These regions are particularly sensitive to climate shift and land-use variation due to the infertile soils and fragile ecosystems (Li et al., 2016; Zhou et al., 2016; Huang et al., 2017). Field observations and model simulations alike indicate that semiarid regions respond more significantly to global warming (Huang et al., 2016). For

instance, during the boreal cold season from 1901 to 2009, the warming observed in global semiarid regions exceeded the global average 1.13°C, reaching 1.53°C (Huang et al., 2012). With the projected increase in precipitation and potential evapotranspiration in drylands, these regions face significant challenges (Bates et al., 2008; Scheff and Frierson, 2014; Zhao et al., 2014; Zhao and Dai, 2017). Additionally, their vulnerability to human activities is compounded by water scarcity and sparse vegetation. The rapid population growth and intensifying human activities further strain the ecosystems of semiarid regions, making them a critical focus for ecological management and restoration efforts (Nyamadzawo et al., 2012; Hoover et al., 2015).

The Loess Plateau (LP), renowned for severe soil erosion, occupies a significant portion of China's north-central region. The arid, semiarid, and semi-humid zones constitute 15%, 53%, and 32% of the LP, respectively, based on the aridity index. Historically, the LP was a lush plain, boasting abundant water resources, lush grasslands, dense forests, and fertile soil (Zhao et al., 2013). However, by the late 20th century, soil erosion and intense human activities had transformed over 70% of the region into hilly-gully landscapes, with natural vegetation coverage dwindling to just 31.6% (Shi and Shao, 2000; Tsunekawa et al., 2014). Alarmingly, the erodible loess soil contributes ~90% of the sediment in the Yellow River (Yu et al., 2020), posing a great threat to the lives and property of downstream communities. To address these challenges, the Chinese government has embarked on a series of environmental rehabilitation initiatives since 1999. These include the "Grain for Green Program" (GFGP) (DELANG and Yuan, 2015), the "Gully Land Consolidation Project" (Kang et al., 2021), and land evaluation and replanning efforts (Chen et al., 2003). These measures have obviously altered the land use patterns in the LP. Specifically, agricultural land has shrunk by 28.3%, while grassland and forestland have expanded by 12.4% and 5.0%, respectively. Additionally, urban development areas have grown by 10.8% (Yu et al., 2020). These rehabilitation efforts have effectively mitigated soil erosion and restored some ecological functions in the LP. However, the increased vegetation cover has also altered the hydrological cycle of the region. The expanded vegetation has resulted in increasing rainfall interception and infiltration, reducing surface runoff (McVicar et al., 2007; Zhao et al., 2017). Coupled with global warming, changes in rainfall patterns and temperature have further influenced evapotranspiration, water yield, and soil moisture in the LP. These interconnected processes pose complex challenges for sustainable water resource management and ecological rehabilitation in the semiarid regions of the LP (Zhao et al., 2018; Ge et al., 2020).

Extreme weather and climatic events were relatively rare, but they have become increasingly frequent and devastating in the context of climate variation and population growth (IPCC, 2023). Numerous studies analyzing extreme indices have revealed a global trend towards a rise in the occurrence of extremely wet days, along with notable increases in rainfall intensity, particularly in semiarid regions (Barry et al., 2018; Di Capua and Rahmstorf, 2023; Otto, 2023). Intermittent flooding or prolonged drought events have profound impacts on sustainable socio-economic development and efforts towards regional vegetation restoration (Mokrech et al., 2008; Adhikari et al., 2010; Zhao et al., 2011; Hao et al., 2012). On the LP, even in areas with seemingly successful ecological restoration, extreme precipitation has triggered severe soil erosion. For instance, the prolonged and intense rainfall during July 2013 in the Yanhe watershed (study area in this research) caused flooding hazards, resulting in 6,645 injuries and property damage worth 27 million. Additionally, water scarcity poses a significant obstacle to environmental restoration efforts in the LP. The formation of a soil dried layer is a negative consequence of the GFGP (Jia et al., 2019). In some man-made mature forest, trees growing to only 20% of their regular height due to water scarcity (Chen et al., 2015). The imbalance between water surplus and deficit also significantly impacts streamflow patterns, influenced by climate shifts and land-use variations.

To investigate the hydrological effect of climate variation and land-use modification in semiarid regions, this study focused on the Yanhe watershed, a representative semiarid area within the LP, as the study area. Firstly, we analyzed the temperature, precipitation and streamflow in the last 50 years by Mann-Kendall trend test. Besides, the standard precipitation evapotranspiration index (SPEI) was utilized to categorize the hydrologic years. And then, the Cellular Automata Markov chain (CA-Markov) was employed to forecast the spatial distribution of landscapes in 2060 (China's carbon-neutral target year). By leveraging the classified representative hydrological years and the predicted land-use layout for 2060, the Soil and Water Assessment Tool (SWAT) was engaged to evaluate the influence of vegetation restoration and urban sprawl on streamflow patterns across a range of hydrological conditions. This comprehensive approach provides a profound insight into the hydrological characteristics under varying climatic and land-use conditions, serving as a crucial reference for environmentally sustainable and economically viable development strategies in semi-arid regions.

2 Materials and methods

2.1 Study area in a semiarid region

The Yanhe watershed, situated in the western reaches of China's LP, serves as a representative semiarid region (Figure 1). Spanning an area of 7,634 km^2, it exhibits a remarkable altitudinal range, varying from 495 to 1,793 m. Within this vast territory, approximately 45% of the landmass comprises gentle slopes ranging from 0 to 25°, while the remaining 55% features steeper slopes exceeding 25°. Over the period of 1970–2019, the Yanhe watershed received an average annual precipitation of 477 mm, with a significant concentration of 60% of this rainfall occurring during the flood season, which spans from July to September. The region's land-use pattern is diverse, encompassing farmland, grassland, forest, urban areas, and waterbodies. Notably, the Ganguyi gauging station, positioned downstream, oversees a significant portion of the watershed, encompassing approximately 77% of its total area. Drawing from extensive long-term observation data, it is recorded that the mean annual streamflow at the Ganguyi station has been 1.83×10^8 m^3 over the past 50 years.

2.2 Data sources and processing

The daily meteorological data during 1970–2019 were collected from five weather stations situated within the Yanhe

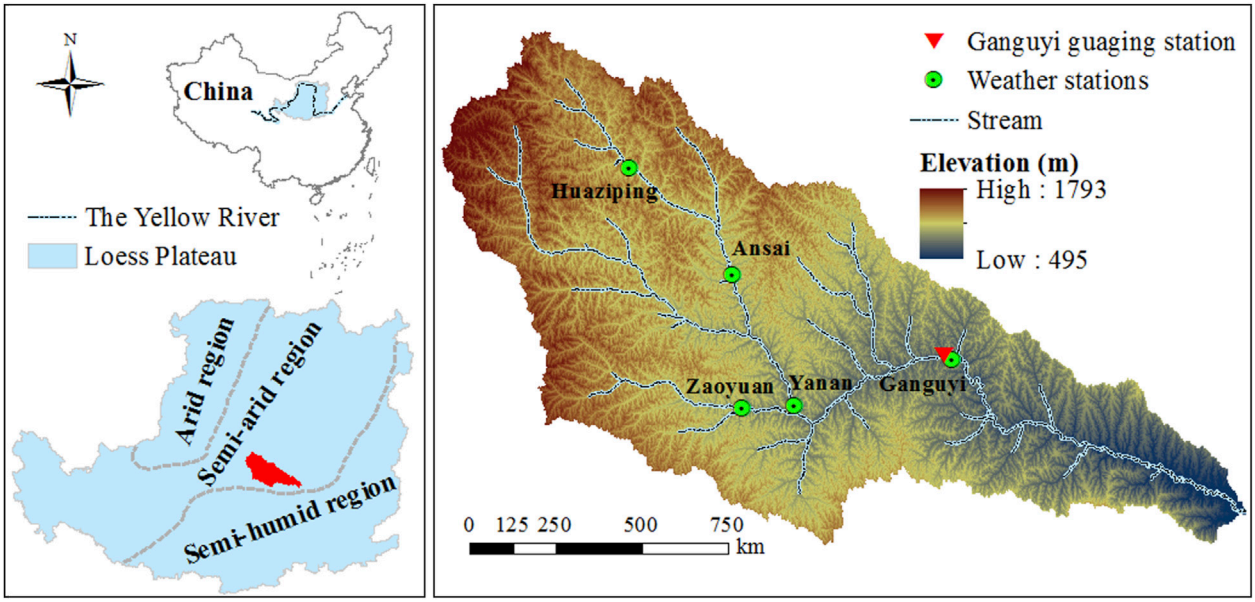

FIGURE 1
Site of the Yanhe watershed and its hydrometeorological stations.

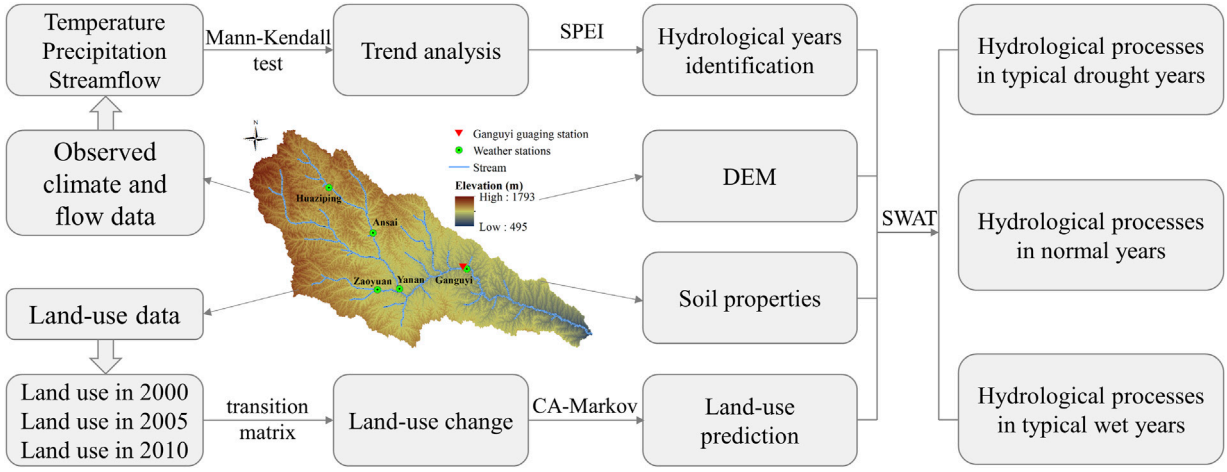

FIGURE 2
Data analysis and model building processes in the Yanhe watershed.

watershed. This data contained precipitation, temperature, solar radiation, humidity, and wind speed. The climate data can reflect the characteristics of climate change during the study period and drive the hydrological model. Additionally, the observed monthly streamflow data from the Ganguyi gauging station, crucial for trend analysis and SWAT model calibration and validation, were accessed from the National Earth System Science Data Center (http://www.geodata.cn) and the Geographic Data Platform of Peking University (https://geodata.pku.edu.cn). Furthermore, to predict land-use patterns and power the SWAT model in the Yanhe watershed, a digital elevation model (DEM) with a high resolution of 30 m × 30 m was procured from the Geospatial Data Cloud (http://www.gscloud.cn). Land-use raster data, also at a resolution of 30 m × 30 m, for the years 1990, 2000, and 2010, were provided by the National Cryosphere Desert Data Center (http://www.ncdc.ac.cn). Additionally, soil properties data with a resolution of 1,000 m × 1,000 m were sourced from the Harmonized World Soil Database (HWSD). This database offers an extensive investigation of global soil attributes at a depth of 1.0 m, including soil texture, organic carbon content, bulk density and others, and the soil properties data can provide a foundation for the localized SWAT model. Utilizing these comprehensive datasets, the hydrological

processes in representative hydrologic years within the Yanhe watershed were researched, leveraging territorial data and multi-field coupling models (Figure 2).

2.3 Research methods

2.3.1 Mann-Kendall test

The Mann-Kendall test is a widely utilized and globally recommended non-parametric approach by the World Meteorological Organization for trend analysis in hydrology and meteorology. Its popularity stems from the fact that it does not assume any specific distribution of samples and is insensitive to seasonality (Van Belle and Hughes, 1984; Nalley et al., 2013). In conducting this test, the null hypothesis (H_0) assumes that the test variables exhibit no trend during the specified period. Conversely, the alternative hypothesis (H_1) rejects H_0 in the presence of a monotonic trend within the test period. The statistical procedures involved in the Mann-Kendall test are outlined as follows (Mann, 1945; Da Silva et al., 2015):

$$S = \sum_{i=1}^{n-1} \sum_{j=i+1}^{n} sgn(X_j - X_i)$$

where the target statistics S is to assess trends in a time series, n denotes the total number of data points in the series, ranging from 1 to n; X_j and X_i represent the respective values at positions j and i within the time series ($i < j$); sgn (X_j–X_i) indicates the difference between X_i and X_j:

$$sgn(X_j - X_i) = \begin{cases} +1 & (X_j - X_i) > 0 \\ 0 & (X_j - X_i) = 0 \\ -1 & (X_j - X_i) < 0 \end{cases}$$

The solution to the series data variance is:

$$Var(S) = \frac{n(n-1)(2n+5) - \sum_{i=1}^{p} t_i(t_i-1)(2t_i+5)}{18}$$

where $Var(S)$ represents the normalized measure of the variance of S; p means the total group of nodes; t_i is the time range at the i node. When the number of samples are over 30 ($n > 30$), the standard normal statistical variable Z_S is:

$$Z_S = \begin{cases} \frac{S-1}{\sqrt{Var(S)}}, & S > 0 \\ 0 & S = 0 \\ \frac{S+1}{\sqrt{Var(S)}}, & S < 0 \end{cases}$$

In the bilateral trend test, if $|Z_S|$ is greater than $Z_{1-\alpha/2}$ within a given confidence level of α, it indicates the sample data have a significant trend in the testing period, which rejects the null hypothesis. If $Z_S > 0$, it means that the sample data have a significant growth trend in testing period, while if $Z_S < 0$, the sample data exhibit a significant downward trend during the testing time. When the $|Z_S|$ is greater than 1.64 and 2.32, which means the variable is significant monotonicity at the 95% and 99% levels, respectively.

TABLE 1 Standard precipitation evapotranspiration index (SPEI) classification.

Range	Categories	Reclassify
SPEI ≤ −2	Extremely dry	Typical drought
−2 < SPEI ≤ −1.5	Very dry	
−1.5 < SPEI ≤ −1	Moderately dry	Normal
−1 < SPEI <1	Normal	
1 ≤ SPEI <1.5	Moderately wet	
1.5 ≤ SPEI <2	Very wet	Typical wet
SPEI ≥2	Extremely wet	

2.3.2 Standard precipitation evapotranspiration index

The SPEI, as a widely employed method for assessing drought conditions, relies on the trade-off between precipitation and potential evapotranspiration (Vicente-Serrano et al., 2010). Consequently, it effectively mirrors the consequences of global warming on drought patterns (Vicente-Serrano et al., 2010). Furthermore, the SPEI exhibits flexibility in adapting to the diverse time scales characteristic of drought events. (Bohn and Piccolo, 2018).

The SPEI possesses a mean value of 0 and a standard deviation of 1, serving as a reliable metric for analyzing drought characteristics. Based on factors such as intensity, magnitude, duration, and frequency, water surplus and deficit are categorized into seven distinct groups (Tan et al., 2015; Bohn and Piccolo, 2018). For the purpose of studying hydrological processes across various hydrologic years, these seven categories are further consolidated into three representative types (Table 1).

2.3.3 Cellular Automata Markov chain

The CA-Markov model integrates the Cellular Automata (CA) and Markov Chain (MC) models, both being discrete dynamic models that operate in terms of time and state. The Markov Chain, as a stochastic model, characterizes the transition probabilities of a sequence of random variables across discrete time intervals (Sang et al., 2011; Du et al., 2012). On the other hand, CA performs spatial operations where each cell's state at time $t + 1$ is influenced by its neighboring cells at time t (Ye and Bai, 1969; Mohamed and Worku, 2020). In landscapes encompassing multiple land-use categories, land-use changes exhibit the Markov property. Therefore, a land-use transition matrix is constructed to capture the probabilities of each land-use type transforming into any other type. This matrix serves as a valuable tool in predicting future land-use changes.

However, the Markov chain model ignores the significant influence of geomorphology on land use and lacks the ability to effectively capture the dynamics of land-use alternation. In contrast, the CA-Markov model leverages the spatial operation capabilities of CA and the transition probability analysis of the Markov chain, enabling it to forecast spatially explicit land-use variation over a specified period. This combined approach provides a more comprehensive and accurate understanding of land-use dynamics,

considering both the spatial context and the probabilistic nature of land-use transitions (Mondal and Southworth, 2010).

The hybrid CA-Markov model was implemented using the IDRISI software platform (Eastman, 1999). Prior to predicting the land use in the Yanhe watershed for the year 2060, the model's accuracy was rigorously tested by comparing real and simulated land-use layouts for the year 2010. Initially, a Markov transition matrix was constructed using land-use maps from 1990 to 2000. This matrix captured the probability of each land-use type transitioning to any other type. Additionally, ancillary images depicting highways, motorways, railways, waterbodies, slopes, and altitudes were employed as part of a multi-criteria decision-making process to generate a transition suitability image collection. This collection provided a spatial representation of the suitability of each land-use type. Subsequently, leveraging the real land-use layout of 2000, the CA-Markov model was utilized to generate a simulated land-use map.

2.3.4 Soil and water assessment tool

SWAT is a semi-distributed, basin-scale hydrological model that incorporates various data sources to simulate the hydrological processes within a research watershed (Gassman et al., 2007; Kang et al., 2021). It relies on daily meteorological data, along with land-use maps and soil attribute data. The model divides the entire watershed into multiple subbasins and further subdivides them into hydrological response units, which share similar land-use categories, management practices, and soil properties (Neitsch et al., 2011). This localized SWAT model is capable of simulating hydrological conditions over extended periods, providing valuable insights into the watershed's water balance and dynamics.

$$SW_t = SW_0 + \sum_{i=1}^{l} \left(R_{\text{day}} - Q_{\text{surf}} - E_a - W_{\text{seep}} - Q_{gw} \right)$$

where SW_t represents the ultimate soil moisture content, indicating the final state of soil water after considering various inputs and outputs over a defined period; SW_0 denotes the initial soil moisture content, serving as the starting point for the model's calculations; t signifies the time phase, specifically measured in days, and encompasses the duration of the simulation; R_{day}, Q_{surf} and E_a are key components that represent daily rainfall, surface runoff, and evapotranspiration, respectively; W_{seep} represents the cumulative amount of water that percolates from the topsoil into the aeration zone on a specific day, marking the downward movement of water within the soil profile; Q_{gw} stands for return flow, referring to the water that recirculates from deeper soil layers or groundwater back to the soil surface.

3 Results and discussion

3.1 Climate and streamflow alterations in recent 50 years

3.1.1 Temperature change

Temperature serves as the most prominent indicator of climate change. Utilizing the mean annual temperature data from five weather stations, we conducted a Mann-Kendall test to analyze the temperature trend (Figure 3). The results revealed that the temperature Z_s statistic stood at 5.24 for the period 1970–2019, exceeding the Z statistic threshold of 2.32 for a 99% confidence interval. Consequently, it is evident that the Yanhe watershed experienced a significant increase in temperature over the past 50 years ($p < 0.01$). Furthermore, the rate of increase was 0.37°C per decade, and a notable abrupt change occurring in 1996. Specifically, the average annual temperature was 10.56°C during 1970–1996, whereas it rose to 11.80°C from 1997 to 2019. Notably, the peak temperature was recorded in 1998.

Over the past century (1905–2005), China experienced two distinct warm periods: the 1940s–1950s and the 1980s–1990s. Notably, 1998 marked the warmest year recorded in China since the inception of meteorological records (Tang and Ren, 2005). Consequently, the Yanhe watershed, influenced by global warming, exhibited similar warming trends and temperature fluctuations.

3.1.2 Precipitation and streamflow variation

The Mann-Kendall test was utilized to ascertain the trends in precipitation and streamflow within the semiarid Yanhe watershed during 1970–2019 (Figure 4). The Z_s statistic for average precipitation in five stations stood at 0.73, falling within the range of zero to 1.64 (the threshold for a 95% confidence interval). Consequently, we observed a slight increased rate of 1.16 mm/yr inter-annual precipitation. Conversely, the Z_s statistic for streamflow was −3.09, indicating a negative trend. Its absolute value exceeded the Z statistic threshold of 2.32 for a 99% confidence interval. Therefore, it is evident that the streamflow has decreased significantly with a rate of 1.60 million m^3/yr over the past 50 years.

Besides, the average streamflow in the period of 2005–2012 was only half of that with the similar precipitation during 1989–1994. It can be ascribed to ecological restoration, because runoff is the synthesis of precipitation and land surface condition. The restored vegetation from GFGP reduced the rainfall-runoff conversion and increases the infiltration of surface runoff during confluence processes. Moreover, the runoff reduction increased with the age of trees planted (Huang et al., 2003). Our findings reveal that ecological restoration lasting between 4 and 7 years can lead to a reduction of half the streamflow in the Yanhe watershed, except for extreme rainfall conditions.

3.2 Hydrologic year classification

SPEI index was utilized at five stations to identify the typical hydrologic years within the Yanhe watershed during 1970–2019. The findings revealed that drought, normal, and wet years comprised 6%, 88%, and 6% of the total, respectively (Figure 5). Notably, a significant climatic shift occurred in the Yanhe watershed in 1996 (Kang et al., 2020). Consequently, we divided the study period into two distinct phases of 1970–1996 and 1997–2019. During the first phase (1970–1996), typical drought, normal, and wet years accounted for 1%, 93%, and 6%, respectively. However, in the second phase (1997–2019), the frequency of typical drought years increased significantly, accounting for 11% of the period, while normal and wet years constituted 83% and 6%, respectively. This increase in drought frequency during the later period underscores the changing climatic patterns in the Yanhe watershed.

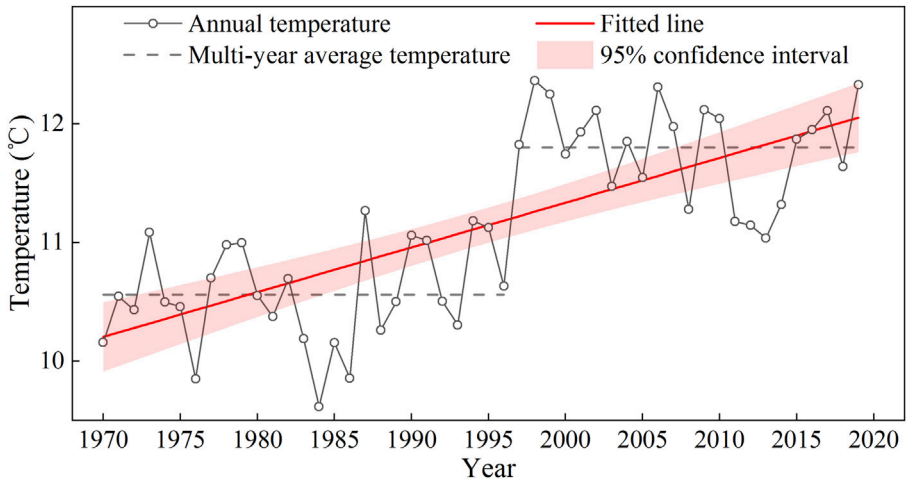

FIGURE 3
Inter-annual temperature variation in the Yanhe watershed from 1970 to 2019.

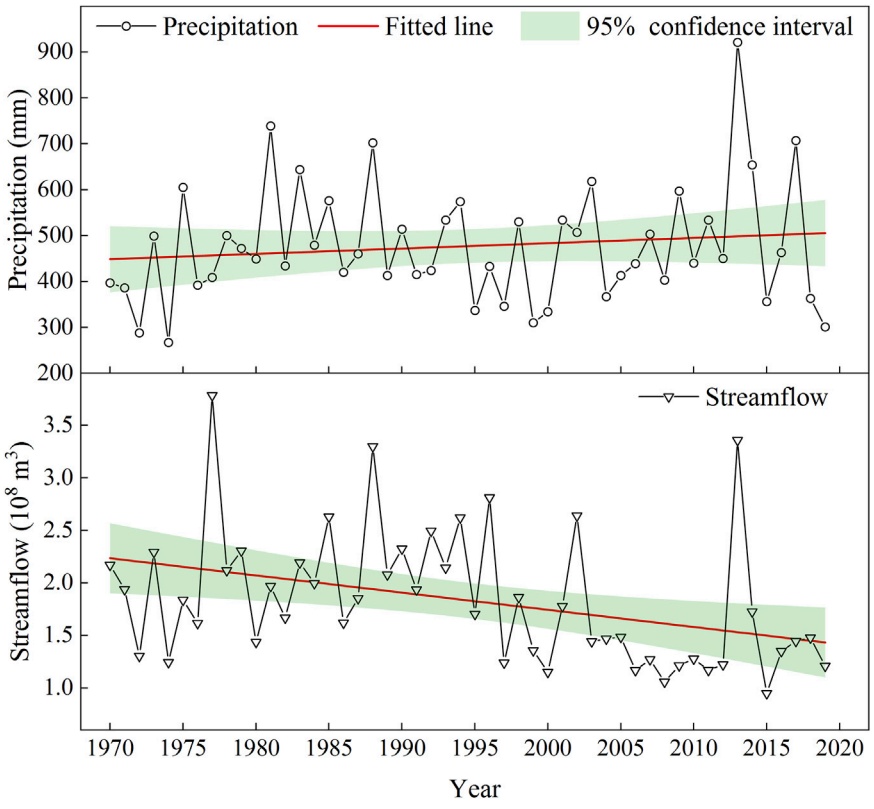

FIGURE 4
Inter-annual precipitation and streamflow variations in the Yanhe watershed during 1970–2019.

The preceding analysis clearly indicates that the frequency of drought years has escalated in recent decades. According to the former studies, the arid area will be drier and the humid area will be wetter influenced by global warming (Durack et al., 2012; Scott et al., 2016). Therefore, the climate in the Yanhe watershed, situated in a semiarid region, tends to dry, and the extreme weather is most likely to increase.

3.3 Model calibration and validation

3.3.1 CA-Markov

To evaluate the precision of the hybrid CA-Markov, the Kappa spatial correlation—a highly regarded metric for accuracy assessment in IDRISI—was employed to contrast the actual and predicted land-use maps for 2010 (Figure 6). The analysis revealed a

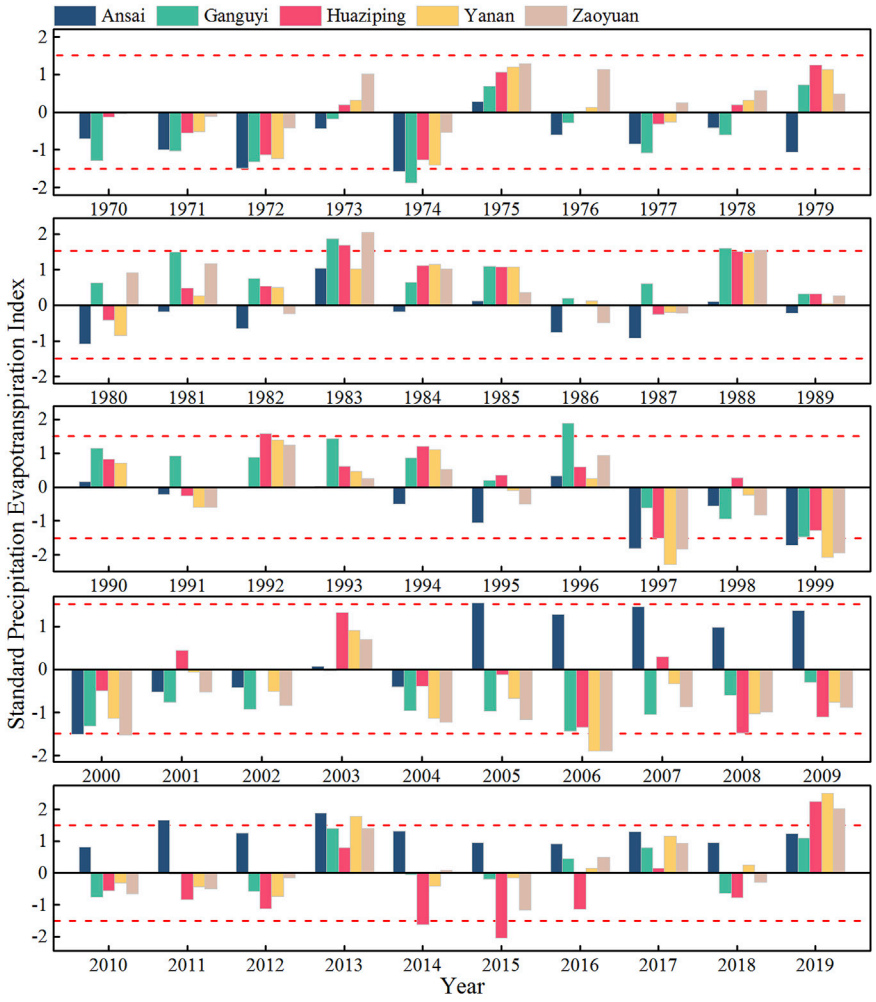

FIGURE 5
Hydrologic years classification by standard precipitation evapotranspiration index; The negative dotted line is the demarcation from normal years to typical drought years and the positive dotted line is the boundary from normal years to typical wet years.

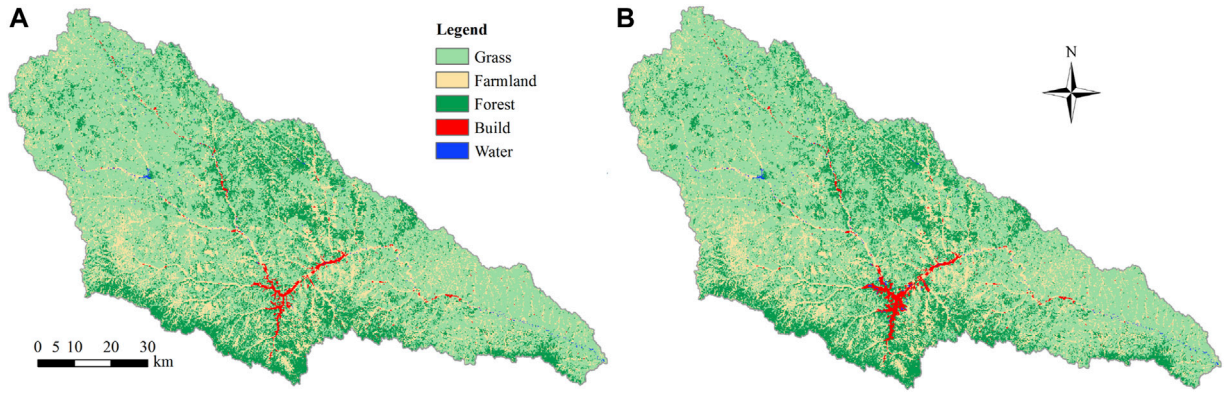

FIGURE 6
Comparison of actual and simulated land use in 2010. **(A)** Represents the actual land-use state in 2010; **(B)** depicts the simulated land-use state in 2010.

TABLE 2 Sensitive parameters on runoff in the Yanhe watershed.

Parameters	Fitted value	Calibrated range		Physical meaning
		Min	Max	
CN2	−15%	−20%	+20%	Initial SCS CN II value
ALPHA_BF	0.47	0.01	0.80	Baseflow alpha factor (day)
GWQMN	−14	−20%	+20%	Threshold depth of water in the shallow aquifer required for return flow to occur (mm)
GW_DELAY	388	30	450	Groundwater delays (day)
ESCO	0.59	0	1	Soil evaporation compensation factor
SOL_K	−17%	−20%	+20%	Saturated hydraulic conductivity (mm/h)

The "+" or "−" symbol indicates a relative change. The "%" signifies multiplying the initial value by (1+fitted value), while numerical values without any sign represent substitute values.

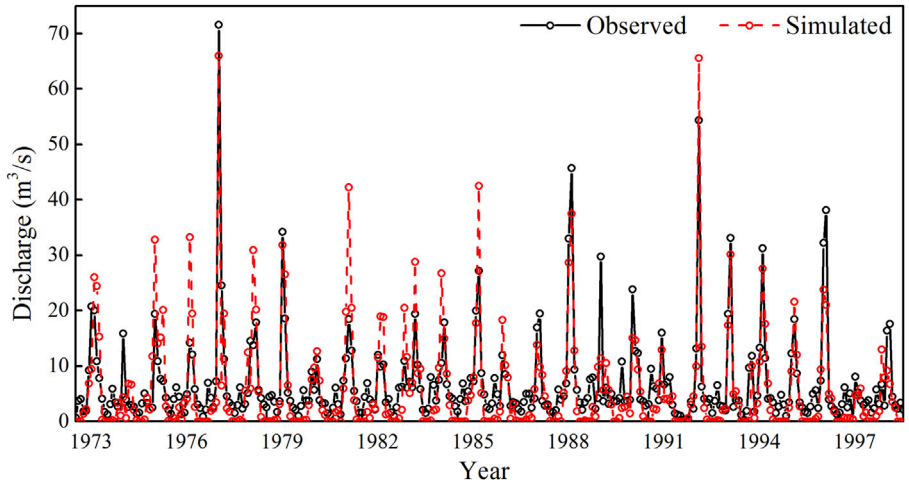

FIGURE 7
SWAT calibration in the Yanhe watershed during 1973–1999.

Kappa spatial correlation of 0.91 between the real and simulated maps, indicating a strong agreement. Drawing from the research conducted by Yang et al. (2021), a Kappa value exceeding 0.75 signifies a high degree of consistency and minimal discernible differences between the two land-use maps. Furthermore, Li and Zhou (2015) used the same method to simulate and predict the land use distribution patterns in the Yanhe watershed for 2010 and 2020, reaching similar conclusions as in this study. Consequently, the hybrid CA-Markov model, with its optimized parameters, exhibits excellent performance in predicting land-use patterns.

3.3.2 SWAT

There are 27 parameters that influence runoff in the SWAT model (Ahn and Merwade, 2016). To localize the general SWAT, we utilized the SWAT-CUP calibration uncertainty program to identify six runoff-sensitive parameters in the Yanhe watershed. Subsequently, the optimal values for these sensitive parameters were determined through Latin hypercube sampling, ensuring a precise and customized model for the watershed (Table 2). Besides, statistical metrics including R^2, Nash-Sutcliffe coefficient (NSE), and percent bias (PBIAS) were employed to assess the accuracy of the SWAT (Gassman et al., 2007; Arnold et al., 2012). The results revealed that during the calibration period (1973–1997), the R^2, NSE, and PBIAS values were 0.73, 0.60, and 18%, respectively (Figure 7). Similarly, in the validation period (2000–2019), these metrics were 0.71, 0.51, and 24%, respectively (Figure 8). According to SWAT accuracy evaluation research, a model is considered acceptable when NES exceeds 0.50 and PBIAS is less than 25% for streamflow predictions (Moriasi et al., 2007). Even though the localized SWAT could satisfy the model accuracy, there exists a discrepancy between the simulated and the observed streamflow. The one possible reason of this discrepancy is that the SWAT model's simulation of snow and ice melt is simple based temperature (Devia et al., 2015), overlooking the impacts of the land use, slope aspect and gradient. The other possible is that the precipitation in the Yanhe River Basin, located in a semi-arid region, exhibits significant interannual variability, and the study period spans a relatively long duration, which leads to the basis between the simulated and observed streamflow. This research focuses on the impacts of land-use change on hydrological processes during the flooding seasons, and selects consecutive typical hydrological years

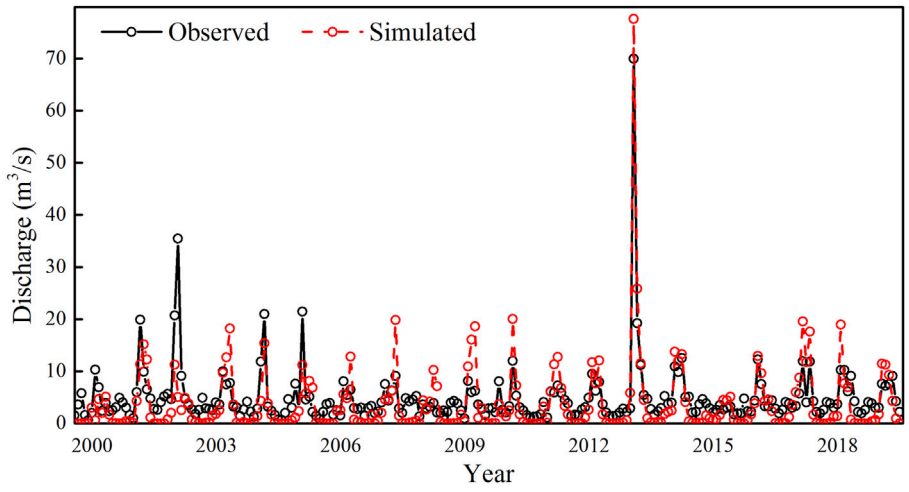

FIGURE 8
SWAT validation in the Yanhe watershed during 2000–2019.

TABLE 3 Changes in land use within the Yanhe watershed from 1990 to 2010.

Year	Type	Grass	Farmland	Forest	Build	Water
1990	Area (km^2)	3,998.84	2,221.53	1,364.40	24.72	24.81
	Percent (%)	52.38	29.10	17.87	0.32	0.32
2000	Area (km^2)	4,715.20	1,369.08	1,481.74	55.50	12.78
	Percent (%)	61.76	17.93	19.41	0.73	0.17
2010	Area (km^2)	4,768.72	1,290.40	1,491.74	69.62	13.81
	Percent (%)	62.46	16.90	19.54	0.91	0.18

to drive the localized SWAT model. Therefore, the calibrated model is able to reflect the characteristics of the impact of land-use variation on hydrology during typical hydrological years.

3.4 Land-use variation and prediction

3.4.1 Land-use variation

According to the SWAT land-use classification system, the Yanhe watershed's land use was reclassified into grassland, farmland, forest, urban/built-up land, and water body. An analysis of land-use changes from 1990 to 2010 revealed several notable trends (Table 3). Specifically, the areas of grassland, forest, and built-up land increased by 9.38%, 1.54%, and 0.40%, respectively, while farmland and water areas decreased by 11.17% and 0.16%, respectively. When comparing the land-use changes between 1990 and 2010 in greater detail, it was observed that from 1990 to 2000, the areas of grassland, forest, built-up land, and water body increased by 0.70%, 0.13%, 0.18%, and 0.01%, respectively, while farmland decreased by 1.03%. However, from 2000 to 2010, the changes were more significant, with grassland, forest, and built-up land continuing to expand, while farmland continued to decline. Overall, the most prominent land-use changes in the Yanhe watershed from 1990 to 2010 were the increasing trend in grassland, forest, and built-up land areas and the decreasing trend in farmland.

3.4.2 Land-use prediction

Using the calibrated IDRISI model with a land-use transition matrix derived from data between 2000 and 2010, predictions were made regarding the land-use layout anticipated for 2060 (Figure 9). When comparing the predicted land-use state of 2060 with the actual state of 2010, it is evident that the most significant change would involve the transformation of 9.21% of grassland. This grassland would primarily be converted into 5.63% of forest and 3.58% of built-up land. Notably, the expansion of forestland is expected to occur primarily in the midstream and downstream regions of the basin. Conversely, the growth of built-up areas is predicted to be concentrated in gullies with flatter terrain and more favorable urban habitat environments.

3.5 Hydrological fluctuations in different hydrological years

3.5.1 Streamflow variation in typical drought years

SWAT models were constructed utilizing five consecutive, representative drought years (comprising two warm-up years and

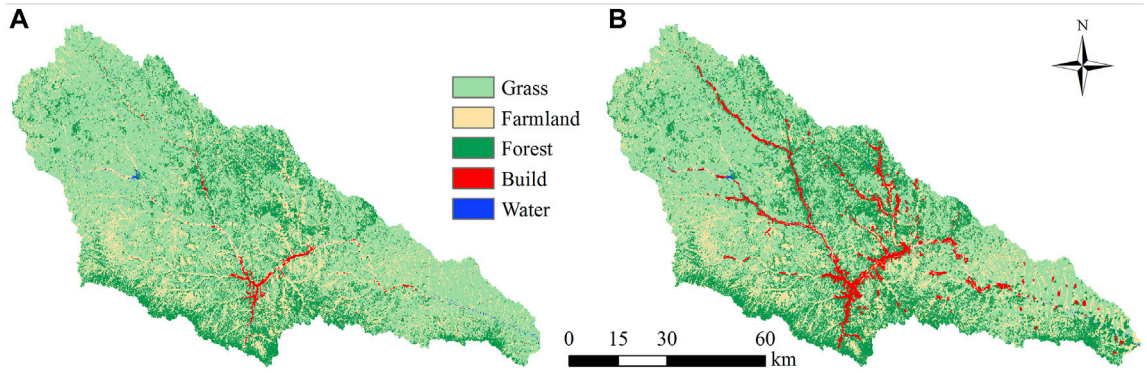

FIGURE 9
Land-use prediction and comparison in the Yanhe watershed. **(A)** Shows the actual land-use state in 2010, and **(B)** depicts the predicted land-use state in 2060.

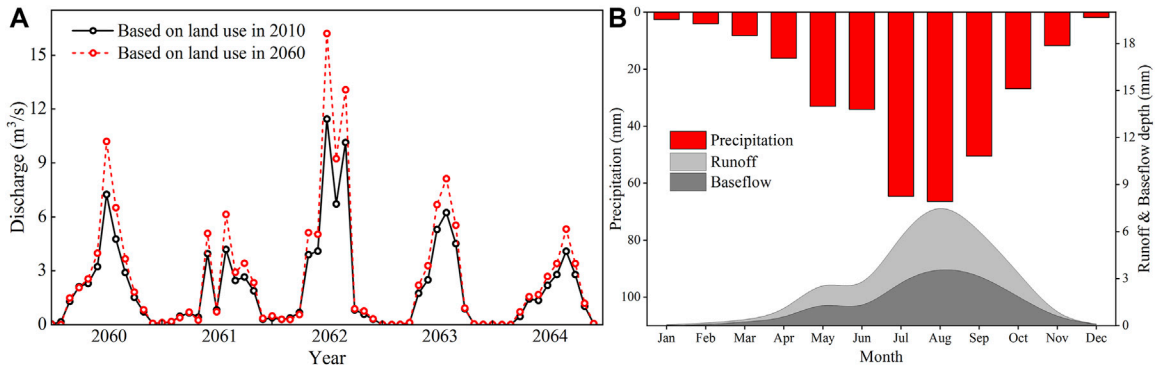

FIGURE 10
Hydrological fluctuations with land-use variation in drought years. **(A)** Is the interannual variation of streamflow, and **(B)** is the inneranual distribution of precipitation, runoff and baseflow.

five simulation years) alongside land-use maps from 2010 to 2060 within the Yanhe watershed. The findings revealed that the impact of arid climatic conditions on streamflow was primarily concentrated during flooding periods. Specifically, the mean discharge rates during these periods were 5.05 m^3/s and 6.69 m^3/s for the 2010 and 2060 scenarios, respectively. Furthermore, the average flood peak in the 2060 landscape scenario exhibited a notable increase of 32.49% compared to that of 2010 (Figure 10A). Overall, during these typical drought years, the Yanhe watershed exhibited low discharge levels and rapid fluctuations in flood peaks.

The significant land-use alteration from 2010 to 2060 is the grassland converted to the forest and built-up land. The transformed forest is primarily located on hilly slopes, situated far from the Yanhe River. Conversely, the converted built-up land is situated in proximity to the river, occupying a broad and flat area. Consequently, the surface runoff generated by limited precipitation on the built-up land drains into the river, leading to a rapid response of low streamflow to rainfall during typical drought years. We refer to this phenomenon, where low streamflow promptly reacts to limited precipitation in close proximity to the land surface, as the “local rainfall-runoff effect".

Utilizing the 2060 landscape as a basis, we conducted a thorough analysis of the intra-annual characteristics of precipitation, runoff, and baseflow to further elucidate the “local rainfall-runoff effect” during typical drought years (Figure 10B). Our findings revealed that rainfall was the primary determinant of surface runoff in these drought-prone years, especially during flooding periods. Specifically, total precipitation amounted to 319.75 mm, with 56.74% of this precipitation occurring exclusively during flooding periods. Notably, 64.66% of this precipitation was converted into surface runoff, serving as the principal mechanism for the rapid increase in streamflow during flooding periods. On the other hand, baseflow contributed 50.72% to streamflow, becoming the primary source of recharge for the river during non-flooding periods.

The aforementioned analysis clearly illustrates the “local rainfall-runoff effect”. This effect refers to the phenomenon where a significant portion of limited precipitation generates surface runoff on impermeable or weakly permeable surfaces. This runoff subsequently recharges nearby streams and rivers, resulting in a rapid increase in discharge. Therefore, the local landscape characteristics play a pivotal role in influencing the streamflow patterns during typical drought years.

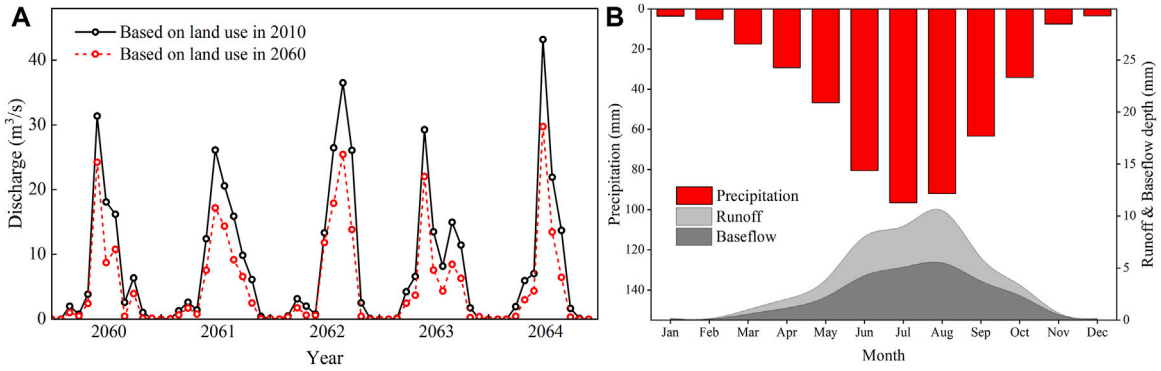

FIGURE 11
Hydrological fluctuations with land-use variation in normal years. **(A)** Is the interannual variation of streamflow, and **(B)** is the inner annual distribution of precipitation, runoff and baseflow.

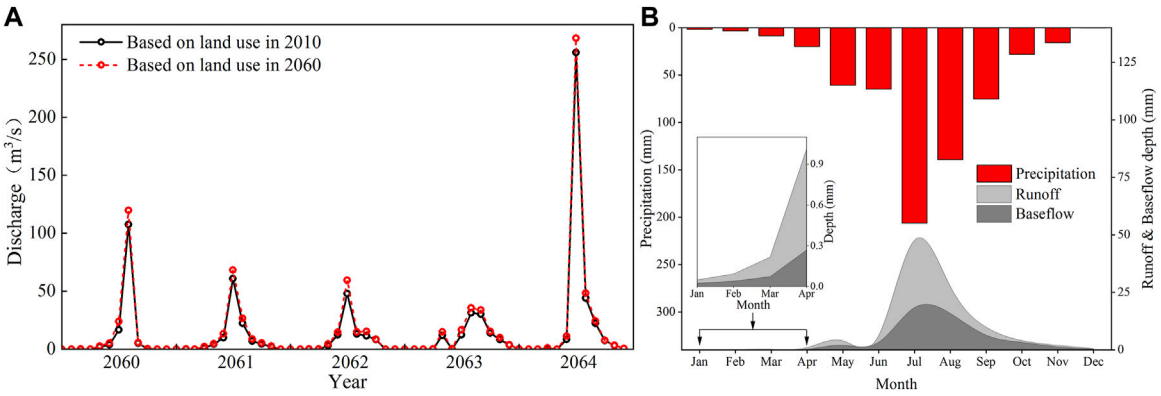

FIGURE 12
Hydrological fluctuations with land-use variation in wet years. **(A)** Is the interannual variation of streamflow, and **(B)** is the inner annual distribution of precipitation, runoff and baseflow.

3.5.2 Streamflow variation in normal years

According to the classification of SPEI, we selected five consecutive normal years (consisting of two warm-up years and five simulation years) to forecast hydrological variations within the Yanhe watershed. Our findings revealed that the influence of a normal climate on surface runoff was primarily concentrated from June to October. When comparing the average discharge based on the landscapes of 2010 and 2060, we observed a decrease from 19.42 m^3/s and 12.40 m^3/s. Notably, during these normal years, the flood peak with the 2060 land use scenario decreased by 36.15% compared to that with the 2010 land use (Figure 11A). Nevertheless, it is worth mentioning that the flooding discharge in normal years is approximately twice as high as that observed during typical drought years.

When comparing the land-use state in 2010 with that of 2060, we observe that the prolonged restoration of forests and grasslands in 2060 effectively limits upstream and local surface runoff generated by relatively abundant precipitation during normal years. This, in turn, reduces the runoff flows into the river. Although the expansion of built-up land (accounting for 4.49% of the entire watershed) converts a significant amount of rainfall into surface runoff, the peak flow in 2060 remains lower than that in 2010. This is attributed to the fact that the surface runoff restricted by restored vegetation outweighs the runoff generated by the built-up land. Furthermore, given the high discharge rates during normal years, the limited surface runoff generated on the relatively small percentage of built-up land has minimal impact on streamflow. Consequently, when compared to the landscape of 2010, the peak flow in 2060 is lower. We refer to this phenomenon as the “global rainfall-runoff effect".

Utilizing the land-use map of 2060, we conducted a thorough analysis of the intra-annual distribution of precipitation, runoff, and baseflow during normal years to elucidate the “global rainfall-runoff effect” (Figure 11B). Our findings revealed that precipitation, streamflow, and baseflow exhibited smooth transitions throughout the normal years, with the timing of peak flow lagging behind the period of maximum precipitation. Notably, the peak volume of precipitation occurred in July, whereas the peak discharge was delayed until early August. On average, the total precipitation amounted to 479.66 mm, with only 3.99% of this precipitation converting into surface runoff and subsequently entering the stream during these normal years.

There are two primary reasons for the observed lag between the flood peak and the maximum precipitation time. Firstly, the smooth fluctuations in rainfall distribution throughout the year maintain the discharge within a consistently high range, rendering it less susceptible to the "local rainfall-runoff effect". Secondly, the well restored vegetation on the slope effectively intercepts surface runoff, and the homogeneous loess soil has high infiltration capacity in the normal hydrological years (Jin et al., 2020). Consequently, when rainfall is relatively abundant and the river maintains a stable discharge, the rainfall-runoff process is primarily influenced by the spatial distribution of major land-use types across the entire basin, giving rise to the "global rainfall-runoff effect".

3.5.3 Streamflow variation in typical wet years

For a comparative analysis with typical drought years and normal years, the SWAT models were driven using data from five consecutive typical wet years. These models were based on the land-use layouts of 2010 and 2060 in the Yanhe watershed. The results indicated that climate was the primary determinant of streamflow in flooding periods of wet years. Specifically, the flood peaks were virtually identical for both the 2010 and 2060 land-use scenarios. During the typical wet years, the discharge was high, and the peak flow was predominantly concentrated in July (Figure 12A).

Previous studies indicated that vegetation (forest and grass) has a good function of soil and water conservation (Jin et al., 2020; Lyu et al., 2023). The area of vegetation in the Yanhe watershed accounts for 82.00% and 78.43% of the entire watershed in 2010 and 2060, respectively. However, it has limited capacity to restrict surface runoff during intense rainstorms or prolonged rainfall. The aggressive surface runoff resulting from extreme rainfall is scarcely intercepted and infiltrated by the forest and grassland. This was evident during the "7.26" rainstorm event in the Wudinghe River basin of the LP on 26 July 2017. Despite decades of ecological restoration efforts, where the area of grassland and forest has exceeded 50% of the watershed, the rainstorm still generated significant flood peaks and caused severe soil erosion (Tang et al., 2020; Wang et al., 2020). Consequently, in typical wet years, the aggressive surface runoff rapidly flows into the river, significantly increasing the peak discharge.

To gain a deeper understanding of the hydrological processes during typical wet years, we analyzed the intra-annual distribution of rainfall, runoff, and baseflow (Figure 12B). The results indicated that the average precipitation in these wet years was 624.01 mm, with significant variations within the year. Notably, approximately 55.38% of the total precipitation occurred primarily in July and August. Concurrently, the surface runoff showed a marked increase during the concentrated rainstorms in July, accounting for a substantial 79.11% of the total surface runoff. During this period, the flood discharge was particularly high and declined rapidly following the intense rainfall. As approximately 90% of the Yanhe watershed comprises hilly-gully regions (Wang et al., 2016), the occurrence of rainstorms frequently triggers infiltration-excess overland flow (Jin et al., 2020), and the resulting stormflow responds promptly to precipitation.

4 Conclusion

Ecological restoration (afforestation and grass planting) can effectively reduce streamflow during the drought and normal years in the semiarid regions. The hydrological processes exhibit distinct response patterns in different hydrologic years. In typical drought years, the streamflow regime primarily follows the "local rainfall-runoff effect", where the landscape in proximity to streams and rivers plays a pivotal role in determining streamflow patterns. Conversely, in normal years, the streamflow is influenced by the "global rainfall-runoff effect", meaning that the major land-use types across the entire basin contribute significantly to the overall flow. However, in typical wet years, the streamflow is primarily controlled by climatic factors. Even under conditions of significant vegetation restoration, land use has a limited impact on surface runoff. This underscores the need for a balanced approach in managing land use and ecological restoration efforts to mitigate the effects of climate change on streamflow patterns in semiarid regions.

Data availability statement

The original contributions presented in the study are included in the article/Supplementary Material, further inquiries can be directed to the corresponding author.

Author contributions

YK: Conceptualization, Formal Analysis, Methodology, Software, Visualization, Writing–original draft. KZ: Data curation, Writing–review and editing. YZ: Formal Analysis, Software, Validation, Visualization, Writing–original draft. LZ: Data curation, Formal Analysis, Writing–review and editing.

Funding

The author(s) declare that financial support was received for the research, authorship, and/or publication of this article. This study was funded by the Natural Science Foundation of Gansu Province (No. 23JRRA702); the Innovation project for Young Science and Technology of Lanzhou (No. 2023-QN-55), and the Gansu Province Higher Education Industry Support Project (2022CYZC-15).

Conflict of interest

The authors declare that the research was conducted in the absence of any commercial or financial relationships that could be construed as a potential conflict of interest.

Publisher's note

References

Adhikari, P., Hong, Y., Douglas, K. R., Kirschbaum, D. B., Gourley, J., Adler, R., et al. (2010). A digitized global flood inventory (1998–2008): compilation and preliminary results. *Nat. Hazards* 55 (2), 405–422. doi:10.1007/s11069-010-9537-2

Ahn, K.-H., and Merwade, V. (2016). The effect of land cover change on duration and severity of high and low flows. *Hydrol. Process.* 31 (1), 133–149. doi:10.1002/hyp.10981

Arnold, J. G., Moriasi, D. N., Gassman, P. W., Abbaspour, K. C., White, M. J., Srinivasan, R., et al. (2012). SWAT: model use, calibration, and validation. *Trans. ASABE* 55, 1491–1508. doi:10.13031/2013.42256

Barry, A. A., Caesar, J., Tank, A., Aguilar, E., Mcsweeney, C., Cyrille, A. M., et al. (2018). West Africa climate extremes and climate change indices. *Int. J. Climatol.* 38, E921–E938. doi:10.1002/joc.5420

Bates, B., Kundzewicz, Z. W., Wu, S., and Palutikof, J. (2008) *Climate change and water: technical paper VI*. Geneva, Switzerland: University of North Texas Libraries, UNT Digital Library.

Bohn, V., and Piccolo, M. (2018). Standardized precipitation evapotranspiration index (SPEI) as a tool to determine the hydrological dynamic of plain regions (Argentina). *Geociencias* 37, 627–637. doi:10.5016/geociencias.v37i3.12236

Chen, L.-D., Messing, I., Zhang, S., Fu, B.-J., and Ledin, S. (2003). Land use evaluation and scenario analysis towards sustainable planning on the Loess Plateau in China—case study in a small catchment. *Catena* 54, 303–316. doi:10.1016/s0341-8162(03)00071-7

Chen, Y., Wang, K., Lin, Y., Shi, W., Song, Y., and He, X. (2015). Balancing green and grain trade. *Nat. Geosci.* 8 (10), 739–741. doi:10.1038/ngeo2544

Da Silva, R. M., Santos, C. a. G., Moreira, M., Corte-Real, J., Silva, V. C. L., and Medeiros, I. C. (2015). Rainfall and river flow trends using Mann–Kendall and Sen's slope estimator statistical tests in the Cobres River basin. *Nat. Hazards* 77 (2), 1205–1221. doi:10.1007/s11069-015-1644-7

Delang, C. O., and Yuan, Z. (2015) *China's grain for green program: a review of the largest ecological restoration and rural development program in the World*. Switzerland: Springer International Publishing.

Devia, G. K., Ganasri, B. P., and Dwarakish, G. S. (2015). A review on hydrological models. *Aquat. Procedia* 4 (2015), 1001–1007. doi:10.1016/j.aqpro.2015.02.126

Di Capua, G., and Rahmstorf, S. (2023). Extreme weather in a changing climate. *Environ. Res. Lett.* 18 (10), 102001. doi:10.1088/1748-9326/acfb23

Du, J., Qian, L., Rui, H., Zuo, T., Zheng, D., Xu, Y., et al. (2012). Assessing the effects of urbanization on annual runoff and flood events using an integrated hydrological modeling system for Qinhuai River Basin, China. *J. Hydrol.* 465, 127–139. doi:10.1016/j.jhydrol.2012.06.057.549

Durack, P. J., Wijffels, S. E., and Matear, R. J. (2012). Ocean salinities reveal strong global water cycle intensification during 1950 to 2000. *Science* 336 (6080), 455–458. doi:10.1126/science.1212222

Eastman, R. J. (1999) *Guide to GIS and image processing volume 1*. Worcester, United States: Clark University: Idrisi Prouduction.

Gassman, P. W., Reyes, M. R., Green, C. H. M., and Arnold, J. G. (2007). The soil and water assessment tool: historical development, applications, and future research directions. *Trans. ASABE* 50 (4), 1211–1250. doi:10.13031/2013.23637

Ge, J., Pitman, A. J., Guo, W. D., Zan, B. L., and Fu, C. B. (2020). Impact of revegetation of the Loess Plateau of China on the regional growing season water balance. *Hydrology Earth Syst. Sci.* 24 (2), 515–533. doi:10.5194/hess-24-515-2020

Hao, L., Zhang, X., and Liu, S. (2012). Risk assessment to China's agricultural drought disaster in county unit. *Nat. Hazards* 61 (2), 785–801. doi:10.1007/s11069-011-0066-4

Hoover, D. L., Duniway, M. C., and Belnap, J. (2015). Pulse-drought atop press-drought: unexpected plant responses and implications for dryland ecosystems. *Oecologia* 179 (4), 1211–1221. doi:10.1007/s00442-015-3414-3

Huang, J., Guan, X., and Ji, F. (2012). Enhanced cold-season warming in semi-arid regions. *Atmos. Chem. Phys.* 12 (12), 5391–5398. doi:10.5194/acp-12-5391-2012

Huang, J., Ji, M., Xie, Y., Wang, S., He, Y., and Ran, J. (2016). Global semi-arid climate change over last 60 years. *Clim. Dyn.* 46 (3), 1131–1150. doi:10.1007/s00382-015-2636-8

Huang, J., Li, Y., Fu, C., Chen, F., Fu, Q., Dai, A., et al. (2017). Dryland climate change: recent progress and challenges. *Rev. Geophys.* 55 (3), 719–778. doi:10.1002/2016rg000550

Huang, M., Zhang, L., and Gallichand, J. (2003). Runoff responses to afforestation in a watershed of the Loess Plateau, China. *Hydrol. Process.* 17 (13), 2599–2609. doi:10.1002/hyp.1281

Ipcc (2023) *Climate change 2023: synthesis report (full volume) contribution of working groups I, II and III to the sixth assessment report of the intergovernmental panel on climate change*. Swizerland: IPCC.

Jia, Y., Li, T., Shao, M. A., Hao, J., Wang, Y., Jia, X., et al. (2019). Disentangling the formation and evolvement mechanism of plants-induced dried soil layers on China's Loess Plateau. *Agric. For. Meteorology* 269, 57–70. doi:10.1016/j.agrformet.2019.02.011

Jin, Z., Guo, L., Yu, Y. L., Luo, D., Fan, B. H., and Chu, G. C. (2020). Storm runoff generation in headwater catchments on the Chinese Loess Plateau after long-term vegetation rehabilitation. *Sci. Total Environ.* 748 (15), 141375. doi:10.1016/j.scitotenv.2020.141375

Kang, Y., Gao, J., Shao, H., and Zhang, Y. (2020). Quantitative analysis of hydrological responses to climate variability and land-use change in the hilly-gully region of the Loess Plateau, China. *Water* 12 (1), 1–18. doi:10.3390/w12010082

Kang, Y., Gao, J. E., Shao, H., Zhang, Y., Li, J., and Gao, Z. (2021). Evaluating the flow and sediment effects of gully land consolidation on the Loess Plateau, China. *J. Hydrology* 600 (2021), 126535. doi:10.1016/j.jhydrol.2021.126535

Li, J., Liu, Z., He, C., Tu, W., and Sun, Z. (2016). Are the drylands in northern China sustainable? A perspective from ecological footprint dynamics from 1990 to 2010. *Sci. Total Environ.* 553, 223–231. doi:10.1016/j.scitotenv.2016.02.088

Li, J., and Zhou, Z. X. (2015). Coupled analysis on landscape pattern and hydrological processes in Yanhe Watershed of China. *Sci. Total Environ.* 505 (2015), 927–938. doi:10.1016/j.scitotenv.2014.10.068

Li, Y., Huang, J., Ji, M., and Ran, J. (2015). Dryland expansion in northern China from 1948 to 2008. *Adv. Atmos. Sci.* 32 (6), 870–876. doi:10.1007/s00376-014-4106-3

Lyu, L., Yang, Y., Zheng, D. F., and Li, Q. (2023). Effects of vegetation distribution and landscape pattern on water conservation in the Dongjiang River basin. *Ecol. Indictors* 155 (2023), 111017. doi:10.1016/j.ecolind.2023.111017

Mann, H. B. (1945). Nonparametric tests against trend. *Econometrica* 13 (3), 245–259. doi:10.2307/1907187

Mcvicar, T. R., Li, L., Van Niel, T. G., Zhang, L., Li, R., Yang, Q., et al. (2007). Developing a decision support tool for China's re-vegetation program: simulating regional impacts of afforestation on average annual streamflow in the Loess Plateau. *For. Ecol. Manag.* 251 (1), 65–81. doi:10.1016/j.foreco.2007.06.025

Mohamed, A., and Worku, H. (2020). Simulating urban land use and cover dynamics using cellular automata and Markov chain approach in Addis Ababa and the surrounding. *Urban Clim.* 31, 100545. doi:10.1016/j.uclim.2019.100545

Mokrech, M., Nicholls, R. J., Richards, J. A., Henriques, C., Holman, I. P., and Shackley, S. (2008). Regional impact assessment of flooding under future climate and socio-economic scenarios for East Anglia and North West England. *Clim. Change* 90 (1), 31–55. doi:10.1007/s10584-008-9449-2

Mondal, P., and Southworth, J. (2010). Evaluation of conservation interventions using a cellular automata-Markov model. *For. Ecol. Manag.* 260 (10), 1716–1725. doi:10.1016/j.foreco.2010.08.017

Moriasi, D. N., Arnold, J. G., Van Liew, M. W., Bingner, R. L., Harmel, R. D., and Veith, T. L. (2007). Model evaluation guidelines for systematic quantification of accuracy in watershed simulations. *Trans. ASABE* 50 (3), 885–900. doi:10.13031/2013.23153

Nalley, D., Adamowski, J., Khalil, B., and Ozga-Zielinski, B. (2013). Trend detection in surface air temperature in Ontario and Quebec, Canada during 1967–2006 using the discrete wavelet transform. *Atmos. Res.* 132-133, 375–398. doi:10.1016/j.atmosres.2013.06.011

Neitsch, S. L., Arnold, J. G., Kiniry, J. R., and Williams, J. R. (2011) *Soil and water assessment tool theoretical documentation version 2009*. Texas: Texas Water Resources Institute.

Nyamadzawo, G., Chirinda, N., Mapanda, F., Nyamangara, J., Wuta, M., Nyamugafata, P., et al. (2012). Land-use and land-use change effects on nitrous oxide emissions in the seasonally dry ecosystems of Zimbabwe: a review. *Actas Urológicas Espaolas* 33 (3), 249–257.

Otto, F. E. L. (2023). Attribution of extreme events to climate change. *Annu. Rev. Environ. Resour.* 48, 813–828. doi:10.1146/annurev-environ-112621-083538

Rotenberg, E., and Yakir, D. (2010). Contribution of semi-arid forests to the climate system. *Science* 327 (5964), 451–454. doi:10.1126/science.1179998

Sang, L., Zhang, C., Yang, J., Zhu, D., and Yun, W. (2011). Simulation of land use spatial pattern of towns and villages based on CA–Markov model. *Math. Comput. Model.* 54 (3–4), 938–943. doi:10.1016/j.mcm.2010.11.019

Scheff, J., and Frierson, D. M. W. (2014). Scaling potential evapotranspiration with greenhouse warming. *J. Clim.* 27 (4), 1539–1558. doi:10.1175/jcli-d-13-00233.1

Scott, D., Hall, C. M., and Gössling, S. (2016). A review of the IPCC Fifth Assessment and implications for tourism sector climate resilience and decarbonization. *J. Sustain. Tour.* 24 (1), 8–30.

Shi, H., and Shao, M. (2000). Soil and water loss from the Loess Plateau in China. *J. Arid Environ.* 45 (1), 9–20. doi:10.1006/jare.1999.0618

Tan, C., Yang, J., and Li, M. (2015). Temporal-spatial variation of drought indicated by SPI and SPEI in ningxia hui autonomous region, China. *Atmosphere* 6 (10), 1399–1421. doi:10.3390/atmos6101399

Tang, B., Jiao, J., Zhang, Y., Chen, Y., Wang, N., and Bai, L. (2020). The magnitude of soil erosion on hillslopes with different land use patterns under an extreme rainstorm on the Northern Loess Plateau, China. *Soil Tillage Res.* 204, 104716. doi:10.1016/j.still.2020.104716

Tang, G., and Ren, G. (2005). Reanalysis of surface air temperature change of the last 100 Years over China. *Clim. Environ. Res.* 10 (4), 791–798.

Tsunekawa, A., Liu, G., Yamanaka, N., and Du, S. (2014) *Restoration and development of the degraded Loess Plateau*. China. Tokyo: Springer Japan.

Van Belle, G., and Hughes, J. P. (1984). Nonparametric tests for trend in water quality. *Water Resour. Res.* 20 (1), 127–136. doi:10.1029/wr020i001p00127

Vicente-Serrano, S. M., Beguería, S., and López-Moreno, J. I. (2010). A multiscalar drought index sensitive to global warming: the standardized precipitation evapotranspiration index. *J. Clim.* 23 (7), 1696–1718. doi:10.1175/2009jcli2909.1

Wang, N., Jiao, J., Bai, L., Zhang, Y., Chen, Y., Tang, B., et al. (2020). Magnitude of soil erosion in small catchments with different land use patterns under an extreme rainstorm event over the Northern Loess Plateau, China. *Catena* 195, 104780. doi:10.1016/j.catena.2020.104780

Wang, Z. J., Jiao, J. Y., Rayburg, S., Wang, Q. L., and Su, Y. (2016). Soil erosion resistance of "Grain for Green" vegetation types under extreme rainfall conditions on the Loess Plateau, China. *Catena* 141 (2016), 109–116. doi:10.1016/j.catena.2016.02.025

Yang, X., Bai, Y., Che, L., Qiao, F., and Xie, L. (2021). Incorporating ecological constraints into urban growth boundaries: a case study of ecologically fragile areas in the Upper Yellow River. *Ecol. Indic.* 124, 107436. doi:10.1016/j.ecolind.2021.107436

Ye, B., and Bai, Z. (1969) *Simulating land use/cover changes of Nenjiang County based on CA-Markov model*. Boston: Springer, 321–319.

Yu, Y., Zhao, W. W., Martinez-Murillo, J. F., and Pereira, P. (2020). Loess Plateau: from degradation to restoration. *Sci. Total Environ.* 738, 140206. doi:10.1016/j.scitotenv.2020.140206

Zeng, N., Neelin, J. D., Lau, K.-M., and Tucker, C. J. (1999). Enhancement of interdecadal climate variability in the sahel by vegetation interaction. *Science* 286 (5444), 1537–1540. doi:10.1126/science.286.5444.1537

Zhao, G. J., Mu, X. M., Jiao, J. Y., An, Z. F., Klik, A., Wang, F., et al. (2017). Evidence and causes of spatiotemporal changes in runoff and sediment yield on the Chinese Loess Plateau. *Land Degrad. Dev.* 28 (2), 579–590. doi:10.1002/ldr.2534

Zhao, G. J., Mu, X. M., Wen, Z. M., Wang, F., and Gao, P. (2013). Soil erosion, conservation, and eco-environment changes in the Loess Plateau of China. *Land Degrad. Dev.* 24 (5), 499–510. doi:10.1002/ldr.2246

Zhao, H., Gao, G., Yan, X., Zhang, Q., Hou, M., Zhu, Y., et al. (2011). Risk assessment of agricultural drought using the CERES-Wheat model: a case study of Henan Plain, China. *Clim. Res.* 50, 247–256. doi:10.3354/cr01060

Zhao, T., Chen, L., and Ma, Z. (2014). Simulation of historical and projected climate change in arid and semiarid areas by CMIP5 models. *Chin. Sci. Bull.* 59 (4), 412–429. doi:10.1007/s11434-013-0003-x

Zhao, T. B., and Dai, A. G. (2017). Uncertainties in historical changes and future projections of drought. Part II: model-simulated historical and future drought changes. *Clim. Change* 144 (3), 535–548. doi:10.1007/s10584-016-1742-x

Zhao, W. W., Liu, Y., Daryanto, S., Fu, B. J., Wang, S., and Liu, Y. X. (2018). Metacoupling supply and demand for soil conservation service. *Curr. Opin. Environ. Sustain.* 33, 136–141. doi:10.1016/j.cosust.2018.05.011

Zhou, L., Chen, H., Hua, W., Dai, Y., and Wei, N. (2016). Mechanisms for stronger warming over drier ecoregions observed since 1979. *Clim. Dyn.* 47 (9-10), 2955–2974. doi:10.1007/s00382-016-3007-9

frontiers | Frontiers in Environmental Science

TYPE Methods
PUBLISHED 10 July 2024
DOI 10.3389/fenvs.2024.1417048

OPEN ACCESS

EDITED BY
Qiang Li,
University of Houston–Downtown,
United States

REVIEWED BY
Mounir Bouassida,
Tunis El Manar University, Tunisia
Zhongnian Yang,
Qingdao University of Technology, China

*CORRESPONDENCE
Ming Huang,
434656873@qq.com

RECEIVED 13 April 2024
ACCEPTED 13 June 2024
PUBLISHED 10 July 2024

CITATION
Huang M, Liu Z, Zhang R, Tao Y and Sun Y-m (2024), Selection of low impact development technical measures in the distribution area of expansive soil: a case study of Hefei, China. *Front. Environ. Sci.* 12:1417048. doi: 10.3389/fenvs.2024.1417048

Selection of low impact development technical measures in the distribution area of expansive soil: a case study of Hefei, China

Ming Huang[1,2]*, Zhen Liu[1,2], Rui Zhang[3], Yong Tao[1] and Ya-min Sun[4]

[1]College of Environmental and Energy Engineering, Anhui Jianzhu University, Hefei, China, [2]Institute of Remote Sensing and Geographic Information Systems, Anhui Jianzhu University, Hefei, China, [3]Shucheng Zhonghe Real Estate Development Co., Ltd, Hefei, China, [4]Anhui Eco-environmental Monitoring Center, Hefei, China

Expansive soils are widely distributed around the world. They have significant characteristics of both hygroscopic expansion and water-loss shrinkage, which have caused serious damage to road paving, construction of low-rise houses, and construction of slopes along the banks of rivers. Similarly, the implementation of low impact development measures can cause considerable difficulties in the distribution area of expansive soil. The entire urban area of Hefei is situated on expansive soil. Although Hefei city has developed a sponge city plan, it has not been carried out on a large scale for implementation of low impact development technical measures. Experimental studies have shown that exposed expansive soils produce fissures that run up and down during wet and dry cycles. These fissures are extremely unfavorable to the infiltration of surface runoff formed by short-term heavy rainfall. This is also one of the reasons for short-term rainfall in Hefei city, resulting in serious flooding in low-lying areas with a poor drainage system. At the same time, initial rainfall is ineffective in cleaning up surface source pollution. Therefore, we can enhance the characteristics of expansive soil, keep the expansive soil unexposed, and maintain a certain level of humidity. These approaches can play a better role in the control of rainfall runoff and surface source pollution. The characteristics of expansive soils can be enhanced by mixing them with weathered sand, a physical improvement, to meet the technical requirements for infiltration, interception, and purification. It is recommended to carefully select low impact development measures in the distribution area of expansive soil to avoid the occurrence of wasteful investment and poor results.

KEYWORDS

low impact development, technical measure, expansive soil, distribution area, selection

1 Introduction

Expansive soil is a kind of special clay widely distributed on the land surface. The clay particles in the soil are mainly composed of hydrophilic minerals, including montmorillonite, illite, and kaolinite. It is a cohesive soil with significant characteristics of water-absorption expansion and water-loss shrinkage. Because of its remarkable properties of expansion and contraction, it often causes serious damage to engineering

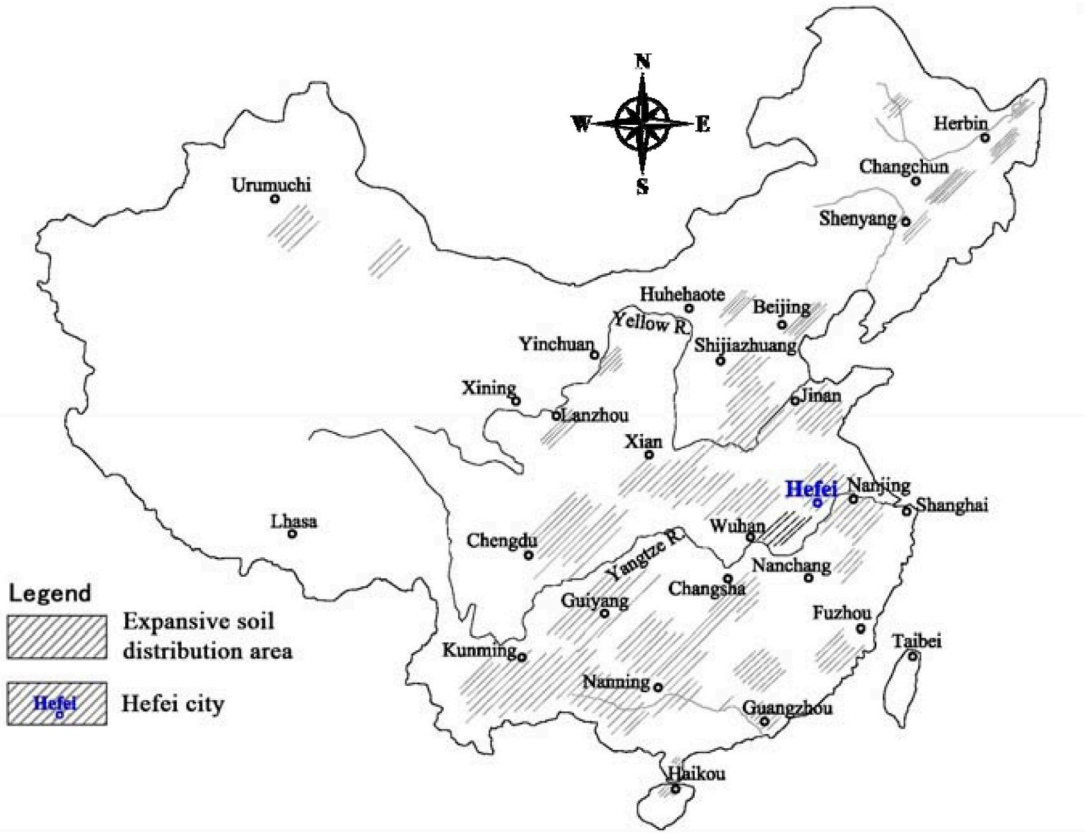

FIGURE 1
China's expansive soil regional distribution map (Ye, 2010).

construction in the expansive soil area. Expansive soil is widely distributed in more than 40 countries across the world (Zhang, 2005).

The hazard and risk due to expansive soils is often overlooked when tabulating natural hazard risk, vulnerability, and resilience (Bin Mostafiz et al., 2021). The randomly distributed fissures and repeated expansion and contraction deformation in the soil mass cause great harm to engineering construction, which is often referred to as disastrous soil in engineering (Jones and Holtz, 1973). Worldwide, the annual economic losses caused by this are up to 15 billion U.S. dollars or more, with China being one of the most seriously affected countries, where the distribution of expansive soil is extremely wide, throughout Anhui, Guangxi, Yunnan, Hunan, Henan, and in more than 20 other provinces and autonomous regions (Figure 1) (Ye, 2010).

From 1959 to 1977, the United Kingdom, the United States, Romania, the former Soviet Union, and Japan have successively added provisions on expansive soil to the officially issued geotechnical and railway specifications and other documents (Sun et al., 1995). In 1987, China officially issued the *Technical Code for Buildings in Expansive Soil Regions* (*GBJ 112-87*), and in 2013, it was revised to the *Technical Code for Buildings in Expansive Soil Regions* (*GB 50112-2013*). The current methods of dealing with expansive soils are mainly chemical modification, such as stabilization of expansive soils by mixing lime, cement, fly ash, sodium chloride, calcium chloride, and phosphoric acid. Among chemical modifications, the treatment of expansive soils with lime is the most common and effective method. It has been widely reported that the addition of an appropriate amount of lime to an expansive soil improves the workability of the soil by causing a reduction in the soil's swelling potential (Locat et al., 1990; Rao and Thyagaraj, 2003; Khattab et al., 2007; Al-Mukhtar et al., 2011; Al-Mukhtar et al., 2012; Obuzor et al., 2012).

Low impact development (LID) is an ecologically based stormwater management approach favoring soft engineering to manage rainfall on a site through a vegetative treatment network. The LID aims to sustain a site's pre-development hydrologic regime by using techniques that infiltrate, filter, store, and evaporate stormwater runoff close to its source. Contrary to the conventional "pipe-and-pond" conveyance infrastructure that channels runoff elsewhere through pipes, catchment basins, and curbs and gutters, LID remediates polluted runoff through a network of distributed treatment landscapes (Low Impact Development, 2010). In developed countries, such as the United States, Australia, and Germany, LID technology has been widely used in rainfall control and utilization projects, renovation of old towns, planning of new towns, and regional development design, and corresponding design standards have been formed. LID technology is the core idea of sponge city planning, which has been well-developed in China in recent years, and it is mainly used to manage urban flooding and to improve urban water treatment methods and water recycling capacity. Future research should include comprehensive and systematic research on the LID technology, research on the effectiveness of removal

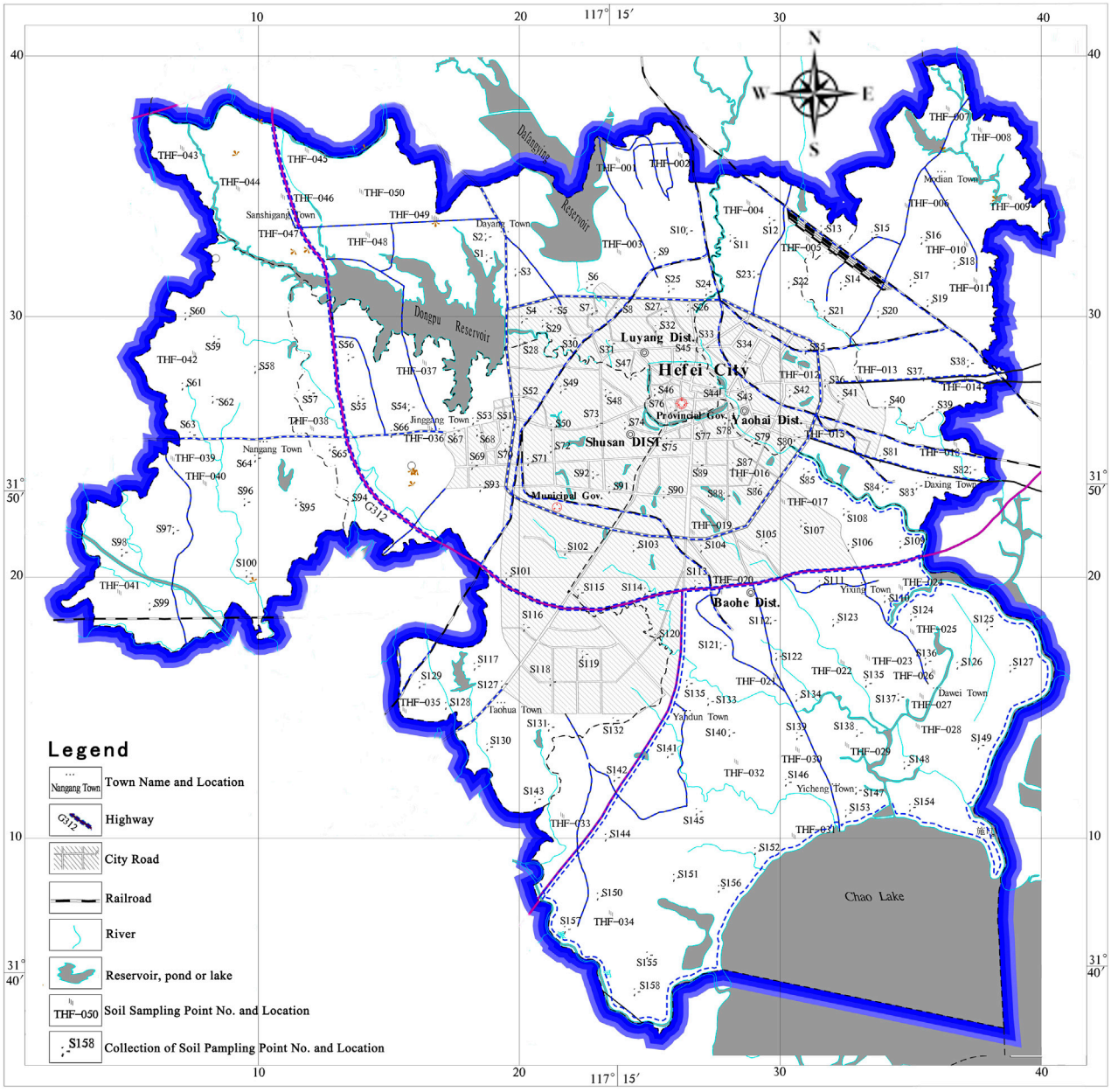

FIGURE 2
Map of the sampling sites in the distribution area of expansive soils in Hefei, China (Anhui Engineering Investigation Institute, 2008).

of difficult-to-detect pollutants, and research on the structure and materials in LID facilities.

In October 2014, Housing and Urban–Rural Development of the People's Republic of China issued the *Technical Guidelines for Sponge City Construction—Low Impact Development Stormwater System Construction* (*Trial*), which clarifies that the total runoff control pathway includes reduction of infiltration and emission of rainwater and direct storage and utilization. LID technologies mainly include infiltration, storage, regulation, transfer and interception, and purification technologies (Beijing University of Civil Engineering and Architecture et al., 2014).

The city of Hefei is located in the central-eastern part of China (Figure 1), and the entire main urban area of Hefei is situated on top of expansive soils. Therefore, the study of both the nature of the expansive soils and their engineering treatment is very significant for the selection of technical measures for LID.

2 Main characteristics of expansive soils in the study area

2.1 Main mineral composition of expansive soil

According to the regional data, the expansive soils of the Upper-Pleistocene Xiashu Group are widely distributed throughout the

TABLE 1 Statistical table showing free swelling ratio results for soil samples in the Hefei urban area (Anhui Engineering Investigation Institute, 2008).

Project	Free swelling ratio (%)		
	30–40	40–50	>50
Sample number	58	42	108
Percentage of total samples	28	20	52
Maximum of the free swelling ratio	76		
Minimum of the free swelling ratio	30		
Average of the free swelling ratio	54		

Note: The free swelling ratios were determined by the Test Center of 327 Geological Team of Anhui Geological and Mineral Exploration Bureau. The free swelling ratios were determined according to the method provided in Appendix D of the *Technical Code for Buildings in Expansive Soil Regions* (*GB50112-2013*) (Ministry of Housing and Urban-Rural Development of the People's Republic of China, 2012).

urban area of Hefei. The expansive soils contain a large number of hydrophilic clay mineral components, of which 35%–43% are hydroclays, 4.6%–6.8% are kaolins, and 2%–2.7% are montmorillonites (Anhui Engineering Investigation Institute, 2008). These mineral components have strong hydrophilicity and have significant characteristics of both water-absorbing expansion and water-losing contraction with change in water content. The change in soil volume, i.e., expansion or contraction, causes damage to engineering structures or slopes.

2.2 Water content of expansive soil

According to regional data, the natural water content of expansive soils widely distributed in the main city of Hefei is 21%–28% (Anhui Engineering Investigation Institute, 2008). Relevant studies show that when the water content of the expansive soil body increases by 1%, the volume of the soil body can increase by 2%–5%. Dry expansive soil has a high swelling potential, and conversely, it has low swelling potential. The soil body has a dry and wet cycle and constantly develops soil fissures, which will have an impact on the LID measures. Therefore, the selection of LID measures should take into account the water content of the soil body of the expansive soil. The "*Sponge City Construction Technical Guidelines—Low impact Development of Stormwater System Construction* (*Trial*)" pointed out that when applying the permeable paving LID measures in the distribution area of expansive soil, necessary preventive and control measures should be taken to prevent the impact of geologic hazards of expansive soil deformation (Shi et al., 2002; Xie, 2009; Beijing University of Civil Engineering and Architecture et al., 2014).

2.3 Free swelling ratio of expansive soil

According to the *Technical Code for Buildings in Expansive Soil Regions* (*GB50112-2013*), the free swelling ratio of expansive soils should be calculated by the following formula (Ministry of Housing and Urban-Rural Development of the People's Republic of China, 2012):

$$\delta_{ef} = \frac{v_w - v_0}{v_0} \times 100, \quad (1)$$

where δ_{ef} is the free swelling ratio of expansive soil (%), v_w is the volume of the soil sample after swelling and stabilization in water (mL), and v_0 is the original volume of the soil sample (mL).

IS 1498 (BUREAU OF INDIAN STANDARDS, 1970) gives a criterion to predict the expansivity of soils, based on the free swell index (BUREAU OF INDIAN STANDARDS, 1977).

$$\mathrm{FSI} = \frac{V_d - V_k}{V_k} \times 100, \quad (2)$$

where V_d is the sediment volume of 10 g of oven-dried soil passing a 425 μm sieve placed in a 100 mL graduated measuring jar containing distilled water and V_k is the sediment volume of 10 g of oven-dried soil passing through a 425 μm sieve placed in a 100 mL graduated measuring jar containing kerosene.

Equations 1 and 2 show that the formula for calculating the free swelling ratio for expansive soil is the same for China and India, but the method of measurement is different. In this paper, the free expansion rate is determined based on the Chinese *Technical Code for Buildings in Expansive Soil Regions* (*GB50112-2013*).

In May 2008, Anhui Engineering Investigation Institute completed collection of 50 soil samples (Figure 2) and testing work in the Hefei city area and collected and utilized data of soil samples testing of 158 boreholes in geotechnical engineering survey projects in the Hefei city area (Figure 2). The soil samples were extracted without disturbance.

The 30%–40% free swelling ratio is 28%. The 40%–50% free swelling ratio is 20%. The greater than 50% free swelling ratio is more than 50% (Table 1). These indicated that clays in the Xiashu group of the Upper Pleistocene distributed in the area generally have a weak potential for expansion (Figure 3) (Anhui Engineering Investigation Institute, 2008).

2.4 Climate effects of expansive soils

2.4.1 Humidity coefficient of expansive soils

The humidity coefficient of expansive soil is the ratio of the minimum value of soil moisture content that may be reached at 1 m depth to its plastic limit value under the influence of natural climate.

According to the *Technical Code for Buildings in Expansive Soil Regions* (*GB50112-2013*) (Ministry of Housing and Urban-Rural

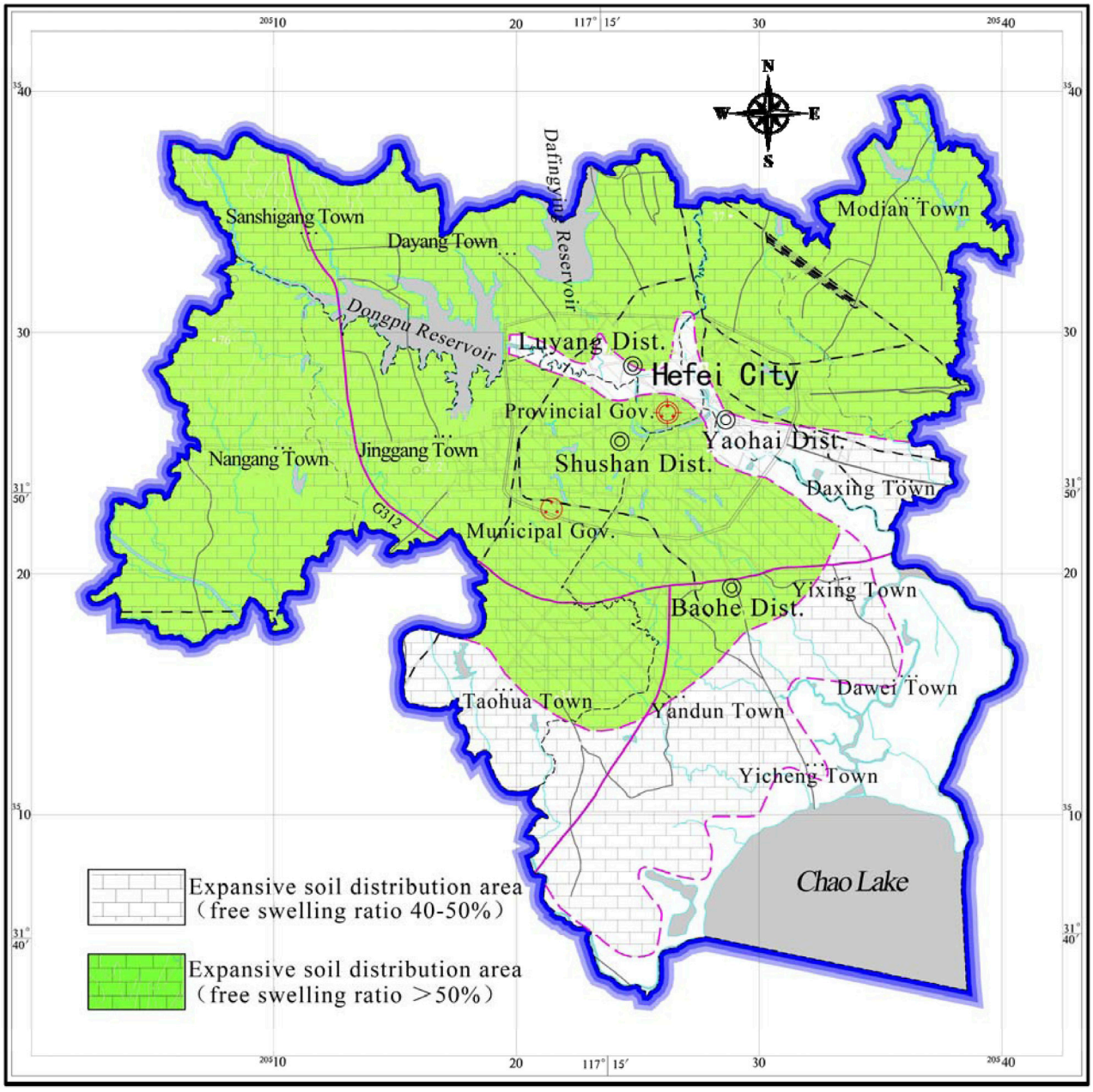

FIGURE 3
Area distribution of expansive soils in Hefei, China (Anhui Engineering Investigation Institute, 2008).

Development of the People's Republic of China, 2012), the humidity coefficient of the soil can be calculated according to the following formula based on the relevant meteorological data of Hefei:

$$\psi_w = 1.152 - 0.726\alpha - 0.00107c, \quad (3)$$

where ψ_w is the humidity coefficient of expansive soil, α is the ratio of the sum of the local evaporation power from September to February to the annual evaporation power, and c is the sum of the difference between the evaporation power and precipitation in the months, with dryness greater than 1.00 in the whole year (mm).

2.4.2 Climate-influenced layer and markedly climate-influenced layer of expansive soils

According to Equation 3, the humidity coefficient (ψ_w) of expansive soil is calculated as 0.868 (Table 2). The thickness of the climate-influenced layer as calculated by the interpolation method is 3.34 m Table 3. The thickness of the markedly climate-influenced layer is 1.50 m, calculated by multiplying the thickness of atmospheric influence by 0.45 (Ministry of Housing and Urban-Rural Development of the People's Republic of China, 2012). The deformation disaster of expansive soil will be more serious at this depth, i.e., the LID measures need to consider the climate-influenced layer of

TABLE 2 Values of the humidity coefficient of expansive soils (Ministry of Housing and Urban-Rural Development of the People's Republic of China, 2012).

Months Parameters	Jan.	Feb.	Mar.	Apr.	May	Jun.	Jul.	Aug.	Sept.	Oct.	Nov.	Dec.
Evaporation power (mm)	19.0	25.6	51.3	71.7	111.5	131.9	150.0	146.3	80.8	59.2	27.9	18.5
Precipitation (mm)	33.6	50.2	75.4	106.1	105.9	96.3	181.5	114.1	80	43.2	52.5	31.5
Dryness	0.57	0.51	0.68	0.68	1.05	1.37	0.83	1.28	1.01	1.37	0.53	0.59
α	0.258											
c	90.20											
ψ_w	0.868											

Note: Data of the evaporation power (mm) and precipitation (mm) are from Appendix D of the *Technical Code for Buildings in Expansive Soil Regions* (*GB50112-2013*) (Ministry of Housing and Urban-Rural Development of the People's Republic of China, 2012).

TABLE 3 Climate-influenced layer thickness (Ministry of Housing and Urban-Rural Development of the People's Republic of China, 2012).

Humidity coefficient of expansive soil (ψ_w)	Thickness of the climate-influenced layer
0.6	5.0
0.7	4.0
0.8	3.5
0.9	3.0

3.34 m and the markedly climate-influenced layer of 1.50 m, which will directly affect the implementation of the LID measures.

3 Test simulation systems and methods

3.1 Test simulation system

A laboratory small-scale multi-nozzle, under spray tank-type artificial rainfall simulation system was built. Spraying was controlled by controlling the switch of the solenoid valve. The pressure of the nozzles was controlled by a pipe pressure gauge, which ultimately enabled the simulation of different rainfall intensities (Figures 4, 5). The main equipment components of the laboratory artificial rainfall simulation system consisted of the expansive soil trough surrounded by rain curtains (Figure 6A), the expansive soil trough support frame (Figure 6B), the top wide-angle cone nozzle (Figure 6C), the pressure gauge and solenoid valve

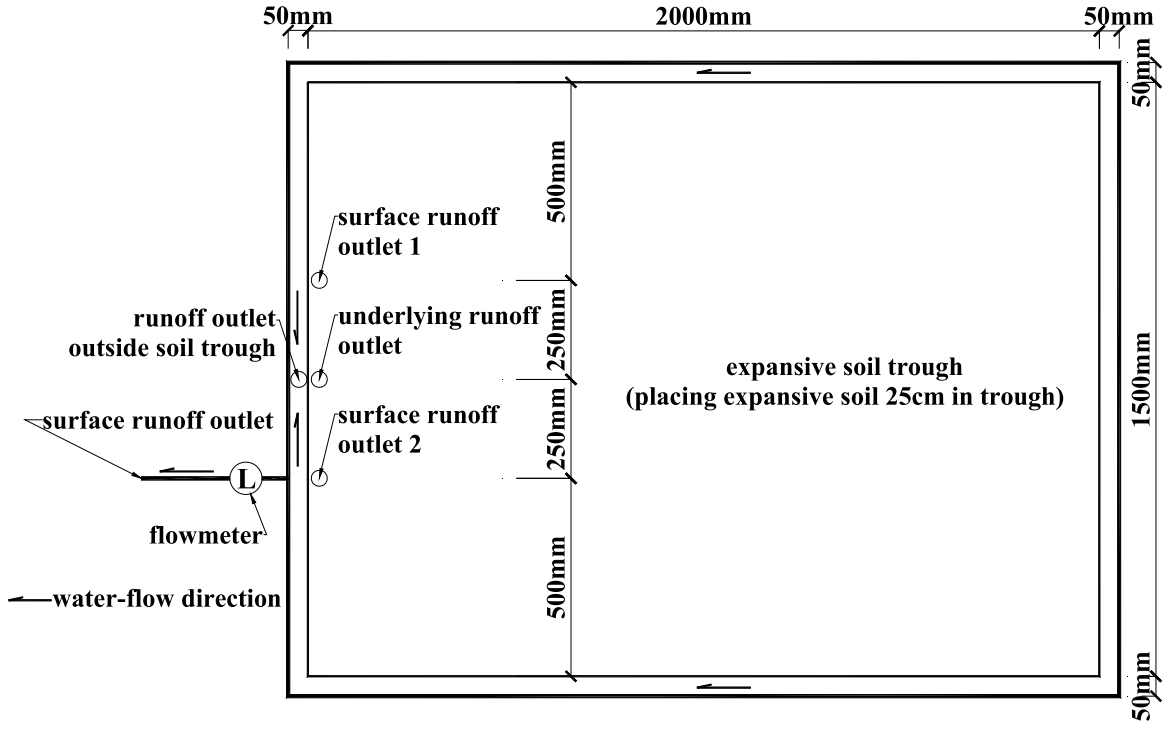

FIGURE 4
Expansive soil trough layout plan.

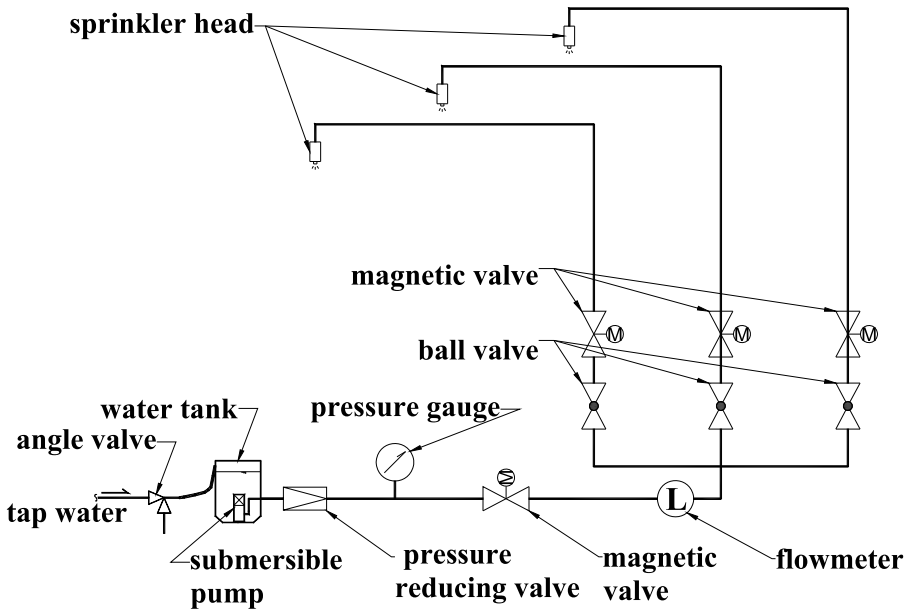

FIGURE 5
System diagram of the simulated rainfall device above the expansive soil trough.

(Figure 6D), the control cabinet (Figure 6E), and the submersible pump (Figure 6F).

The purpose of establishing this test simulation system was to study the infiltration capacity and runoff generation characteristics of expansive soils under different rainfall intensities. In addition, the test simulation system also studied the infiltration capacity of expansive soils and the characteristics of runoff generation under different levels of initial water content in expansive soils.

According to Chinese meteorology data, rainfall of 16 mm or more per hour is called "torrential rain." Rainfall intensities of 0.25 mm/min, 0.44 mm/min, 0.57 mm/min, 0.67 mm/min, and 1.04 mm/min were designed for simulation tests in combination with historical rainfall statistics from Hefei meteorological stations.

3.2 Test methods

The test expansive soil was taken from the bare expansive soil excavated from the longitudinal section of the local newly repaired road in order to simulate the natural compaction of the real expansion soil body. The test fill thickness was 25 cm (Figure 6A). The expansion soil body was wetted by rainfall three times, with an interval of 3 days. Each time, the wetting was to be stopped by the production of streams, and it was covered with a rain cloth until the expansion soil body was sufficiently settled and sinked (Figure 6A). The surface soil was sampled and observed, and the average dry bulk weight was 1.41 g/cm^3, which was close to the bulk weight of the expansive soil after natural consolidation.

Before the beginning of the test, the water content of the surface layer of the expansive soil body was maintained at 23% (±0.3%) to ensure that the water content of the soil body itself does not affect the generation time of rainfall runoff and runoff volume, respectively, in the rainfall intensity of 0.25 mm/min, 0.44 mm/min, 0.57 mm/min, 0.67 mm/min, and 1.04 mm/min; the surface of the expansive soil body was stimulated to produce the runoff process.

3.3 Test results

3.3.1 Infiltration capacity of expansive soils

It was found that at rainfall intensities of 0.25 mm/min and 0.44 mm/min, no runoff was generated from the surface of the expansive soil mass within 1 h. Under the rainfall intensities of 0.57 mm/min (Figure 7A), 0.67 mm/min (Figure 7B), and 1.04 mm/min (Figure 7C), the time to start generating runoff was 44 min, 30 min, and 17 min, respectively, and the time to reach the maximum runoff was 47 min (Figure 7A), 33 min (Figure 7B), and 19 min (Figure 7C), respectively. The time intervals between the start of generation of runoff and reaching the maximum level of runoff were 3 min, 3 min, and 2 min, respectively. The maximum runoff intervals are similar for rainfall intensities of 0.57 mm/min (Figure 7A), 0.67 mm/min (Figure 7B), and 1.04 mm/min (Figure 7C). The test results show that the exposed expansive soil has a rapid infiltration capacity and a short time interval to reach the maximum runoff volume under higher rainfall intensity, which is not very effective in reducing surface runoff.

Relevant studies have shown that with the continuation of rainfall, the infiltration potential gradient of expansive soils decreases after water absorption, and the surface cracks of land with expansive soils are closed due to soil expansion, resulting in a decrease in soil infiltration capacity. When encountering strong rainfall, due to the expansion, the cracks in the soil will be rapidly

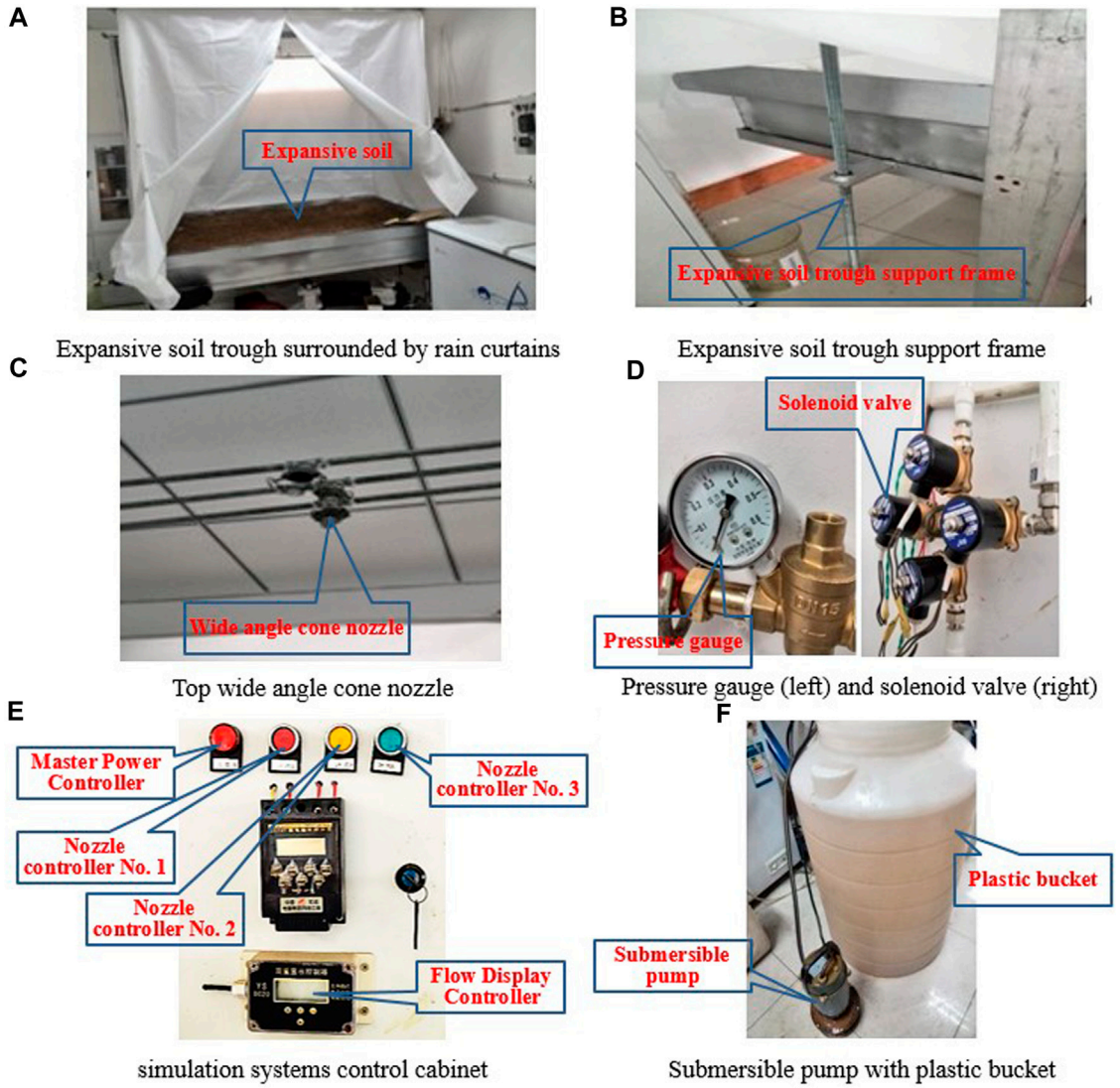

FIGURE 6
Main equipment components of the laboratory artificial rainfall simulation system.

closed. This leads to a rapid decline in soil infiltration capacity (Lei et al., 2020).

3.3.2 Initial water content of expansive soils

It was found that the simulated surface layer of expansive soil was operated under the initial water content of 21.6%, 24.8%, 26.3%, and 27.5%, and the time for starting generating of runoff was 49 min (Figure 8A), 31 min (Figure 8B), 22 min (Figure 8C), and 16 min (Figure 8D), respectively. The time taken for reaching the maximum runoff was 66 min (Figure 8A), 48 min (Figure 8B), 40 min (Figure 8C), and 33 min (Figure 8D), respectively. The time interval of arriving at maximum runoff was 17 min (Figure 8A), 17 min (Figure 8B), 18 min (Figure 8C), and 17 min (Figure 8D), respectively. It can be seen that the four simulated water content rates were similar to the natural water content of local expansive soil. The time interval for producing maximum runoff was similar as well, indicating that there is a certain effect of abatement of runoff generated by rainfall under the natural water content of expansive soils. This further demonstrates that maintaining the natural water content of expansive soils can reduce the occurrence of geologic hazards and surface runoff from rainfall.

4 Selection of LID technical measures

Low impact development technologies can generally be categorized into several types according to their main functions, such as infiltration, storage, regulation, transfer, interception, and purification.

In October 2014, the *Technical Guidelines for Sponge City Construction—Construction of Low Impact Development Stormwater System* (*Trial*) listed the relevant LID technical measures (Table 4).

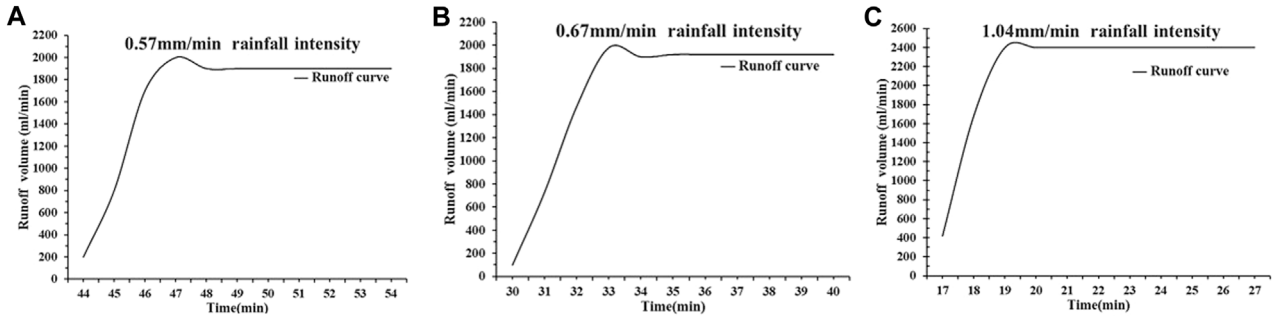

FIGURE 7
Runoff curves under different rainfall intensities.

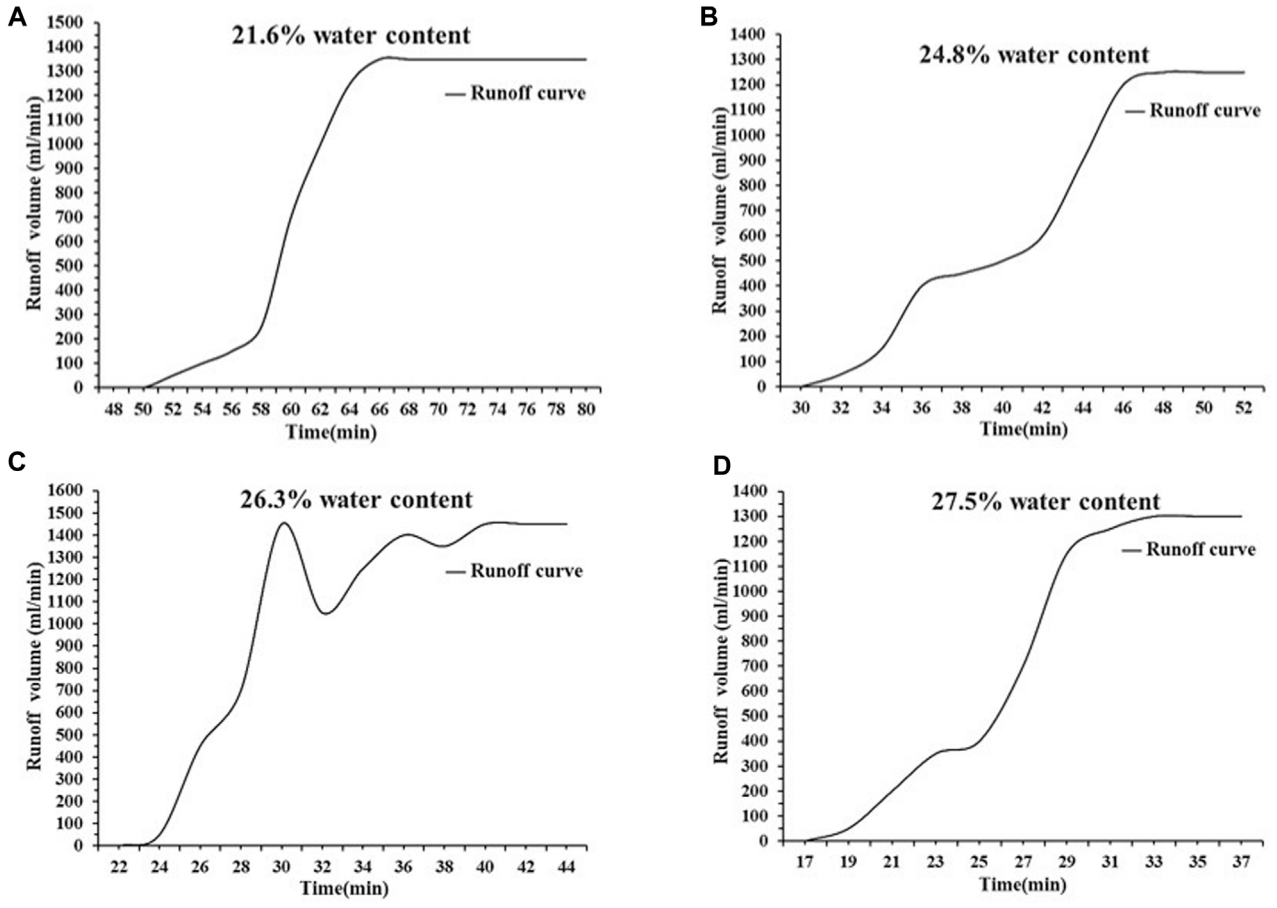

FIGURE 8
Runoff curves under different water contents.

Some of the low impact development technical measures listed in Table 4, such as infiltration, sewage interception, and purification, are not suitable to be selected in expansive soil development areas. If necessary, infiltration and decontamination measures can be selected after enhancement of expansive soil properties, but this implies an increase in the cost. This is a particular concern for our municipal, environmental, and landscape design engineers.

At present, the treatment for enhancing the properties of expansive soil roadbeds all over the world generally adopts the mixing of lime, cement, fly ash, and other mineral cementing materials. First of all, all the above materials are in powder form, and it is difficult to mix the expanded soil sufficiently. Second, the cost of improvement is high, and it also has a greater impact on the surrounding environment and the health of the construction workers (Chen et al., 2006; Yang et al., 2014).

TABLE 4 Comparison of low impact development facilities (Beijing University of Civil Engineering and Architecture et al., 2014).

Technology types	Single facilities	Function				
		Rainwater collection and utilization	Supplementary groundwater	Peak flow reduction	Rainwater purification	Transfer
Infiltration technology	Pervious pavement	○	●	◎	◎	○
	Green roof	○	○	◎	◎	○
	Sunken green space	○	●	◎	◎	○
	Bioretention facility	○	●	◎	◎	○
	Infiltration pond	○	●	◎	◎	○
	Percolation well	○	●	◎	◎	○
Storage technology	Rainwater tank	●	○	◎	◎	○
	Impoundment	●	○	◎	◎	○
	Wet pond	●	○	●	◎	○
	Stormwater wetland	●	○	●	●	○
Regulation technology	Regulating pool	○	○	●	○	○
	Regulating pond	○	○	●	◎	○
Transfer technology	Grassed swales	◎	○	○	●	●
	Infiltration pipe/ ditch	○	◎	○	○	●
Sewage interception and purification technology	Vegetation buffer strips	○	○	○	●	-
	Initial rainwater split-flow facility	◎	○	○	●	-
	Artificial soil infiltration	●	○	○	●	-

Notes: ●: strong; ◎:stronger; ○: weak; -: little.

The characteristics of expansive soils can be enhanced by mixing them with weathered sand, which is a physical improvement. The weathered sand particles have a certain particle size, and adding it to the expansive soil can result in better mixing and homogeneous nature. Second, the surrounding environment and the health of the construction workers will face a smaller impact. In addition, the low price of weathered sand can vastly reduce the cost related to improvement. Therefore, the improvement strategies involving the mixing of weathered sand compared with the traditional means of improvement have the advantages of simple construction process, environmental protection, and low cost (Chen et al., 2006; Yang et al., 2014).

Bouassida et al. (2022) proposed a new method for characterizing expansive clays after barometer test results on intact saturated clay specimens. Oedometer tests performed on a 53% thickness clay specimen overlaid by a 47% thickness of sand showed a significant reduction in the swelling pressure compared to that measured on a full expansive clay specimen. The mitigation solution reduced the swelling effect by placing a compacted granular layer as an interface between the expansive clay and the foundation (Bouassida et al., 2022).

In summary, the mixing of weathered sand can effectively inhibit the expansion of expansive soil. This ensures the implementation of LID techniques.

5 Conclusion

The selection of the LID technical measures in the expansive soil distribution area cannot be generalized, and the following points should be paid attention to in particular:

To carry out the technical measures of infiltration, sewage interception, and purification, it is necessary to enhance the expansive soil properties. Weathered sand is easy to pick up and is inexpensive; hence, mixing of weathered sand in the improvement treatment of expansive soil should be prioritized, which is a means of physical improvement. It can meet the technical requirements of infiltration, sewage interception, and purification.

The depth of atmospheric influence and the depth of the acute layer of atmospheric influence directly affect the selection of the LID technical measures; for example, the depth of atmospheric influence in Hefei city is 3.34 m, and the depth of the acute layer of

atmospheric influence is 1.5 m. When LID facilities are constructed, the adopted LID technical measures must take into account the impact of these two depths on the LID facilities. Otherwise, the expansive soils will cause damage to the LID facilities.

The continuous cycle of drying and wetting of expansive soil causes cracks to develop continuously, resulting in the surface cracks of expansive soil extending deeper. When encountering strong rainfall, the cracks close rapidly due to soil expansion, which leads to a rapid decrease in soil infiltration capacity. Therefore, maintaining the natural water content of the expansive soil can not only better inhibit the expansion of the soil body to produce cracks, which can reduce the frequency of expansion of the soil rise and fall, but also help reduce the surface runoff generated by rainfall.

The results of the test simulation system show that the exposed expansive soil has a fast infiltration capacity and a short time interval to reach the maximum runoff volume under larger rainfall intensity, which is not very effective in reducing surface runoff. In addition, maintaining the natural water content of expansive soils can reduce the occurrence of geologic hazards and surface runoff from rainfall.

Therefore, the natural water content of expansive soil can be maintained by avoiding exposing expansive soils to vegetative cover. Granular materials can be used to mitigate swelling when LID techniques such as infiltration, filtration, and water storage are used. More research studies must be carried out on granular materials to alleviate the swelling phenomenon in the distribution area of expansive soil so as to provide technical support for the upcoming *Special Plan of Hefei City Sponge City*.

Data availability statement

The original contributions presented in the study are included in the article/Supplementary Material; further inquiries can be directed to the corresponding author.

Author contributions

MH: conceptualization, funding acquisition, investigation, software, writing–original draft, and writing–review and editing. ZL: formal analysis, investigation, and writing–review and editing. RZ: data curation, project administration, and writing–original draft. YT: data curation, software, and writing–review and editing. Y-MS: writing–review and editing and conceptualization.

Funding

The author(s) declare that financial support was received for the research, authorship, and/or publication of this article. This study was funded by the Science and Technology Major Project for Water Pollution Control and Management (2014ZX07303003) and the Anhui Provincial Department of Education Quality Engineering Project (2020rcsfjd05).

Conflict of interest

Author RZ was employed by Shucheng Zhonghe Real Estate Development Co.Ltd.

The remaining authors declare that the research was conducted in the absence of any commercial or financial relationships that could be construed as a potential conflict of interest.

Publisher's note

Supplementary material

The Supplementary Material for this article can be found online at: https://www.frontiersin.org/articles/10.3389/fenvs.2024.1417048/full#supplementary-material

References

Al-Mukhtar, M., Khattab, S., and Alcover, J. F. (2011). Stabilization of expansive soils for use in construction. *Appl. Clay Sci.* 51 (3), 348–352. doi:10.1016/j.clay.2010.12.027

Al-Mukhtar, M., Khattab, S., and Alcover, J. F. (2012). Microstructure and geotechnical properties of lime-treated expansive clayey soil. *Eng. Geol.* 139, 17–27. doi:10.1016/j.enggeo.2012.04.004

Anhui Engineering Investigation Institute (2008). *Report on geological hazard survey and zoning in Hefei city, Anhui province*. 1:100,000. (in Chinese).

Beijing University of Civil Engineering and Architecture, Urban Water Affairs Management Office of the Ministry of Housing and Urban-Rural Development, China Academy of Urban Planning and Design, Urban Planning and Design Institute of Shenzhen, China Construction Technology Consulting Co., Ltd., Beijing Garden Ancient Architecture Design and Research Institute Co., Ltd. et al. (2014). *Technical Guidelines for sponge city construction-construction of low impact development stormwater system (trial)*. Beijing, China: China Architecture and Building Press. Available at: https://www.mohurd.gov.cn/gongkai/zhengce/zhengcefilelib/201411/20141103_219465.html.

Bin Mostafiz, R., Friedland, C. J., Rohli, R. V., Bushra, N., and Held, C. L. (2021). Property risk assessment for expansive soils in Louisiana. *Front. Built Environ.* 7, 754761. doi:10.3389/fbuil.2021.754761

Bouassida, M., Manigniavy, S. A., Azaiez, D., and Bouassida, Y. (2022). New approach for characterization and mitigation of the swelling phenomenon. *Front. Built Environ.* 8, 836277. doi:10.3389/fbuil.2022.836277

BUREAU OF INDIAN STANDARDS. *Indian standard classifcation and identifcation of soils for general engineering purposes*. BIS, New Delhi, 1970, (Reaffirmed 1987), IS 1498.

BUREAU OF INDIAN STANDARDS (1977). *Indian standards method of test for soils*. New Delhi: BIS. IS 2720: Part 40.

Chen, X. H., Zhang, S., Chen, W. C., and Qin, W. (2006). Study on California Bearing Ratio (CBR) strength characterization of expansive soils in central Anhui, China. *J. Eng. Geol.* 14 (3), 386–389. doi:10.3969/j.issn.1004-9665.2006.03.018

Jones, D. E., and Holtz, W. G. (1973). Expansive soils-the hidden disaster. *Civ. Eng. ASCE* 43 (8), 49–51. Available at: https://trid.trb.org/view/133235.

Khattab, S. A., Al-Mukhtar, M., and Fleureau, J. M. (2007). Long-term stability characteristics of a lime-treated plastic soil. *J. Mater Civ. Eng.* 19 (4), 358–366. doi:10.1061/(ASCE)0899-1561(2007)19:4(358)

Lei, W. K., Dong, H. Y., Chen, P., Lv, H. B., Fan, L. Y., and Mei, G. X. (2020). Study on runoff and infiltration for expansive soil slopes in simulated rainfall. *Water*, 12, 222. doi:10.3390/w12010222

Locat, J., Bérubé, M. A., and Choquette, M. (1990). Laboratory investigations on the lime stabilization of sensitive clays: shear strength development. *Can. Geotech. J.* 27 (3), 294–304. doi:10.1139/t90-040

Low Impact Development (2010). *A design manual for urban areas*. Fayetteville: Fay Jones School of Architecture University of Arkansas Press a Collaboration. Available at: https://uacdc.uark.edu/work/low-impact-development-a-design-manual-for-urban-areas.

Ministry of Housing and Urban-Rural Development of the People's Republic of China (2012). *Technical code for buildings in expansive soil regions (GB50112-2013)*. Beijing, China: China Architecture and Building Press. Available at: https://www.mohurd.gov.cn/gongkai/zhengce/zhengcefilelib/201301/20130105_224623.html.

Obuzor, G. N., Kinuthia, J. M., and Robinson, R. B. (2012). Soil stabilisation with lime-activated-GGBS—a mitigation to flooding effects on road structural layers/embankments constructed on floodplains. *Eng. Geol.* 151, 112–119. doi:10.1016/j.enggeo.2012.09.010

Rao, S. M., and Thyagaraj, T. (2003). Lime slurry stabilisation of an expansive soil. *Proc. Instit. Civ. Eng. Geotech. Eng.* 156 (3), 139–146. doi:10.1680/geng.2003.156.3.139

Shi, B., Jiang, H., Liu, Z., and Fang, H. (2002). Engineering geological characteristics of expansive soils in China. *Eng. Geol.* 67, 63–71. doi:10.1016/S0013-7952(02)00145-X

Sun, C. L., Yin, Z. Z., Wang, F. S., and Liu, H. Z. (1995). A review of research on the properties of expansive soils. *Adv. Sci. Technol. Water Resour.* 15 (6), 10–14. Available at: https://www.cqvip.com/doc/journal/991981602

Xie, C. (2009). *Research on the engineering geology condition and the engineering geology problem of viaduct on jinzhai road in Hefei*. Hefei, P.R. China: Hefei University of Technology. doi:10.7666/d.y1507766

Yang, J., Tong, L., Zhang, G. D., and Tang, Y. W. (2014). Improving expansive soil weathered sand California Bearing Ratio (CBR) test. *J. Yunnan Agric. Univ.* 29 (4), 566–571. doi:10.3969/j.issn.1004-390X(n).2014.04.019

Ye, K. R. (2010). *Comprehensive research expansive soil in Hefei*. Hefei, Anhui, P.R. China: Hefei University of Tecnology. doi:10.3969/j.issn.1004-9665.2006.03.018

Zhang, S. N. (2005). *Experimental research on lime-stabilized expansive soil*. Nanjing, P.R. China: Hohai University. doi:10.7666/d.y693549

frontiers | Frontiers in Environmental Science

TYPE Original Research
PUBLISHED 18 July 2024
DOI 10.3389/fenvs.2024.1421320

OPEN ACCESS

EDITED BY
Zisheng Xing,
Agriculture and Agri-Food Canada (AAFC), Canada

REVIEWED BY
Taek-Keun Oh,
Chungnam National University, Republic of Korea
Yuan Li,
Lanzhou University, China

*CORRESPONDENCE
Pil Joo Kim,
pjkim@gnu.ac.kr

RECEIVED 22 April 2024
ACCEPTED 18 June 2024
PUBLISHED 18 July 2024

CITATION
Canatoy RC, Cho SR, Galgo SJC, Park SY and Kim PJ (2024), Biochar manure decreases ammonia volatilization loss and sustains crop productivity in rice paddy.
Front. Environ. Sci. 12:1421320.
doi: 10.3389/fenvs.2024.1421320

Biochar manure decreases ammonia volatilization loss and sustains crop productivity in rice paddy

Ronley C. Canatoy[1,2], Song Rae Cho[3], Snowie Jane C. Galgo[1,4], So Yeong Park[1] and Pil Joo Kim[1,4]*

[1]Division of Applied Life Science (BK21+ Program), Gyeongsang National University, Jinju, Republic of Korea, [2]Department of Soil Science, College of Agriculture, Central Mindanao University, Maramag, Philippines, [3]Soil and Fertilizer Management Division, National Institute of Agricultural Sciences, Rural Development Administration, Wanju, Republic of Korea, [4]Institute of Agriculture and Life Sciences, Gyeongsang National University, Jinju, Republic of Korea

Manure application is a recommended method to improve soil quality and mitigate global warming via soil carbon (C) sequestration. However, such application can significantly increase ammonia (NH_3) volatilization loss and cause secondary environmental problems, such as acidification, eutrophication, and particulate matter formation. To investigate the potential of reducing NH_3 emissions in flooded rice paddies, three types of stabilized swine manure amendments (fresh, composted, and biochar) were applied at a rate of 12 Mg ha^{-1} (dry weight) under standard fertilization ($N–P_2O_5–K_2O$ = 90–45–57 kg ha^{-1}), and NH_3 emission was characterized using the static chamber method. Regardless of manure management practices, NH_3 fluxes increased significantly immediately after application of an inorganic nitrogen (N) fertilizer (urea). The manure was applied completely as the basal fertilizer before rice transplanting, but the NH_3 emission rates increased more dramatically following urea application in the manure treatments. Fresh and composted manure applications significantly increased seasonal NH_3 volatilization losses compared to the control but the biochar did not. Compost manure significantly increased rice grain productivity owing to the higher N content, while fresh and biochar manures did not increase rice productivity because of fewer panicles per hill and fewer grains per panicle. Consequently, biochar application resulted in lower NH_3 flux intensity and seasonal NH_3 flux per grain yield, whereas fresh and compost manures substantially increased this intensity. Therefore, biochar manure may be a more reasonable organic amendment than fresh and composted manures for reducing NH_3 emission impacts on rice paddies.

KEYWORDS

ammonia emission intensity, compost, swine manure, grain yield, biochar

1 Introduction

Livestock manure is considered to be a practical organic amendment for enhancing soil productivity as substitutes to chemical fertilizers in croplands (Du et al., 2020; Hua et al., 2020). However, improper application of livestock manure can create various environmental problems. Manure-derived nitrogen (N) can be lost through leaching, runoff, volatilization, denitrification, and other processes. Significant proportions of N

are often lost via ammonia (NH_3) emissions from manure-amended soils. For instance, an average of 12.8% and 17.9% of the applied N was reported to have volatilized as NH_3 gas in Chinese upland and paddy fields, respectively (Zhang et al., 2013). The emitted NH_3 can lead to increased N deposition and contribute to soil acidification, water eutrophication, and particulate matter (PM) formation (Wu et al., 2016; Ehrnsperger and Klemm, 2021).

Primary PM comprise mixed liquid droplets and solid particles in the air (e.g., soot, dust, smoke). However, secondary $PM_{2.5}$ having diameters less than 2.5 μm may be formed through reactions of NH_3 with other gaseous acidic precursors (e.g., NO_x, SO_x). NH_3 is a reactive gas that readily combines with sulfate (SO_4^{2-}) and nitrate (NO_3^-) components in acidic cloud droplets to form particulates (Asman et al., 1998). When $PM_{2.5}$ is inhaled, it penetrates deep into the lungs to impair respiration by irritating and corroding the alveolar walls (Xing et al., 2016). Globally, over 4.2 million premature deaths and 103 million disability-adjusted life years have been attributed to $PM_{2.5}$ pollution (Cohen et al., 2017).

Global N losses via NH_3 emissions are estimated to be 51–54 Tg N $year^{-1}$ (Bouwman et al., 1997). Approximately 10%–20% of these emissions originate from natural sources, while the remaining 80%–90% are from anthropogenic sources (Zhang et al., 2018). Among the anthropogenic activities, agriculture contributes to about 80%–90% of NH_3 emissions, with 63% from livestock feeding and 37% from crop cultivation (Bouwman et al., 1997; Piwowar, 2020). In soils, NH_3 emission intensities are influenced by several factors, such as N fertilization level and soil conditions (e.g., temperature, moisture content, pH) (Kang et al., 2016; Klimczyk et al., 2021). Compared to upland soils, flooded rice paddies may provide more favorable conditions for higher NH_3 emissions. Applied N in soils can mineralize into ammonium (NH_4^+) and then be aerobically nitrified into nitrate (NO_3^-) (Sah and Mikkelsen, 1983). However, the nitrification rate is strongly regulated by oxygen availability (Jechalke et al., 2011; Yang et al., 2016), which generally results in the prolonged presence of inorganic NH_4^+ in flooded rice paddies and increased volatilization into NH_3 gas (Buresh et al., 2008).

Hypothetically, stabilized organic amendments (e.g., biochar, compost) may be more effective at reducing NH_3 emissions than fresh manures. In compost, inorganic N is predominantly available in the form of NO_3^-, which does not revert to NH_4^+. Stabilized organic matter can slow mineralization and thereby decrease NH_3 emissions (Lü et al., 2013; Agyarko-Mintah et al., 2017). Similarly, biochar contains less inorganic N owing to the expulsion of labile compounds during the pyrolysis process (Bruun et al., 2011; Buss et al., 2022). The organic C and inorganic N in biochar are hence more stable and resistant to decomposition (Haider et al., 2020). However, there are no readily available reports on the potentials of these stabilized organic amendments to reduce NH_3 emissions in flooded rice paddy soils.

To investigate the feasibility of stabilized manure amendments in reducing NH_3 emissions in rice paddies, three types of manures (fresh, composted, and biochar) were selected as the main treatments. The NH_3 emission losses and rice yield properties were characterized during rice cultivation to identify the organic amendment with the lowest NH_3 flux intensity.

2 Materials and methods

2.1 Preparation of manure amendments

To evaluate the impacts of manure amendments on NH_3 emissions during rice cultivation, three types of swine manures were prepared: fresh, compost, and biochar. Fresh swine manure was collected from a medium-scale pig farm in Jinju, South Korea; this manure was combined with sawdust in equal proportions (50% kg kg^{-1}) and air-dried inside a greenhouse. The air-dried manure mixture had a neutral pH (6.7 with H_2O) and contained 44.8% total C and 1.8% total N (Table 1).

To prepare the compost, 1 Mg of the manure mixture was moistened to 60% (wt wt^{-1}) and placed in a 1.2 m^3 (1 m (width) × 1 m (length) × 1.2 m (height)) box covered with Styrofoam to retain heat. The manure pile was periodically mixed for aeration and adequately moistened during the 45-day composting period; the pile temperature increased sharply to 65–75°C immediately after piling and was maintained for approximately 3 weeks before gradually declining to the background temperature. The compost had an alkaline pH (7.4 with H_2O) and contained 43.4% total C and 2.2% total N.

To prepare the biochar, the dried manure mixture was pyrolyzed using a muffle furnace under closed conditions at 400°C for 4 h; the mixture was then placed inside the furnace and gradually heated at a rate of 10°C per minute before being stabilized at 400°C. The biochar had an alkaline pH (8.2 with H_2O) and contained 42.2% total C and 1.2% total N.

2.2 Experimental plot preparation for rice cultivation

A typical mono-rice paddy field was selected at the Gyeongsang National University experimental station (latitude 35° 8′56.73″ N, longitude 128° 5′46.27″ E) in the Republic of Korea. The paddy field has been exclusively used for rice farming for over 50 years, and the soil is classified as belonging to the Jisan series (fine silty, mixed, non-acid mesic Typic Endoaquepts). Before the experiments, the soil had a slightly acidic pH (6.0 in H_2O) and low fertility, with total C and N contents of 18.9 and 1.4 g kg^{-1}, respectively.

A total of four treatments (control, fresh, compost, and biochar) were assigned with three replications each. The experimental plots (10 m × 10 m in size) were arranged in a randomized complete block design (RCBD). Irrigation inlets and outlets were prepared in each plot to control the flooded water levels; a metal barrier was deeply installed around each plot to avoid lateral water flow and fertilizer treatment mixing. In South Korea, the general recommendation for organic amendment application is 12 Mg ha^{-1} (RDA, 2017). One day before transplanting in the manure treatment plots, 12 Mg ha^{-1} of each of the manure amendments (on a dry weight basis) were manually mixed into the surface layers of the corresponding plots. The recommended levels of chemical fertilizers for rice cultivation (N–P_2O_5–K_2O = 90–45–57 kg ha^{-1}) were applied to all the treatment plots (RDA, 2017). Based on the recommended rates, 50% of N, 100% of P_2O_5, and 70% of K_2O were applied as the basal fertilizers. The remaining fertilizers were side dressed on the 15th day (20% of N) and 45th day (30% of N and K_2O) after transplanting.

TABLE 1 Chemical properties of the manure amendments used.

Property	First year			Second year		
	Fresh	Compost	Biochar	Fresh	Compost	Biochar
pH (1:5 with H_2O)	6.7 ± 0.2	7.5 ± 0.2	8.1 ± 0.3	6.8 ± 0.2	7.3 ± 0.3	8.4 ± 0.2
Electrical conductivity (dS^{-1})	2.9 ± 0.1	7.7 ± 0.2	0.5 ± 0.0	2.4 ± 0.1	7.2 ± 0.2	0.6 ± 0.0
Total C (g C kg^{-1})	455 ± 16	437 ± 12	426 ± 15	441 ± 12	432 ± 16	417 ± 11
Total N (g N kg^{-1})	17 ± 0.6	23 ± 0.6	12 ± 0.4	19 ± 0.5	21 ± 0.8	13 ± 0.3
C/N ratio	27 ± 1.0	19 ± 0.5	36 ± 1.3	23 ± 0.6	21 ± 0.7	32 ± 0.8
Inorganic N (g N kg^{-1})						
NH_4^+	4.2 ± 0.2	5.2 ± 0.1	0.1 ± 0.0	5.0 ± 0.1	5.5 ± 0.2	0.2 ± 0.0
NO_3^-	1.5 ± 0.1	6.1 ± 0.2	0.04 ± 0.0	1.9 ± 0.1	6.4 ± 0.2	0.03 ± 0.0

Twenty-five-day-old Dongjinbyeo cultivar (Japonica) rice seedlings were used in this study. Three to five seedling plants were manually transplanted per hill, with distances of 15 cm each between the hills and 30 cm each between the rows. The irrigated water in each plot was maintained at 5–7 cm above the surface soil layer. The floodwater was drained 4 weeks before rice harvesting. At the harvesting stage, 10 representative rice plants were collected from each plot. The plant samples were air-dried for a week in the greenhouse, and the seeds were detached from the panicles before counting. Finally, the harvest index was determined as the ratio of grain yield to total aboveground biomass.

2.3 Evaluation of ammonia volatilization loss

To assess the influences of manure amendment applications on NH_3 emissions during rice cultivation, the static chamber method was used. The chamber (inner diameter: 12 cm; height: 25 cm) was inserted into the soil to a depth of 15 cm without the rice plants. Two acid-impregnated sponges (diameter: 12 cm; height: 2 cm) were placed inside the chamber to trap the NH_3 gas from the soil and outside air separately. Phosphoric acid was used to trap the NH_3 gas, and 4% glycerin was used to maintain the moisture in the sponge. NH_3 samples were collected daily for 1 week after N fertilization, followed by collection at 2- to 3-day intervals for 2 weeks, and finally once per week during the rest of the rice cultivation period.

During sampling, the lower sponges were collected and placed in an icebox for preservation. They were then completely immersed in a 2 M KCl solution and shaken using a rotating shaker for 1 h. Subsequently, the sponges were squeezed by hand, and the NH_4^+–N concentration was quantified using the indophenol blue method (Novamsky et al., 1974). The NH_3 emission rate was estimated from the amount of NH_3 trapped per unit area over a specific sampling interval:

$$NH_3\ emission\ rate\ (mg\ N\ m^{-2}\ day^{-1}) = \frac{M}{A\,x\,D}$$

where M (mg) is the NH_4^+–N collected in the chamber, A (m^2) is the chamber area, and D (day) is the duration for NH_3 sampling.

The seasonal NH_3 flux was calculated using the daily NH_3 emission rate and sampling interval:

$$\text{Seasonal } NH_3 \text{ flux } (\text{kg N ha}^{-1}) = \sum_i^n (R_i \times D_i),$$

where R_i is the daily NH_3 emission rate (kg N ha^{-1} day^{-1}) in the *ith* sampling interval, D_i is the number of days between the *ith* and $(i–1)th$ sampling, and n is the number of samplings.

2.4 Analysis of manure amendment, soil, and water characteristics

The manure amendments were sampled and their chemical properties analyzed for pH and electrical conductivity (EC) (1: 10 wt v^{-1}, sample: H_2O); total C and N contents using an automated true macro element analyzer; and inorganic NH_4^+ and NO_3^- contents using 2 M KCl extraction and measurement with the indophenol blue and brucine methods, respectively. During rice cultivation, the soil temperature and redox potential (Eh) changes were continually recorded using an automatic sensor at a soil depth of 15–20 cm. The floodwater and surface soil were sampled periodically to monitor changes in pH and NH_4^+ concentration following the same analysis procedures as noted above.

2.5 Statistical analysis

The Statistical Tool for Agricultural Research 2.0.1 (STAR) software was used for the statistical analyses. The data were analyzed using one-way analysis of variance (ANOVA) for the RCBD; the statistically significant results were subjected to comparison of means using the honestly significant difference (HSD) test at the 5% significance level.

3 Results

3.1 Changes in soil temperature and Eh values

During rice cultivation, the soil temperature and Eh values were continuously monitored at the surface layer (Figure 1). The soil temperature fluctuated similarly to the air temperature but showed no significant differences among the treatments or years; the

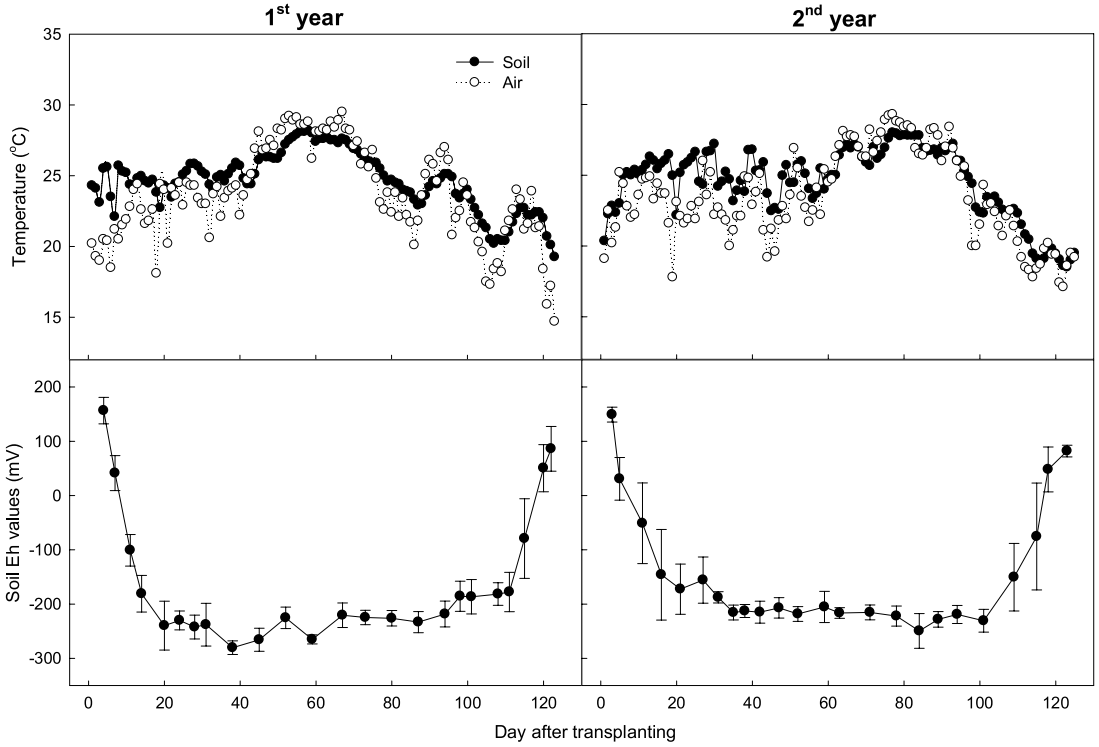

FIGURE 1
Changes in soil and air temperatures, as well as soil Eh values, during rice cultivation.

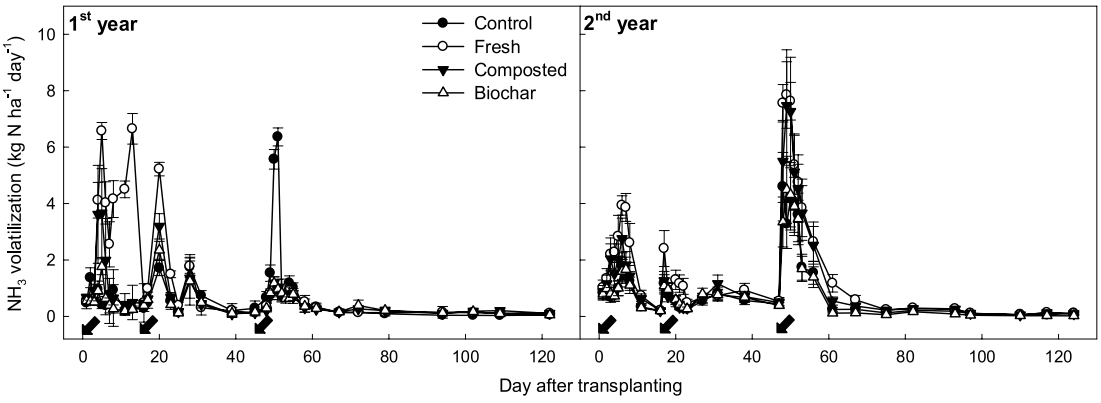

FIGURE 2
Changes in NH_3 emission rates of rice paddy supplied with different types of manure amendments. The arrows indicate split N fertilization days, while the vertical bars indicate standard deviations (n = 3).

temperature increased gradually after rice transplantation, reached a peak value during the reproductive stage, and declined gradually thereafter. The soil Eh values exhibited a typical pattern throughout the entire rice cultivation period, with no marked differences among the various manure treatments. Within 2 weeks of submerging for rice transplanting, the Eh value declined sharply to −200 mV, indicating a highly reduced soil environment that persisted throughout the flooded cropping period. Following water drainage 1 month before rice harvesting, the soil Eh value increased rapidly, but no significant differences were observed among the different fertilizer treatments.

3.2 Changes in NH_3 emissions

Irrespective of the manure types and investigation years, NH_3 gas was emitted in a similar pattern (Figure 2). The recommended levels of chemical fertilizers were applied in all the treatments; the NH_3 emission rates increased sharply immediately after the addition of N fertilizer (urea). The total urea was split into three applications as the basal (50%) fertilizer 1 day before rice transplantation, at tillering (20%) 15 days after transplantation, and at panicle initiation (30%) 45 days after

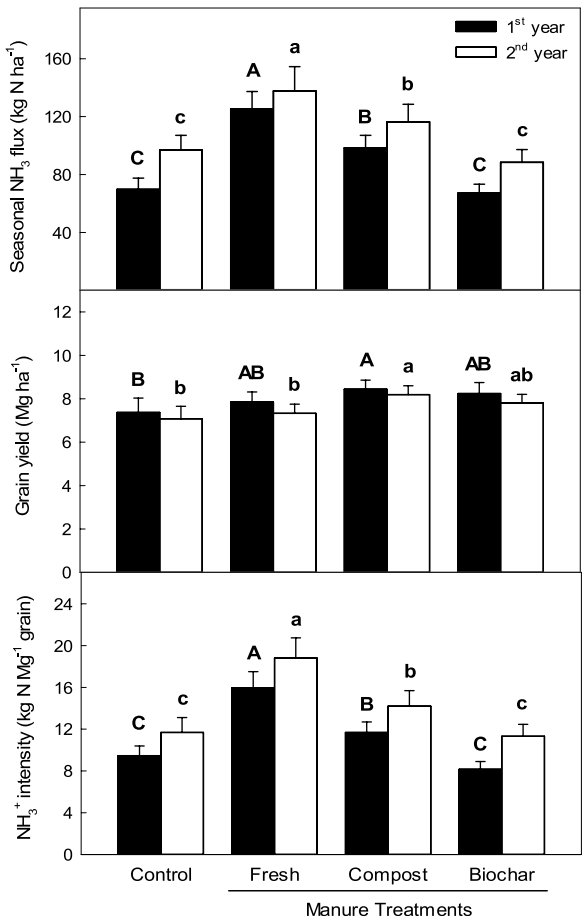

FIGURE 3
Seasonal NH_3 fluxes, grain yields, and NH_3 flux intensities during rice cultivation when supplied with different types of manure amendments. The vertical bars indicate standard deviations (n = 3).

transplantation. However, manure addition significantly increased the NH_3 emission rates.

In the no-manure treatment (control), a total of 70–97 kg N ha^{-1} of NH_3 gas was emitted over the entire rice cultivation period, but the addition of 12 Mg ha^{-1} (dry weight) of fresh manure largely increased this seasonal flux by 42%–80% over the control (Figure 3). Stable manure types, such as the biochar and compost, were effective at reducing the increased NH_3 fluxes. Compost manure reduced the seasonal NH_3 flux by approximately 16%–21% compared to fresh manure. However, biochar exhibited even greater efficacy, reducing the seasonal NH_3 flux by 36%–46% compared to fresh manure. Furthermore, biochar showed a 4%–9% lower seasonal NH_3 flux than the control, although no statistically significant difference was observed between the two treatments.

3.3 Changes in floodwater and soil chemical properties

The floodwater pH and NH_4^+ concentrations fluctuated similarly during the 2 years of rice cultivation (Figure 4). Regardless of manure application, these two properties increased sharply after urea addition and then decreased gradually. Manure treatments had more pronounced influences on these properties. Fresh manure application significantly increased the water pH and NH_4^+ concentration during the early rice cropping season, but these changes were less evident in the late cropping season.

In contrast to the floodwater changes, the soil properties (pH and inorganic NH_4^+ concentration) remained relatively stable during rice cultivation (Figure 5). The soil pH was initially low when the soil Eh value was higher; as the soil condition became highly reduced, the soil pH increased. Manure application enhanced soil pH during the early rice-growing season, with biochar proving more effective than fresh and compost manures in this regard. Regardless of the fertilization background, the soil NH_4^+ concentration increased slightly over time. Manure application comparably increased the inorganic NH_4^+ contents in the soils. Among the manure treatments, biochar application significantly increased the soil NH_4^+ level throughout the cropping period, although the differences were comparable among the various manure treatments.

3.4 Rice productivity and ammonia flux intensity

The rice yield properties differed between the cropping years, but the organic amendment application increased rice productivity consistently (Figure 3). The average grain yield was 7.2 Mg ha^{-1} for the control treatment. Compost application significantly increased grain productivity owing to the higher panicle numbers per hill and number of seeds per panicle, whereas the fresh and biochar manure applications increased rice productivity slightly without any statistically significant differences (Table 2). The NH_3 flux intensity, indicating the seasonal NH_3 flux per grain yield, was approximately 9.5 kg NH_3–N Mg^{-1} grain for the control treatment (Figure 3). The fresh and compost manure applications significantly increased the average NH_3 flux intensities by 69% and 38% over the control, respectively; however, biochar manure application did not increase the flus intensity over that of the control.

4 Discussion

The N losses via NH_3 emissions from the field-applied amendments have garnered significant attention, owing to their impacts on reduced fertilizer effectiveness and more environmental problems (Misselbrook and Powell, 2005; Monaco et al., 2012). Flooded rice paddies possess soil conditions that are particularly conducive to NH_3 volatilization compared to upland conditions owing to the reduced oxygen levels and higher pH during the flooded cropping season (Ventura and Yoshida, 1977; Zhao et al., 2009; Zhang et al., 2013). Urea-N applied to the soil is rapidly converted to NH_4^+ ions, which can either volatilize into NH_3 gas or undergo biological nitrification to form NO_3^- ions (Saggar et al., 2013; Barth et al., 2019). However, the rate of nitrification is influenced by oxygen availability (Jechalke et al., 2011; Hsiao et al., 2014). In flooded rice paddies, NH_4^+ ions can persist due to the low-oxygen environment, leading to higher NH_3 volatilization losses.

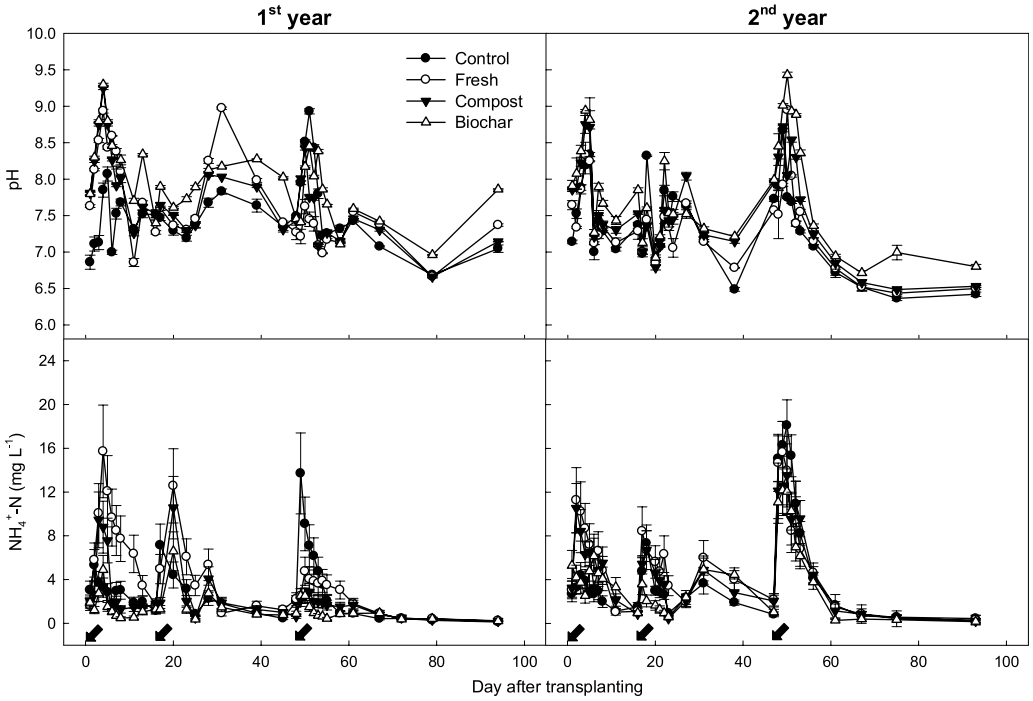

FIGURE 4
Changes in the pH and NH_4^+ concentrations in rice paddy floodwaters supplied with different types of manure amendments. The arrows indicate split N fertilization days, and the vertical bars indicate standard deviations (n = 3).

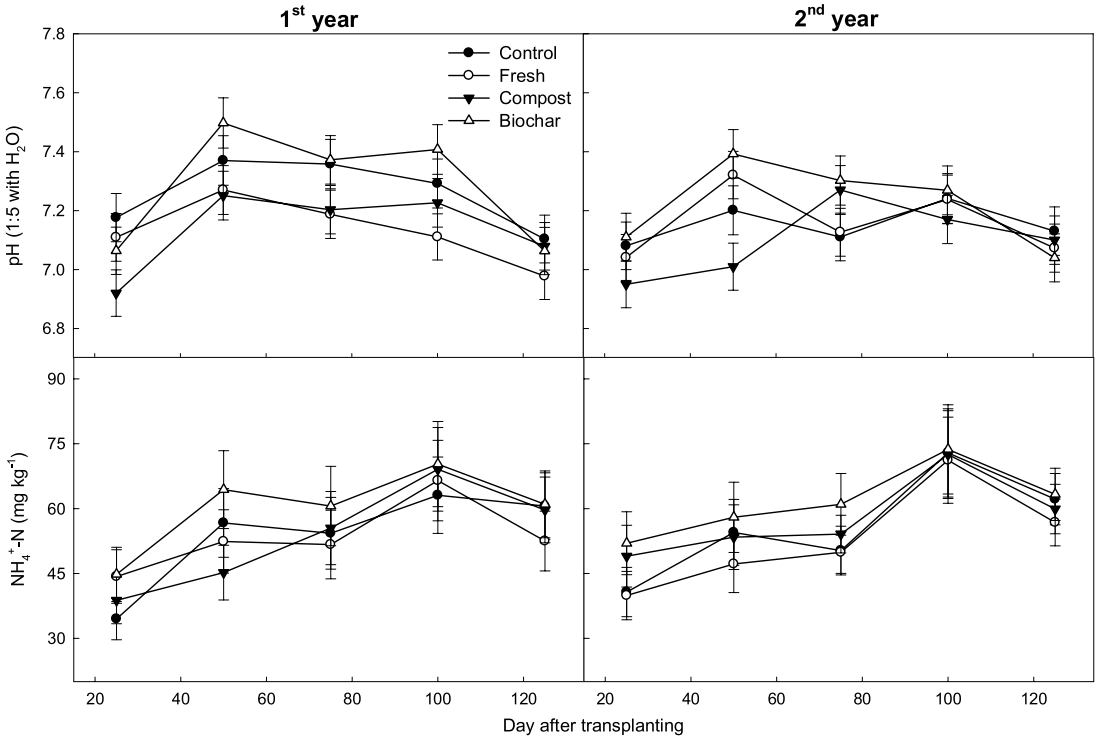

FIGURE 5
Changes in the pH and NH_4^+ concentrations in rice paddy soils supplied with different types of manure amendments. The vertical bars indicate standard deviations (n = 3).

TABLE 2 Rice yield properties in different types of manure-amended soils.

Year (A)	First year				Second year			
Amendments (B)	Control	Fresh	Compost	Biochar	Control	Fresh	Compost	Biochar
Panicle number per hill	13.6^{a}	13.9^{a}	14.6^{a}	14.4^{a}	13.1^{C}	13.6^{BC}	16.4^{A}	15.1^{AB}
Number of grains per panicle	112.2^{b}	126.1^{a}	127.3^{a}	122.3^{ab}	102.7^{A}	108.4^{A}	114.7^{A}	106.3^{A}
Ripened grains (%)	92.4^{a}	90.5^{a}	91.1^{a}	91.6^{a}	93.5^{A}	91.1^{A}	92.3^{A}	92.7^{A}
1,000 grain weight (g)	23.6^{a}	22.1^{a}	22.7^{a}	22.5^{a}	24.2^{A}	23.2^{A}	23.7^{A}	23.0^{A}
Straw yield (Mg ha^{-1})	8.6^{b}	9.4^{ab}	11.6^{a}	11.7^{a}	8.2^{C}	9.2^{BC}	11.2^{A}	10.7^{AB}
Harvest index (%)	46^{a}	45^{a}	42^{a}	41^{a}	46^{A}	44^{A}	42^{A}	42^{A}

Note: Different letters indicate significant differences, as determined by the HSD method with $p < 0.05$.

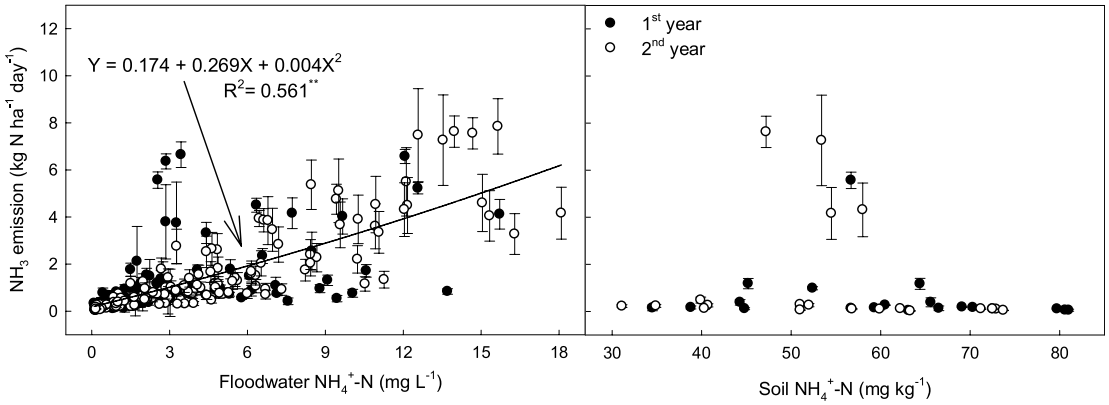

FIGURE 6
Relationship between NH_3 emission rates and NH_4^+ concentrations in floodwaters and soils supplied with different types of manure amendments. The vertical bars indicate standard deviations (n = 3).

In the present study, soil Eh values indicating the oxidation and reduction states decreased rapidly from 150 mV to −260 mV immediately after flooding (Figure 1). This decrease signifies a significant reduction in the soil oxygen concentration after flooding, creating favorable conditions for NH_3 volatilization loss. The low-oxygen environment inhibits the activity of the nitrifying bacteria, which normally convert NH_4^+ to NO_3^-. Consequently, the NH_4^+ ions accumulate in the soil and are more prone to volatilization as NH_3 gas (Cui et al., 2021). Furthermore, this soil reduction increases the soil pH to 7.5–9.0, which is another favorable condition for NH_3 emission that persists throughout the flooded period (Figure 4).

In the field study, similar levels of chemical fertilizers were applied to all treatments, and the N fertilizer (urea) was split into three application times (basal, tillering, and panicle initiation stages) during rice cultivation. Regardless of the manure management conditions, the NH_3 gas emissions fluctuated in similar patterns (Figure 2), sharply increasing within 2–3 days after urea application and then rapidly decreasing to the background levels. The results indicate that the NH_3 emission rates were highly correlated with NH_4^+ concentrations in the floodwaters rather than in the soils (Figure 6). Unlike the general notion that NH_3 volatilization loss is influenced by inorganic NH_4^+ content in the soil (Du Plessis and Kroontje, 1964), inorganic NH_4^+–N concentration in the floodwater was found to be the most influential factor determining NH_3 flux in the rice paddy (Figure 6).

Interestingly, while the entire manure amendment was incorporated into the surface soil as the basal fertilizer before transplanting, the addition of urea through side-dressing significantly increased NH_3 volatilization loss in the manure treatments. This suggests that the added urea may have stimulated microbial activity (Xiang et al., 2023). Under favorable conditions, the soil microorganisms can metabolize urea and organic matter more rapidly, leading to increased NH_3 production as a metabolic byproduct (Lee et al., 2021; Li et al., 2022).

For example, the same amounts of urea N were applied in all treatments at the tillering stage (15 days after transplanting), but this addition increased NH_3 emission rates from tillering to panicle initiation fertilization by an average of 60% and 12% in the fresh and compost treatments, respectively. However, under biochar manure treatment, the NH_3 emissions were comparable to those without manure (Figure 2). The applied urea-N might boost microbial activity in the soil, accelerate the decomposition of organic amendments and soil organic matter, and subsequently increase NH_3 volatilization under anaerobic and high-pH conditions (He and Suzuki, 2004; Wang et al., 2021).

Among the selected manure amendments, the fresh and compost applications significantly increased the average seasonal NH_3 fluxes by 58% and 29% over no manure application, respectively (Figure 3). Biochar had an alkaline pH (8.4 ± 0.2 in water suspension) (Table 1), but its application did not increase NH_3 volatilization loss during the cropping season; instead, it decreased the seasonal NH_3 flux by approximately 7% compared to no manure application. Biochar is a C-rich solid product produced by the low-temperature pyrolysis of biomass (Lehmann and Joseph, 2015; Tomczyk et al., 2020); it contains oxygen functional groups, such as carboxyl and keto groups, which are responsible for NH_4^+ adsorption through hydrogen bonding and electrostatic interactions (Cai et al., 2016). The reduction in NH_3 emission loss may be related to biochar's high negativity (Gundale and DeLuca, 2007) and low inorganic N content (Table 1). Labile N in the biomass could volatilize during pyrolysis, resulting in biochar having very low inorganic N content (Ohtsuka et al., 1994; Clark et al., 2017). Some studies have shown the effectiveness of biochar in reducing N leaching losses (Major et al., 2012), with a high C/N ratio enhancing N immobilization (DeLuca et al., 2015).

However, compost contains higher concentrations of inorganic N (NH_4^+ and NO_3^-) compared to fresh manure (see Table 1), which makes it a less-effective application for reducing NH_3 volatilization losses. Rice grain productivity significantly increased with compost manure application (Figure 3), likely due to the higher N content (Table 1). However, fresh and biochar applications increased the average rice productivities by 5% and 11% over the control, respectively, although this was not a statistically significant difference compared to the control. The NH_3 intensity, indicating seasonal NH_3 flux per grain yield, was 12 kg NH_3–N Mg^{-1} grain for the control treatment. Fresh and compost manure applications significantly increase this intensity by approximately 50% and 12% over the control, respectively (Figure 3), primarily due to the higher NH_3 emissions. However, biochar application decreased NH_3 intensity during rice cultivation by around 16% compared to that of the control.

5 Conclusion

Regardless of the organic amendment management condition, NH_3 gas was mainly volatilized immediately after application of the chemical N fertilizer (urea). However, manure-based amendments, when incorporated as basal fertilizers before rice transplantation, can significantly increase NH_3 emission rates following urea application. Both fresh and compost manures, which are characterized by high contents of inorganic N, notably increase NH_3 volatilization during rice cultivation. In contrast, biochar having high material pH but low inorganic N content, does not elevate NH_3 emission loss over that of the control. Notably, NH_3 emission rates are primarily governed by the NH_4^+ contents in the flooded waters, rather than those in the soils. Although compost manure application significantly boosts rice grain yield, fresh and biochar manure applications result in slight productivity increments without statistical significance. Consequently, the application of fresh and compost manures can markedly increase NH_3 emission intensities, indicating the seasonal NH_3 flux per grain yield, whereas biochar manure does not exhibit such intensity. In summary, biochar as an organic amendment is a more viable option compared to fresh and compost manures for mitigating NH_3 emissions and enhancing soil productivity in rice paddies.

Data availability statement

The original contributions presented in the study are included in the article/Supplementary Material; further inquiries can be directed to the corresponding author.

Author contributions

RC: formal analysis, investigation, writing–original draft, and writing–review and editing. SC: methodology and writing–review and editing. SJG: formal analysis and writing–review and editing. SP: investigation and writing–review and editing. PK: conceptualization, writing–original draft, and writing–review and editing.

Funding

The author(s) declare that financial support was received for the research, authorship, and/or publication of this article. This work was funded by the Basic Science Research Program through the National Research Foundation of Korea funded by the Ministry of Education (No. NRF-2023R1A2C3004842). Authors RC, SG, and SP were supported by scholarships from the BK21 Four Program of the Ministry of Education and Human Resources Development, Republic of Korea.

Acknowledgments

The authors gratefully acknowledge Gyeongsang National University for granting the necessary permissions and providing the facilities to carry out this work.

Conflict of interest

The authors declare that the research was conducted in the absence of any commercial or financial relationships that could be construed as a potential conflict of interest.

Publisher's note

References

Agyarko-Mintah, E., Cowie, A., Van Zwieten, L., Singh, B. P., Smillie, R., Harden, S., et al. (2017). Biochar lowers ammonia emission and improves nitrogen retention in poultry litter composting. *Waste Manag.* 61, 129–137. doi:10.1016/j.wasman.2016.12.009

Asman, W. A., Sutton, M. A., and Schjørring, J. K. (1998). Ammonia: emission, atmospheric transport and deposition. *New phytol.* 139 (1), 27–48. doi:10.1046/j.1469-8137.1998.00180.x

Barth, G., Otto, R., Almeida, R. F., Cardoso, E. J. B. N., Cantarella, H., and Vitti, G. C. (2019). Conversion of ammonium to nitrate and abundance of ammonium-oxidizing-microorganism in Tropical soils with nitrification inhibitor. *Sci. Agric.* 77. doi:10.1590/1678-992x-2018-0370

Bouwman, A. F., Lee, D. S., Asman, W. A., Dentener, F. J., Van Der Hoek, K. W., and Olivier, J. G. J. (1997). A global high-resolution emission inventory for ammonia. *Glob. Biogeochem. cycles* 11 (4), 561–587. doi:10.1029/97gb02266

Bruun, E. W., Müller-Stöver, D., Ambus, P., and Hauggaard-Nielsen, H. (2011). Application of biochar to soil and N_2O emissions: potential effects of blending fast-pyrolysis biochar with anaerobically digested slurry. *Eur. J. Soil Sci.* 62 (4), 581–589. doi:10.1111/j.1365-2389.2011.01377.x

Buresh, R. J., Ramesh Reddy, K., and Van Kessel, C. (2008). Nitrogen transformations in submerged soils. *Nitrogen Agric. Syst.* 49, 401–436. doi:10.2134/agronmonogr49.c11

Buss, W., Wurzer, C., Manning, D. A., Rohling, E. J., Borevitz, J., and Mašek, O. (2022). Mineral-enriched biochar delivers enhanced nutrient recovery and carbon dioxide removal. *Commun. Earth Environ.* 3 (1), 67–11. doi:10.1038/s43247-022-00394-w

Cai, Y., Qi, H., Liu, Y., and He, X. (2016). Sorption/desorption behavior and mechanism of NH4+ by biochar as a nitrogen fertilizer sustained-release material. *J. Agric. food Chem.* 64 (24), 4958–4964. doi:10.1021/acs.jafc.6b00109

Clark, S. C., Ryals, R., Miller, D. J., Mullen, C. A., Pan, D., Zondlo, M. A., et al. (2017). Effluent gas flux characterization during pyrolysis of chicken manure. *ACS Sustain. Chem. Eng.* 5 (9), 7568–7575. doi:10.1021/acssuschemeng.7b00815

Cohen, A. J., Brauer, M., Burnett, R., Anderson, H. R., Frostad, J., Estep, K., et al. (2017). Estimates and 25-year trends of the global burden of disease attributable to ambient air pollution: an analysis of data from the Global Burden of Diseases Study 2015. *Lancet* 389 (10082), 1907–1918. doi:10.1016/s0140-6736(17)30505-6

Cui, L., Li, D., Wu, Z., Xue, Y., Xiao, F., Zhang, L., et al. (2021). Effects of nitrification inhibitors on soil nitrification and ammonia volatilization in three soils with different pH. *Agronomy* 11 (8), 1674. doi:10.3390/agronomy11081674

DeLuca, T. H., Gundale, M. J., MacKenzie, M. D., and Jones, D. L. (2015). Biochar effects on soil nutrient transformations. *Biochar Environ. Manag. Sci. Technol. Implement.* 2, 421–454.

Du, Y., Cui, B., Wang, Z., Sun, J., and Niu, W. (2020). Effects of manure fertilizer on crop yield and soil properties in China: a meta-analysis. *Catena* 193, 104617. doi:10.1016/j.catena.2020.104617

Du Plessis, M. C. F., and Kroontje, W. (1964). The relationship between pH and ammonia equilibria in soil. *Soil Sci. Soc. Am. J.* 28 (6), 751–754. doi:10.2136/sssaj1964.03615995002800060022x

Ehrnsperger, L., and Klemm, O. (2021). Source apportionment of urban ammonia and its contribution to secondary particle formation in a mid-size European city. *Aerosol Air Qual. Res.* 21 (5), 200404. doi:10.4209/aaqr.2020.07.0404

Gundale, M. J., and DeLuca, T. H. (2007). Charcoal effects on soil solution chemistry and growth of *Koeleria macrantha* in the ponderosa pine/Douglas-fir ecosystem. *Biol. Fertil. soils* 43 (3), 303–311. doi:10.1007/s00374-006-0106-5

Haider, G., Joseph, S., Steffens, D., Müller, C., Taherymoosavi, S., Mitchell, D., et al. (2020). Mineral nitrogen captured in field-aged biochar is plant-available. *Sci. Rep.* 10 (1), 13816–13912. doi:10.1038/s41598-020-70586-x

He, X., and Suzuki, A. (2004). Effects of urea treatment on litter decomposition in *Pasania edulis* forest soil. *J. Wood Sci.* 50 (3), 266–270. doi:10.1007/s10086-003-0546-6

Hsiao, S. Y., Hsu, T. C., Liu, J. W., Xie, X., Zhang, Y., Lin, J., et al. (2014). Nitrification and its oxygen consumption along the turbid Chang Jiang River plume. *Biogeosciences* 11 (7), 2083–2098. doi:10.5194/bg-11-2083-2014

Hua, W., Luo, P., An, N., Cai, F., Zhang, S., Chen, K., et al. (2020). Manure application increased crop yields by promoting nitrogen use efficiency in the soils of 40-year soybean-maize rotation. *Sci. Rep.* 10 (1), 14882–14910. doi:10.1038/s41598-020-71932-9

Jechalke, S., Rosell, M., Vogt, C., and Richnow, H. H. (2011). Inhibition of nitrification by low oxygen concentrations in an aerated treatment pond system with biofilm promoting mats. *Water Environ. Res.* 83 (7), 622–626. doi:10.2175/106143011x12928814444493

Kang, Y., Liu, M., Song, Y., Huang, X., Yao, H., Cai, X., et al. (2016). High-resolution ammonia emissions inventories in China from 1980 to 2012. *Atmos. Chem. Phys.* 16 (4), 2043–2058. doi:10.5194/acp-16-2043-2016

Klimczyk, M., Siczek, A., and Schimmelpfennig, L. (2021). Improving the efficiency of urea-based fertilization leading to reduction in ammonia emission. *Sci. Total Environ.* 771, 145483. doi:10.1016/j.scitotenv.2021.145483

Lee, J., Choi, S., Lee, Y., and Kim, S. Y. (2021). Impact of manure compost amendments on NH3 volatilization in rice paddy ecosystems during cultivation. *Environ. Pollut.* 288, 117726. doi:10.1016/j.envpol.2021.117726

Lehmann, J., and Joseph, S. (2015). "Biochar for environmental management: an introduction," in *Biochar for environmental management* (Earthscan, London: Routledge), 1–13.

Li, Y., Moinet, G. Y., Clough, T. J., and Whitehead, D. (2022). Organic matter contributions to nitrous oxide emissions following nitrate addition are not proportional to substrate-induced soil carbon priming. *Sci. Total Environ.* 851, 158274. doi:10.1016/j.scitotenv.2022.158274

Lü, D. A., Yan, B. X., Wang, L. X., Deng, Z. Q., and Zhang, Y. B. (2013). Changes in phosphorus fractions and nitrogen forms during composting of pig manure with rice straw. *J. Integr. Agric.* 12 (10), 1855–1864. doi:10.1016/s2095-3119(13)60400-1

Major, J., Rondon, M., Molina, D., Riha, S. J., and Lehmann, J. (2012). Nutrient leaching in a Colombian savanna Oxisol amended with biochar. *J. Environ. Qual.* 41 (4), 1076–1086. doi:10.2134/jeq2011.0128

Misselbrook, T. H., and Powell, J. M. (2005). Influence of bedding material on ammonia emissions from cattle excreta. *J. dairy Sci.* 88 (12), 4304–4312. doi:10.3168/jds.s0022-0302(05)73116-7

Monaco, S., Sacco, D., Pelissetti, S., Dinuccio, E., Balsari, P., Rostami, M., et al. (2012). Laboratory assessment of ammonia emission after soil application of treated and untreated manures. *J. Agric. Sci.* 150 (1), 65–73. doi:10.1017/s0021859611000487

Novamsky, I., Van Eck, R., Van Schouwenburg, C. H., and Walinga, I. (1974). Total nitrogen determination in plant material by means of the indophenol-blue method. *Neth. J. Agric. Sci.* 22 (1), 3–5. doi:10.18174/njas.v22i1.17230

Ohtsuka, Y., Mori, H., Watanabe, T., and Asami, K. (1994). Nitrogen removal during atmospheric-pressure pyrolysis of brown coal with iron. *Fuel* 73 (7), 1093–1097. doi:10.1016/0016-2361(94)90243-7

Piwowar, A. (2020). Farming practices for reducing ammonia emissions in Polish agriculture. *Atmosphere* 11 (12), 1353. doi:10.3390/atmos11121353

Rural Development Administration (RDA) (2017). *Fertilization standard of crop plants*. Jeonju, South Korea: National Institute of Agricultural Science and Technology.

Saggar, S., Singh, J., Giltrap, D. L., Zaman, M., Luo, J., Rollo, M., et al. (2013). Quantification of reductions in ammonia emissions from fertiliser urea and animal urine in grazed pastures with urease inhibitors for agriculture inventory: New Zealand as a case study. *Sci. Total Environ.* 465, 136–146. doi:10.1016/j.scitotenv.2012.07.088

Sah, R. N., and Mikkelsen, D. S. (1983). Availability and utilization of fertilizer nitrogen by rice under alternate flooding: I. Kinetics of available nitrogen under rice culture. *Plant soil* 75, 221–226. doi:10.1007/bf02375567

Tomczyk, A., Sokołowska, Z., and Boguta, P. (2020). Biochar physicochemical properties: pyrolysis temperature and feedstock kind effects. *Rev. Environ. Sci. Bio/Technology* 19 (1), 191–215. doi:10.1007/s11157-020-09523-3

Ventura, W. B., and Yoshida, T. (1977). Ammonia volatilization from a flooded tropical soil. *Plant Soil* 46 (3), 521–531. doi:10.1007/bf00015911

Wang, Y., Wang, H., Gao, C., Seglah, P. A., and Bi, Y. (2021). Urea Application rate for crop straw decomposition in temperate China. *Appl. Environ. Soil Sci.* 2021, 1–12. doi:10.1155/2021/2240807

Wu, Y., Gu, B., Erisman, J. W., Reis, S., Fang, Y., and Lu, X. (2016). PM2. 5 pollution is substantially affected by ammonia emissions in China. *Environm. polluti.* 218, 86–94.

Xiang, Y., Liu, Y., Niazi, N. K., Bolan, N., Zhao, L., Zhang, S., et al. (2023). Biochar addition increased soil bacterial diversity and richness: large-scale evidence of field experiments. *Sci. Total Environ.* 893, 164961. doi:10.1016/j.scitotenv.2023.164961

Xing, Y. F., Xu, Y. H., Shi, M. H., and Lian, Y. X. (2016). The impact of PM2.5 on the human respiratory system. *J. Thorac. Dis.* 8 (1), E69–E74. doi:10.3978/j.issn.2072-1439.2016.01.19

Yang, M., Fang, Y., Sun, D., and Shi, Y. (2016). Efficiency of two nitrification inhibitors (dicyandiamide and 3, 4-dimethypyrazole phosphate) on soil nitrogen transformations and plant productivity: a meta-analysis. *Sci. Rep.* 6 (1), 22075–22110. doi:10.1038/srep22075

Zhang, L., Chen, Y., Zhao, Y., Henze, D. K., Zhu, L., Song, Y., et al. (2018). Agricultural ammonia emissions in China: reconciling bottom-up and top-down estimates. *Atmos. Chem. Phys.* 18 (1), 339–355. doi:10.5194/acp-18-339-2018

Zhang, W. F., Dou, Z. X., He, P., Ju, X. T., Powlson, D., Chadwick, D., et al. (2013). New technologies reduce greenhouse gas emissions from nitrogenous fertilizer in China. *Proc. Natl. Acad. Sci.* 110 (21), 8375–8380. doi:10.1073/pnas.1210447110

Zhao, X., Xie, Y. X., Xiong, Z. Q., Yan, X. Y., Xing, G. X., and Zhu, Z. L. (2009). Nitrogen fate and environmental consequence in paddy soil under rice-wheat rotation in the Taihu lake region, China. *Plant soil* 319 (1), 225–234. doi:10.1007/s11104-008-9865-0

frontiers | Frontiers in Environmental Science

TYPE Original Research
PUBLISHED 05 August 2024
DOI 10.3389/fenvs.2024.1427928

OPEN ACCESS

EDITED BY
Qiang Li,
University of Houston–Downtown,
United States

REVIEWED BY
Dong Wang,
Henan University, China
Wenbo Luo,
Northeast Normal University, China

*CORRESPONDENCE
H. D. Du,
dhuadong@gmail.com

RECEIVED 05 May 2024
ACCEPTED 12 July 2024
PUBLISHED 05 August 2024

CITATION
Nie WJ, Du HD, Xie SS and Bi YL (2024), The function of phytogenic mounds in the accumulation and conservation of soil seed banks in semiarid areas with water erosion. *Front. Environ. Sci.* 12:1427928. doi: 10.3389/fenvs.2024.1427928

The function of phytogenic mounds in the accumulation and conservation of soil seed banks in semiarid areas with water erosion

W. J. Nie[1,2,3], H. D. Du[1,2,3]*, S. S. Xie[1] and Y. L. Bi[1,2]

[1]College of Geology and Environment, Xi'an University of Science and Technology, Xi'an, China, [2]Institute of Ecological Environment Restoration in Mine Areas of West China, Xi'an University of Science and Technology, Xi'an, China, [3]Shaanxi Provincial Key Laboratory of Geological Support for Coal Green Exploitation, Xi'an, China

Background: Phytogenic mounds are a type of microtopography formed under perennial plants canopies in water erosion areas. However, the function of phytogenic mounds in seed assemblages and their ecological consequences remain poorly understood in semiarid areas with water erosion. Thus, understanding the characteristics of seed banks on mounds is crucial for ecosystem conservation and management in water-eroded areas.

Methods: We compared the quantity and composition of soil seed banks on the upslope and downslope parts of mounds and intercanopy surfaces along four slope gradients. We also explored the relationships among the soil seed bank, aboveground vegetation, and environmental factors. Furthermore, the species similarity between the soil seed bank and aboveground vegetation was analyzed to clarify the important ecological consequences of phytogenic mounds for plant community construction in serious soil erosion area.

Results: For slopes with $\alpha \leq 46.6\%$, the intercanopy surfaces had greater soil seed bank species composition, density, and diversity than did the phytogenic mounds, and these characteristics showed no significant differences between the upslope and downslope parts of the mounds. As the slope increased, the soil seed bank density and species composition increased on the upslope part of the mound, and reached a maximum for slopes with $\alpha > 70\%$, while the downslope part of the mound negatively effected on seed aggregation. The sediment accumulation rate, soil moisture, particle size distribution, pH, organic matter carbon, and hardness were significantly correlated with the soil seed bank density and diversity in the study area. For slopes with $0 < \alpha \leq 26.8\%$, the species similarity coefficient between the soil seed bank and aboveground vegetation was the highest for the intercanopy surface. This species similarity on the upslope part of the mound showed an increasing trend with increasing slope gradient, while the downslope part of the mound had the opposite trend. For slopes with $\alpha > 70\%$, the upslope part of the mound did not only have more species in the soil seed bank but also had more species in aboveground vegetation than did the downslope part of the mound and intercanopy surface.

Conclusion: For slopes with $\alpha \leq 46.6\%$, phytogenic mounds had barely impact soil seed bank accumulation and conservation in semiarid and eroded areas. For slopes with $\alpha > 46.6\%$, the mounds (particularly on the upslope part of the mound) showed seed assemblage functions, which are coupled with improving edaphic

conditions and decreasing microhabitat stress; thus, phytogenic mounds, or areas of microtopography, can be used to promote restoration success in semiarid eroded areas.

KEYWORDS

soil seed bank, phytogenic mound, vegetation restoration, sediment accumulation rate, water erosion, microtopography

1 Introduction

Perennial plants can be physical barriers, accumulating runoff sediments from uphill areas, and their canopy can protect the underlying soil from erosion in arid and semiarid eroded areas. These effects lead to a microtopography called phytogenic mounds (Bochet et al., 2000). These mounds cause spatial heterogeneity in biotic or abiotic resources, which may be important in determining soil biological activity and plant community structure in harsh environments (El-Bana et al., 2007). Thus, understanding the ecological consequences of phytogenic mounds has become a popular topic in semiarid and arid ecosystems (Venier et al., 2023).

Phytogenic mounds, or areas of microtopography, are important in promoting important ecosystem functions in arid and semiarid regions. First, phytogenic mounds can act as "fertility islands" by capturing nutrient-rich surface runoff and sediment eroded from uphill positions (Goudie, 2022); thus, the soil on phytogenic mounds has a higher water content and more nutrients than surrounding interplant spaces (Escudero et al., 2004). This improvement in soil physicochemical properties also enhances soil biological activity, such as high soil enzymatic activity and microbial biomass (Deák et al., 2017). Second, the host plants of mounds can act as "nurse plants," providing more suitable habitats for understory plant establishment and development (Ba et al., 2022). For example, the host plant canopy can decrease soil temperature (da Silva et al., 2024), and underlying litter can improve water infiltration, which is important for improving microhabitats for flora in semiarid zones (Du et al., 2017). Therefore, phytogenic mounds have generally been regarded as "safe sites" that can create, modify and maintain habitats by improving and conserving soil water availability and accumulating and conserving soil nutrients, thus increasing the productivity and biodiversity of plants in arid and semiarid lands. However, studies have shown that the host plants of mounds may compete with other plants for resources such as water, nutrients, and sunlight, potentially limiting the growth and survival of neighboring plant species, this can negatively impact the diversity and abundance of plant species in the area (Bennett and Klironomos, 2019). Additionally, the continuous accumulation of sediment in mounds negatively impacts plant growth because these processes disturb seedling establishment (Huang et al., 2018). Therefore, the ecological consequences of phytogenic mounds in improving soil properties and maintaining biodiversity need further study.

Phytogenic mounds also represent a "species pool" for many species by altering seed capture processes, especially on eroded land (Melnik et al., 2018). Soil erosion leads to recurrent superficial soil loss and seed removal through runoff or windflow on barren interplant spaces (Bochet et al., 2000). Moreover, mounds and their host plants can restrict seed loss by reducing runoff or wind velocity within or around the canopy, and can trap seeds and propagules carried by runoff or wind from nearby areas (Vulliet et al., 2024). Thus, mounds have greater soil seed banks than adjacent area (Farrell et al., 2012). Moreover, improving soil quality on mounds and enhancing habitats under the host plant canopy may affect seed viability and longevity, which is conducive to long-term conservation and prolonged seed life (Shang et al., 2016). This seed aggregation effect, coupled with rich soil water and nutrient resources, enables the seeds on mounds to germinate and grow efficiently (Braz et al., 2014), which leads to more plant species on mounds than the surrounding areas. Moreover, it seems that mound are important in structuring the plant community through the growth of some keystone plant species, which in turn influence long-term vegetation dynamics and ecosystem processes (Pongen, 2024). On the other hand, research has shown that the host plant canopy can prevent anemophilous seeds from falling on mounds (Bohrer et al., 2008), thereby reducing the seed accumulation on mounds. Therefore, both the positive and negative effects of phytogenic mounds occur simultaneously and shift with environmental conditions, which seems to be more complex than previously assumed. Information regarding seed assemblages on phytogenic mounds or "nebkhas" and their ecological consequences is available mainly for arid desert regions, while there is little evidence about which of these seed trapping affect in semiarid soil erosion areas. The relative importance of trapping seeds and prolonging seed life induced by the mound and its host plants is not clear and requires further investigation.

In a study (Du et al., 2013; Du et al., 2017; Du et al., 2020), we experimentally demonstrated that phytogenic mounds in water erosion areas are formed due to water erosion on bare soil and sediment accumulation under plants; thus, these mounds maintain high soil quality and plant diversity, especially on steep slopes. As a result, we hypothesized that sediment accumulation on mounds is accompanied by seed trapping. However, seed trapping has not been sufficiently researched in water erosion areas. Understanding composition and quantity of seed banks on phytogenic mounds and their influencing factors not only enables us to theoretically predict the ecological resilience of the seed bank, which is an important indicator of ecosystem resilience (Ma et al., 2019) but also enables us to assess the potential of the seed bank for natural restoration processes in eroded areas because the seed bank could represent the local species pool for restoration (Ludewig et al., 2021).

In this paper, we investigated soil seed bank on phytogenic mounds to determine whether they can trap seeds eroded from uphill positions to build a large seed bank. Therefore, the quantity and composition of soil seed banks on the upslope and downslope areas of mounds and intercanopy surfaces at four slope gradients were analyzed. The relationships among aboveground vegetation, soil factors, and the soil seed bank were analyzed to explore the ecological functions of seed bank on phytogenic mound in semiarid areas with water erosion. We addressed the following hypotheses: (I)

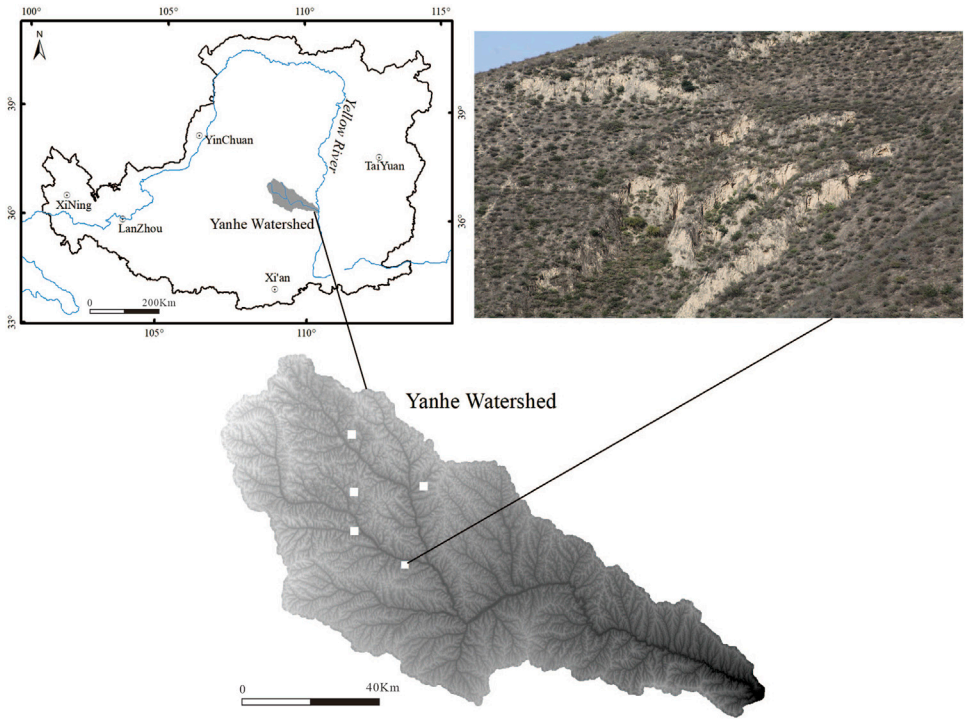

FIGURE 1
Location of the study area in the Yanhe Watershed, Loess Plateau (top left) and the five small watersheds sampled in this study (filled white squares, bottom left image); the vegetation distribution pattern of the study area is also shown (images taken during sampling).

Seed trapping effects lead to greater density and diversity of the soil seed bank on phytogenic mounds than on intercanopy surfaces, especially on the upslope side of the mound. (II) The spatial heterogeneity of soil sediment accumulation and environmental factors may be vital in determining soil seed bank structure. (III) There is a high level of species composition similarity between the soil seed bank on the mound and the surrounding aboveground vegetation, therefore, phytogenic mounds should have important effects on the natural restoration of soil erosion-disturbed areas.

2 Materials and methods

2.1 Study site description

Five small watersheds with an area of 32 km^2 in the Yanhe watershed in northern China (109 15′N, 3644′E) were selected for this study (Figure 1). The study area is a typical loess area with hills and gullies, and the soil type is dominated by loessal soil (FAO). The rainfall is distributed unevenly throughout the year, and the annual precipitation is mainly concentrated in summer. The area has a semiarid climate, with an average annual precipitation of 542.5 mm, an average annual temperature of 8.8°C, an average elevation of 1010–1430 m (average topographic slope of 54%), and an average aridity index of 1.5. The area is characterized as a forest-grassland vegetation zone, and the vegetation consists mostly of Gramineae, Asteraceae, Leguminosae and Rosaceae species (Wang et al., 2020).

2.2 Plot selection

The sample plot selected in this study was in a loess gully area, where the vegetation has been naturally restored for 40 years. The sampling plots was arranged on the southern slope where vegetative coverage is approximately 10%–25%. The vegetation was discontinuous, with isolated plants growing in bare soil, and mounds always developed under plant canopies (Figure 2A). The phytogenic mound was approximately 0.15–0.50 m high, with an area of 0.4–1.5 m^2. To compare the changes in soil seed bank characteristics on phytogenic mounds across slope gradients, four slope gradient classifications were established according to the Soil Erosion Classification and Gradation Standard set forth by the Ministry of Water Resources of the People's Republic of China (MWR, 2008), i.e. $0 < \alpha \leq 26.8\%$, $26.8 < \alpha \leq 46.6\%$, $46.6 < \alpha \leq 70\%$, and $\alpha > 70\%$. Fifteen phytogenic mounds were randomly selected and sampled from each slope class.

2.3 Sampling method

2.3.1 Vegetation survey on phytogenic mounds

For each phytogenic mound, two parts were set up based on the slope runoff direction: the upslope and downslope parts (Figure 2B). Before soil seed bank sampling, vegetation surveys were first conducted on each part of the mound and intercanopy surface. The full upslope and downslope parts of the mound were included in the vegetation survey area. The number, coverage, crown width, and

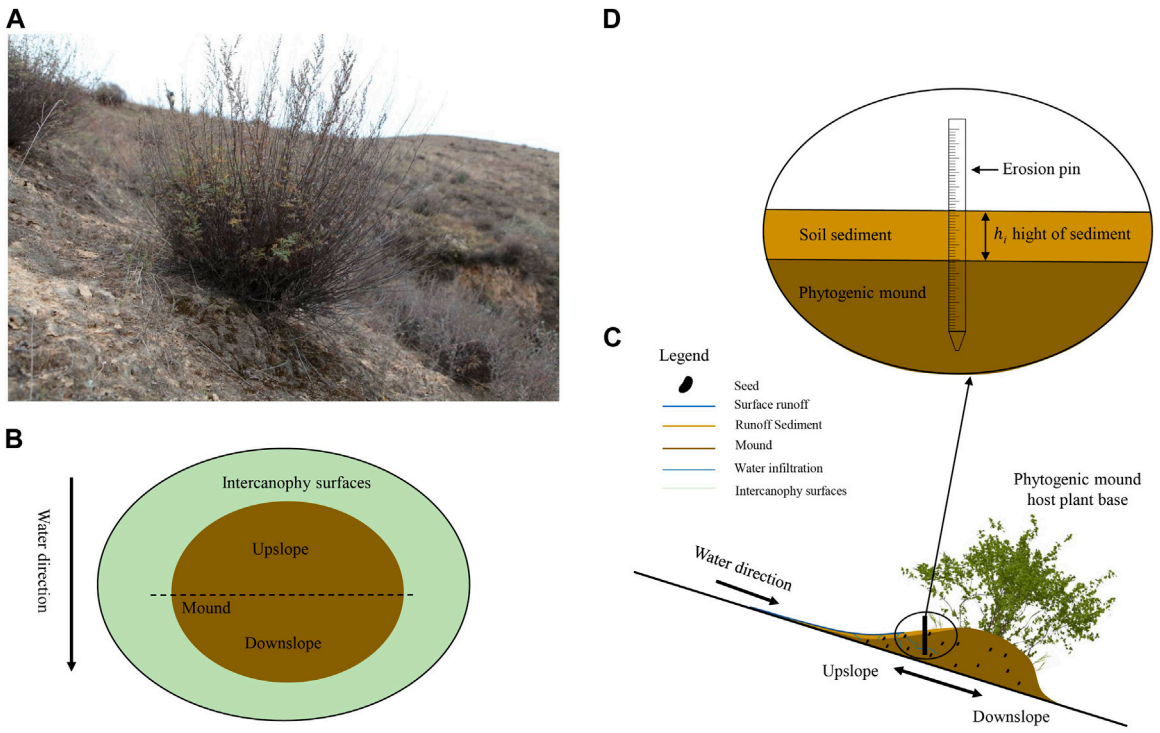

FIGURE 2
Development of a phytogenic mound under a plant canopy in the Yanhe Watershed, Loess Plateau, China. Phytogenic mound under an isolated plant **(A)**; schematic top view of a mound and the sampling sites **(B, C)**; and erosion pin **(D)** for measuring sediment accumulation rates.

height of each plant species were recorded separately. After the vegetation survey, the radius of the base of the mound and the height of the mound were measured to calculate the vegetation survey area (Du et al., 2020).

2.3.2 Soil seed bank sampling method

After the vegetation survey, the soil seed banks on the upslope and downslope parts of the phytogenic mound were sampled. Ten soil cores were collected from each part, and each core had a depth of 10 cm and dimensions of 5 cm in both width and length. They were later mixed to form a single representative soil sample. After manually removing the gravel and incidental debris, the soil samples were placed in fabric bags, transported to the laboratory, and subsequently subjected to an air-drying process.

2.4 Experimental methods

2.4.1 Seed germination

The seedling emergence method was used in this study to determine the species composition and abundance of the soil seed banks (Thompson and Grime, 1979). First, the air-dried soil samples were concentrated following the method of Ter Heerdt et al. (1996). Briefly, soil with particle sizes less than 0.2 mm was screened through a soil sieve to remove fine soil material without seeds. The concentrated samples were spread evenly into germination trays with sterilized sand (115°C–120°C for 48 h), and the soil layer was kept maintained at 2 cm depth. Germination experiments were carried out in a temperature- and light-controlled greenhouse at which the temperature was maintained at 20°C–30°C. Four hundred-watt high-pressure sodium lamps provided growth illumination, with a light regime of 10 h of darkness and 14 h of light. The resulting 180 trays and 5 additional sample-free control trays (to recognize potential airborne seed contamination) were randomly arranged within the greenhouse.

From early April until early October, trays were irrigated daily or every other day, as necessary, to preserve soil moisture. Germinated seedlings were regularly counted and identified, while seedlings that were challenging to identify were transferred to separate containers to promote continued growth until identification became feasible. When there was no seedling emergence within 2 weeks, the soil sample was stirred and persistently observed for germination until plant emergence ceased. When no more seedlings emerged after the second germination period, a gibberellin solution (1 g L^{-1}) was sprayed on the soil samples to prevent seed dormancy. The germination experiment was finished when there was no seedling emergence for 4 weeks.

2.4.2 Analysis of soil physical and chemical properties

To explore the relationships among the soil seed bank, aboveground vegetation, and environmental factors, soil samples were collected at a depth of 0–10 cm on each part of mound and intercanopy surface. The soil hardness was directly assessed from the profile wall using a TF-3 measuring device. The soil bulk density was measured for the soil cores using a cutting ring with dimensions of

50.46 mm in diameter and 50 mm in height (volume:100 cm^3). The soil water content was determined through a 24-h drying process at 105°C. The soil samples used for other physical and chemical property analyses were air-dried before analysis. The pH levels were assessed using a pH meter. A Bettersize 2000 E laser particle size analyzer was utilized for particle size determination. Soil organic carbon was measured using the dichromate oxidation method. The above soil properties were analyzed following the methods of Jones (2018).

To measure surface light intensity, a Vantage Pro 2 handheld mini-automated weather station was used. Measurements of sediment accumulation rates were carried out over 1 year, from July 2020 through July 2021. The sediment accumulation rates were recorded using erosion needles laid out on a 5 cm × 5 cm grid on the UP and DN and on the IS (Figures 2C, D). The erosion needles indicated changes in the soil surface level over time. Sedimentation was recorded every year, and the annual rates were calculated as following Eq. 1; (Du et al., 2020):

$$SA = \frac{\left(\sum_{i=1}^{n} h_i\right)}{n} \times A \times BD = \frac{\left(\sum_{i=1}^{n} h_i\right)}{n} \times BD \quad (1)$$

where SA is the sediment accumulation rate (SA, g cm^{-2} $year^{-1}$), n is the number of erosion needles, h_i is the increase or decrease in the soil surface height (cm), i is monitoring grid i, A is the upslope or downslope mound area (cm^2) and BD is the average soil bulk density (g cm^{-3}).

2.5 Statistical analysis

Seed density was 4 calculated as the average number of emerged seedlings per square meter from the soil samples. Species diversity indices of the soil seed banks were measured based on the following Eqs 2–5 (Begon and Townsend, 2021):

The Margalef index:

$$R = (S - 1)/\ln N \quad (2)$$

Shannon–Wiener index:

$$H = -\sum (P_i \ln P_i) \quad (3)$$

Simpson index:

$$D = 1 - \sum P_i^2 \quad (4)$$

Pielou index:

$$E = H/\ln S \quad (5)$$

where S represents the number of plant species, N represents the total number of individuals of all plant species in one quadrat, and Pi represents the relative abundance of plant species i in one quadrat. Pi was calculated as follows: $Pi = ni/N$.

The species similarity between the soil seed bank and standing vegetation was calculated using the following Eq. 6 (Hopfensperger, 2007):

$$S_c = 2c/(b + a) \quad (6)$$

where Sc is Sorensen similarity index, a is the number of species in the soil seed bank, b is the number of species in the standing vegetation, and c is the number of species shared by both.

The comparison of plant community attributes on distinctive mound sections with diverse slope gradients was performed using one-way analysis of variance (ANOVA) and least significant difference (LSD) multiple comparisons at a significance level of $p < 0.05$. These analyses were performed utilizing IBM SPSS statistics software package 24.0. Canoco 5.0 software was used to conduct a redundancy analysis (RDA) of the impact of environmental variables on the plant community composition within the soil seed banks present on the mounds. To explore the similarity between the soil seed banks and aboveground vegetation species, the Sorensen similarity index was calculated using Excel 16.0, and the UpSet R v1.4.0 package was used to visualize the intersecting species between soil seed banks and aboveground vegetation in different sampling plots (Conway, et al., 2017).

3 Results

3.1 Characteristics of the soil seed bank

3.1.1 Density

Overall, the soil seed bank densities on the intercanopy surfaces and downslope part of the mound decreased as the slope increased, but the density in the upslope part of the mound increased with increasing slope (except for slopes with α > 70%). The soil seed bank density on the intercanopy surfaces was 99% greater than that on the mounds with slopes showing 0<α ≤ 26.8% ($p < 0.05$) (Figure 3), and it was significantly greater on the intercanopy surfaces and upslope part of the mounds than on the downslope part of the mounds at 26.8 < α ≤ 46.6% ($p < 0.05$). However, the soil seed bank densities on the upslope part of the mound increased by 307% and 152% compared with those on the downslope part of the mound and intercanopy surface for slopes with α > 46.6%, respectively. There was no significant difference in the soil seed bank density between the intercanopy surface and downslope parts of the mound for slopes with α > 46.6% ($P < 0.05$).

3.1.2 Species composition

A total of 44 species were identified from seeds germinated from all soil seed banks collected from the four slope gradients on phytogenic mounds. The top three families were Compositae (11 species), Fabaceae (8 species), and Poaceae (8 species) (Supplementary Table S1). Overall, annual and perennial herbs constituted a large proportion of the seed bank (Figure 4). For slopes with 0 < α ≤ 46.6%, the proportion of annual plants accounted for 52% on average. Moreover, it decreased by 36% and 55% on mounds and intercanopy surfaces, respectively, for slopes with α > 46.6%. Except for 46.6 < α ≤ 70%, the proportion of annual plants did not significantly differ among the parts of the mound for 26.8 < α ≤ 46.6% and α > 46.6%. In contrast to annual plants, the proportion of perennial plants in the seed bank increased with increasing slope gradient and increased from 31% on slopes with α ≤ 46.6%–63% with α > 46.6%. The shrub and tree seeds appeared only on the upslope part of the mound at α > 46.6%, and the proportion was approximately 2%.

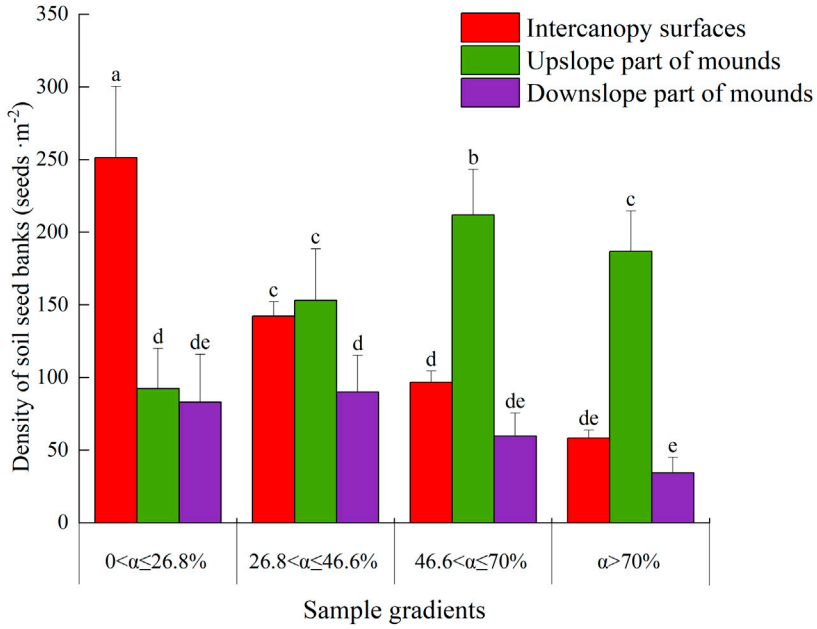

FIGURE 3
The seed density of the soil seed bank on phytogenic mounds and intercanopy soil surfaces at different slope gradients. The values are denoted as the mean ± SD, and the differences among means were determined by ANOVA and LSD. Different letters denote significant differences on the upslope and downslope parts of the mounds and intercanopy surfaces at different slope gradients ($P < 0.05$).

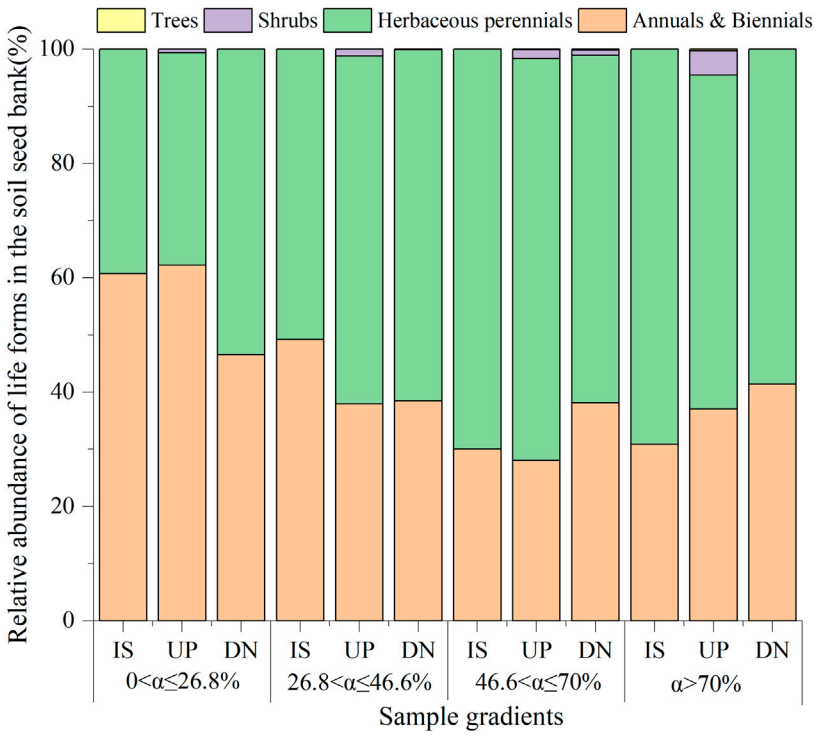

FIGURE 4
Relative abundance of different growth forms for the soil seed bank on phytogenic mounds and intercanopy soil surfaces at different slope gradients. IS: intercanopy surfaces, UP: upslope part of mounds, DN: downslope part of mounds.

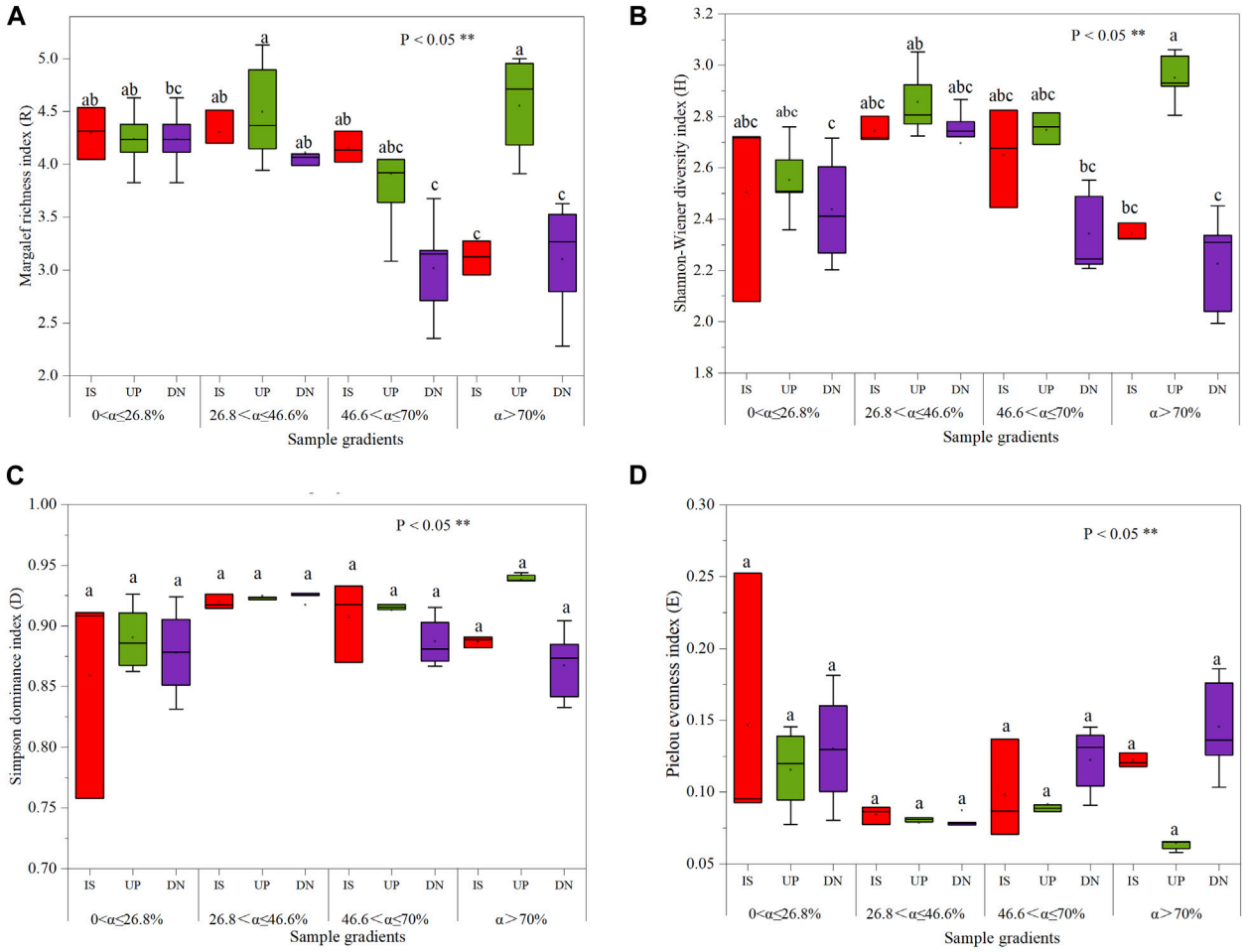

FIGURE 5
The Margalef index **(A)**, Shannon–Wiener index **(B)**, Simpson dominance index **(C)**, and Pielou index **(D)** of soil seed bank on phytogenic mounds and intercanopy soil surfaces at different slope gradients. Two different lowercase letters indicate statistically significant differences concerning the index (significance level $P < 0.05$). IS: intercanopy surfaces, UP: upslope part of mounds, DN: downslope part of mounds.

3.1.3 Species diversity

The Margalef richness index, Shannon-Wiener diversity index, Simpson dominance index and Pielou evenness index did not significantly differ among the intercanopy surface and upslope and downslope parts of the mound for slopes with α ≤ 70%, even though the Simpson index did not significantly differ for slopes with α > 70% (Figure 5). At α > 70%, the Margalef index in the upslope part of the mound increased by 41% and 46% (Figure 6A), the Shannon–Wiener index increased by 25% and 32% (Figure 6B), and the Pielou index decreased by 46% and 55% (Figure 6D), respectively, compared to those on the intercanopy surface and downslope parts of the mound.

3.2 Relationships between the soil seed bank and soil factors

In general, the sediment accumulation rate, soil water content, particle size distribution were the most critical soil environmental factors affecting the soil seed bank species composition (Table 1). For slopes of 0 < α ≤ 26.8%, the upslope and downslope parts of the mound were clustered on the left side of Axis 1, indicating that there was no difference in the soil physiochemical properties or seed bank species composition on the different parts of the mound. The species richness of the soil seed bank was greater on intercanopy surfaces than on the upslope and downslope parts of the phytogenic mounds, and the species richness was mostly positively correlated with the sediment accumulation rate, soil hardness, and soil water content (Figure 6A). For slopes with 26.8 < α ≤ 46.6%, the species richness was greater on the intercanopy surfaces and the upslope part of the mound. Species richness was positively correlated with the soil clay content, soil particles, soil organic carbon content, and surface illumination intensity (Figure 6B). At α > 46.6%, the species composition of the seed banks had similar distribution patterns according to the RDA ordination diagram (Figures 6C,D). The intercanopy surfaces and downslope part of the mound clustered to the left of Axis 1, and the seed bank species richness was relatively low. The species richness on the upslope part of the mound clustered to the right of Axis 1, where most of the seed bank species were included. Species richness was positively correlated with sediment accumulation rate, soil organic carbon, soil water content, soil clay, and soil porosity but negatively correlated with soil sand, soil bulk density, and soil hardness.

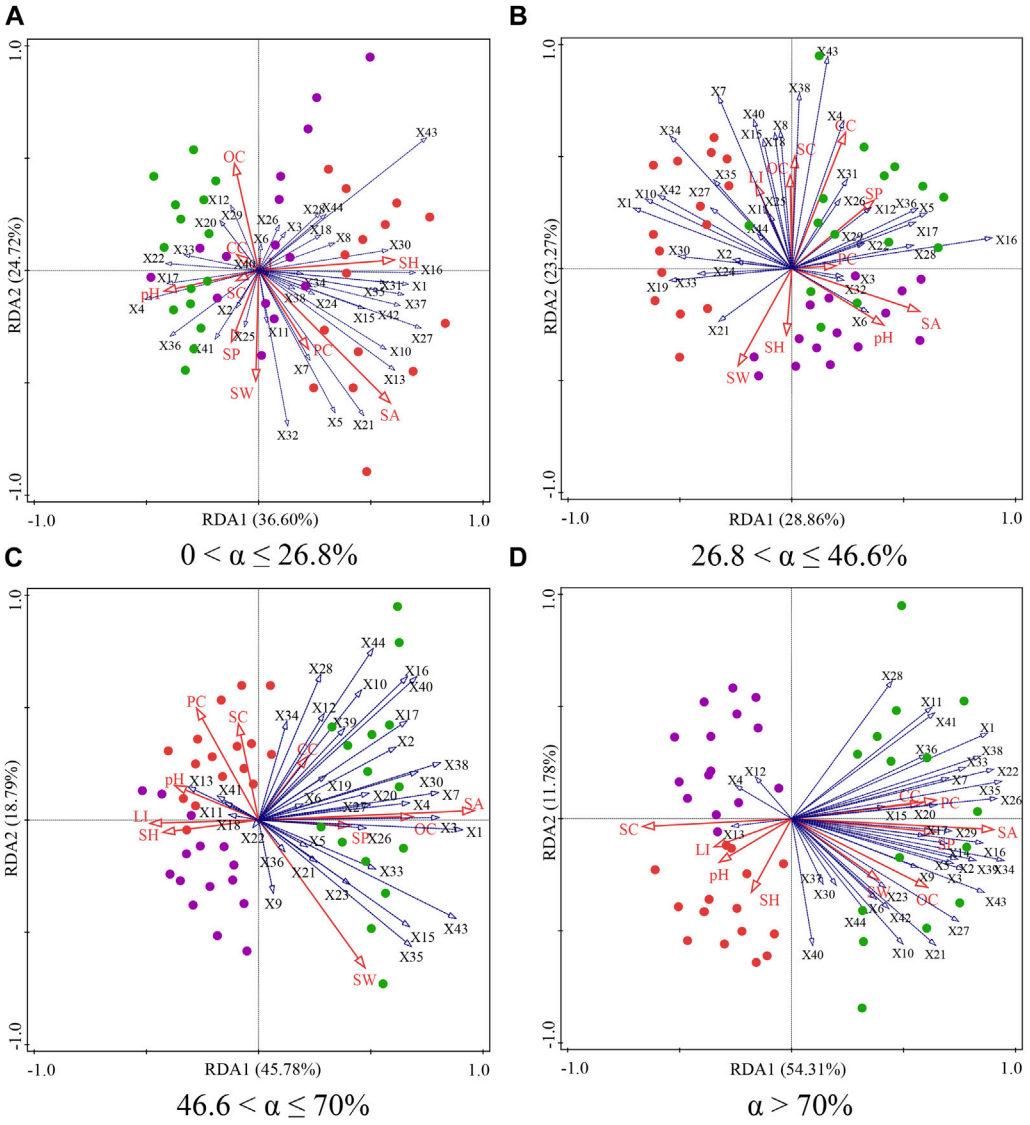

FIGURE 6
Biplot of the two axes for the RDA (redundancy analysis) for soil factors and soil seed bank on phytogenic mounds and intercanopy soil surfaces at 0 < α ≤ 26.8% **(A)**, 26.8 < α ≤ 46.6% **(B)**, 46.6 < α ≤ 70% **(C)**, and α > 70% **(D)** slope gradients. ●Intercanopy surfaces; ●Upslope part of mounds; ●Downslope part of mounds. The red arrows represent soil factors and the blue arrows represent plant species. Note:X1, *Aster altaicus*; X2, *Bothriochloa ischaemum*; X3, *Ixeris polycephala*; X4, *Cleistogenes hancei*; X5, *Melilotus officinalis*; X6, *Cleistogenes squarrosa*; X7, *Astragalus scaberrimus*; X8, *Corispermum mongolicum*; X9, *Robinia pseudoacacia*; X10, *Lespedeza davurica*; X11, *Viola philippica*; X12, *Euphorbia humifusa*; X13, *Androsace umbellata*; X14, *Syringa oblata*; X15, *Elymus kamoji*; X16, *Sibbaldianthe bifurca*; X17, *Oxytropis racemosa*; X18, *Saussurea japonica*; X19, *Glycyrrhiza uralensis*; X20, *Periploca sepium*; X21, *Setaria viridis*; X22, *Scorzonera albicaulis*; X23, *Clematis fruticosa*; X24, *Bidens pilosa*; X25, *Oxybasis glauca*; X26, *Artemisia giraldii*; X27, *Potentilla tanacetifolia*; X28, *Ixeris sonchifolia*; X29, *Sophora davidii*; X30, *Erodium stephanianum*; X31, *Taraxacum mongolicum*; X32, *Rubia cordifolia*; X33, *Artemisia gmelinii*; X34, *Gueldenstaedtia verna*; X35, *Dracocephalum moldavica*; X36, *Cirsium setosum*; X37, *Linum stelleroides*; X38, *Poa sphondylodes*; X39, *Polygala tenuifolia*; X40, *Stipa bungeana*; X41, *Cleistogenes hackelii*; X42, *Salsola collina*; X43, *Artemisia scoparia*; X44, *Stenosolenium saxatile*; OC, soil organic carbon; SW, soil water content; SH, soil hardness; SA, sediment accumulation rate; LI, surface illumination intensity; PC, Soil silt particle; SC, Soil sand particle; CC, Soil clay particle; SP, soil porosity.

3.3 Relationships between the soil seed banks and aboveground vegetation

On the upslope part of the phytogenic mound, the species similarity between the soil seed bank and aboveground vegetation showed an increasing trend with increasing slope, while the downslope part of the mound had the opposite trend. For slopes with 0 < α ≤ 26.8%, the species similarity coefficient between the soil seed bank and aboveground vegetation was the highest on the intercanopy surface, and the species similarity on the mounds decreased by 22% compared with that on the intercanopy surface (Figure 7). Along this slope gradient, there were 5 overlapping species between the soil seed bank and aboveground vegetation, including *Potentilla tanacetifolia*, *Artemisia scoparia*, *Taraxacum mongolicum*, *D. moldavica*, and *Polygala tenuifolia* (Figure 8A). For slopes with

TABLE 1 Importance and signification level of soil factors affecting the soil seed bank species composition.

Slope (%)	The top six soil factors of importance						
0 < α ≤ 26.8	Soil Factor	SA	SH	SW	PC	OC	SC
	Explains %	21.9	12.9	17.6	8.0	5.9	5.4
	pseudo-F	3.1	2.0	3.3	1.6	1.2	1.2
	P	0.018	0.122	0.016	0.16	0.29	0.396
26.8 < α ≤ 46.6	Soil Factor	SA	pH	CC	SW	SP	PC
	Explains %	13.5	15.5	13.8	10.6	8.5	6.8
	pseudo-F	1.7	2.2	2.2	1.8	1.6	1.3
	P	0.088	0.034	0.036	0.07	0.162	0.268
46.6 < α ≤ 70	Soil Factor	SA	SW	SC	PC	pH	CC
	Explains %	43.4	12.4	10.5	4.7	4.2	4.2
	pseudo-F	8.4	2.8	2.8	1.3	1.2	1.2
	P	0.002	0.008	0.006	0.254	0.344	0.284
α > 70	Soil Factor	SA	OC	SW	PC	pH	SH
	Explains %	45.1	12.8	7.4	7.0	4.0	3.5
	pseudo-F	9.0	3.0	1.9	2.0	1.2	1.1
	P	0.002	0.012	0.066	0.046	0.366	0.432

Note: This table shows only the top six soil factors of importance; SA, sediment accumulation rate; SH, soil hardness; SW, soil water content; PC, soil silt particle; OC, soil organic carbon; SC, soil sand particle; CC, soil clay particle; SP, soil porosity.

26.8 < α ≤ 46.6%, the species similarity between the soil seed bank and aboveground vegetation ranged from 0.41 to 0.47, and there was no difference between the intercanopy surface and different parts of the mound (Figure 7). The overlapping species between the soil seed bank and aboveground vegetation included *Stipa bungeana*, *P. tanacetifolia*, *D. moldavica*, *A. scoparia*, *Melilotus suaveolens*, and *Poa sphondylodes* (6 species) (Figure 8B). For slopes with α > 46.6%, the species similarity between the soil seed bank and aboveground vegetation on the upslope part of the mound increased by 36% and 32%, respectively, compared with that on the downslope part of the mound and intercanopy surface (Figures 7, 8C). For slopes with α > 70%, the upslope part of the mound not only had a greater number of aboveground vegetation species but also had a greater number of specific species in the soil seed bank than did the downslope part of the mound and intercanopy surface, such as the arbor *Robinia pseudoacacia*; shrubs *Ocimum gratissimum*, *Clematis fruticosa*, and *Sophora davidii*; and herbs *Agropyron ciliare* and *Salsola collina* (6 species) (Figure 8D).

4 Discussion

4.1 Accumulation of soil seed banks on phytogenic mounds

Our results indicated that phytogenic mounds exhibit large variations in soil seed bank size across slopes in semiarid and water erosion regions. The soil seed bank density and species number on the phytogenic mounds are significantly lower than those on intercanopy surfaces for slopes with 0 <α ≤ 26.8%, while these soil seed bank characteristics on the upslope part of the mound increase with slope and reach the highest values on slopes with α > 46.4%. This observation confirms Hypotheses I and II in which sediment and seed trapping effects lead to soil seed banks formation on phytogenic mounds. In a previous study, we showed that mounds on gentler slopes are formed due to differences in rain splash erosion beneath plant canopies and surrounding bare surfaces (Du et al., 2013). Thus, only small amounts of sediment and litter that are rich in plant propagules accumulate on the mounds. Moreover, the dense plant canopy blocks windborne seeds from dropping on the mound (Miri et al., 2021). Consequently, mounds seem to negativly effect seed trapping on slopes with α < 46.6%. In contrast, mounds on slopes with α > 46.4% are formed due to sediment accumulation under plants. The topsoil and litter enriched in plant propagules on intercanopy surfaces are removed by slope flow due to the high carrying capacity of surface runoff (Liu et al., 2020), which causes low soil seed bank density and species diversity on slopes with α > 46.6% (Figure 9). The washed material is intercepted by plants and deposited on phytogenic mounds, and the upslope part of the mounds is the main area of seed accumulation (Peralta et al., 2016). This can explain the formation of high soil seed bank density on the upslope part of the mounds. A counterexample of the effects of seed trapping on soil seed bank formation is the characteristics of the seed bank on the downslope part of the mound on slopes with α > 46.6%, which cannot directly block or intercept sediments in runoff from higher slope positions. Thus, the downslope part of mounds with α > 46.6% have the lowest seed bank density and diversity.

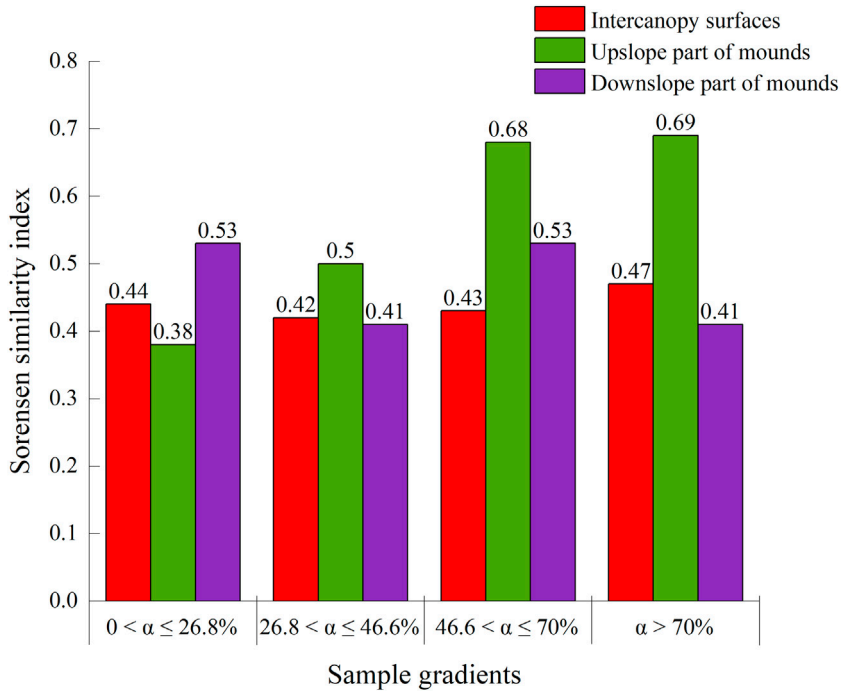

FIGURE 7
The species similarity matrix of aboveground vegetation and soil seed bank on phytogenic mounds and intercanopy soil surfaces at different slope gradients.

Analysis of the seed bank composition revealed that annual plants predominate in the soil seed bank on intercanopy surfaces and on mounds with different slopes. This is consistent with several studies conducted on the Loess Plateau of China and those conducted in other regions of the world (Rago et al., 2020). Annual plants always produce many seeds, which enables annual plants to quickly colonize disturbed or vacant areas by seed rain or slope runoff, and their seeds can accumulate in the soil over time. In this study, the arbor and shrub seeds appeared only on the upslope part of the mound on slopes with α > 46.6%. These seeds, such as *Sophora viciifolia*, *R. pseudoacacia*, and *C. fruticosa*, commonly have relatively large masses (20–40 mg per seed) and nearly circular shapes (Wang et al., 2011). These seed masses resist water erosion and seed removal processes on slopes with α < 46.6%. However, the transporting power of runoff can move large, round seeds on steep slopes (Janeau et al., 2022), and the mounds intercept slope runoff and intercept these seeds. Moreover, larger seeds are less likely to be incorporated into the soil because they have a lower chance of passively entering through cracks and are more vulnerable to environmental determinants on intercanopy surfaces (Bekele et al., 2022). Moreover, the runoff sediments on the upslope part of mounds can bury seeds and prevent their inactivation from the severe external environment in arid zones. Moreover, mound host plants are nurse plants, reducing soil water evaporation, decreasing thermal stress (Pugnaire et al., 2004), and improving soil quality under the plant canopy, which reduces damage to seed activity from the external environment on steep slopes (Li et al., 2022). This suitable habitat is important for shrubs and trees, which otherwise may fail to establish in more hostile environments (Varela et al., 2021). The emergence of trees and shrubs is not only essential in maintaining species diversity on steep slopes in semiarid areas but also benefits the positive succession of plant communities on steep slopes because trees and shrubs are considered late-stage species in plant community succession (Kalacska et al., 2004). Therefore, our results reaffirmed that phytogenic mounds not only promote seed bank density and diversity but are also refuges for seeds, which can determine plant community dynamics during natural vegetation restoration in areas disturbed by soil erosion (Figure 9).

4.2 Relationships between soil seed banks, soil factors and aboveground vegetation

Contrary to Hypothesis III, our results showed that the species occurring in the seed banks on the mounds had low similarity to the aboveground vegetation except for those on the upslope part of the mounds with slopes at α > 46.6%. These results were consistent with studies on perennial grasslands showing a low correspondence between the species composition of the seed bank and aboveground vegetation (Birhanu et al., 2022). The main reason for this pattern in this research may be that the density of the mound host plant canopy hinders the settlement of seeds on mounds, while the open area of the intercanopy surface can accept seeds from the surrounding area and from distant regions or ecosystems (Witkowski and Garner, 2000). These seeds are also not easily carried away by slope runoff on slopes with α < 46.6%. Another reason for the low level of species similarity between aboveground vegetation and the soil seed bank is that the soil seed

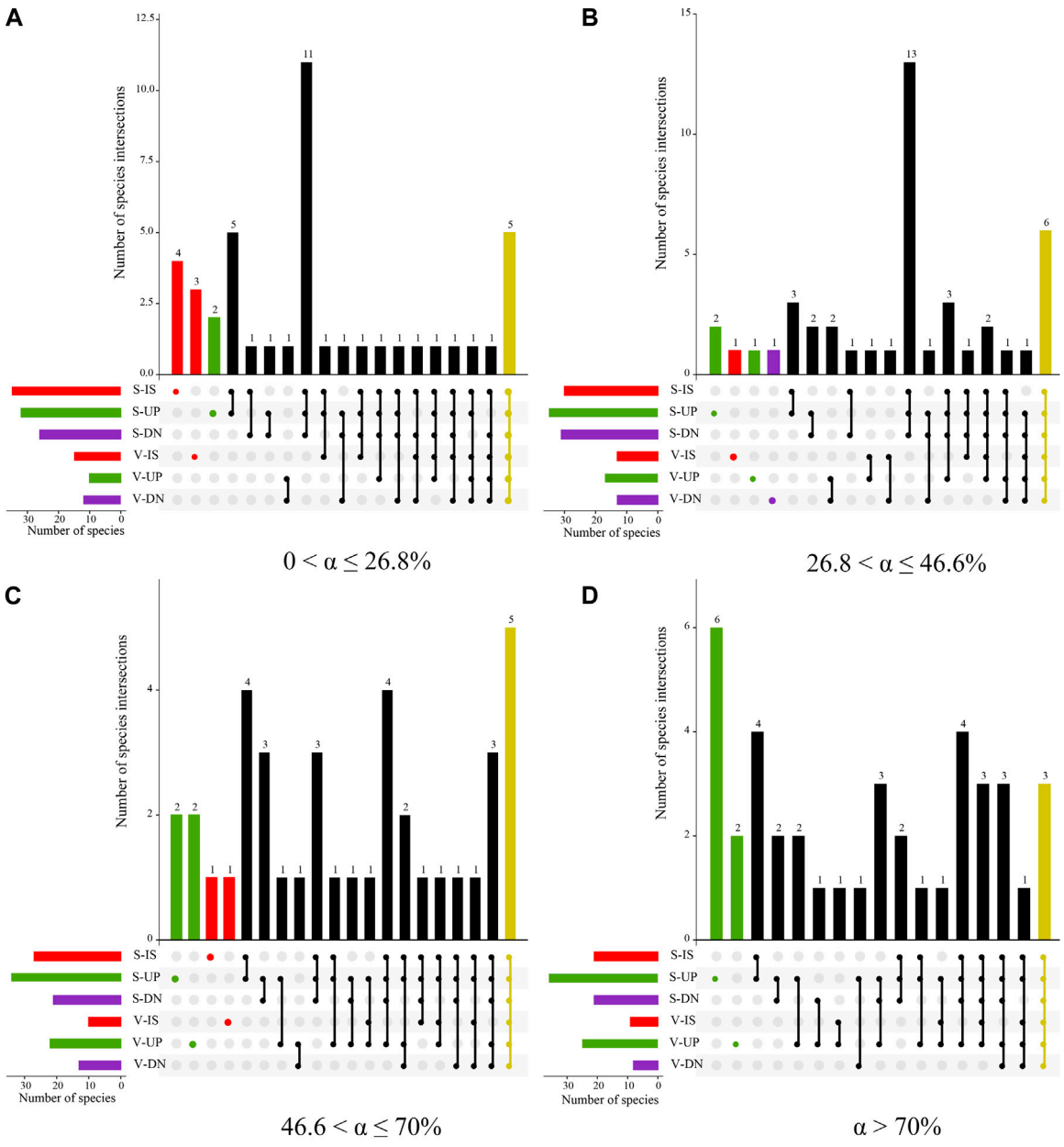

FIGURE 8
UpSet plot of seedling bank and aboveground vegetation species at 0 < α ≤ 26.8% **(A)**, 26.8 < α ≤ 46.6% **(B)**, 46.6 < α ≤ 70% **(C)**, and α > 70% **(D)** slope gradients. The horizontal bar on the left represents the number of seedling bank and aboveground vegetation species in sampling plots of different parts of mounds and intercanopy surface. Dots and lines represent two plot associations. Vertical histogram represents the number of intersecting species between these associative plots. Note: I: 0 < α ≤ 26.8%, II: 26.8 < α ≤ 46.6%, III: 46.6 < α ≤ 70%, IV: α > 70%, S, soil seed bank species; V: aboveground vegetation species; IS: intercanopy surfaces, UP: upslope part of mounds, and DN: downslope part of mounds.

bank contains seeds that disappear from aboveground vegetation early in succession and that can survive underground according to their opportunistic species strategy (Amiaud and Touzard, 2004), such as *Linum usitatissimum*, *S. collina*, *Stenosolenium saxatile*, and *Androsace umbellate*, in this study. However, analysis indicated that the similarity of the seed bank and aboveground vegetation is greater on the upslope part of the mound on slopes with α > 46.6%. This strong similarity between vegetation and the seed bank is attributed to the interception of seed-rich runoff sediments and litter at this site, which, coupled with improving soil physicochemical properties on the upslope part of the mound, may be beneficial for seed viability (Leicht-Young et al., 2009; Wang et al., 2023). Our results indicated that the species composition of the soil seed bank is positively correlated with the soil sediment accumulation rate, soil water content, and particle size distribution. These results are different from those in humid areas where excessively moist soil may reduce seed respiration leading to more seed rot or deterioration (Ma et al., 2017; Zhong et al., 2019), and indicate that good soil aeration and appropriate soil moisture are beneficial for soil seed banks conservation in semiarid areas. In contrast, the intercanopy surfaces and downslope parts of mounds on steep slopes are exposed to strong surface light

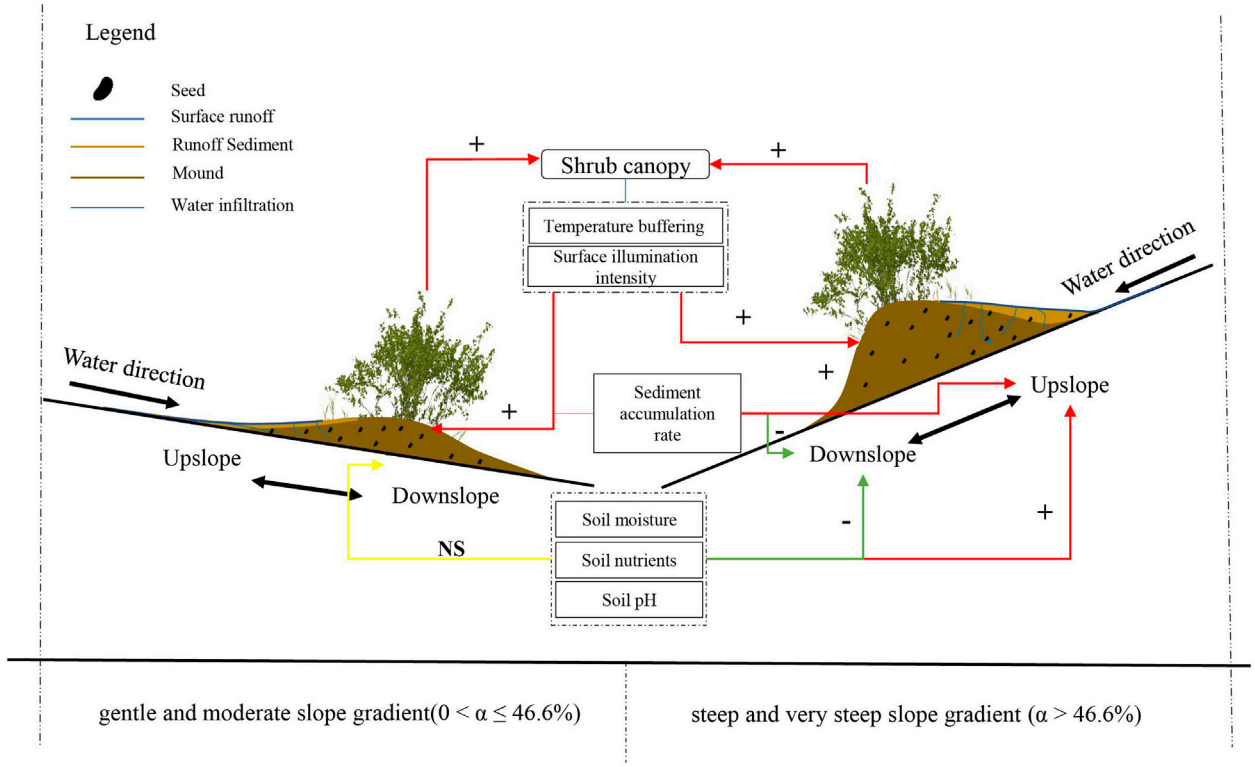

FIGURE 9
Effects of aboveground vegetation and environmental factors on soil seed bank on a phytogenic mound in water erosion area. Note: The red arrow indicates that the external environment positively effects the accumulation and preservation of soil seed banks. The yellow arrow indicates that the external environment does not significantly effect the accumulation and preservation of soil seed banks. Green arrows indicate that the external environment negatively impacts the accumulation and preservation of soil seed banks.

intensity and excessively dry soil, which potentially accelerate seed inactivation (Figure 9).

The seed bank is generally considered a crucial parameter for plant communities community regeneration in ecologically disturbed areas (Dölle and Schmidt, 2009). Our resluts demonstrated that phytogenic mounds barely impact soil seed bank accumulation and seed bank activity on slopes with α < 46.6%, where plant habitats are less disturbed by soil erosion. The mounds (particularly on the upslope part) maintain greater soil seed bank density and species diversity than do the intercanopy surface on slopes with α > 46.6%, where severe soil erosion interference makes it difficult to renew vegetation (Zuazo and Pleguezuelo, 2009). In this situation, the soil seed bank on the upslope part of the mound serves as a "species pool" for plant propagules accumulation, which provides the necessary foundation for future vegetation restoration and renewal. However, it appears that this promoting effect of plant establishment and growth needs to be accompanied by improved edaphic conditions and decreased microhabitat stress, as in the upslope part of phytogenic mounds. The number and diversity of grass and shrub species established on mounds are evidence that the upslope part of phytogenic mounds on slopes with α > 46.6% is important for natural vegetation restoration in ecosystems degraded by erosion. These results showed that small microtopography, such as phytogenic mounds, can concentrate nutrients and seed resources, which increase seed survival and plant establishment in in severely disturbance areas. Thus, mounds, or areas of microtopography, can be used to promote restoration success in arid and semiarid eroded areas.

5 Conclusion

(1) Phytogenic mounds for slopes with α < 46.6% barely impact soil seed bank accumulation in semiarid and eroded areas, while mounds (particularly those on the upslope part) intercept and preserve plant propagules, leading to high soil seed bank density and species diversity compared with those on intercanopy surfaces for slopes with α > 46.6%.

(2) The sediment accumulation rate, soil water content, and particle size distribution have been suggested as crucial determinants of soil seed bank density and species composition in semiarid regions.

(3) Phytogenic mounds, or small areas of microtopography, can trap runoff, nutrients, and plant seeds. Such simultaneous improvements in abiotic and biotic resources create different habitats that promote the recruitment of species with different growth forms on the mound, which is not only essential in maintaining species diversity in semiarid areas but also benefits the positive succession of plant communities in environments disturbed by severe soil erosion.

Data availability statement

The original contributions presented in the study are included in the article/Supplementary Material, further inquiries can be directed to the corresponding author.

Author contributions

NWJ: Conceptualization, Investigation, Methodology, Writing–original draft, Writing–review and editing. DHD: Formal Analysis, Investigation, Methodology, Resources, Writing–original draft, Writing–review and editing. XSS: Data curation, Investigation, Methodology, Writing–original draft, Writing–review and editing. BYL: Conceptualization, Funding acquisition, Supervision, Writing–review and editing.

Funding

The author(s) declare that financial support was received for the research, authorship, and/or publication of this article. This work was supported by Shaanxi Natural Science Foundation Program [2024JC-YBMS-234]; National key research and development program [2022YFF1303303], National Natural Science Foundation of China [41401306], and Scientific Research Foundation for Doctor, Xi'an University of Science and Technology [8150124007].

Acknowledgments

Acknowledge the assistance of the Shaanxi Provincial Key Laboratory of Geological Support for Coal Green Exploitation and the Institute of Ecological Environment Restoration in Mine Areas of West China.

Conflict of interest

The authors declare that the research was conducted in the absence of any commercial or financial relationships that could be construed as a potential conflict of interest.

Publisher's note

Supplementary material

The Supplementary Material for this article can be found online at: https://www.frontiersin.org/articles/10.3389/fenvs.2024.1427928/full#supplementary-material

References

Amiaud, B., and Touzard, B. (2004). The relationships between soil seed bank, aboveground vegetation and disturbances in old embanked marshlands of Western France. *Flora* 199, 25–35. doi:10.1078/0367-2530-00129

Ba, Z. D., Du, H. S., and Wang, S. H. (2022). A review of research on the development and evolution of scrub dunes. *Appl. Ecol. Environ. Res.* 20, 2343–2363. doi:10.15666/aeer/2003_23432363

Begon, M., and Townsend, C. R. (2021). *Ecology: from individuals to ecosystems*. New Jersey, USA: John Wiley and Sons.

Bekele, M., Demissew, S., Bekele, T., and Woldeyes, F. (2022). Soil seed bank distribution and restoration potential in the vegetation of Buska Mountain range, Hamar district, southwestern Ethiopia. *Heliyon* 8, e11244. doi:10.1016/j.heliyon.2022.e11244

Bennett, J. A., and Klironomos, J. (2019). Mechanisms of plant–soil feedback: interactions among biotic and abiotic drivers. *New Phytol.* 222, 91–96. doi:10.1111/nph.15603

Birhanu, L., Bekele, T., Tesfaw, B., and Demissew, S. (2022). Soil seed bank composition and aboveground vegetation in dry Afromontane forest patches of Northwestern Ethiopia. *Trees, For. People* 9, 100292. doi:10.1016/j.tfp.2022.100292

Bochet, E., Poesen, J., and Rubio, J. L. (2000). Mound development as an interaction of individual plants with soil, water erosion and sedimentation processes on slopes. *Earth Surf. Process. Landforms* 25, 847–867. doi:10.1002/1096-9837(200008)25:8<847::AID-ESP103>3.0.CO;2-Q

Bohrer, G., Katul, G. G., Nathan, R., Walko, R. L., and Avissar, R. (2008). Effects of canopy heterogeneity, seed abscission and inertia on wind-driven dispersal kernels of tree seeds. *J. Ecol.* 96, 569–580. doi:10.1111/j.1365-2745.2008.01368.x

Braz, M. I. G., Rodin, P., and de Mattos, E. A. (2014). Soil seed bank in a patchy vegetation of coastal sandy plains in southeastern B razil. *Plant Species Biol.* 29, e40–e47. doi:10.1111/1442-1984.12033

Conway, J. R., Lex, A., and Gehlenborg, N. (2017). UpSetR: an R package for the visualization of intersecting sets and their properties. *Bioinformatics* 33, 2938–2940. doi:10.1093/bioinforma10.1093/bioinformatics/btx364tics/btx364

da Silva, I. A., Merritt, D. J., Erickson, T. E., Mayfield, M. M., and Dwyer, J. M. (2024). Annual species' experimental germination responses to light and temperature do not correspond with their microhabitat associations in the field. *J. Veg. Sci.* 35, e13252. doi:10.1111/jvs.13252

Deák, B., Tölgyesi, C., Kelemen, A., Bátori, Z., Gallé, R., Bragina, T. M., et al. (2017). The effects of micro-habitats and grazing intensity on the vegetation of burial mounds in the Kazakh steppes. *Plant Ecol. Divers.* 10, 509–520. doi:10.1080/17550874.2018.1430871

Dölle, M., and Schmidt, W. (2009). The relationship between soil seed bank, above-ground vegetation and disturbance intensity on old-field successional permanent plots. *Appl. Veg. Sci.* 12, 415–428. doi:10.1111/j.1654-109X.2009.01036.x

Du, H. D., Jiao, J. Y., Jia, Y. F., Wang, N., and Wang, D. L. (2013). Phytogenic mounds of four typical shoot architecture species at different slope gradients on the Loess Plateau of China. *Geomorphology* 193, 57–64. doi:10.1016/j.geomorph.2013.04.002

Du, H. D., Jiao, J. Y., and Zhao, X. G. (2017). Significance and pedogenic variability of phytogenic mounds on the Loess Plateau of China. *J. Arid Environ.* 146, 53–63. doi:10.1016/j.jaridenv.2017.06.003

Du, H. D., Ning, B. Y., Jiao, J. Y., and Cao, Y. C. (2020). Spatial heterogeneity of plant community composition and diversity on phytogenic mounds caused by water erosion. *Plant Ecol. Divers.* 13, 425–436. doi:10.1080/17550874.2021.1897700

El-Bana, M. I., Li, Z. Q., and Nijs, I. (2007). Role of host identity in effects of phytogenic mounds on plant assemblages and species richness on coastal arid dunes. *J. Veg. Sci.* 18, 635–644. doi:10.1111/j.1654-1103.2007.tb02577.x

Escudero, A., Giménez-Benavides, L., Iriondo, J. M., and Rubio, A. (2004). Patch dynamics and islands of fertility in a high mountain Mediterranean community. *Arct. Antarct. Alp. Res.* 36, 518–527. doi:10.1657/1523-0430(2004)036[0518:PDAIOF]2.0.CO;2

Farrell, C., Hobbs, R. J., and Colmer, T. D. (2012). Microsite and litter cover effects on seed banks vary with seed size and dispersal mechanisms: implications for revegetation of degraded saline land. *Plant Ecol.* 213, 1145–1155. doi:10.1007/s11258-012-0072-y

Goudie, A. S. (2022). Nebkhas: an essay in aeolian biogeomorphology. *Aeolian Res.* 54, 100772. doi:10.1016/j.aeolia.2022.100772

Hopfensperger, K. N. (2007). A review of similarity between seed bank and standing vegetation across ecosystems. *Oikos* 116, 1438–1448. doi:10.1111/j.0030-1299.2007.15818.x

Huang, T., Zhang, H., Dai, L., Cong, X., and Ma, S. (2018). Formation of banded vegetation patterns resulted from interactions between sediment deposition and vegetation growth. *Comptes Rendus. Biol.* 341, 167–181. doi:10.1016/j.crvi.2018.01.008

Janeau, J. L., Intanon, S., Pansak, W., Rodprai, C., Anusorn, K., Hammecker, C., et al. (2022). Slope position and biochar influence soil properties and seed displacement in a tropical agroecosystem. *Eur. J. Soil Sci.* 73, e13216. doi:10.1111/ejss.13216

Jones, J. (2018). *Soil analysis handbook of reference methods*. Florida, USA: CRC Press. doi:10.1201/9780203739433

Kalacska, M., Sanchez-Azofeifa, G. A., Calvo-Alvarado, J. C., Quesada, M., Rivard, B., and Janzen, D. H. (2004). Species composition, similarity and diversity in three successional stages of a seasonally dry tropical forest. *For. Ecol. Manag.* 200, 227–247. doi:10.1016/j.foreco.2004.07.001

Leicht-Young, S. A., Pavlovic, N. B., Grundel, R., and Frohnapple, K. J. (2009). A comparison of seed banks across a sand dune successional gradient at Lake Michigan dunes (Indiana, USA). *Plant Ecol.* 202, 299–308. doi:10.1007/s11258-008-9484-0

Li, M., Xiao, H., Xin, Z., Li, X., Li, J., Miri, A., et al. (2022). Soil seed bank characteristics of *Nitraria tangutorum* nebkhas in a desert–oasis ecotone. *Front. Environ. Sci.* 10, 937257. doi:10.3389/fenvs.2022.937257

Liu, J. X., Li, P. P., Liu, G. B., and Flanagan, D. C. (2020). Quantifying the effects of plant litter in the topsoil on the soil detachment process by overland flow in typical grasslands of the Loess Plateau, China. *Hydrol. Process.* 34, 2076–2087. doi:10.1002/hyp.13713

Ludewig, K., Hansen, W., Klinger, Y. P., Eckstein, R. L., and Otte, A. (2021). Seed bank offers potential for active restoration of mountain meadows. *Restor. Ecol.* 29, e13311. doi:10.1111/rec.13311

Ma, M., Baskin, C. C., Li, W., Zhao, Y., Zhao, Y., Zhao, L., et al. (2019). Seed banks trigger ecological resilience in subalpine meadows abandoned after arable farming on the Tibetan Plateau. *Ecol. Appl.* 29, e01959. doi:10.1002/eap.1959

Ma, M., Baskin, C. C., Yu, K., Ma, Z., and Du, G. (2017). Wetland drying indirectly influences plant community and seed bank diversity through soil pH. *Ecol. Indic.* 80, 186–195. doi:10.1016/j.ecolind.2017.05.027

Melnik, K., Landhäusser, S. M., and Devito, K. (2018). Role of microtopography in the expression of soil propagule banks on reclamation sites. *Restor. Ecol.* 26, S200–S210. doi:10.1111/rec.12587

Miri, A., Dragovich, D., and Dong, Z. (2021). Wind flow and sediment flux profiles for vegetated surfaces in a wind tunnel and field-scale windbreak. *Catena* 196, 104836. doi:10.1016/j.catena.2020.104836

MWR (2008). *Standard for classification and gradation of soil erosion*. Beijing, China: Waterpower Press.

Peralta, A. M. L., Sánchez, A. M., Luzuriaga, A. L., and Escudero, A. (2016). Factors driving species assemblage in Mediterranean soil seed banks: from the large to the fine scale. *Ann. Bot.* 117, 1221–1228. doi:10.1093/aob/mcw039

Pongen, R. (2024). Keystone species: ecological architects of biodiversity and stability: review. *Int. J. Sci. Res. Archive* 11, 1137–1152. doi:10.30574/ijsra.2024.11.1.0175

Pugnaire, F. I., Armas, C., and Valladares, F. (2004). Soil as a mediator in plant-plant interactions in a semi-arid community. *J. Veg. Sci.* 15, 85–92. doi:10.1111/j.1654-1103.2004.tb02240.x

Rago, M. M., Urretavizcaya, M. F., Orellana, I. A., and Defossé, G. E. (2020). Strategies to persist in the community: soil seed bank and above-ground vegetation in Patagonian pine plantations. *Appl. Veg. Sci.* 23, 254–265. doi:10.1111/avsc.12482

Shang, Z., Yang, S., Wang, Y., Shi, J., Ding, L., and Long, R. (2016). Soil seed bank and its relation with above-ground vegetation along the degraded gradients of alpine meadow. *Ecol. Eng.* 90, 268–277. doi:10.1016/j.ecoleng.2016.01.067

Ter Heerdt, G. N. J., Verweij, G. L., Bekker, R. M., and Bakker, J. P. (1996). An improved method for seed-bank analysis: seedling emergence after removing the soil by sieving. *Funct. Ecol.* 10, 144–151. doi:10.2307/2390273

Thompson, K., and Grime, J. P. (1979). Seasonal variation in the seed banks of herbaceous species in ten contrasting habitats. *J. Ecol.* 67, 893–921. doi:10.2307/2259220

Varela, O., Ordano, M., Toledo, G., Lizardo, G., Rotger, S., Montero, A., et al. (2021). Diversity and density of the desert seed bank: interplays between cacti and nurse shrub species. *J. Arid Environ.* 191, 104536. doi:10.1016/j.jaridenv.2021.104536

Venier, P., Ferreras, A. E., Lauenstein, D. L., and Funes, G. (2023). Nurse plants and seed provenance in the restoration of dry Chaco forests of central Argentina. *For. Ecol. Manag.* 529, 120638. doi:10.1016/j.foreco.2022.120638

Vulliet, C., Koci, J., Sheaves, M., and Waltham, N. (2024). Linking tidal wetland vegetation mosaics to micro-topography and hydroperiod in a tropical estuary. *Mar. Environ. Res.* 197, 106485. doi:10.1016/j.marenvres.2024.106485

Wang, N., He, X., Zhao, F., Wang, D., and Jiao, J. Y. (2020). Soil seed bank in different vegetation types in the Loess Plateau region and its role in vegetation restoration. *Restor. Ecol.* 28, A5–A12. doi:10.1111/rec.13169

Wang, N., Jiao, J. Y., Jia, Y. F., and Zhang, X. A. (2011). Soil seed bank composition and distribution on eroded slopes in the hill-gully Loess Plateau region (China): influence on natural vegetation colonization. *Earth Surf. Process. Landforms* 36, 1825–1835. doi:10.1002/esp.2209

Wang, Y., Wang, Y., Wang, S., Wang, M., and Chai, W. (2023). Assessment of topsoil removal as an effective method for vegetation restoration in farmed peatlands. *Front. Environ. Sci.* 10, 1110057. doi:10.3389/fenvs.2022.1110057

Witkowski, E. T. F., and Garner, R. D. (2000). Spatial distribution of soil seed banks of three African savanna woody species at two contrasting sites. *Plant Ecol.* 149, 91–106. doi:10.1023/A:1009850706843

Zhong, M., Miao, Y., Han, S., and Wang, D. (2019). Nitrogen addition decreases seed germination in a temperate steppe. *Ecol. Evol.* 9, 8441–8449. doi:10.1002/ece3.5151

Zuazo, V. H. D., and Pleguezuelo, C. R. R. (2009). Soil-erosion and runoff prevention by plant covers: a review, in *Sustainable agriculture*. Dordrecht: Springer. doi:10.1007/978-90-481-2666-8_48

frontiers | Frontiers in Environmental Science

TYPE Original Research
PUBLISHED 06 August 2024
DOI 10.3389/fenvs.2024.1425199

OPEN ACCESS

EDITED BY
Xudong Peng,
Guizhou University, China

REVIEWED BY
Fengling Gan,
Chongqing Normal University, China
Hongliang Kang,
Chang'an University, China

*CORRESPONDENCE
Wang Jing,
wangjing0722@126.com

RECEIVED 29 April 2024
ACCEPTED 12 July 2024
PUBLISHED 06 August 2024

CITATION
Jing W, Yang Z, Longfei X, Jianfeng L, Huan H and Siqi L (2024), Soil conservation and water conservation services and trade-offs following the land consolidation project: a case study of Yan'an city, China.
Front. Environ. Sci. 12:1425199.
doi: 10.3389/fenvs.2024.1425199

Soil conservation and water conservation services and trade-offs following the land consolidation project: a case study of Yan'an city, China

Wang Jing[1,2,3]*, Zhang Yang[1,3], Xia Longfei[1,3], Li Jianfeng[1,3], He Huan[4] and Liu Siqi[1,2,3]

[1]Shaanxi Provincial Land Engineering Construction Group Co., Ltd., Land Engineering Technology Innovation Center, Ministry of Natural Resources, Xi'an, China, [2]Key Laboratory of Natural Resource Coupling Process and Effects, Beijing, China, [3]Institute of Land Engineering and Technology, Shaanxi Provincial Land Engineering Construction Group Co., Ltd., Key Laboratory of Cultivated Land Quality Monitoring and Conservation, Ministry of Agriculture and Rural Affairs, Xi'an, China, [4]Xi'an University of Architecture and Technology, Xi'an, China

The Loess Plateau is an important region for soil and water conservation and ecological construction in China. Exploring the spatio-temporal variations in soil conservation and water conservation services and their relationships in Loess Plateau under the background of land consolidation projects is of great significance for ecological protection and quality development in the Yellow River Basin. Taking Yan'an city as the research area, this paper used the InVEST model to quantitatively evaluated spatio-temporal variation characteristics and trade-off/synergy relationship of the soil conservation and water conservation services from 2010 to 2018. According to the implementation data, the relationship between the gully control and land consolidation (GCLC) project in various counties of Yan'an city and soil conservation and water conservation service was analyzed. The results showed that the total amount of soil conservation services in Yan'an City were 4.07×10^6 t and 3.75×10^6 t in 2010 and 2018 with a decrease of 7.76%, and with low spatial clustering characteristic. The total amount of water conservation services were 2.01×10^{10} mm and 2.03×10^{10} mm in 2010 and 2018 with a increase of 0.56%, and with high spatial clustering characteristic. There is a synergistic relationship between soil conservation and water conservation services in most area of Yan'an city. From 2010 to 2018, the effect of the GCLC projects on soil conservation and water conservation services in Yan'an city is not significant. The GCLC project can effectively alleviate the situation of sharp decline of cultivated land area and insufficient food production capacity.

KEYWORDS

soil conservation, water conservation, gully control and land consolidation, spatiotemporal variations, trade-offs, Yan'an city

1 Introduction

Ecosystem services refer to the biological resources, natural environmental conditions and utility provided for human survival through ecosystems and ecological processes (Costanza et al., 1997). Ecosystem service assessment plays an important role in regional development, ecological protection and human wellbeing. Ecosystem services are mainly divided into four types: supply, regulation, support and cultural services (Costanza et al., 1997; Ouyang and Wang, 2000). Among them, soil conservation and water conservation are two ecosystem service functions, which play important regulating and supporting roles in precipitation storage, runoff regulation, soil erosion prevention and groundwater replenishment, etc. (Costanza et al., 1998; MEA, 2005). It also plays an important role in the energy flow and material circulation of the ecosystem (Li et al., 2013). As different types of ecological services have different emphases on human well-being, and their spatial distribution is unbalanced, there are competition or mutually beneficial relations between ecological components and natural resources, and there are synergistic or tradeoff relations of mutual influence (Jopke et al., 2015). Therefore, exploring the temporal and spatial characteristics of soil conservation and water conservation ecosystem service functions and their relationships can provide scientific basis for the formulation of ecological protection policies and the implementation of ecological projects. A number of scholars have analyzed the characteristics of soil conservation and water conservation services changes and their relationships in different regions. Turner et al. (2014) studied the spatial distribution and interaction of 11 ecosystem services in Denmark, and analyzed the relationship between them and the cultural landscape of Denmark. Mousavi et al. (2023) regarded soil conservation and water conservation services as the two main ecosystem services provided by the rangeland ecosystem, and studied the external costs caused by the loss of rangeland ecosystem services in the central part of Iran. Gao and Zuo (2021) used models to evaluate and simulate the functions of soil conservation and water conservation at various scales in Beijing, China, and analyzed the trade-offs among them.

The Loess Plateau located in the middle of the Yellow River Basin, and it is the region with most serious soil and water loss in the world. According to the "Bulletin on Soil and Water Conservation in the Yellow River Basin (2021)" (Yellow River Conservancy Commission, 2022), the soil and water loss area of the Loess Plateau is 231,300 square kilometers, accounting for 89.2% of the soil and water loss area of the Yellow River Basin. It is also an important area of soil and water conservation and ecological construction in China, which plays a very important role in the ecological protection and high-quality development strategy of the Yellow River basin. Yan'an city is the most representative city on the Loess Plateau in northern Shaanxi province. As the key and demonstration area of "Grain for Green" (GFG) project, the largest ecological environment construction project in China in the 21st century, the vegetation area of the Yan'an city has been greatly increased during this period, effectively curbing soil erosion, greatly improving the natural ecological environment and the value of regional ecosystem services (He, 2015; Han et al., 2021). However, with the further advancement of the project, problems such as the reduction of cultivated land, the tension between people and land, and the prominent contradiction between people and grain in some areas have emerged (Chen et al., 2015). In view of the special geomorphology in the hilly and gully region of the Loess Plateau, in order to increase the cultivated land area and ensure food security, Yan'an city has carried out the The Gully Control and Land Consolidation (GCLC) project, which is a new management model that includes dam system construction, old dam restoration, saline-alkali land transformation, development and utilization of waste and unused land and ecological construction (Han et al., 2021). The comprehensive remediation of mountains, water, forests, fields, trees and villages aims to increase the cultivated land area in the Loess Plateau, ensure food security and solve the contradiction between people and land (Li et al., 2016).

At present, the research on the ecosystem service value in the Loess Plateau and Yan'an city mainly focuses on the period of the GFG projects, which is manifested as the improvement of regional ecosystem service value, such as the increase of soil conservation (Deng et al., 2020) and the synergistic development of relations (Wang et al., 2021). There are also some studies on ecological and environmental changes under the background of the GCLC projects, mainly focusing on soil fertility (Ma et al., 2020), hydrological changes (Jin et al., 2019) and vegetation cover changes (He et al., 2020). However, there are few quantitative studies on ecosystem services of soil conservation and water conservation.

Therefore, taking Yan'an city as the study area, this study used InVEST model and ArcGIS to quantitatively analyze the temporal and spatial distribution and variation characteristics of regional water conservation and soil conservation ecosystem service functions before and after the GCLC project from 2010 to 2018, and revealed their tradeoff/synergy relationship. On this basis, the study analyzes the relationship between the project and the change of two ecosystem services. The aim is to provides scientific basis and decision support for the ecological benefit evaluation, the formulation of ecological protection policy and the implementation of ecological projects of the Loess Plateau.

2 Materials and methods

2.1 Study area

Yan'an city (35°20′39′–37°53′31′N, 107°38′59′–110°34′46′E) is located in the hinterland of the Loess Plateau, in the middle reaches of the Yellow River, and is 256 km wide from east to west and 236 km long from south to north, with a total area of 37,037 km^2 (Figure 1). It is characterized by a semi-humid and semi-arid continental monsoon climate, with cold and dry winters and hot and rainy summers. The average annual precipitation is 562.1 mm, and is relatively concentrated in summer (July–September). The annual average temperature is 9°C, and the average frost-free period is 179 days. There is more than one crop but less than two crops a year. Yan'an city is a loess hilly and gully region, with high terrain in the northwest and low terrain in the southeast. The north is dominated by loess hills and gullies, accounting for 72% of the total area. The south is dominated by loess plateau gullies, accounting for 19% of the total area and stone mountains account for 9% of the total area. The main feature of the river

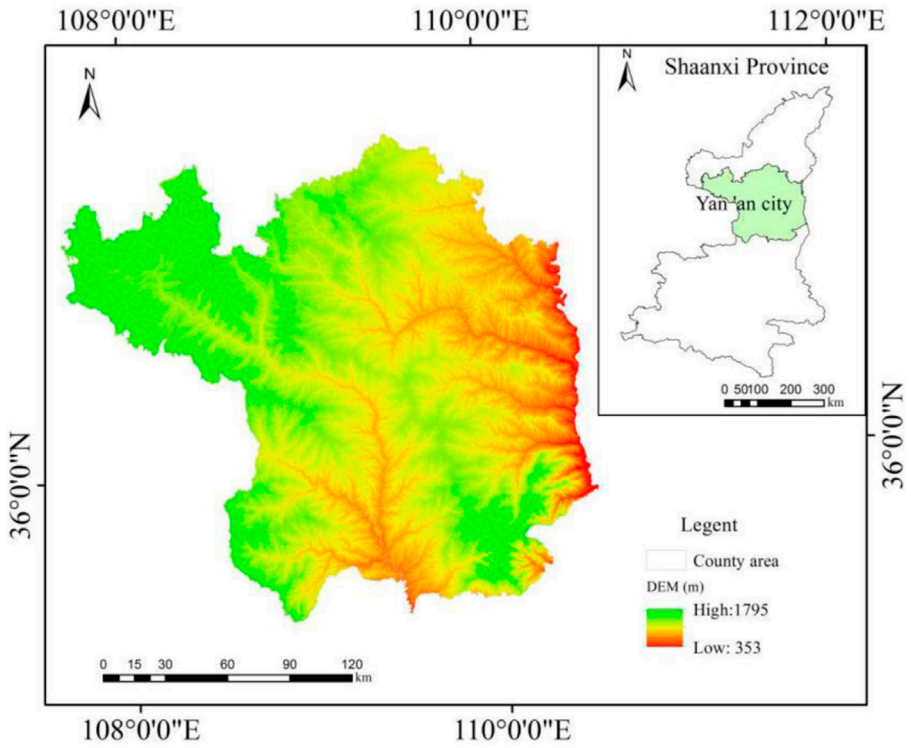

FIGURE 1
Location and elevation of the study area.

system distribution in Yan'an city is a deep trunk with dense branches. There are 20,889 channels over 1,000 m in the territory. The terrain in the area is fragmented, with various gullies and ravines. The gully is strongly cut down by a large slope and serious soil erosion. Yan'an city has 1 district and 12 counties, 16 street offices, 84 towns and 12 townships, with a total population of 2.19 million.

The GCLC project of Yan'an city was first piloted in Baota District, Zichang County and Yanchuan County in 2010. In September 2012, it was listed as a major national land consolidation project and given support. In November 2013, it was officially approved (Liu, 2013). The project involved 13 counties and districts of the city, with a total of 197 subprojects, which were implemented intensively from 2013 to 2017. The construction scale was 36,986.22 hm^2, the new farmland area was 7,848.72 hm^2, and the high-standard farmland area was 28,233.29 hm^2, with an investment of 3.664 billion yuan (Table 1). At the same time, the GFG project in Yan'an city has entered the consolidation stage in 2010. The forest coverage rate of the city reached 36.6%, and the regional ecological environment was greatly restored. In 2013, Yan'an city carried out a new round of the GFG project, planning to gradually return all sloping farmland above 25° to forest, and achieve full afforestation of steep slopes and full forest and grass cover.

2.2 Data sources

The basic data used in this study include land use data, elevation data, meteorological data, soil data, and data on the GCLC project. The land use data in 2010 and 2018 are from the Data Center for Resources and Environmental Sciences, Chinese Academy of Sciences (http://www.resdc.cn), with a spatial resolution of 30 m. According to the land use/land cover change (LUCC) classification system established by Liu (1996), land use types were divided into 6 primary classifications and 18 secondary classifications. Elevation data were obtained from the Geospatial Data Cloud Platform (http://www.gscloud.cn) (ASTER GDEM data product) with a spatial resolution of 30 m. The DEM was used to fill the depressions, calculate the flow direction, calculate the cumulative amount of convergence and other operations in ArcGIS to extract the vector map of sub-basins. Meteorological data were obtained from the National Scientific Data Center for the Tibetan Plateau (tpdc.ac.cn) -China 1 km resolution Monthly Precipitation Dataset (1901–2020), with a spatial resolution of 1 km. The soil data were from the Harmonized World Soil Database (HWSD) soil dataset (v1.2) of the National Scientific Data Center for the Tibetan Plateau (https://data.tpdc.ac.cn), which included soil texture, soil organic carbon content, vegetation available water content, root depth and other data, with a spatial resolution of 1 km. The data on the GCLC project are from The GCLC project leading group office of Yan'an city.

2.3 Research method

2.3.1 Soil conservation

The SDR (sediment transport ratio) module of the InVEST model is used to calculate potential soil erosion based on terrain, climate and soil data, and actual soil erosion based on the cover-management factor and soil and water conservation factor. The

TABLE 1 Implementation scale of GCLC project in various counties of Yan'an city.

Number	District	Projects number	Construction scale/hm^2	New cultivated land/hm^2	High-standard farmland/hm^2	Investment amount/ten thousand yuan	Implementation time
1	Baota district	34	7,734.74	1,190.8	6,183.23	80,892.24	2010–2019
2	Yanchang county	16	3,403.09	831.10	2,698.84	34,277.77	2013–2018
3	Yanchuan county	14	3,561.59	801.65	2,795.02	38,754.82	2010–2018
4	Zichang county	29	4,919.54	817.47	3,214.24	50,370.23	2010–2019
5	Ansai county	20	2,405.95	631.72	1,910.32	21,229.54	2013–2018
6	Zhidan county	3	330.95	95.94	134.13	3,375.71	2014–2017
7	Wuqi county	10	2,159.59	838.22	1,244.78	19,880.75	2013–2018
8	Ganquan county	19	3,278.88	529.10	2,625.58	30,824.60	2013–2018
9	Fu county	16	3,070.66	428.47	2,460.37	28,438.50	2013–2017
10	Luochuan county	13	2,191.04	616.59	1,782.51	22,917.90	2013–2018
11	Yichuan county	8	1,873.35	611.62	1,423.52	16,289.26	2013–2017
12	Huanglong county	7	820.93	157.38	707.20	7,518.75	2013–2018
13	Huangling county	8	1,235.91	297.66	1,053.55	11,637.61	2013–2018
	Total	197	36,986.22	7,847.72	28,233.29	366,407.68	

difference between the two is the soil conservation amount on the raster unit. The calculation formulas are Equations 1–3:

$$RKLS_i = R_i \times K_i \times LS_i \tag{1}$$

$$USLE_i = R_i \times K_i \times LS_i \times C_i \times P_i \tag{2}$$

$$SR_i = RKLS_i - USLE_i \tag{3}$$

where, $RKLS_i$ is the potential soil erosion of pixel i (t/hm^2) and $USLE_i$ is the soil erosion amount of pixel i under the action of cover-management factors and soil and water conservation factors (t/hm^2). SR_i is the actual soil retention on pixel i(t/hm^2); R_i is the rainfall erosivity factor, calculated by Wischmeier's monthly scale formula (Wischmeier and Smith, 1958). K_i is the soil erodibility factor estimated by EPIC model (Williams, 1990); LS_i is the slope length-gradient factor, which is calculated from DEM data; C_i is the cover-management factor and P_i is the soil and water conservation factor.

2.3.2 Water conservation

Based on the principle of the water cycle, the water conservation module of the InVEST model obtains water yield by calculating parameters such as precipitation, plant transpiration, surface evaporation, root depth and soil depth. The calculation formulas are Equations 4–10:

$$Y_{xj} = P_x \times \left(1 - \frac{AET_{xj}}{P_x}\right) \tag{4}$$

$$\frac{AET_{xj}}{P_x} = \frac{1 + w_x R_{xj}}{1 + w_x R_{xj} + \frac{1}{R_{xj}}} \tag{5}$$

$$w_x = z \times \frac{AWC_x}{P_x} + 1.25 \tag{6}$$

$$AWC_x = min\left(max\,Soil\,Dep_{thx}, Root\,Dep_{thx}\right) \times PAWC_x \tag{7}$$

$$PAWC_x = 54.509 - 0.132 \times SAN - 0.003 \times SAN^2 - 0.055 \times SIL - 0.006 \times SIL^2 - 0.738 \times CLA + 0.007 \times CLA^2 - 2.688 \times C + 0.501 \times C^2 \tag{8}$$

$$R_{xj} = \frac{k_{xj} \times ET_{0x}}{P_x} \tag{9}$$

$$ET_{0x} = 0.0013 \times 0.408 \times RA \times \left(T_{avg} + 17.8\right) \times \left(TD - 0.0123 P_x\right)^{0.76} \tag{10}$$

where, Y_{xj} is the annual water yield (mm) in pixel x of land use type j; P_X is the annual precipitation in pixel x (mm); AET_{xj} is the annual actual evapotranspiration in pixel x (mm). ω_X is the ratio of annual water requirement to annual precipitation on vegetation; R_{xj} is the

Budyko dryness index in pixel x of land use type j, and represents the ratio of potential evaporation to precipitation. Z is the seasonal constant between 0 and 30; AWC_X is the available water content of vegetation (mm). $PAWC_x$ is vegetation available water; SAN, SIL, CLA, and C are the contents of sand, silt, clay and organic carbon (%), respectively. k_{xj} is the evapotranspiration coefficient of vegetation, representing the ratio of vegetation evapotranspiration ET and potential evapotranspiration ET_{0x} at different growth stages. RA is the radiation from the top layer of the atmosphere (MJ/m^2/d); T_{avg} is the average of the mean daily maximum temperature and the mean daily minimum temperature (°C). TD is the difference between the mean daily maximum temperature and the mean daily minimum temperature (°C).

2.3.3 Spatial autocorrelation analysis

Spatial autocorrelation is a quantitative description of the similarity degree and spatial correlation pattern of the attribute values of spatially adjacent regional units, which is used to reveal the spatial distribution characteristics of a certain geographical phenomenon between adjacent regions and the aggregation degree of variables. It is divided into global spatial autocorrelation and local spatial autocorrelation. This paper uses these two methods to further explore the spatial distribution of soil conservation and water conservation services in Yan'an city.

Global spatial autocorrelation analysis can identify the spatial correlation of regional overall ecological quality, which can be used to describe whether soil conservation and water conservation services has agglomeration effect in the whole region. In this paper, Moran's I index is used to explore the spatial correlation, and the calculation formula is Equation 11 (Moran, 1950):

$$I = \frac{n}{\sum_{i=1}^{n}\sum_{j=1}^{n} W_{ij}} \times \frac{\sum_{i=1}^{n}\sum_{j=1}^{n} W_{ij}(x_i - \bar{x})(x_j - \bar{x})}{\sum_{i=1}^{n}(x_i - \bar{x})^2} \tag{11}$$

where x_i and x_j are the observed values of coordination efficiency; W_{ij} is the weight connection matrix of i and j; The value of Moran's I is between −1 and 1. A value greater than 0 indicates a positive correlation of spatial unit attributes, otherwise it indicates a negative correlation, and a larger value indicates a higher degree of correlation. If it goes to 0, it indicates that the spatial units are randomly distributed.

Local autocorrelation can identify the association patterns of elements and attributes between local adjacent regions. In this paper, LISA (Local indicators of spatial associations) proposed by Anselin (1995) was used to identify the spatial difference degree and significance level between the soil conservation and water conservation services of each grid and its surrounding grid in Yan'an city, and reveal the agglomeration and dispersion characteristics of the same attribute value in space. The calculation formulas are Equations 12–14:

$$I_i = z_i \sum_{j}^{n} w_{ij} z_j \tag{12}$$

$$z_i = \frac{n(x_i - \bar{x})^2}{\sum_{i=1}^{n}(x_i - \bar{x})} \tag{13}$$

$$z_j = \left(x_j - \bar{x}\right) \tag{14}$$

where: z_i and z_j are the standardization of the observed values in regions i and j, respectively.

LISA clustering analysis divided the spatial pattern of soil conservation and water conservation services into five types: H-H (high-high cluster), H-L (high-low outlier, high value surrounded by surrounding low value), L-H (low-high outlier, low value surrounded by surrounding high value), L-L (low-low cluster) and NS (not significant, there is no significant spatial clustering phenomenon). Among them, H-H and L-L are positive correlation types, while H-L and L-H are negative correlation types.

2.3.4 Ecosystem service trade-offs and synergies

To further explore the trade-offs and synergistic relationships among the ecosystem services in the study area, correlation analysis was applied to calculate the amount of ecosystem service changes in each pixel between 2010 and 2018 to identify the interrelationships among the two ecosystem services. The formula is Equation 15:

$$R_{xy} = \frac{\sum_{i=1}^{n}(x_i - \bar{x})(y_i - \bar{y})}{\sqrt{\sum_{i=1}^{n}(x_i - \bar{x})^2 \sum_{i=1}^{n}(y_i - \bar{y})^2}} \tag{15}$$

where, R_{xy} is the correlation coefficient of two ecosystem services; x_i, y_i are the ith pixel values of ecosystem services x, y; $\bar{x}$, $\bar{y}$ are the mean values of ecosystem services x, y; n is the time series of raster data. When the correlation result is positive, it indicates that there is a synergistic relationship between the two kinds of ecosystem services, that is, the increase of one kind of ecosystem service will promote another kind of ecosystem service, whereas there is a trade-off relationship, that is, the increase of one kind of ecosystem service will lead to the decrease of the supply of another kind of ecosystem service.

3 Results

3.1 Spatio-temporal variation characteristics of soil conservation service

3.1.1 Spatio-temporal variation

From the perspective of spatial distribution, the spatial differentiation characteristics of soil conservation service in 2010 and 2018 were relatively large. In 2010, the unit soil conservation amount in the eastern and southwestern regions was higher than that in the northwest (Figure 2A). It was higher in Yanchuan, Yanchang, Yichuan, and Huanglong counties in the east and Huangling county in the southwest, while it was lower in Wuqi, Zhidan, Ansai, and Zichang counties in the north. In 2018, the amount of soil conservation in Wuqi, Zhidan, Ansai, and Zichang counties in the northwest was higher than that in other areas (Figure 2B), and the gap between the highest and the lowest amount of soil conservation showed a trend of narrowing.

From 2010 to 2018, the total amount of soil conservation in Yan'an city showed a decreasing trend. In 2010, the total amount of soil conservation in Yan'an city was 4.07×10^6 t, with an average value of per unit area was 109.86 t/hm^2. In 2018, the total amount of

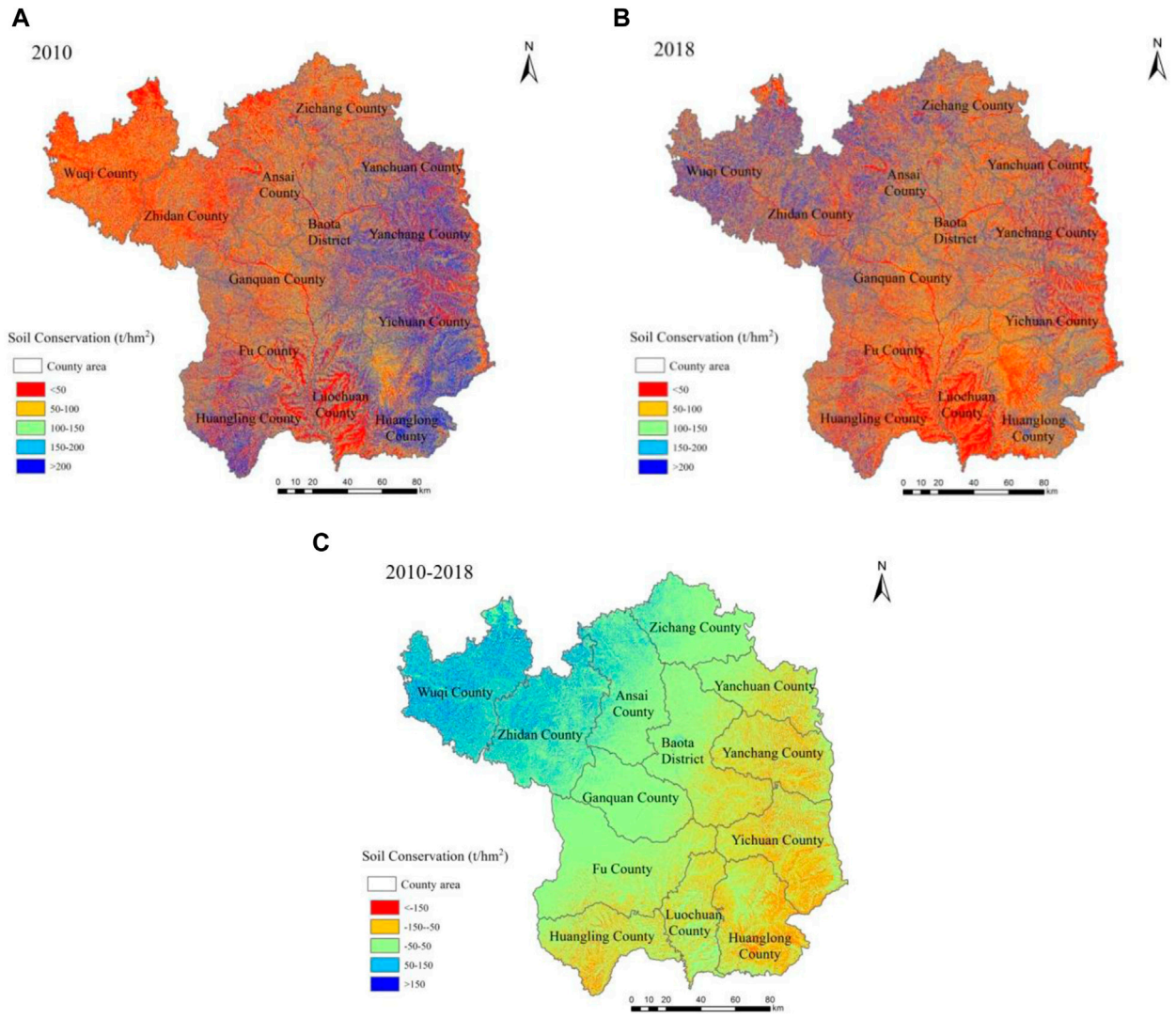

FIGURE 2
Spatial distribution of soil conservation services of Yan'an city in 2010 **(A)**, 2018 **(B)** and the change **(C)**.

soil conservation in Yan'an city decreased to 3.75×10^6 t, with an average value of per unit area was 101.33 t/hm^2. That is a decrease of 7.76%.The basic trend of soil conservation value change was increasing in the northwest and decreasing in the southeast. According to grid statistics, 7.57% of the areas where soil conservation value increased by more than 50 t/hm^2, 37.76% of the areas where soil conservation value decreased by more than 50 t/hm^2, and 54.68% of the areas had small changes between 50 t/hm^2. Except for Wuqi, Zhidan, Ansai, and Zichang counties, the amount of soil conservation decreased in all districts and counties. The area with the largest decrease was Huangling County, which decreased by 66.87 t/hm^2, and the area with the largest increase was Wuqi County, which increased by 79.03 t/hm^2 (Figure 2C).

3.1.2 Clustering characteristics

Moran's I index of soil conservation service in the study area was calculated by ArcGIS software. The Moran's I index of soil conservation service in Yan'an in 2010 and 2018 was 0.1047 ($p = 0$, Z = 443) and 0.0707 ($p = 0$, Z = 359.17). This indicates that soil conservation service has a small positive spatial correlation, and there was a certain clustering characteristics in Yan'an city. The Moran's I index in 2018 showed a decrease compared to 2010, indicating a dispersed trend in the spatial clustering of soil conservation.

According to the LISA clustering analysis (Figure 3), in 2010, the area of soil conservation service"H-H" accounted for 1.40% of the city's area. The proportion of "H-L" area was very small, only 0.04%. The "L-H" area accounted for 5.19%, which was relatively concentrated in the eastern part of Yan'an city and Huangling County. The area of the "L-L" area accounted for 1.94%. More than 90% of the city has no significant clustering effect. From the perspective of time changes, from 2010 to 2018, the "H-H" area decreased by 0.43%, while the "H-L" area increased by 0.20%. The "L-H" area decreased by 0.21%, and the area shifted from the southeast to the northwest. The "L-L" area increased by 1.6%, with a increase in the northern counties.

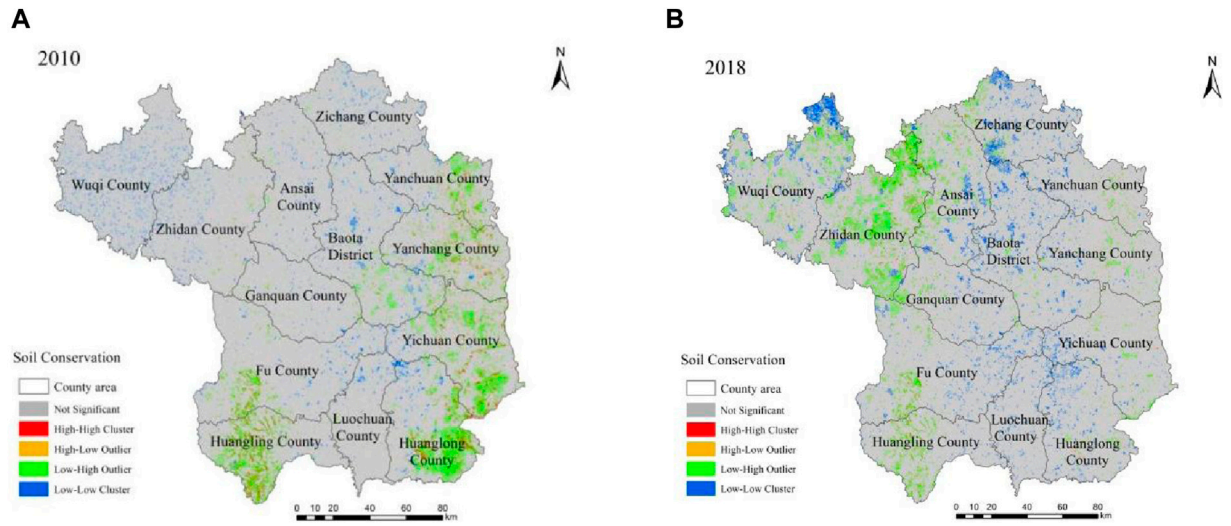

FIGURE 3
LISA clustering of soil conservation services of Yan'an city in 2010 **(A)** and 2018 **(B)**.

3.2 Spatio-temporal variation characteristics of water conservation service

3.2.1 Spatio-temporal variation

The spatial distribution of water conservation service in Yan'an city is greatly affected by rainfall, and the water yield is larger in areas with relatively abundant rainfall. In 2010, the amount of water conservation showed a decreasing trend from south to north (Figure 4A), which was higher in Huanglong, Huangling and Luochuan counties in the south and lower in Wuqi, Zichang and Yanchuan counties in the north. In 2018, the spatial distribution of water conservation service in Yan'an city underwent significant changes, showing a trend of being higher in the southwest and lower in the northeast (Figure 4B). From 2010 to 2018, the amount of water conservation in Yan'an city showed an upward trend. In 2010, the total amount of water production was 2.01×10^{10} mm, with an average value of 489.52 mm per unit area. In 2018, the total amount increased to 2.03×10^{10} mm, with an average value of 492.30 mm per unit area, with an increase of 0.56%. In terms of spatial distribution, it mainly increased in the north and decreased in the south, and the gap between the highest and lowest tended to narrow. According to grid statistics, 25.97% of the areas have increased their water conservation service by more than 50 mm, mainly distributed in the northern counties of Wuqi, Zhidan, Ansai, and Zichang, with the largest increase of 82.46 mm in Wuqi. The decrease area accounted for 22.85%, mainly distributed in the south, and Huanglong County was the most significant, with a decrease of 90.60 mm. 51.18% of the regional change was between 50 mm (Figure 4C).

3.2.2 Clustering characteristics

The Moran's I index of water conservation service in Yan'an in 2010 and 2018 were 0.8044 ($p = 0$, Z = 379) and 0.6849 ($p = 0$, Z = 294.83), indicating a positive spatial correlation in the amount of water conservation in Yan'an city and a high spatial clustering feature. The Moran's I index in 2018 was lower than that in 2010, indicating a dispersed trend in spatial clustering of water conservation service.

According to the LISA clustering analysis (Figure 5), water conservation service in Yan'an city was dominated by "H-H″ cluster and "L-L" cluster. In 2010, the "H-H" area and the "L-L" area accounted for 36.93% and 36.57% of the city. "H-H" was located in Huangling, Fuxian, Luochuan, and Huanglong counties in the southern while "L-L" was located in Zhidan, Zichang, Ansai, Yanchuan, and Yanchang counties in the northern of Yan'an city. The proportion of "H-L" and "L-H" areas was very small, only 0.04% and 0.006%, and the remaining 26.5% area has no significant cluster effect. From the perspective of time changes, the "H-H" area increased by 14.3%, while the "L-L" area decreased by 16.16% from 2010 to 2018, mainly due to the transformation from "L-L" area to "H-H" area in the northwest of Zhidan, Ansai counties, and Baota District. The changes in the "H-L" and "L-H" areas were not significant.

3.3 Trade-off and synergy relationship analysis

At the spatial pixel scale, the trade-off and synergistic relationship between soil conservation and water conservation services in Yan'an city were quantitatively analyzed. As shown in Figure 6, the area of the synergy relationship accounts for 77.05%, and that of the trade-off relationship is 22.95%. The synergy area is much larger than the trade-off area. In terms of spatial distribution, the trade-off relationship is mainly distributed in the northern of Yanchuan, Yanchang and Baota districts, while the synergy relationship are mainly distributed in other areas of Yan'an city.

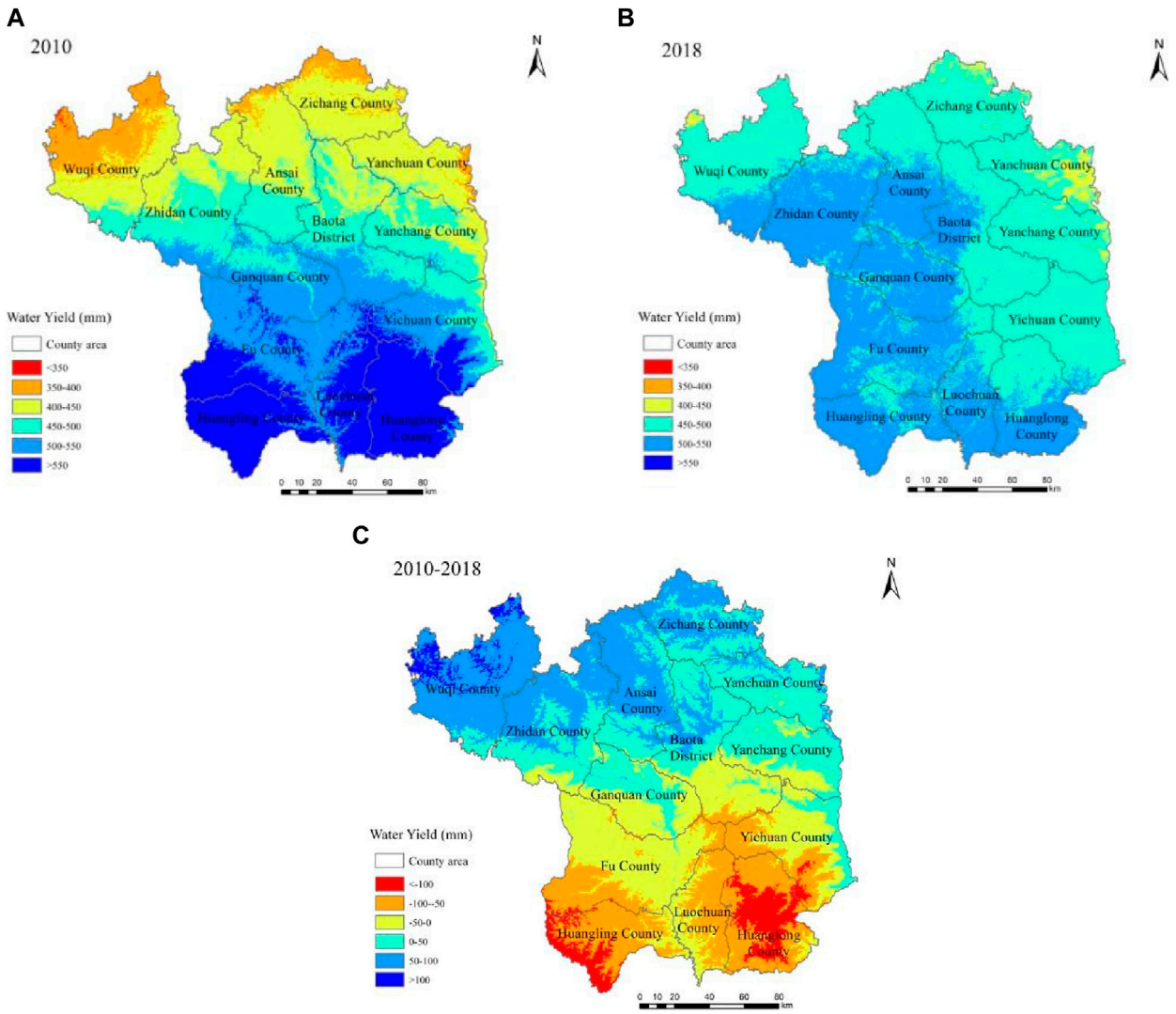

FIGURE 4
Spatial distribution of water conservation services of Yan'an city in 2010 **(A)**, 2018 **(B)** and the change **(C)**.

3.4 Correlation analysis between ecosystem service change and implementation data of the GCLC project

Based on Pearson correlation coefficient, SPSS18.0 software was used to analyze the correlation between the implementation scale data of GCLC projects in 13 districts and counties of Yan'an city (Table 1) and the change values of soil conservation and water conservation. The results showed (Table 2) that from 2010 to 2018, there was a positive correlation between soil conservation services and the number of the projects, as well as the newly added cultivated land area. There was a negative correlation between soil conservation services and the construction scale, the construction scale of high-standard farmland, and the investment amount. There was a positive correlation between water conservation and the GCLC projects, but all correlations were not significant.

According to the change values of soil conservation and water conservation in 13 districts and counties of Yan'an city (Figure 7), from 2010 to 2018, due to different natural conditions and habitat characteristics, each district and county in Yan'an played different roles in ecological protection, food security and economic development, and the implementation priorities of GCLC projects and their impacts on soil conservation and water conservation services changes were also different.

As the municipal government of Yan'an city is located, The rapid urbanization makes a large amount of cultivated land in Baota District occupied by construction land, so it is necessary to implement the GCLC project to develop agriculture intensively and improve the economic and population capacity. Baota District has the largest area of construction scale, and the newly added cultivated land in Yan'an city. The implementation of the project and urban construction made the the amount of soil conservation in Baota District has decreased.

In the east, Zichang, Yanchuan and Yanchang counties have low terrain, which is more suitable for the development of agriculture. Therefore, the implementation of GCLC projects covers a large area. Except for Zichang County, there was a

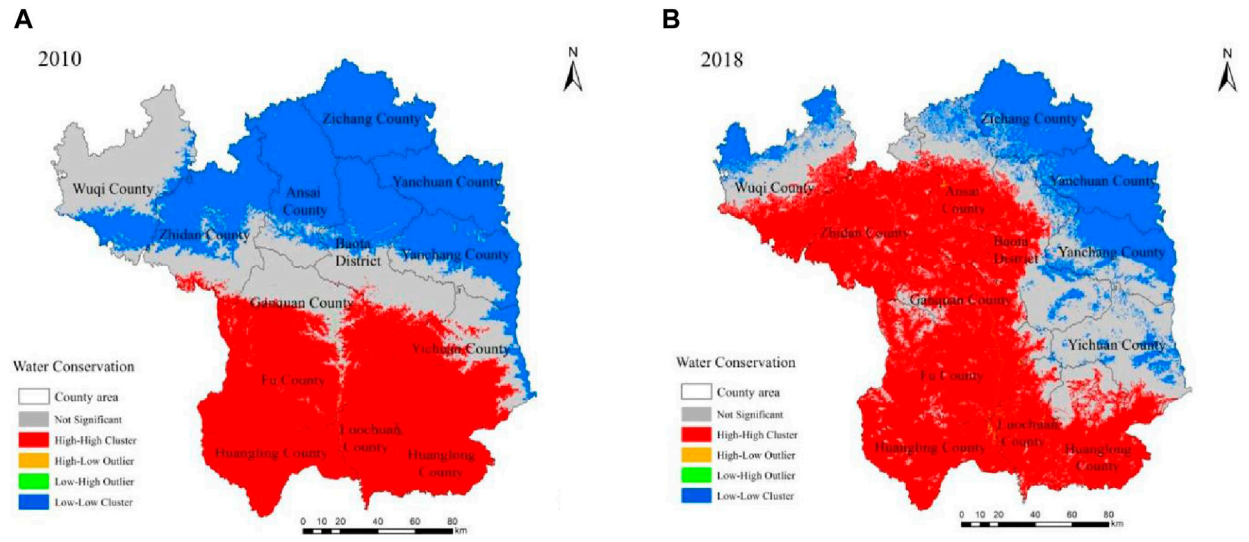

FIGURE 5
LISA clustering of water conservation services of Yan'an city in 2010 **(A)** and 2018 **(B)**.

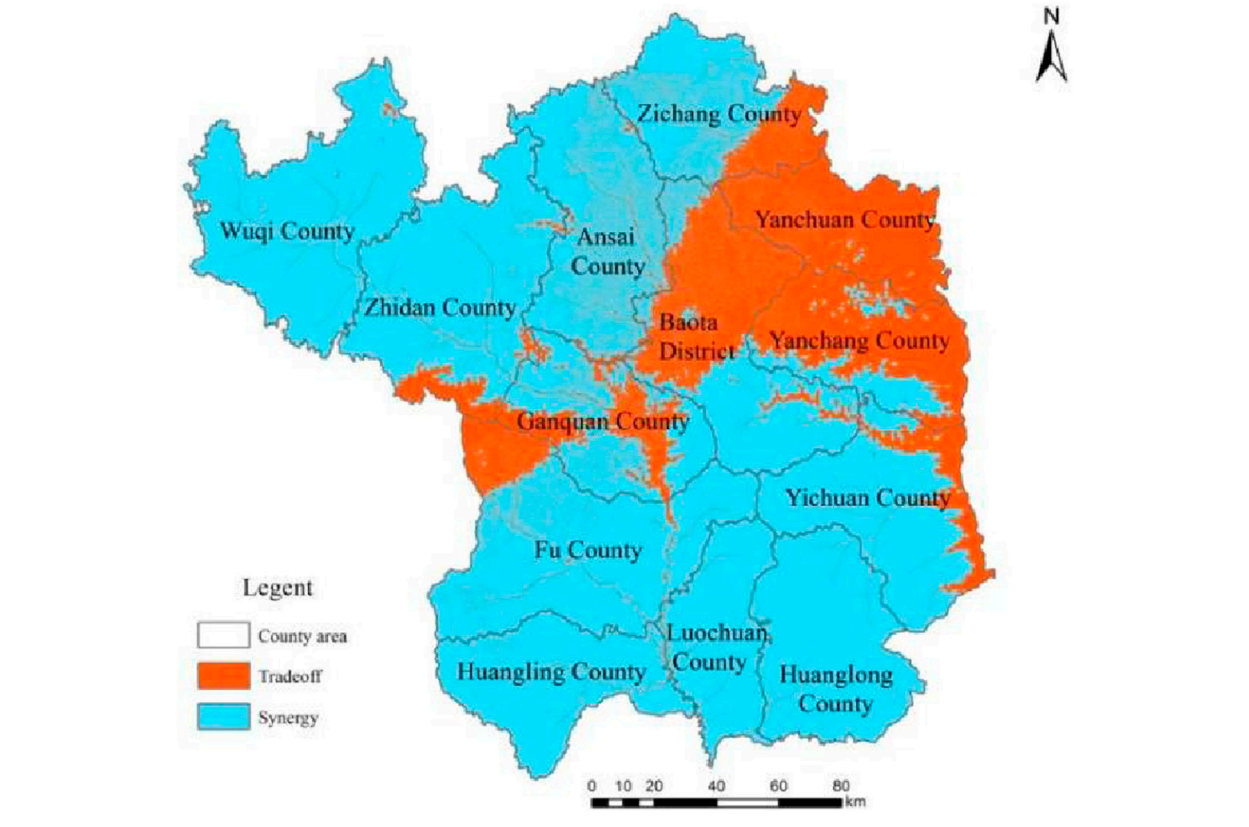

FIGURE 6
Distribution of trade-offs between soil conservation and water conservation services of Yan'an city.

slight decreased of soil conservation in Yanchuan and Yanchang counties.

The southeast and southwest of Yan'an city, especially, Huangling and Huanglong counties are important ecological protection and water conservation areas in the province. So the amount of water conservation and soil conservation has decreased due to the impact of the project. Although the scale and the new cultivated land of the project is small, the human disturbance and

TABLE 2 Correlation between implementation index of GCLC project and soil conservation and water conservation service change.

Implementation index of GCLC project	Projects number	Construction scale/hm^2	Newly increased cultivated land/hm^2	High standard farmland/hm^2	Investment amount/ten thousand yuan
Soil conservation	0.033	−0.066	0.030	−0.157	−0.083
Water conservation	0.316	0.295	0.475	0.204	0.289

landscape fragmentation still cause a large degree of decline in water conservation and soil conservation.

Wuqi, Zhidan and Anseh counties in the north have poor ecological environment background conditions, high altitude and wide distribution of grassland. Although the scale of GCLC projects implemented is not large, they can effectively improve the level of agricultural infrastructure, fully guarantee and improve people's livelihood, and play a positive role in the restoration of ecological environment. Therefore, the service functions of soil conservation and water conservation have been slightly improved.

4 Discussion

4.1 Changes and synergistic relationship between soil conservation and water conservation services in Yan'an city

From 2010 to 2018, the total amount of soil conservation in Yan'an city decreased by 7.7%, while the water conservation increased by 0.56%. The general trend of both is a decrease in the south and an increase in the north. Studies have shown that large-scale ecosystem service changes and their synergies and trade-offs are mainly caused by climate factors such as temperature and precipitation, while small-scale changes are caused by human activities and land use changes (Wang et al., 2021).

Precipitation is the biggest influencing factor of water conservation services (Wang X. et al., 2022). The spatial variation of water conservation services in Yan'an City was basically consistent with the variation trend of precipitation in Yan'an City during this period (Xu and Zhang, 2020), but the total amount of water conservation in Yan'an City remained stable. It may be that the increase in vegetation cover increased plant transpiration, so the total amount of water conservation did not increase much. In addition to precipitation, soil conservation is also closely related to topography and land use type, which affect soil conservation function by affecting rainfall erosivity (Xu and Zhang, 2020). The overall change of soil conservation service in Yan'an city is greater than that of water conservation service, which may be because human activities have changed the topography and land use types on a small scale, so the amount of soil conservation has decreased to a certain extent.

On the whole, there is a synergistic relationship between soil conservation and water conservation services, which is consistent with the research results of other scholars in the Loess Plateau region (Ren et al., 2022; Lan et al., 2023). Due to the consistent impact of precipitation, land use types, and vegetation cover, as well as relatively similar biophysical linkages and soil hydrological processes, the two services exhibit synergy (Li and Zhang, 2021; Wang S. et al., 2022). However, in the study area, Yanchuan, Yanchang and the northern part of Baota districts in the east of Yan'an city show a certain tradeoff. According to Table 1, the largest area of GCLC projects was implemented in this three areas. Therefore, this may be related to human disturbance. Xue et al. (2024) research in the Loess Plateau region also shows that places with low elevation are more susceptible to human disturbance. The higher the elevation, the stronger the synergistic effect between soil conservation and water conservation services (Xue et al., 2024).

4.2 Effects of the GCLC project on soil conservation and water conservation services

The results showed that the effect of the GCLC projects on soil conservation and water conservation services in Yan'an city is not significant. Many studies have shown that land consolidation has a negative impact on soil and water loss and significantly increases the amount of soil erosion (Evrard et al., 2010; Chartin et al., 2013). On the other hand, the change of slope gradient in land leveling projects can increase infiltration, reduce runoff rate and soil erosion intensity (Gao et al., 2012; Liu et al., 2013; Liu et al., 2015). In terms of ecosystem services, most studies have shown that land consolidation improves food production services of ecosystems while weakening other services and total value (Zhao et al., 2004; Kindu et al., 2016). The Loess Plateau is vulnerable to erosion due to its broken topography and poor impact resistance, and the implementation of land consolidation project has a certain negative impact on soil conservation. Meanwhile, compared with the forest and grass ecosystem, the vegetation coverage of farmland is relatively lower, so the soil conservation service is relatively low (Sun et al., 2014). However, engineering measures such as hydraulic engineering effectively reduced the occurrence of drought and flooding events, promoted the protection of vegetation in the whole basin, and thus prevented soil and water erosion. Therefore, in general, the negative impact of the project on soil conservation is not large, and the changes of soil conservation and water conservation services in Yan'an city during the GCLC project are relatively stable.

Yin's research shows that Nature-based Solution (NCS) practices can improve multiple ecosystem services. However, unsustainable NCS implementation such as over-afforesting may result in a trade-off of reduced water supply, grassland and farmland (Yin et al., 2023). The GCLC project implemented in Yan'an city after the GFG project can not only increase the quantity and quality of cultivated land, and ensure food security, but also provide

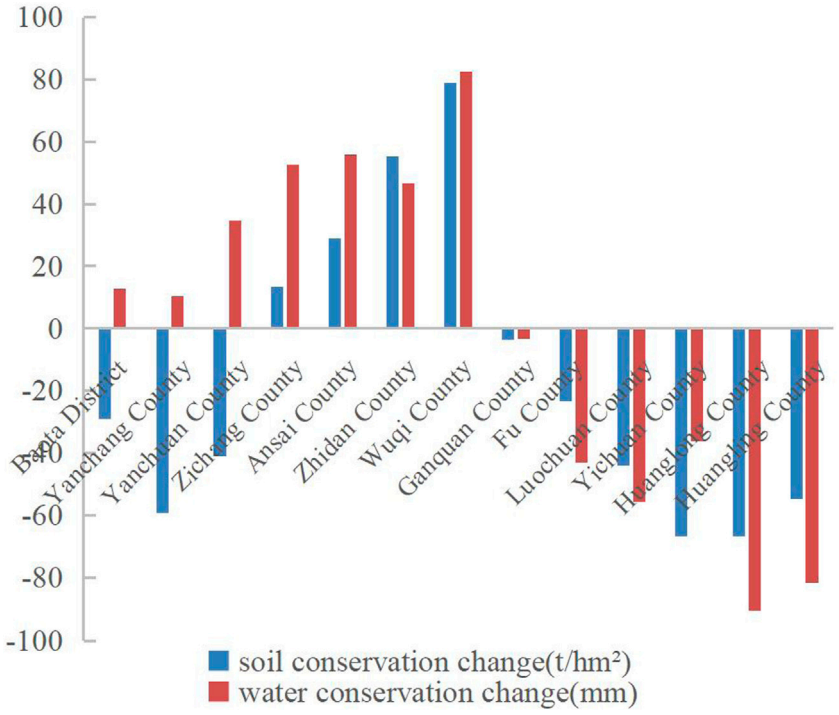

FIGURE 7
The soil conservation and water conservation services variations in different districts and counties of Yan'an city.

relatively stable and coordinated soil conservation and water conservation services in Yan'an city during this period, achieving the effect of "expanding ecosystem area" to "improving ecosystem management efficiency."

4.3 Limitations and prospects

Based on the InVEST model, this study analyzed the temporal and spatial evolution of soil conservation and water conservation services in Yan'an city under the background of GCLC project. It could not only obtain quantitative analysis results, but also visually analyzed the results of ecosystem service value, providing a basis for the benefit assessment of regional GCLC project. However, the research on its impact mechanism was not deep enough in this paper. In addition, the scale of the study can also affect the results. Due to the influence of climate, terrain, land use and other conditions, the trade-offs among ecosystem services are spatial-heterogeneous and temporal-dynamic, and change with the passage of spatial-temporal scales (Ren et al., 2022). In the next step, on the basis of obtaining the spatial information of the project, the relationship between land consolidation at different scales and ecosystem service function should be further obtained by means of spatial analysis, and the influence mechanism and law of long-term comprehensive benefits after the implementation of the project should be revealed through reasonable model simulation. It provide a more effective theoretical basis for land consolidation technology innovation and ecological protection of the Loess Plateau.

5 Conclusion

The total amount of soil conservation decrease of 7.76% in Yan'an city between 2010 and 2018, and the basic trend of spatial variation was an increase in the northwest and a decrease in the southeast. The spatial clustering of soil conservation was relatively low. The total amount of water conservation in Yan'an city remained relatively stable, increasing by 0.56% in 8 years, with the basic trend of increasing in the north and decreasing in the south. There is a high spatial clustering feature in water conservation service. There is a synergistic relationship between soil conservation and water conservation services in most area of Yan'an city. From 2010 to 2018, the effect of the GCLC projects on soil conservation and water conservation services in Yan'an city is not significant. Due to the different natural conditions and habitat characteristics, the implementation focus of GCLC project and its impact on soil conservation and water conservation services are also different.

These results show that the GCLC project can effectively alleviate the situation of sharp decline of cultivated land area and insufficient food production capacity under the condition of maintaining relatively stable and coordinated regional soil conservation and water conservation services, ensure the red line of cultivated land and food security, and balance the conflict between ecological protection and farmers' livelihood. The balanced between ecological security and food security, high-quality development and ecological protection has been achieved. Our work could be cited as a reference for other comprehensive ecological control projects in the Loess Plateau.

Data availability statement

The original contributions presented in the study are included in the article/Supplementary Material, further inquiries can be directed to the corresponding author.

Author contributions

WJ: Conceptualization, Investigation, Writing–original draft, Writing–review and editing, Data curation, Formal Analysis. ZY: Methodology, Writing–review and editing. XL: Supervision, Validation, Writing–review and editing. LJ: Resources, Software, Writing–original draft. HH: Visualization, Writing–review and editing. LS: Funding acquisition, Writing–review and editing.

Funding

The authors declare that financial support was received for the research, authorship, and/or publication of this article. This work was funded by the Technology Innovation Center for Land Engineering and Human Settlements, Shaanxi Land Engineering Construction Group Co., Ltd. and Xi'an Jiaotong University (2024WHZ0238), the Open Foundation of the Key Laboratory of Natural Resource Coupling Process and Effects (No. 2023KFKTB008), the Key Research and Development Program of Shaanxi (No. 2022ZDLSF06-04), the project of Shaanxi Province Land Engineering Construction Group (No. DJTD-2022-4).

Conflict of interest

Authors WJ, ZY, XL, LJ, and LS were employed by Shaanxi Provincial Land Engineering Construction Group Co., Ltd.

The remaining author declares that the research was conducted in the absence of any commercial or financial relationships that could be construed as a potential conflict of interest.

Publisher's note

References

Anselin, L. (1995). Local indicators of spatial association-LISA. *Geogr. Anal.* 27, 93–115. doi:10.1111/j.1538-4632.1995.tb00338.x

Chartin, C., Evrard, O., Salvador-Blanes, S., Hinschberger, F., Van Oost, K., Lefèvre, I., et al. (2013). Quantifying and modelling the impact of land consolidation and field borders on soil redistribution in agricultural landscapes (1954–2009). *Catena* 110, 184–195. doi:10.1016/j.catena.2013.06.006

Chen, Y. P., Wang, K., Lin, Y., Shi, W., Song, Y., and He, X. (2015). Balancing green and grain trade. *Nat. Geosci.* 8 (10), 739–741. doi:10.1038/ngeo2544

Costanza, R., d'Arge, R., de Groot, R., Farber, S., Grasso, M., Hannon, B., et al. (1998). The value of the world's ecosystem services and natural capital. *Ecol. Econ.* 25 (1), 3–15. doi:10.1016/s0921-8009(98)00020-2

Costanza, R., D'Arger, R., De Groot, R., Farber, S., Grasso, M., Hannon, B., et al. (1997). The value of the world's ecosystem services and natural capital. *Nature* 387 (6630), 253–315. doi:10.1016/s0921-8009(98)00020-2

Deng, Y. J., Hou, M. Y., Xie, Y. F., et al. (2020). Impact of the Grain for Green Project on the temporal and spatial evolution of ecosystem service value in northern Shaanxi. *Acta Ecol. Sin.* 40 (18), 6597–6612.

Evrard, O., Nord, G., Cerdan, O., Souchère, V., Le Bissonnais, Y., and Bonté, P. (2010). Modelling the impact of land use change and rainfall seasonality on sediment export from an agricultural catchment of the northwestern European loess belt. *Agric. Ecosyst. Environ.* 138 (1), 83–94. doi:10.1016/j.agee.2010.04.003

Gao, H. D., Li, Z. B., Li, P., et al. (2012). Influences of terrace construction and check dam silting-up on soil erosion. *Acta Geogr. Sin.* 67 (5), 599–608.

Gao, J. B., and Zuo, L. Y. (2021). Revealing ecosystem services relationships and their driving factors for five basins of Beijing. *J. Geogr. Sci.* 31 (1), 111–129. doi:10.1007/s11442-021-1835-y

Han, L., Huo, H., Liu, Z., Zhao, Y. H., Zhu, H. L., Chen, R., et al. (2021). Spatial and temporal variations of vegetation coverage in the middle section of Yellow River Basin based on terrain gradient: taking Yan'an City as an example. *Chin. J. Appl. Ecol.* 32 (5), 1581–1592. doi:10.13287/j.1001-9332.202105.014

He, C. X. (2015). The situation, characteristics and effect of the gully reclamation project in Yan'an. *J. Earth Environ.* 6, 255–260.

He, M. N., Wang, Y. Q., Tong, Y. P., Zhao, Y., Qiang, X., Song, Y., et al. (2020). Evaluation of the environmental effects of intensive land consolidation: a field-based case study of the Chinese Loess Plateau. *Land Use Policy* 94, 104523. doi:10.1016/j.landusepol.2020.104523

Jin, Z., Guo, L., Wang, Y. Q., Yu, Y., Lin, H., Chen, Y., et al. (2019). Valley reshaping and damming induce water table rise and soil salinizationon the Chinese Loess Plateau. *Geoderma* 339, 115–125. doi:10.1016/j.geoderma.2018.12.048

Jopke, C., Kreyling, J., Maes, J., and Koellner, T. (2015). Interactions among ecosystem services across Europe: bagplots and cumulative correlation coefficients reveal synergies, trade-offs, and regional patterns. *Ecol. Indic.* 49, 46–52. doi:10.1016/j.ecolind.2014.09.037

Kindu, M., Schneider, T., Teketay, D., and Knoke, T. (2016). Changes of ecosystem service values in response to land use/land cover dynamics in Munessa-Shashemene landscape of the Ethiopian highlands. *Sci. Total Environ.* 547, 137–147. doi:10.1016/j.scitotenv.2015.12.127

Lan, Y. Z., Sun, T. S., and Li, W. W. (2023). Trade-offs and synergies of farmland ecosystem services in Loess Plateau: a case study of Longdong Region, Northwest China. *Trans. Chin. Soc. Agric. Eng.* 39 (12), 238–246.

Li, S. C., Zhang, C. Y., Liu, J. L., et al. (2013). The tradeoffs and synergies of ecosystem services: research progress, development trend, and themes of geography. *Geogr. Res.* 32 (8), 1379–1390.

Li, Y. H., Du, G. M., and Liu, Y. S. (2016). Transforming the loess plateau of China. *Front. Agric. Sci. Eng.* 3 (3), 181–185. doi:10.15302/j-fase-2016110

Li, Z., and Zhang, Y. F. (2021). Spatiotemporal evolution of ecosystem services in the main and Tributaries of Weihe River basin based on InVEST model. *J. Soil Water Conservation* 35 (4), 178–185.

Liu, J. Y. (1996). *Remote sensing macroscopic survey and dynamic study of resources and environment in China*. Beijing: China Science and Technology Press.

Liu, S. L., Dong, Y. H., Li, D., Liu, Q., Wang, J., and Zhang, X. (2013). Effects of different terrace protection measures in a sloping land consolidation project targeting soil erosion at the slope scale. *Ecol. Eng.* 53, 46–53. doi:10.1016/j.ecoleng.2012.12.001

Liu, Y. S. (2013). *Feasibility study report of major project of gully control and land consolidation in yan 'an city, Shaanxi province*. Beijing: Institute of Geographic Sciences and Natural Resources Research, Chinese Academy of Sciences, 1–5.

Liu, Y. S., Guo, Y. J., Li, Y. R., et al. (2015). Gis-based effect assessment of soil erosion before and after gully land consolidation: a case study of wangjiagou project region, loess plateau. *Chin. Geogr. Sci.* 25 (2), 137–146. doi:10.1007/s11769-015-0742-5

Ma, J. F., Chen, Y. P., Wang, H. J., Wu, J., Su, C., et al. (2020). Newly created farmland should be artificially ameliorated to sustain agricultural production on the Loess Plateau. *Land Degrad. Dev.* 31 (17), 2565–2576. doi:10.1002/ldr.3618

MEA (2005). *Ecosystems and human well-being: current state and trends*. Washington, DC: Island Press.

Moran, P. A. P. (1950). Notes on continuous stochastic phenomena. *Biometrika* 37 (1/2), 17–23. doi:10.2307/2332142

Mousavi, S. A., Ghahfarokhi, M. S., and Koupaei, S. S. (2023). Negative impacts of nomadic livestock grazing on common rangelands' function in soil and water conservation - science Direct. *Ecol. Indic.* 110(3), 105946. doi:10.1016/j.ecolind.2019.105946

Ouyang, Z. Y., and Wang, R. S. (2000). Ecosystem services and their economic valuation. *World Sci. Technol. Res. Dev.* 22 (5), 45–50.

Ren, J., Zhao, X. Y., Xu, X. C., et al. (2022). Spatial-temporal evolution, tradeoffs and synergies of ecosystem services in the middle Yellow River. *J. Earth Environ.* 13 (4), 477–490.

Sun, W. Y., Shao, Q. Q., and Liu, J. Y. (2014). Assessment of soil conservation function of the ecosystem services on the Loess Plateau. *J. Nat. Resour.* 29 (3), 365–376.

Turner, K. G., Odgaard, M. V., Bøcher, P. K., Dalgaard, T., and Svenning, J. C. (2014). Bundling ecosystem services in Denmark: trade-offs and synergies in a cultural landscape. *Landsc. Urban Plan.* 125, 89–104. doi:10.1016/j.landurbplan.2014.02.007

Wang, S., Li, Y. W., Li, Q., et al. (2022b). Water and soil conservation and their trade-off and synergistic relationship under changing environment in Zhangjiakou-Chengde area. *Acta Ecol. Sin.* 42 (13), 5391–5403. doi:10.5846/stxb202105291417

Wang, X., Wu, J., Liu, Y., Hai, X., Shanguan, Z., and Deng, L. (2022a). Driving factors of ecosystem services and their spatiotemporal change assessment based on land use types in the Loess Plateau. *J. Environ. Manag.* 311, 114835. doi:10.1016/j.jenvman.2022.114835

Wang, X. Z., Wu, J. S., Wu, P. X., et al. (2021). Spatial and temporal distribution and trade-off of water conservation, soil conservation and NPP services in the ecosystems of the loess plateau from 2000 to 2015. *J. Soil Water Conservation* 35 (4), 114–121.

Williams, J. R. (1990). The erosion-productivity impact calculator (EPIC) model: a case history. *Philosophical Trans. R. Soc. B-Biological Sci.* 329 (1255), 421–428.

Wischmeier, W. H., and Smith, D. D. (1958). Rainfall energy and its relationship to soil loss. *Trans. Am. Geophys. Union* 39, 285–291.

Xu, E. Q., and Zhang, H. Q. (2020). Change pathway and intersection of rainfall, soil, and land use influencing water-related soil erosion. *Ecol. Indic.* 113, 106281. doi:10.1016/j.ecolind.2020.106281

Xue, Z. H., Gao, Y. Y., Lu, P. D., et al. (2024). Spatial distribution and tradeoff synergy-independence relationships of ecosystem services based on land use and topography. *Res. Soil Water Conservation* 31 (2).

Yellow River Conservancy Commission (2022). Bulletin of soil and water conservation in the Yellow River Basin (2021) [R]. *Zhengzhou Yellow River Conservancy Comm. Ministry Water Resour.*

Yin, C. C., Pereira, P., Zhao, W. W., and Barcelo, D. (2023). Natural climate solutions. The way forward. *Geogr. Sustain.* 4 (2), 179–182. doi:10.1016/j.geosus.2023.03.005

Zhao, B., Kreuter, U., Li, B., Ma, Z., Chen, J., and Nakagoshi, N. (2004). An ecosystem service value assessment of land-use change on Chongming Island, China. *Land Use Policy* 21, 139–148. doi:10.1016/j.landusepol.2003.10.003

frontiers | Frontiers in Environmental Science

TYPE Original Research
PUBLISHED 03 January 2025
DOI 10.3389/fenvs.2024.1512973

OPEN ACCESS

EDITED BY
Xudong Peng,
Guizhou University, China

REVIEWED BY
Tianyang Li,
Southwest University, China
Zhenqi Yang,
China Institute of Water Resources and Hydropower Research, China
Youcai Kang,
Northwest Normal University, China

*CORRESPONDENCE
Shangxuan Zhang,
2683854478@qq.com

RECEIVED 17 October 2024
ACCEPTED 27 November 2024
PUBLISHED 03 January 2025

CITATION
Sheng Y, Zhang S, Li L, Cao Z and Zhang Y (2025) Simulation of slope soil erosion intensity with different vegetation patterns based on cellular automata model.
Front. Environ. Sci. 12:1512973.
doi: 10.3389/fenvs.2024.1512973

Simulation of slope soil erosion intensity with different vegetation patterns based on cellular automata model

Yan Sheng[1], Shangxuan Zhang[1]*, Long Li[1,2], Zhiming Cao[1] and Yu Zhang[1]

[1]College of Desert Control, Science, and Engineering, Inner Mongolia Agricultural University, Hohhot, China, [2]Key Laboratory of Desert Ecosystem Protection and Restoration, State Forestry Administration, Hohhot, China

Introduction: Soil erosion plays a crucial role in soil and water conservation management, as well as in ecological construction planning. This study focuses on the slopes of three planting patterns (uniform distribution, aggregation distribution, and random distribution), along with bare slopes, in the Baojiagou watershed of the Pisha Sandstone area, based on soil erosion intensity grade maps after rainfall from 2021 to 2023.

Methods: A method combining Multi-Criteria Evaluation (MCE) and the CA-Markov model is used to analyze the spatial variation of soil erosion intensity types on different slopes. This approach integrates multiple influencing factors and generates a suitability map for the conversion of soil erosion intensity types. Ultimately, the dynamic characteristics of soil erosion in 2023 are simulated under various slope conditions.

Results: Results indicated: (1) The spatial distribution of simulated soil erosion intensity grade maps for different slopes largely aligned with actual maps, and regions with soil erosion depth greater than 3 cm were resistant to transitioning to lower erosion zones. (2) The Kappa coefficients for simulated soil erosion intensity in uniform distribution, random distribution, aggregate distribution, and bare control slopes were 65.24%, 73.62%, 75.88%, and 69.06%, respectively, confirming the feasibility of the CA-Markov model for simulating soil erosion dynamics. (3) The simulation of soil erosion intensity on different slopes in 2023 revealed that erosion intensity on uniformly distributed, aggregated, and bare control slopes remained predominantly in the erosion zone with a depth of 1–2 cm, while randomly distributed slopes experienced a shift from mild erosion area to slight erosion area.

Discussion: This study improves the understanding of soil erosion across different vegetation patterns and demonstrates the applicability of the CA-Markov model for simulating dynamic erosion on slopes. The findings contribute to the development of broader ecological models and offer insights into vegetation management and erosion control strategies for similar landscapes.

KEYWORDS

soil erosion, slope stability, vegetation patch pattern, CA-Markov model, erosion simulation

1 Introduction

Erosion is a continuous natural process occurring on the Earth's surface, especially in arid and semi-arid regions (Zhang et al., 1996; Grazhdani and Shumka, 2007; Liu et al., 2016). Soil erosion depletes land resources, worsens ecological degradation, and threatens human survival and development (Nurlina et al., 2022; Porto et al., 2022). In the Pisha sandstone region of the Yellow River Basin, water and soil loss has led to desertification of one-third of fertile soil, severely impacting agriculture and the environment (Yeh et al., 2006; Liu and Zhang, 2015). Research has shown that vegetation plays a critical role in slope soil erosion, making it central to erosion control and watershed management (BriniImen et al., 2021). However, vegetation on slopes in this region often fails to provide sufficient coverage. More commonly, vegetation appears in patchy or strip patterns, resulting in a fragmented vegetation structure (Pajouhesh et al., 2020; Eigentler and Sherratt, 2020). This pattern of vegetation influences the redistribution of runoff and sediment during hydraulic erosion on slopes. Therefore, simulating soil erosion dynamics under the influence of vegetation patterns is essential.

With the advancement of quantitative analysis of vegetation pattern indices, combined with remote sensing and geographic information systems, various mathematical models have been applied to studying soil erosion and vegetation patterns. Among them, the cellular automata (CA) model effectively utilizes vegetation pattern characteristics to explain key processes influencing soil erosion (Xiang et al., 2019; Fazlolah et al., 2018; Zhang et al., 2017). CA (cellular automata), as a tool for studying complex spatial phenomena, offers excellent simulation capabilities and has been widely recognized in the geographic research community (Qun et al., 2019). Currently, many scholars have applied CA for spatio-temporal dynamic simulation and prediction of various geographical phenomena. For instance, Yuan et al. (2008) used the CA model to develop a small watershed erosion and sediment production process model, CASEM, and explored its application in simulating soil erosion processes. Ma et al. (2003) utilized the CA model, supported by GIS technology, to analyze the spatial evolution of soil erosion under different land-use models and predict erosion development trends based on various land-use plots. Chase Clement, 1992 developed a CA model to simulate rainfall spatter erosion and runoff on slopes using simple rules, achieving notable results. D'Ambrosio et al. (2001) developed SCAVATU, a CA-based model to simulate hydraulic soil erosion, and obtained favorable simulation results. Although the CA model has been successfully applied to simulate the spatial development of soil erosion in large watersheds, building a dynamic slope soil erosion model based on CA remains in the exploratory phase. Slope erosion, as a typical nonlinear dynamic system, involves highly complex internal development and evolutionary processes, characterized by significant uncertainty and chaos. Therefore, it is imperative to develop a slope soil erosion model capable of simulating complex spatio-temporal dynamics and the spatial evolution of erosion. The CA-Markov model, based on transition probability matrices and suitability maps, leverages CA's spatial transformation capability to simulate complex systems and utilizes Markov's strengths to predict future trends in soil erosion intensity. In CA-Markov model simulations, complex spatio-temporal processes and interactions occur between various erosion intensity levels, necessitating a simulation model for transforming different soil erosion intensities and expanding its application scope. Vegetation patterns regulate and redistribute runoff and sediment during slope hydraulic erosion (Crompton and Thompson, 2020). Thus, investigating the relationship between vegetation patterns and soil erosion at the slope scale is crucial for comprehensive soil and water conservation.

While much research has explored soil erosion in various contexts, few studies have focused on simulating slope erosion under different vegetation patch patterns. Unlike earlier models that predominantly consider uniform vegetation distributions, this study investigates the impact of varied vegetation patterns, such as random and aggregated distributions, on erosion dynamics. This approach provides a more nuanced understanding of the role of vegetation in regulating runoff and sediment flow, offering valuable insights for erosion control in challenging environments. Therefore, this study focuses on the slopes of three planting patterns (uniform distribution, random distribution, and aggregation distribution) and bare control slopes in the Baojiagou Watershed of the Pisha Sandstone area. Starting with the rainfall-soil-erosion relationship at the slope scale, field monitoring experiments were conducted using runoff plots under natural rainfall conditions. Based on soil erosion intensity maps of slopes with varying vegetation patterns over a 3-year rainfall period, the spatial variation and intensity of soil erosion types were analyzed across slopes with different vegetation patch patterns. The CA-Markov model in IDRISI software was used to examine the conversion rules of soil erosion intensity types, integrating various influencing factors. A suitability map for soil erosion intensity conversion was developed to simulate the dynamic characteristics of erosion on slopes with different vegetation patch patterns, further verifying the ecological benefits of vegetation and providing valuable references for soil and water conservation management in the Pisha sandstone region.

2 Research methodology and methods

2.1 Study area

The study area is located in Nuanshui Town, Zhungeer Banner, Ordos City, Inner Mongolia (110°31′–110°35′E, 39°46′–39°48′N) (Figure 1). The elevation ranges from 1,145 to 1,330 m, with higher terrain in the north and lower in the south. The main zonal soil is chestnut-calcium soil, which has low organic matter content. The study area can be divided based on the type of surface cover and the degree of bedrock exposure into sand-covered sandstone areas, soil-covered sandstone areas, and exposed sandstone areas, with the exposed sandstone area having the harshest ecological environment. This area has a typical continental climate, with an average annual temperature of 6–9°C, a large diurnal temperature range, cold and dry winters with long seasons, and hot summers with short seasons. The average annual rainfall is 400 mm, and the rainfall is mainly concentrated in the summer (July-August). The average annual rainfall in summer is 256.4 mm, accounting for 64.1% of the total annual rainfall. Most of the rainfall is rainstorm (more than 50 mm), and the rainfall erosivity is high (489.87 MJ mm hm^{-2} h^{-1} a^{-1}). The frost-free

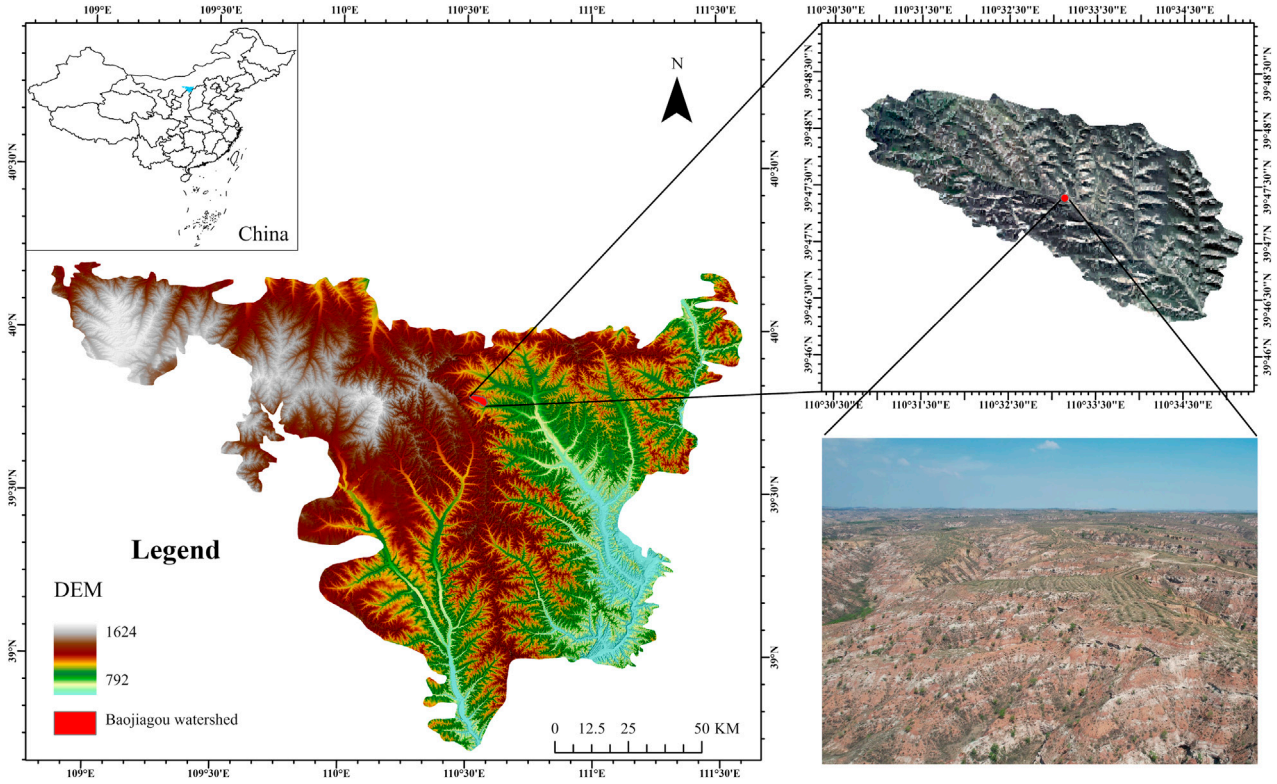

FIGURE 1
Location map of the study area.

period is 100–140 days, with abundant sunshine and an average annual wind speed of 2–4 m/s. The main vegetation includes *Pinus tabuliformis* Carr., *Caragana korshinskii*, *Hippophae rhamnoides*, *Leymus chinensis*, *Salsola collina*, as well as other psammophytes, swamp meadows, and degraded grasslands.

2.2 Determination of vegetation pattern and plot layout

Based on ecological principles, three vegetation distribution patterns are identified: uniform, clustered, and random. Uniform distribution is typically observed in undisturbed wastelands, where vegetation is evenly spread across the surface. Random distribution patterns are often seen in areas with degraded surfaces or sparse vegetation. Clustered distribution is common in semi-arid or degraded ecosystems. These three vegetation patterns reflect the spatial distribution characteristics of vegetation within the study area. Due to the harsh ecological conditions, high rainfall intensity, and erosion-prone soils in the region, a comparison of these patterns reveals their differential impacts on soil and water conservation. When selecting sampling plots, it is ensured that the soil structure of the three types of plots is consistent, the vegetation species and coverage are similar, the slope gradient and aspect are the same, the slope length is greater than 20 m, and there is no human interference. At the same time, a slope with natural conditions identical to the research plots was selected, and all vegetation on the slope was removed to serve as a control plot (bare ground). After selecting the slope, adjacent 1 m × 1 m grid plots were delineated on the slope, for a total of 60 plots, and each plot was surveyed for plant community characteristics in sequence.

The study uses the variance-to-mean ratio method (Equations 1, 2) (Elias and Schindler, 2015) to determine the vegetation distribution patterns. This method is based on statistical principles and reveals the distribution characteristics of a sample by comparing the degree of dispersion (variance) of the data with its average level (mean). The ratio of variance to mean is relatively simple and can quickly identify and explain the distribution pattern of vegetation in a specific ecological environment. If $S^2/m = 0$, it indicates a uniform distribution; If $S^2/m = 1$, it indicates a random distribution; If S^2/m is significantly greater than 1, it indicates an aggregated distribution (Table 1). The calculation formula is:

$$M = \sum_{i}^{N} M_i \Big/ N \tag{1}$$

$$S^2 = \sum_{i}^{N} (M_i - \bar{M})^2 \Big/ (N - 1) \tag{2}$$

In the formula, N represents the number of basic plots, and M_i represents the number of individuals in the ith plot.

This experiment is a field runoff plot natural rainfall *in-situ* monitoring experiment, preparation began on 30 June 2021, and the observation period is the three rainy seasons (June-August) from 2021 to 2023. Based on the local topographic conditions, stainless steel plates were used to establish a runoff plot with dimensions of 10 m (length) × 2 m (width) on the slope (Figure 2). The plot

TABLE 1 Vegetation distribution patterns determined by the variance-to-mean ratio method.

Sample area	Quadrat number (N)	Variance (S^2)	Mean value (M)	S^2/M	Pattern of vegetation	Coverage of vegetation	Type of vegetation
1	20	0.15	0.81	0.18 < 1	Uniform distribution	32.6%	*Asparagus cochinchinensis, Kali collinum, Artemisia stechmanniana, Sophora davidii, Melilotus officinalis*
2	20	0.64	0.56	1.14≈1	Random distribution	30.5%	*Asparagus cochinchinensis, Kali collinum, Artemisia stechmanniana, Sophora davidii*
3	20	3.46	0.33	2.6 > 1	Gather distribution	31.1%	*Asparagus cochinchinensis, Kali collinum, Artemisia stechmanniana, Sophora davidii, Melilotus officinali*

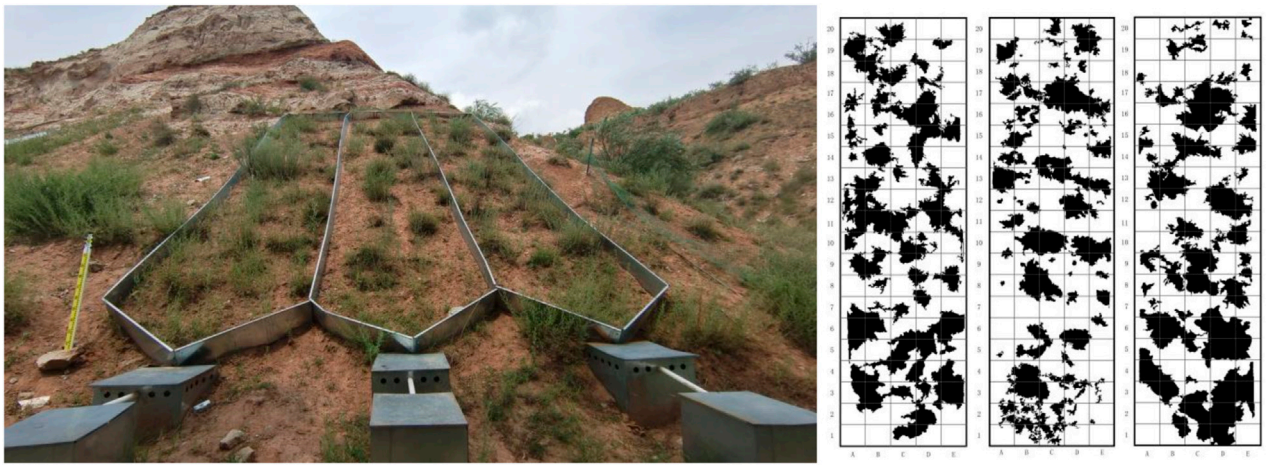

FIGURE 2
The layout of the runoff plot. Notes: In the figure, the vegetation patterns from left to right are uniform distribution, random distribution, and aggregated distribution.

boundaries are perpendicular to the contour lines and are driven 30 cm into the ground with a rubber mallet, leaving 20 cm above ground to block external runoff. The soil texture in the runoff plot is mainly composed of silt particles, accounting for 50.86%, followed by sand particles at 43.86%, and the smallest proportion is clay particles at 5.35%. A fixed rainfall monitoring point was set up next to the runoff plot, using a siphon-type automatic rain gauge to record atmospheric precipitation, and rain gauges were used for cross-validation to measure basic data such as rainfall amount, rainfall intensity, and duration of rainfall (Table 2).

2.3 Determination of soil erosion intensity

The Austrian-made RIGEL-400 3D laser scanner is used. This instrument uses a near-infrared laser beam with a rapid scanning mechanism to obtain 3D point cloud data and is characterized by high speed, non-contact, and high precision. The laser emission frequency is 300,000 bit/s, and the scanning accuracy (for a single 100 m measurement) is 3 mm (horizontal accuracy) × 2 mm (vertical accuracy). The instrument's vertical scanning range is 270°, and the horizontal range is 360°. Scanning one slope takes about 1 min.

At both the bottom and top of each observed runoff plot, a fixed concrete stake is placed as a scanning station, and 5 to 8 fixed reference points are selected as stitching reference points for the scanned data of each station. Before the rainfall starts, an initial scan of the runoff plot is conducted to obtain the original slope point cloud data. After each rainfall, the slope is scanned again after the water has fully infiltrated, capturing the data on slope morphology changes. Before each scan, high-definition video equipment is used to record the process. The instrument is set up at the same position and tripod height for each scan, and reflective sample markers are placed along the plot boundaries to facilitate data trimming and overlay.

After completing data collection before and after rainfall, the "Camera" function of the 3D laser scanner is first used to inspect the scanned slope, ensuring that the surface is within the camera's visible range and that the laser line's visibility is optimized. Then, RiCAN PRO software is used to ensure that the input scan range allows the laser line's intensity to fully pass through. The laser scan dataset is initially filtered through binarization, followed by point cloud registration and coordinate system transformation using the "Plane Surface Filter" and "Backsighting Orientation" functions in the software on the 668,431 scanned points. Since all data

TABLE 2 Statistical table of rainfall characteristics.

Number	Rainfall time	Duration of rainfall (min)	Rainfall amount (mm)	I_{30} (mm/h)	Rainfall intensity (mm/h)
R1	2021.08.15	253	22.60	14.20	5.36
R2	2021.08.18	297	23.60	15.20	4.77
R3	2021.08.29	207	16.50	16.20	4.78
R4	2022.06.29	16	5.80	0.80	21.75
R5	2022.07.05	15	10.50	1.20	42.00
R6	2022.07.11	313	17.00	6.80	3.26
R7	2022.07.26	247	15.00	12.40	3.64
R8	2022.08.06	93	18.60	31.60	12.00
R9	2022.08.12	41	15.80	30.40	23.12
R10	2022.08.13	14	7.40	14.40	31.71
R11	2022.08.14	164	36.60	30.00	13.39
R12	2022.08.18	446	96.60	22.00	13.00
R13	2022.08.21	258	30.80	16.80	3.98
R14	2022.09.03	196	12.40	4.40	3.80
R15	2023.07.20	48	3.20	5.20	4.00
R16	2023.07.21	45	4.00	6.40	5.33
R17	2023.07.24	115	10.60	12.00	5.53
R18	2023.07.27	95	22.60	21.60	14.27
R19	2023.07.31	93	10.00	6.00	6.45
R20	2023.08.03	221	17.60	16.00	4.78
R21	2023.08.04	147	21.60	28.80	8.82
R22	2023.08.10	81	16.20	29.20	12.00

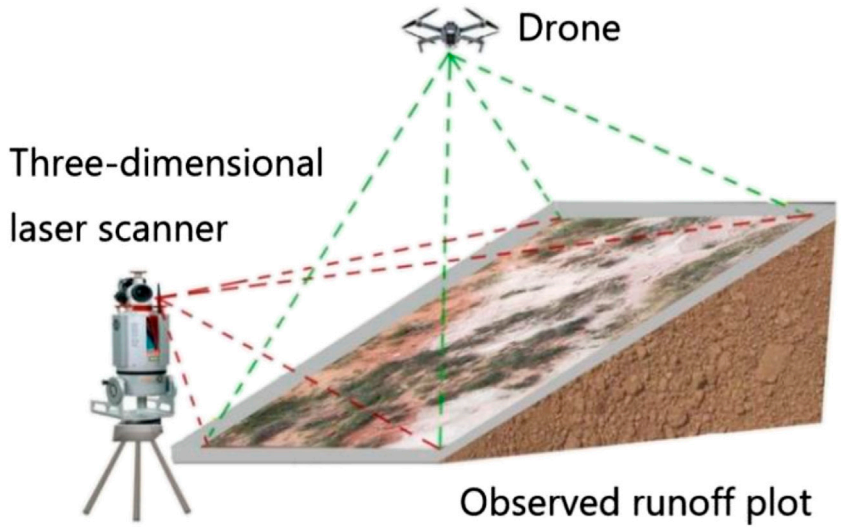

FIGURE 3
Schematic diagram of scanning runoff plot.

captured by the laser line are retained, there may still be non-terrain noise, such as vegetation, leading to a significant amount of redundant point cloud data. Therefore, further denoising and vegetation removal are performed using the "Filtering" and "Multi-Station Processing" functions in RiCAN PRO software, while controlling the standard deviation to ensure the quality of the point cloud data. After collecting elevation point cloud data from the slope, the point cloud data is converted into raster data using the "Data Conversion Module" in the ArcGIS software platform. Ultimately, an M-DEM with a resolution of 2 mm × 2 mm can be generated (Figure 3).

By subtracting the post-rainfall M-DEM from the pre-rainfall M-DEM, the difference can quantitatively describe the changes in the slope's microtopography. In the ArcGIS spatial analysis module, spatial overlay analysis combined with the raster calculator is used to perform raster overlay subtraction and complete the calculation analysis. If the microtopography model after rainfall (M-DEM after) minus the microtopography model before erosion (M-DEM before) results in ΔM-DEM being negative, it indicates that the corresponding area is an erosion zone; if it is positive, it indicates that the corresponding area is a deposition zone. Specifically, erosion zone = ($M\text{-}DEM_{after}$)—($M\text{-}DEM_{before}$) < 0; deposition zone = ($M\text{-}DEM_{after}$)—($M\text{-}DEM_{before}$) > 0. Based on this calculation rule, the slope erosion intensity is classified according to the magnitude of ΔM-DEM.There are five levels of classification: >0 cm is a deposition zone; 0 to (−1) cm is slight erosion; (−1) to (−2) cm is mild erosion; (−2) to (−3) cm is moderate erosion; and <(−3) cm is severe erosion (Wan et al., 2022).

2.4 CA-Markov modeling method

CA-Markov modeling was performed using IDRISI Selva version 18.0. In the Markov model, the system's state at a given time is only related to the previous state, and thus the Markov chain is realized by calculating the transition matrix of soil erosion intensity type changes over a certain period. This refers to the area of mutual conversion between soil erosion intensity types or the state transition probabilities (Zhang et al., 2021). The prediction formula for the probability of soil erosion intensity type changes is (Aguejdad, 2021):

$$S_{t+1} = P_{ij} S_t \tag{3}$$

S_t and S_{t+1} represent the soil erosion intensity types at time t and t + 1, respectively.

P_{ij}—the transfer probability matrix of soil erosion intensity types, i.e., the transfer probability of the soil erosion intensity type i to type j.

P_{ij} was obtained by overlaying data from two consecutive periods. Since the time interval between the two datasets is difficult to control, the transition probabilities need to be adjusted to match the predicted time length, which works well when simulating relatively uniform spatial changes (Yi et al., 2021). However, soil erosion is intense and varies greatly across time scales. If time length is used to adjust the transition probabilities, it becomes difficult to reflect the characteristics of soil erosion, resulting in low accuracy in the simulation results. Soil erosion is caused by hydraulic erosion, with the primary hydraulic force coming from surface runoff scouring after rainfall. Therefore, rainfall plays a decisive role in soil erosion. Therefore, this study uses rainfall to adjust the transition probabilities, and the formula is as follows:

$$P'_{ij} = 1 - e^{\frac{R'}{R} In\left(1-P_{ij}\right)}, i \neq j$$
$$P'_{ij} = 1 - \sum_{j=1}^{i\neq 1} P'_{ij}, i = j \tag{4}$$

Where P'_{ij} stands for the transfer probability after transformation, (%); R and R' denote the rainfall before and after transformation, respectively, (mm).

In Cellular Automata (CA), each variable only takes a finite number of states, and the rules governing state changes are local in both time and space (Zhang et al., 2023). Therefore, the CA model has strong spatial computing capabilities. The expression formula for the CA model is:

$$S_{t+1} = f\left(A_t, N\right) \tag{5}$$

Where A_t and A_{t+1}—finite and discrete state sets at time t and t + 1, respectively.

N—size of cellular filter.

f —cellular transformation rule in local space.

The CA-Markov model combines the features of two models, integrating them to complement each other's strengths. It fully utilizes the powerful spatial simulation capabilities of the CA model and the long-term prediction ability of the Markov model. In this paper, the specific process of using the CA-Markov model to simulate and predict the spatial evolution of soil erosion intensity is as follows (Figure 4):

(1) Create a suitability map set. The paper sets the variation patterns between vegetation patterns and soil erosion intensity types as limiting factors based on the variation rules of soil erosion intensity types on slopes with different vegetation patterns. Slope, elevation, and the conditional probability images of various soil erosion intensity transfers are used as constraints, in combination with the influence of constraints and limiting factors on the transformation of soil erosion intensity types. Evolution rules or standards are defined based on the suitability map set generated by the MCE and COLLECTION EDIT modules, and the state of a cell at the next time step is determined based on the suitability map set.
(2) Define the size of the cells and construct a cell filter. The cell size is the same as the raster image size, and in this study, the raster size is set to 2 mm × 2 mm.
(3) Determine the starting time and the number of CA cycles. The post-rainfall slopes with different vegetation patterns from the first period are used as the initial data, and the number of CA cycles is set to 1. Combined with the soil erosion intensity transfer probability matrix for different periods, the suitability map set is obtained based on the transformation rules. This allows the simulation of soil erosion intensity grade maps for slopes with different vegetation patterns after the third period of rainfall.

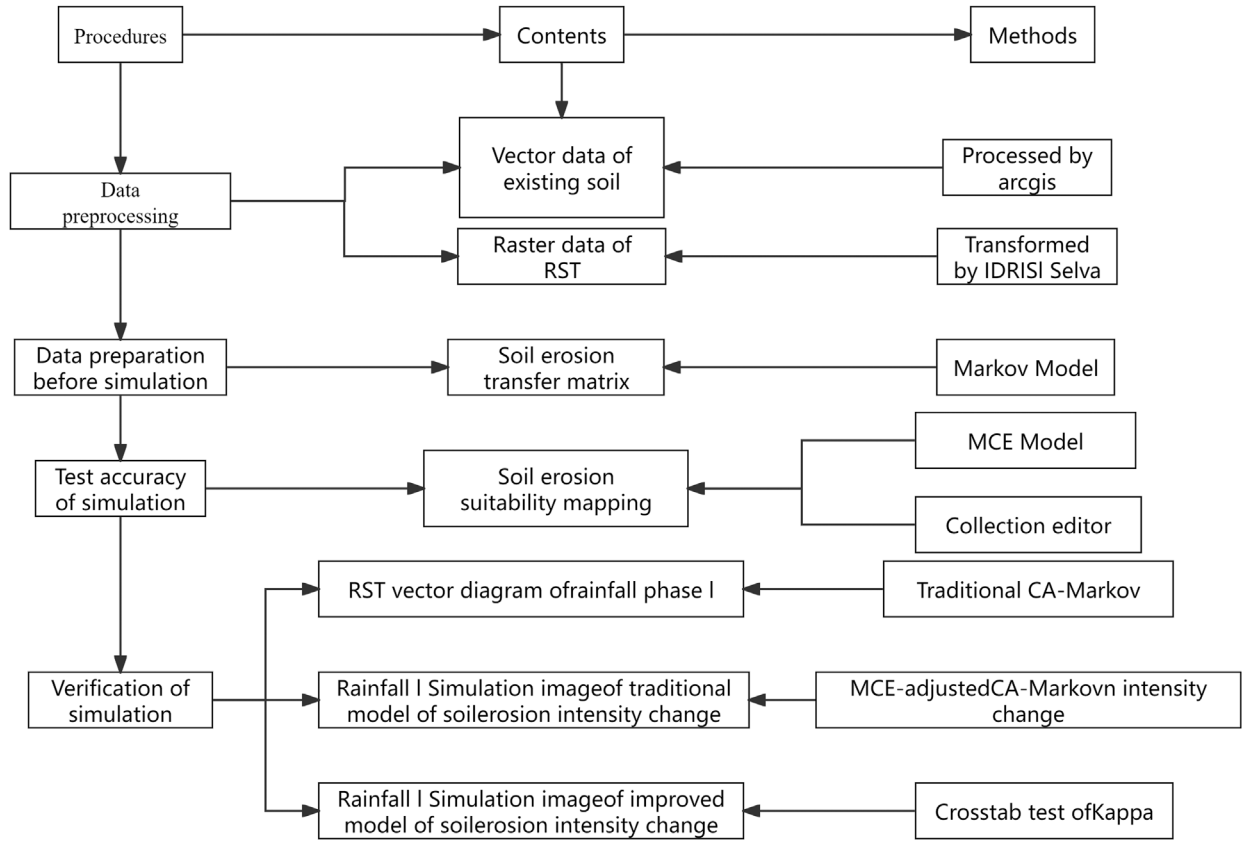

FIGURE 4
Flowchart of the soil erosion intensity change simulation method.

2.5 Evaluation of simulation accuracy

The Kappa consistency test is a method for verifying the accuracy of model results. This coefficient is a commonly used indicator to measure the accuracy of predicted results (Cai and Wang, 2020), which allows the analysis of simulation results from both quantitative and spatial perspectives. The formula for calculating the validation accuracy of simulation results is as follows:

$$kappa = \frac{P_0 - P_e}{1 - P_e} \quad (6)$$

Where Kappa—verification accuracy.

$p_e p_0$— overall simulation accuracy and theoretical simulation accuracy.

Kappa coefficient = 0-0.20 represents extremely low simulation accuracy; Kappa coefficient = 0.20–0.40 indicates ordinary simulation accuracy; Kappa coefficient = 0.40–0.60 denotes moderate simulation accuracy; Kappa coefficient = 0.60–0.80 stands for high simulation accuracy; Kappa coefficient = 0.80–1.00 reflects very high simulation accuracy.

2.6 Data processing

Statistical analysis of soil erosion intensity levels on slopes, under various vegetation patch patterns, was performed using ArcGIS 10.7.0.10450 software. Spatial overlay analysis of vegetation pattern and soil erosion intensity maps was conducted to determine the distribution of soil erosion in vegetation and non-vegetation areas on each slope. The classified micro-slope map and soil erosion intensity map were subsequently analyzed through spatial overlay to identify soil erosion distribution patterns at different slopes and reveal the micro-slope characteristics of soil erosion at varying gradients. Finally, the actual results were compared with the simulated data in ArcGIS to validate the accuracy of the simulated soil erosion intensity map under different vegetation patterns.

3 Results

3.1 Change analysis of slope soil erosion intensity

3.1.1 Analysis of area variation of soil erosion intensity on slope

As shown in Figure 5, following erosion on slopes with varying vegetation patch patterns, the eroded area is larger than the deposition area.

As shown in Figure 6, on the uniformly distributed slope, the areas of the non-erosive zone and slight erosion area both show an upward trend. Slight erosion area saw the most significant increase,

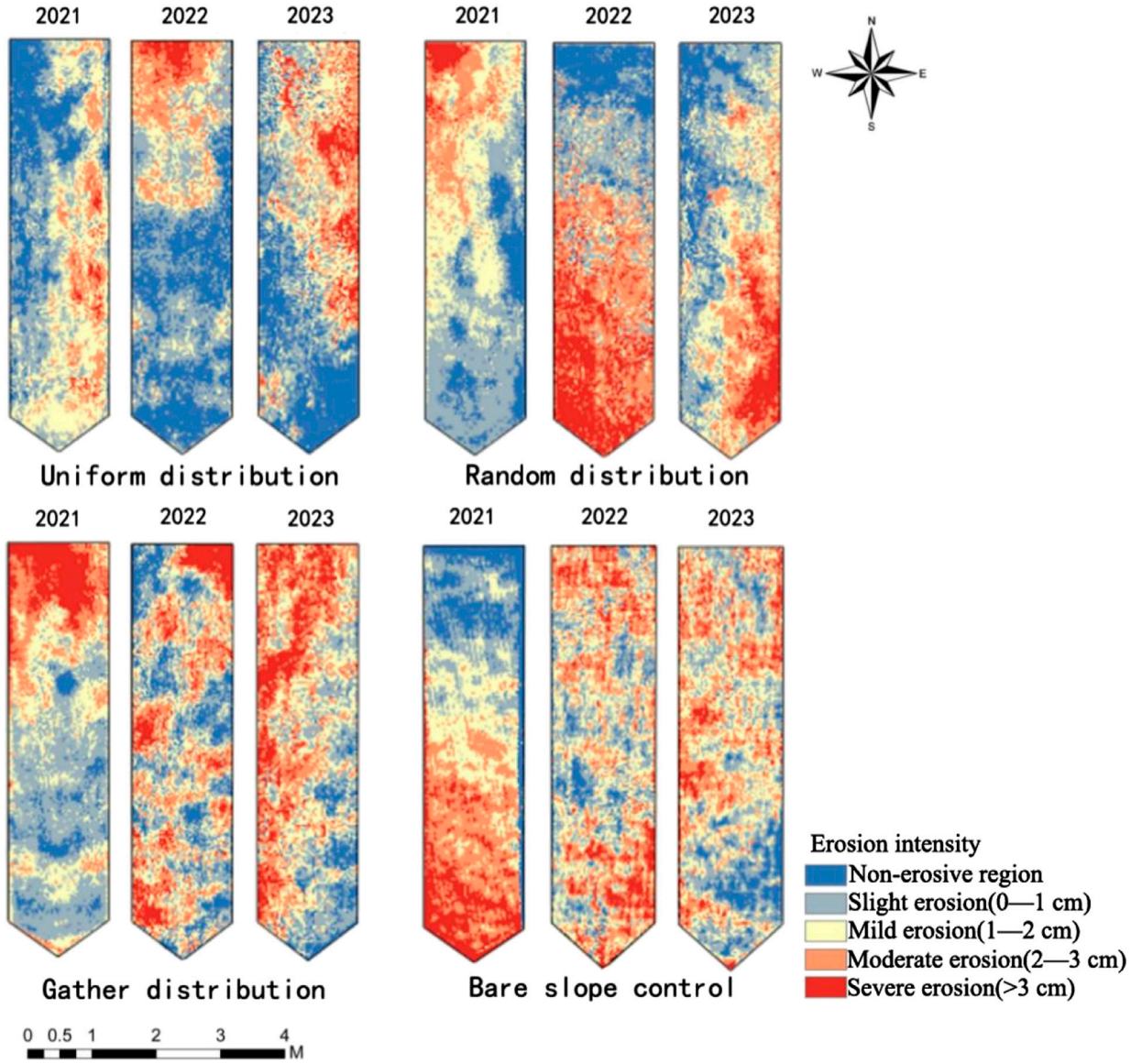

FIGURE 5
Grade map of slope soil erosion intensity in 2021–2023.

rising from 3.22 m^2 in 2011 to 3.76 m^2 in 2023, an increase of 0.54 m^2 or 3.10%. The areas of the mild erosion, moderate erosion, and severe erosion are all decreasing. On the randomly distributed slope, the areas of mild erosion and moderate erosion area both show an increasing trend. The moderate erosion area saw the most pronounced increase, rising from 3.08 m^2 in 2021 to 4.08 m^2 in 2023, an increase of 1.00 m^2 or 5.73%. However, the areas of the non-erosion zone, slight erosion area, and severe erosion area are all decreasing.

On the aggregate distribution slope, the areas of the non-erosive zone, moderate erosion area, and severe erosion area all exhibit an increasing trend. The severe erosion area saw the most significant growth, increasing from 1.67 m^2 in 2021 to 2.16 m^2 in 2023, an increase of 0.49 m^2 or 2.81%. However, the areas of the slight erosion and mild erosion are decreasing. On the bare slope control surface, the areas of the slight erosion and moderate erosion area both increased, with slight erosion area showing the most significant growth, rising from 2.22 m^2 in 2021 to 4.15 m^2 in 2023, an increase of 1.93 m^2 or 11.08%. However, the areas of the non-erosion zone, mild erosion area, and severe erosion area are all decreasing.

3.1.2 Analysis of the change of slope soil erosion intensity transfer direction

Figure 7 illustrates the changes in the transfer directions of soil erosion intensity on different slopes from 2021 to 2023. It provides a quantitative explanation of how the types of soil erosion intensity shift across slopes with varying vegetation patterns.

As shown in Figure 7, on slopes with uniform vegetation distribution, the non-erosive zone and the mild erosion area can only transition to slight erosion area or moderate erosion area. Slight erosion area can transition to any other zone, whereas the moderate erosion area can only transition to the non-erosive or mild erosion

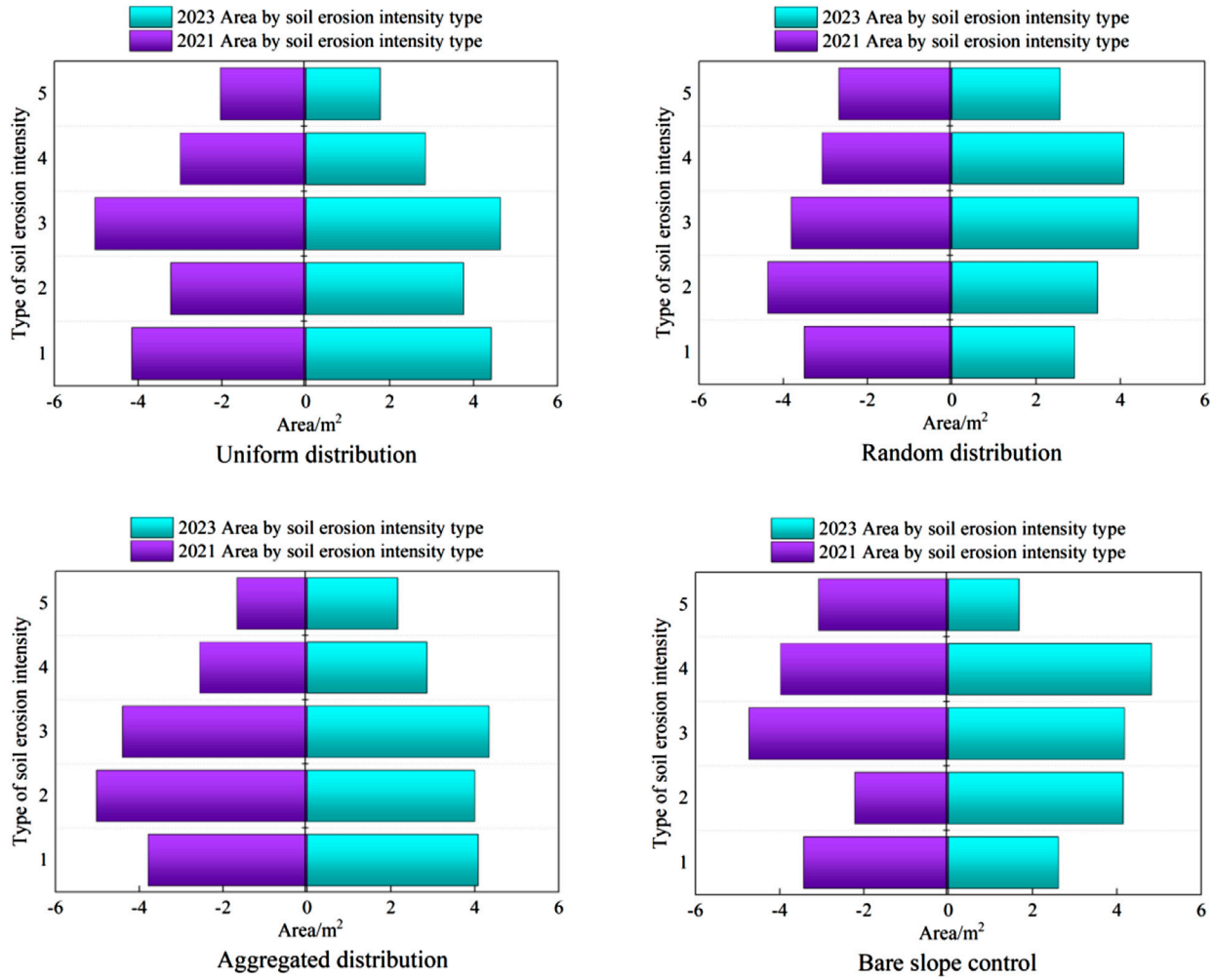

FIGURE 6
Area changes of soil erosion intensity on different slopes from 2021 to 2023. Note: 1, 2, 3, 4 and 5 are respectively non-erosive zones, slight erosion area, mild erosion area, moderate erosion area and severe erosion.

area. The severe erosion area transitions solely to the mild erosion area.

On slopes with random vegetation distribution, the non-erosive zone and the severe erosion area can only transition to slight erosion area or moderate erosion area. mild erosion area can transition to any zone, while the mild erosion area transitions only to the non-erosive, slight erosion area, and moderate erosion area. The moderate erosion area can only transition to the mild erosion area and severe erosion area.

On slopes with aggregate vegetation distribution, the non-erosive zone can only transition to the mild erosion area, moderate erosion area, or severe erosion area. Slight erosion area transitions only to the non-erosive, mild erosion area, or moderate erosion area, whereas the mild erosion area can transition to any zone. The moderate erosion area and severe erosion area transition only to slight erosion area or mild erosion area.

On the bare slope control surface, the non-erosive zone, mild erosion area, and severe erosion area can transition to any other zone. Slight erosion area can transition only to the non-erosive, mild erosion area, or moderate erosion area, while the moderate erosion area can transition only to slight erosion area, mild erosion area, or severe erosion area.

3.2 Analysis of influencing factors of slope soil erosion intensity

3.2.1 Superposition analysis of vegetation pattern and soil erosion intensity

Vegetation patterns can effectively impede sediment movement, thereby influencing slope soil erosion. Based on the vegetation distribution characteristics of each slope, areas are classified into vegetated and non-vegetated zones, and the patterns and characteristics of soil erosion in these zones are analyzed. As shown in Figure 8, on the uniformly distributed slope, the non-erosive zone and slight erosion area have the largest areas within the vegetated zone, measuring 2.87 m^2 and 3.01 m^2, respectively. The mild erosion area, moderate erosion area, and severe erosion area are largest in the non-vegetated area, at 2.88 m^2, 1.79 m^2, and 3.04 m^2, respectively. On the randomly distributed slope, the non-erosive

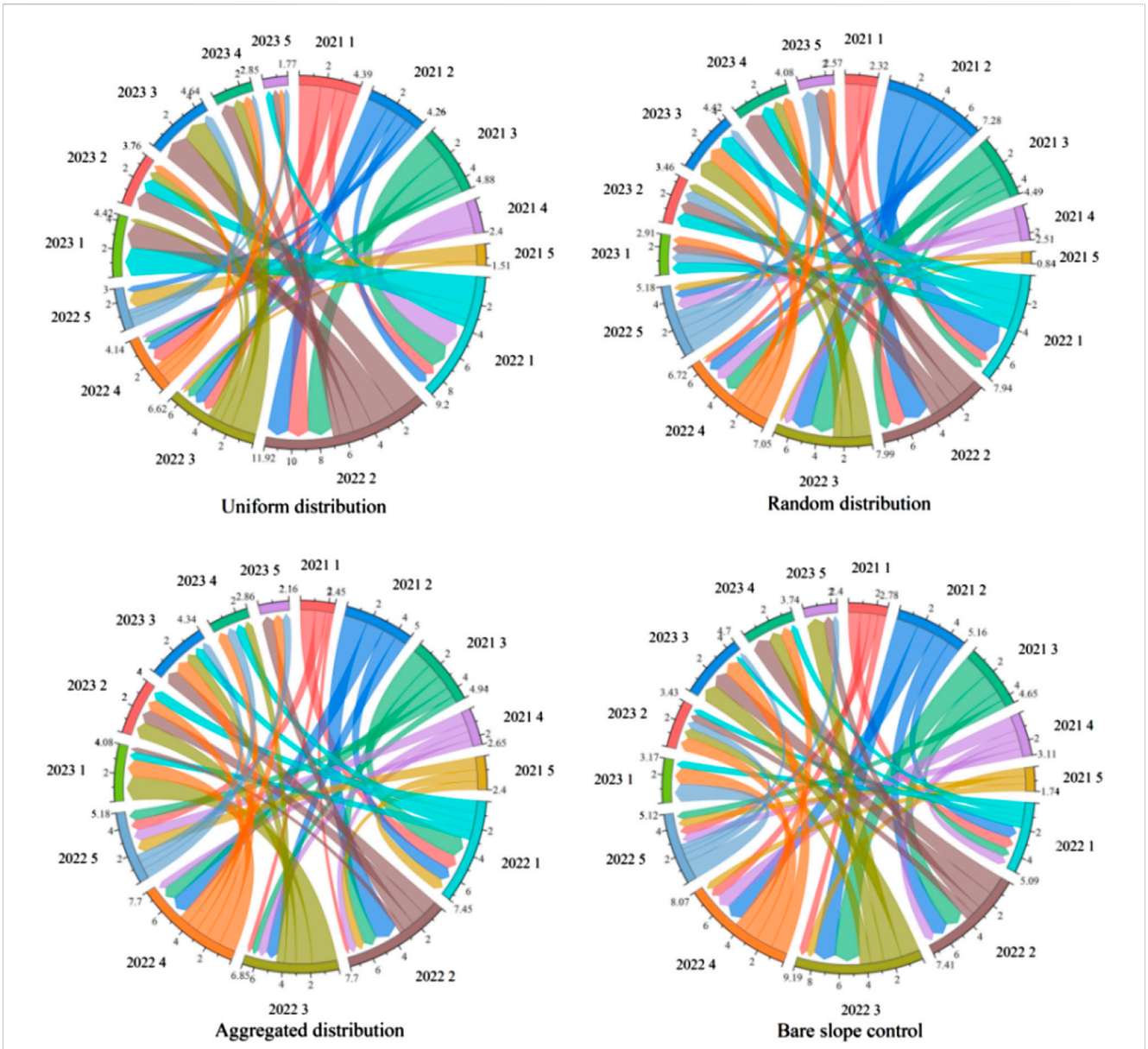

FIGURE 7
Transfer direction of soil erosion intensity.

zone and slight erosion area have the largest areas in the vegetated region (2.87 m^2, 3.01 m^2), while the mild erosion area, moderate erosion area, and severe erosion area are largest in the non-vegetated region (2.88 m^2, 1.79 m^2, 3.04 m^2). On the aggregate distribution slope, the non-erosive zone and the moderate erosion area have the largest areas in the vegetated region (2.87 m^2, 3.01 m^2). Slight erosion area, mild erosion area, and severe erosion area are largest in the non-vegetated region (2.88 m^2, 1.79 m^2, 3.04 m^2).

3.2.2 Superposition analysis of micro-slope and soil erosion intensity

As shown in Figure 9, on the uniformly distributed slope, the largest areas of the non-erosive zone, slight erosion area, mild erosion area, moderate erosion area, and severe erosion area occur on micro-slopes of 20°–30°, 0°–10°, 20°–30°, 40°–50°, and 40°–50°, respectively, with areas of 1.20 m^2, 1.12 m^2, 1.38 m^2, 1.23 m^2, and 0.87 m^2. On the randomly distributed slope, the largest areas of the non-erosive zone, slight erosion area, mild erosion area, moderate erosion area, and severe erosion area are found on micro-slopes of 20°–30°, 30°–40°, 10°–20°, 10°–20°, and 30°–40°, respectively, with areas of 1.25 m^2, 1.38 m^2, 1.12 m^2, 0.96 m^2, and 0.82 m^2. On the aggregate distribution slope, the largest areas of the non-erosive zone, slight erosion area, mild erosion area, moderate erosion area, and severe erosion area are found on micro-slopes of 30°–40°, 10°–20°, 20°–30°, 0°–10°, and 40°–50°, respectively, with areas of 1.52 m^2, 1.58 m^2, 1.06 m^2, 0.60 m^2, and 0.50 m^2. On the bare slope control surface, the largest areas of the non-erosive zone, slight erosion area, mild erosion area, moderate erosion area, and severe erosion area are on micro-slopes of 10°–20°, 20°–30°, 0°–10°, 30°–40°, and 40°–50°, respectively, with areas of 1.18 m^2, 0.92 m^2, 1.77 m^2, 1.58 m^2, and 1.33 m^2.

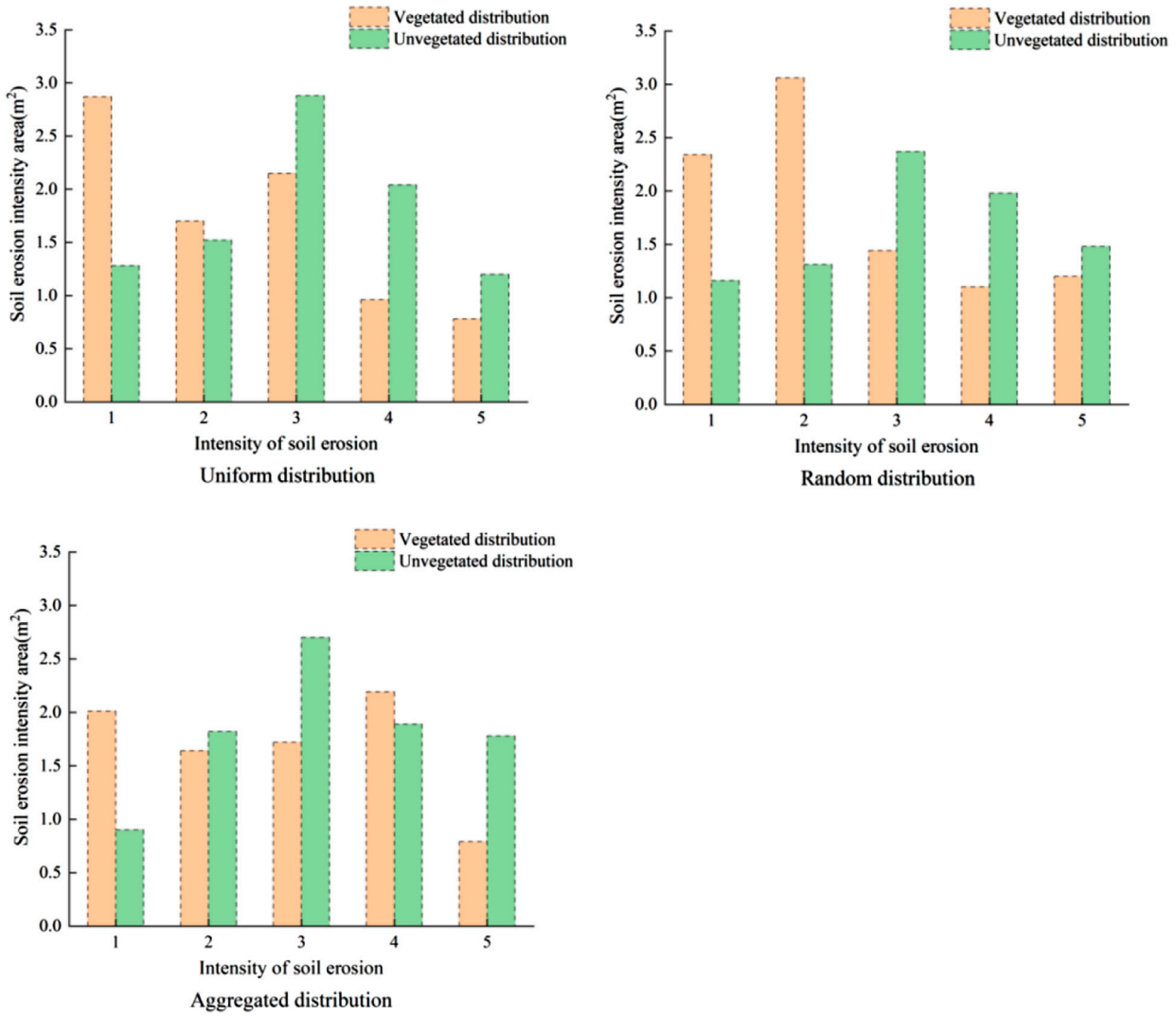

FIGURE 8
Soil erosion distribution in vegetated and non-vegetated areas.

3.2.3 Superposition analysis of micro-slope direction and soil erosion intensity

The micro-slope directions were reclassified into four ranges: north to northeast (337.5°–22.5°), east to southeast (22.5°–67.5°), south to southwest (157.5°–202.5°), and west to northwest (247.5°–337.5°). As shown in Figure 10, on the uniformly distributed slope, the largest upward distribution areas of the non-erosive zone, slight erosion area, mild erosion area, moderate erosion area, and severe erosion area are found in the north-northeast, east-southeast, east-southeast, west-northwest, and south-southwest, respectively, with areas of 1.38 m^2, 1.05 m^2, 1.47 m^2, 1.32 m^2, and 0.77 m^2. On the randomly distributed slope, the largest upward distribution areas of the non-erosive zone, slight erosion area, mild erosion area, moderate erosion area, and severe erosion area are found in the west-northwest, south-southwest, east-southeast, north-northeast, and south-southwest, respectively, with areas of 1.25 m^2, 1.43 m^2, 1.22 m^2, 0.99 m^2, and 0.91 m^2. On the aggregate distribution slope, the largest upward distribution areas of the non-erosive zone, slight erosion area, mild erosion area, moderate erosion area, and severe erosion area are found in the north-northeast, west-northwest, east-southeast, east-southeast, and south-southwest, respectively, with areas of 1.36 m^2, 1.77 m^2, 1.81 m^2, 1.00 m^2, and 0.72 m^2. On the bare slope control surface, the largest areas of the non-erosive zone, slight erosion area, mild erosion area, moderate erosion area, and severe erosion area are found in the east-southeast, south-southwest, north-northeast, west-northwest, and south-southwest, respectively, with areas of 1.19 m^2, 0.77 m^2, 1.63 m^2, 1.34 m^2, and 1.37 m^2.

3.3 Simulation and precision inspection of slope soil erosion intensity

3.3.1 Markov transfer probability matrix

In this study, rainfall is very important as an indicator of the corrected transfer probability. The rainfall corresponding to the 3-year soil erosion data (29 August 2021–10 August 2023) was

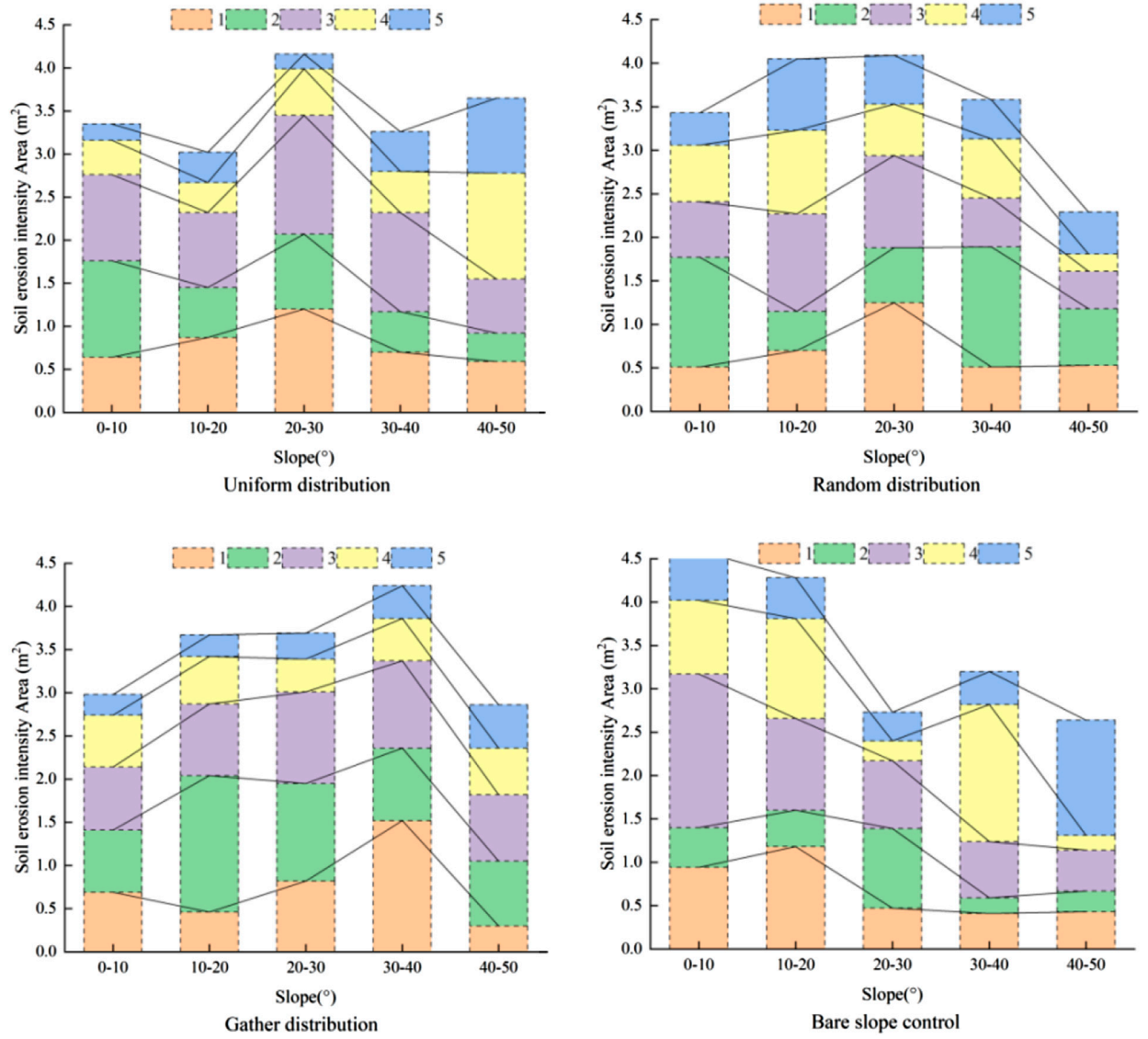

FIGURE 9
Micro slope characteristics of soil erosion distribution.

recorded by a siphon self-counting rain gauge. Firstly, the transfer probability matrix of 29 August 2021 and 3 September 2022 is calculated, and the conversion is carried out according to the rainfall during this period and the rainfall from 3 September 2022 to 10 August 2023. The transfer probability matrix for 29 August 2021 and 3 September 2022 is converted into the transfer probability matrix for 3 September 2022–10 August 2023, as shown in Table 3 (Equations 3, 4).

3.3.2 Analysis of suitability rules of slope soil erosion intensity types

Soil erosion intensity types, vegetation distribution areas, micro-slope, and micro-aspect are key factors that influence the soil erosion process. These factors interact according to specific rules and mechanisms, determining both the intensity and spatial distribution of soil erosion in different regions. When formulating suitability rules, it is important to consider the protective effect of different vegetation types and distribution patterns on areas with varying erosion intensities. Erosion intensity types are classified according to slope steepness, while changes in micro-slope lead to variations in local erosion intensity. Micro-aspect, referring to the orientation of the slope surface, directly affects water flow direction, sunlight exposure, and rainfall distribution. Therefore, variations in micro-aspect must also be considered when developing soil erosion intensity suitability rules. Therefore, these factors are treated as constraints, and to ensure objectivity in evaluation, Boolean mapping (where areas outside the scope of consideration are assigned a value of 0, and areas to be considered are assigned a value of 1) is employed in MCE (Multi-Criteria Evaluation). For each type of soil erosion intensity, locations where transformation is not possible are set to 0, while those where transformation is possible are set to 1. This process involves analyzing the suitability rules for soil erosion intensity on different slopes and generating suitability

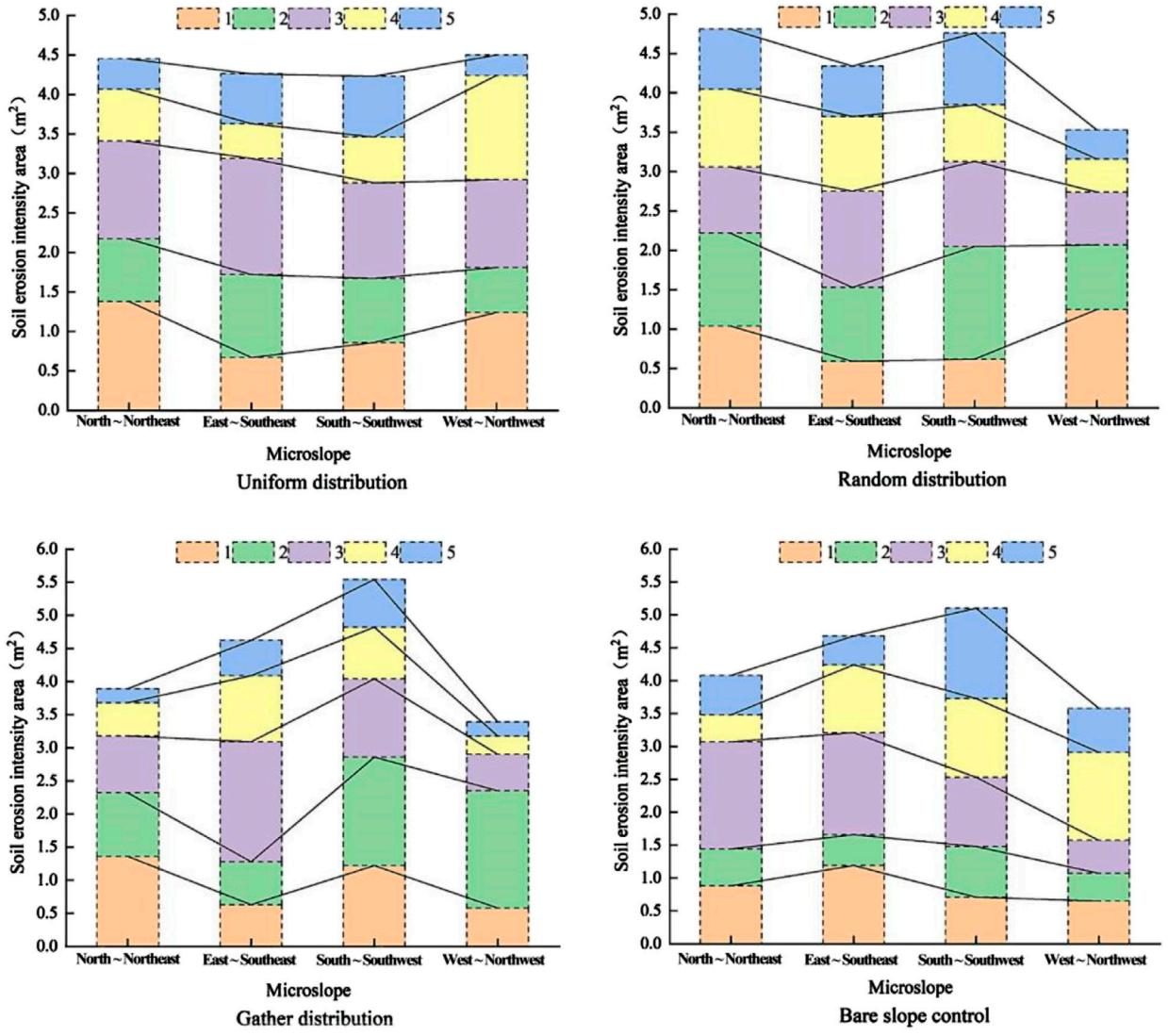

FIGURE 10
Micro-slope characteristics of soil erosion distribution.

maps for different soil erosion intensity types (Figure 11). Taking the uniform distribution of vegetation pattern as an example:

(1) Rules for the conversion of non-erosive zones.
① Limitations: Restrict conversion to >3 cm erosive zones (0 for >3 cm, 1 for others).
② The area with a slight slope of 20°–30° is designated as a suitable development area for non-erosion areas (1 for this range, 0 otherwise).
③ The area with a micro-slope direction of north to northeast is designated as a suitable development area of non-erosion area (1 for these directions, 0 otherwise).
④ The area with vegetation distribution is designated as a non-erosion area suitable for development (1 for vegetated, 0 otherwise).

(2) Rule of 0–1 cm erosion zone (slight erosion area) conversion.
① Conversion Flexibility: No restrictions on conversion (all zones set to 1).
② The area with a slight slope of 0°–10° is designated as the suitable development area of the erosion area of 0–1 cm (1 within this range, 0 otherwise).
③ The area with micro-slope direction from east to southeast is designated as the suitable development area of slight erosion area (1 within this range, 0 otherwise).
④ The area with vegetation distribution is designated as the suitable development area of slight erosion area (1 within this range, 0 otherwise).

(3) Conversion rules of 1–2 cm erosion zone (mild erosion area).
① Limitations: Restrict conversion to >3 cm zones (0 for >3 cm, 1 for others).
② The area with a slope of 20°–30° is designated as a suitable development area of mild erosion area (1 within this range, 0 otherwise).
③ The area with micro-slope direction from east to southeast is designated as the suitable development

TABLE 3 Type transfer probability matrix of slope soil erosion on slopes (m^2).

Distribution mode	2021/2022	1	2	3	4	5	2022/2023	1	2	3	4	5
Uniform distribution	1	0.168	0.287	0.159	0.217	0.000	1	0.329	0.226	0.000	0.000	0.154
	2	0.290	0.407	0.155	0.116	0.213	2	0.324	0.194	0.242	0.174	0.224
	3	0.430	0.336	0.121	0.085	0.000	3	0.257	0.268	0.293	0.215	0.000
	4	0.398	0.000	0.119	0.088	0.000	4	0.000	0.256	0.000	0.169	0.127
	5	0.000	0.000	0.115	0.000	0.165	5	0.000	0.000	0.319	0.229	0.044
Random distribution	1	0.137	0.193	0.000	0.189	0.000	1	0.089	0.274	0.310	0.238	0.000
	2	0.146	0.249	0.279	0.245	0.143	2	0.074	0.150	0.000	0.291	0.188
	3	0.148	0.242	0.254	0.252	0.000	3	0.000	0.283	0.254	0.232	0.000
	4	0.000	0.000	0.270	0.203	0.263	4	0.174	0.000	0.344	0.131	0.009
	5	0.000	0.000	0.217	0.136	0.152	5	0.264	0.386	0.204	0.000	0.021
Gather distribution	1	0.137	0.193	0.261	0.000	0.237	1	0.081	0.234	0.243	0.271	0.000
	2	0.146	0.249	0.279	0.245	0.211	2	0.043	0.192	0.280	0.000	0.186
	3	0.148	0.242	0.254	0.252	0.269	3	0.182	0.215	0.259	0.295	0.000
	4	0.000	0.229	0.270	0.203	0.000	4	0.153	0.234	0.330	0.223	0.144
	5	0.151	0.265	0.000	0.000	0.152	5	0.000	0.000	0.306	0.360	0.159
Bare slope control	1	0.261	0.000	0.116	0.372	0.356	1	0.207	0.112	0.314	0.420	0.000
	2	0.391	0.331	0.086	0.135	0.000	2	0.000	0.127	0.355	0.390	0.114
	3	0.020	0.303	0.107	0.000	0.192	3	0.000	0.280	0.324	0.285	0.175
	4	0.017	0.135	0.000	0.269	0.203	4	0.135	0.353	0.324	0.141	0.000
	5	0.000	0.000	0.100	0.197	0.687	5	0.145	0.343	0.200	0.000	0.124

area of mild erosion area (1 within this range, 0 otherwise).

④ The vegetation distribution area is designated as the suitable development area of mild erosion area (1 within this range, 0 otherwise).

(4) Conversion rules of 2–3 cm erosion zone (moderate erosion area).

① Limitations: Restrict conversion to slight erosion area and >3 cm zones (0 for these, 1 for others).

② The area with a slight slope of 40°–50° is designated as a suitable development area of moderate erosion area (1 within this range, 0 otherwise).

③ The area with micro-slope direction from west to northwest is designated as the suitable development area of moderate erosion area (1 within this range, 0 otherwise).

④ The non-vegetation distribution area is designated as the suitable development area of moderate erosion area (1 within this range, 0 otherwise).

(5) >3 cm erosion zone (severe erosion area) conversion rules.

① Limitations: Restrict conversion to non-erosion, slight erosion area, and moderate erosion area (0 for these, 1 for others).

② The area with a slight slope of 40°–50° is designated as the suitable development area of the erosion area of >3 cm (1 within this range, 0 otherwise).

③ The area with a micro-slope direction of south to southwest is designated as the suitable development area of the erosion area of >3 cm (1 within this range, 0 otherwise).

④ The non-vegetation distribution area is designated as the suitable development area of the erosion area of >3 cm (1 within this range, 0 otherwise).

3.3.3 Simulation of slope soil erosion intensity

Based on the data preparation outlined above, the simulation of the 2023 soil erosion intensity grade charts for different slopes was conducted, with the resulting charts displayed in Figure 12 (Equation 5). As shown in Figure 12, the spatial layout of the actual soil erosion intensity grade diagram generally aligns with that of the simulated diagram. The uniformly distributed slope remains dominated by the mild erosion area, while the randomly distributed slope primarily transitions from the mild erosion area to the moderate erosion area. The aggregate slope shifted from the mild erosion area to slight erosion area, while the bare slope continues to be dominated by the moderate erosion area.

The simulated results were further compared with the actual areas of soil erosion intensity types (Figure 13). As shown in Figure 13, on the uniformly distributed slope, the simulated areas of slight erosion area, mild erosion area, and severe erosion area all increased, with the severe erosion area showing the largest increase (0.71 m^2). Conversely, the areas of the non-erosive zone and

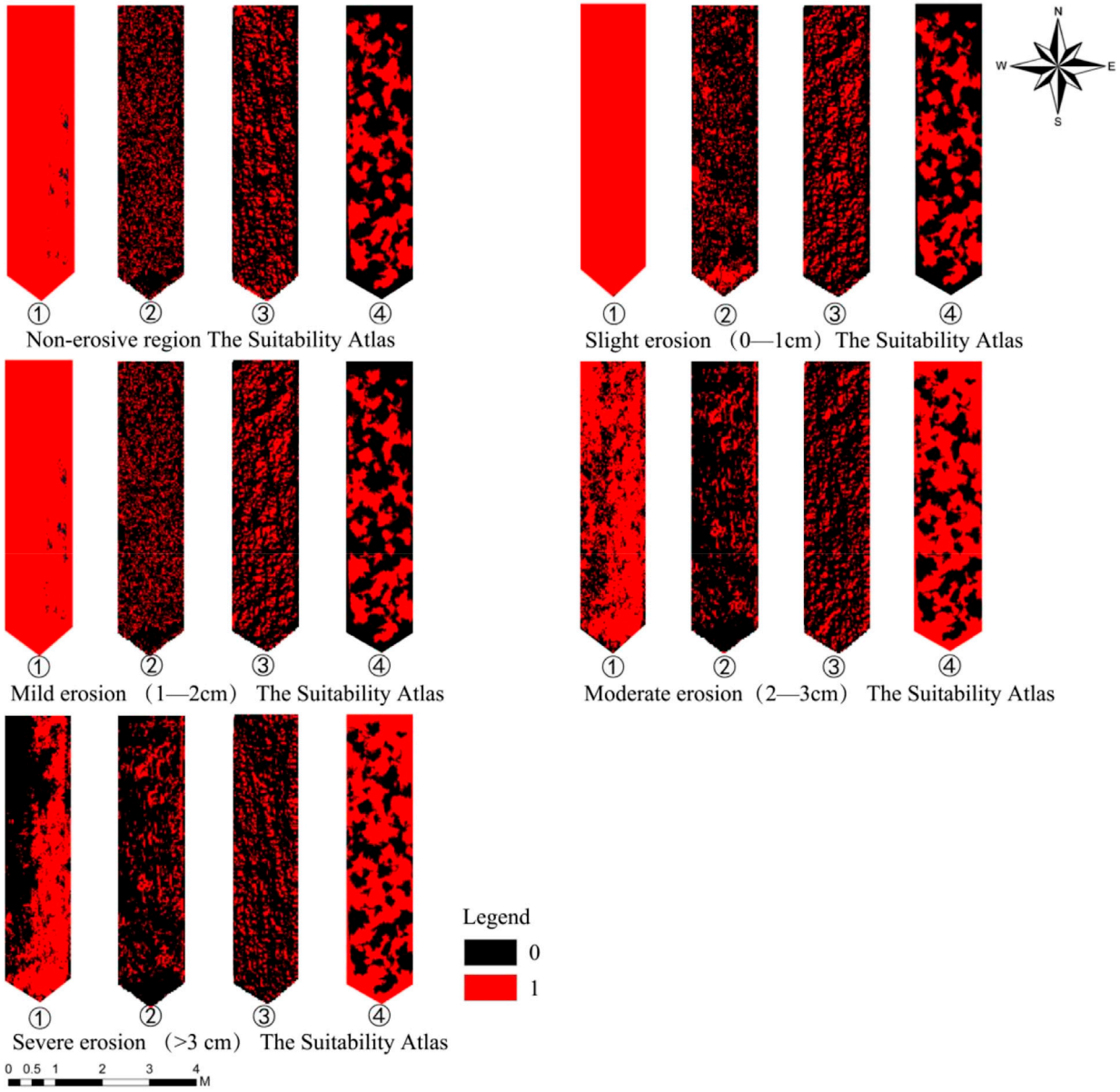

FIGURE 11
Suitability atlas of evenly distributed soil erosion intensity types.

moderate erosion area decreased, with the moderate erosion area experiencing the most significant decrease (0.9 m^2). On the randomly distributed slope, the simulated areas of the non-erosive zone, slight erosion area, moderate erosion area, and severe erosion area all increased, with the moderate erosion area showing the greatest increase (0.42 m^2). Meanwhile, the area of the mild erosion area decreased by 1.15 m^2. On the aggregate distribution slope, the simulated areas of slight erosion area, moderate erosion area, and severe erosion area all increased, with the moderate erosion area experiencing the largest increase (0.69 m^2). In contrast, the areas of the non-erosive zone and the mild erosion area both decreased significantly (0.72 m^2). On the bare slope control surface, the simulated areas of the non-erosive zone and severe erosion area increased, with the severe erosion area showing the greatest increase (0.73 m^2). In contrast, the areas of slight erosion, mild erosion area, and moderate erosion area zone decreased, with the moderate erosion area experiencing the largest decrease (0.49 m^2).

3.3.4 Simulation accuracy test

The soil erosion intensity grade map of different slopes in 2023 was simulated, and the accuracy of the simulation was tested by using the measured data of soil erosion intensity of different slopes in 2023. As shown in Table 4, the Kappa coefficients for soil erosion intensity simulation (Equation 6) on the uniformly distributed slope, randomly distributed slope, aggregate distributed slope, and control slope were 65.24%, 73.62%, 75.88%, and 69.06%, respectively. These values indicate a

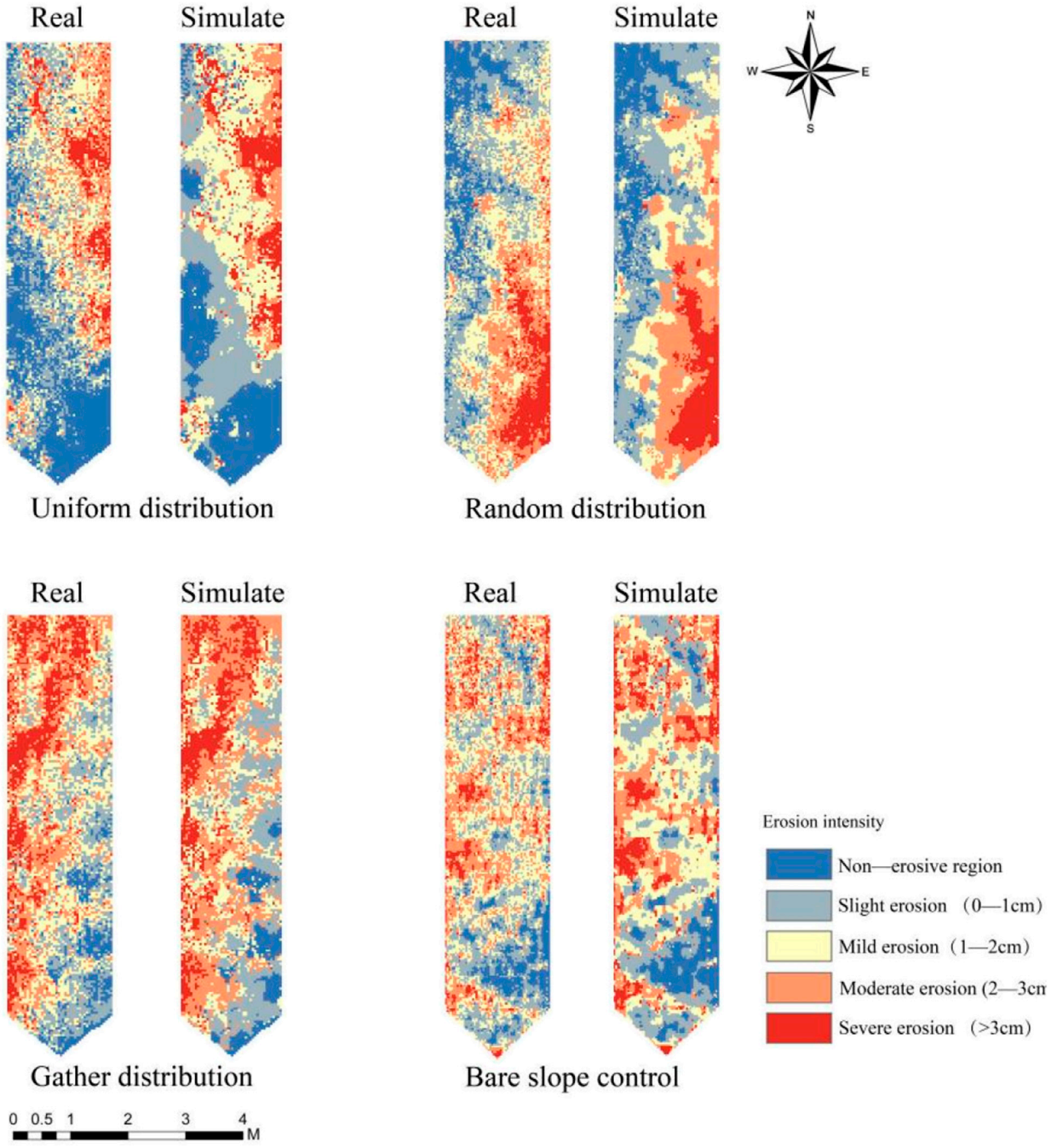

FIGURE 12
Simulation of soil erosion intensity levels.

good fit and suggest that the simulated data effectively represents the mutual transformation trends among various types. This indicates that the model can predict future changes in soil erosion intensity.

The accuracy of slight erosion area is high at 92.02%, while the accuracies of the moderate erosion area and severe erosion area are lower at 68.42% and 59.89%, respectively. The simulation accuracies for the non-erosive zone, moderate erosion area, and severe erosion area were higher, reaching 91.41%, 90.69%, and 96.11%, respectively. In contrast, the accuracies of slight erosion area and mild erosion area are lower, at 87.86% and 73.98%, respectively. The simulation accuracies for the non-erosive zone, slight erosion area, and severe erosion area are notably high, reaching 99.02%, 98.75%, and 99.07%, respectively. In contrast, the accuracies of the mild erosion area and moderate erosion area are lower, at 83.41% and 75.87%, respectively. The simulation accuracies for the non-erosive zone, slight erosion area, mild erosion area, and moderate erosion area are higher than those for the bare slope, reaching 91.8%, 96.39%, 92.11%, and 89.83%, respectively. Conversely, the accuracy of the severe erosion area is lower, at only 56.55%.

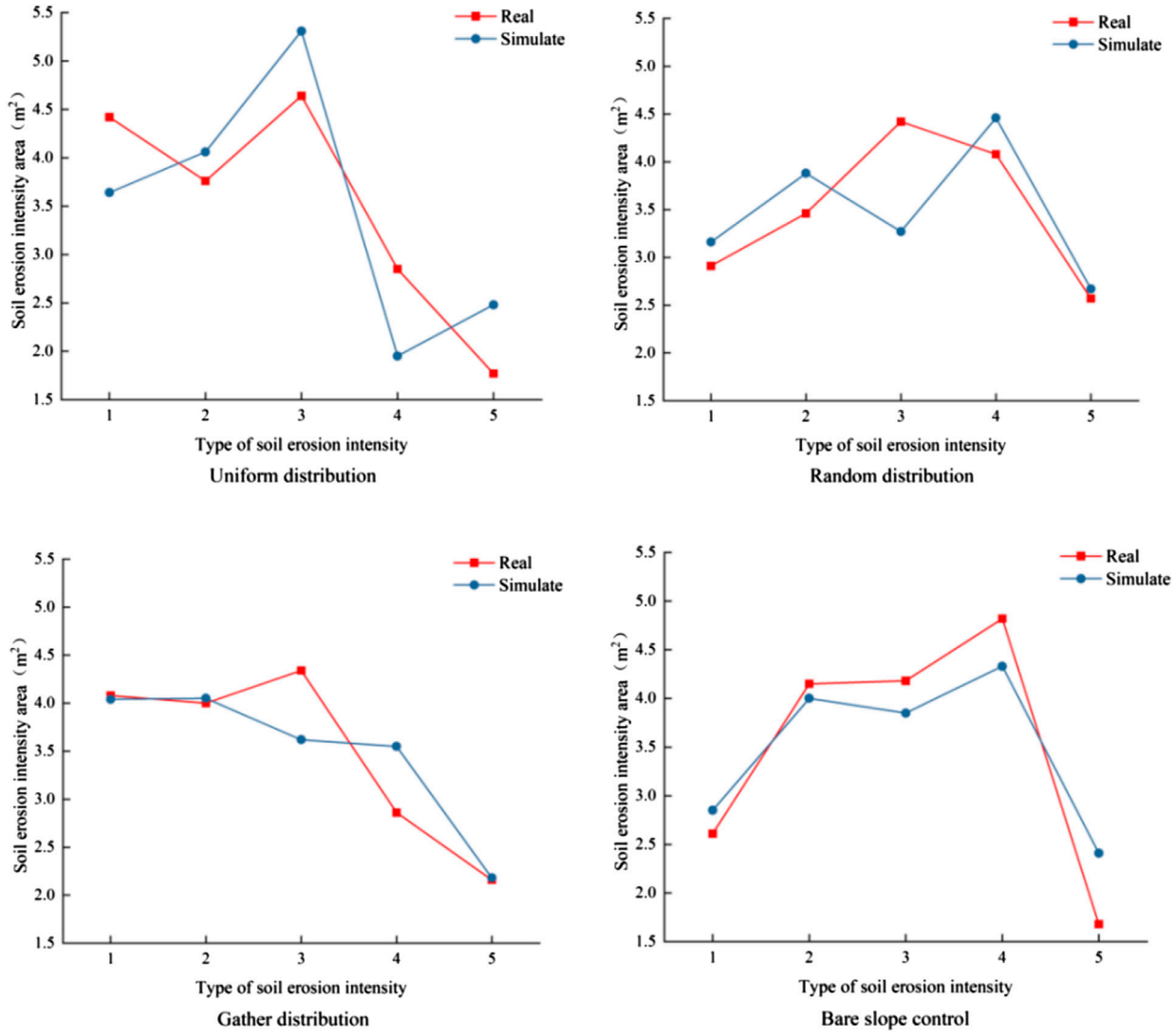

FIGURE 13
Comparison of simulated area of soil erosion intensity.

4 Discussion

4.1 Applicability of MCE-CA-Markov model

Slope is a fundamental component of soil erosion control and research within a basin or region. The occurrence, development, and evolution of soil erosion on slopes are complex phenomena, with vegetation being the primary factor influencing the erosion process. However, current research on soil erosion on slopes with vegetation patterns primarily focuses on post-event control measures. Relatively few studies have been conducted on simulating soil erosion on slopes with vegetation patch patterns (Chen, 2006). Typically, soil erosion intensity is simulated using the RUSLE equation as a variable. He et al. (2014) analyzed the soil erosion status of three experimental plots and two control plots under three rainfall conditions, applying the CA-Markov method to simulate soil erosion across five plots (Sun and Deng, 2015). The results were very close to the observed outcomes. This approach not only offers a novel idea and method for simulating slope soil erosion but also serves as a reference for vegetation management in controlling slope erosion.

The CA-Markov model is empirical, predicting changes in the subsequent period based on prior changes. This model treats the simulated ecological process as uniform, with rainfall serving as the primary driving force for soil erosion, which varies significantly over time. Consequently, this study employs a method to fit the characteristics of runoff, sediment yield, and rainfall for different slopes. The results indicated that rainfall, runoff, and sediment yield had the most significant effects. Therefore, rainfall was chosen to replace the time step in the modified transfer probability matrix (Ji et al., 2019), and the multi-criteria evaluation method in IDRISI was utilized to integrate various influencing factors, completing the simulation of the spatial evolution of soil erosion intensity changes across different vegetation patch patterns on slopes.

The Kappa coefficients for the simulated maps of soil erosion intensity for uniform distribution, random distribution, aggregate distribution, and bare slope control were 65.24%, 73.62%, 75.88%,

TABLE 4 Simulation and accuracy test of slope soil erosion intensity on slopes.

Slope	Type of soil erosion intensity	Real	Simulation	Contrast of area		Kappa coefficient %
		Area/m^2	Area/m^2	Area difference/m^2	Precision %	
Uniform distribution	Non-erosive region	4.42	3.64	−0.78	82.35	
	Slight erosion	3.76	4.06	0.30	92.02	
	Mild erosion	4.64	5.31	0.67	85.56	65.24
	Moderate erosion	2.85	1.95	−0.9	68.42	
	Severe erosion	1.77	2.48	0.71	59.89	
Random distribution	Non-erosive region	2.91	3.16	0.25	91.41	
	Slight erosion	3.46	3.88	0.42	87.86	
	Mild erosion	4.42	3.27	−1.15	73.98	73.62
	Moderate erosion	4.08	4.46	0.38	90.69	
	Severe erosion	2.57	2.67	0.10	96.11	
Gather distribution	Non-erosive region	4.08	4.04	−0.04	99.02	
	Slight erosion	4.00	4.05	0.05	98.75	
	Mild erosion	4.34	3.62	−0.72	83.41	75.88
	Moderate erosion	2.86	3.55	0.69	75.87	
	Severe erosion	2.16	2.18	0.02	99.07	
Bare slope control	Non-erosive region	2.61	2.85	0.24	91.80	
	Slight erosion	4.15	4.00	−0.15	96.39	
	Mild erosion	4.18	3.85	−0.33	92.11	69.06
	Moderate erosion	4.82	4.33	−0.49	89.83	
	Severe erosion	1.68	2.41	0.73	56.55	

and 69.06%, respectively. These results demonstrate that the MCE-CA-Markov model is effective for simulating the evolution of soil erosion, with high simulation accuracy. However, when simulating slopes under 3 years of erosion conditions, the model assumes that the effects of slope length and soil erodibility (K value) are uniform across all slopes. It only considers several factors, including rainfall, soil transformation status, vegetation patch patterns, micro-slope, and micro-slope orientation. Among these factors, soil transformation status pertains to the transfer of various soil erosion intensity types. Internal transfers are frequent, and the vegetation patch pattern, micro-slope, and micro-slope direction interact with soil erosion intensity to establish rules based on the most suitable areas for each type of soil erosion intensity. Consequently, the naming rules are somewhat subjective, introducing a degree of instability into the simulation. This leads to relatively large errors in the simulation results of the CA-Markov model (Sun and Deng, 2015).

Since simulation research on slope soil erosion is still in an exploratory phase, some theoretical methods remain underdeveloped. The Pisha sandstone area is characterized by unique eroded soil and semi-arid climate, providing a unique test site. However, due to differences in soil erodibility, cohesion and hydraulic properties, the performance of the model in other environments (e.g., wet, clay-rich soils or dry sandy land) may vary. For example, in areas with high clay content, the soil is not easily moved by rainfall immediately, but may experience slow and continuous erosion under saturated conditions. Integrating soil composition factors (such as clay and organic matter content) in the model can improve adaptability and enable more accurate erosion simulation in different landscapes. To address these shortcomings, the author plans to use MCE to spatialize additional data and integrate it into conversion rules for creating suitability maps in future research. Adjusting the cell size to the most appropriate grid dimension could significantly enhance the accuracy of the simulation (Zhao et al., 2013).

4.2 Difference analysis of simulation accuracy of soil erosion intensity on slopes

The simulation revealed that the erosion area of severe erosion increased the most on both the uniformly distributed slope (0.71 m^2) and the bare control slope (0.73 m^2). In contrast, the simulated erosion area of moderate erosion increased the most on the randomly distributed slope (0.42 m^2) and the aggregated distributed slope (0.69 m^2). Generally, the simulated areas of different slopes show the most significant increase in the >2 cm erosion zone. This trend occurs because, during model simulation,

as rainfall causes erosion, the model tends to simulate a transformation from lower to higher erosion zones. Consequently, the simulated area of the higher erosion zone is much greater than the actual area.

The results indicate significant differences in the simulation precision of soil erosion intensity across different slopes. In comparison to other slopes, the Kappa coefficient for the soil erosion intensity grade simulation map of uniformly distributed slopes is relatively low at 65.24%. This is attributed to the more frequent internal transfers occurring on uniformly distributed slopes during the third phase of rainfall (Nikolaos et al., 2020). This introduces some instability into the simulation, leading to reduced accuracy in the simulated soil erosion intensity grade map. Table 4 shows that the simulation accuracies for slight erosion area on uniformly distributed, randomly distributed, clustered distributed, and bare control slopes are 92.02%, 87.86%, 98.7 5%, and 96.39%, respectively. Overall, the simulation accuracy of slight erosion area across different slopes is generally high. This is because slight erosion area represents a low-intensity erosion zone, which typically does not transform into a lower intensity zone after erosion (Mohamed et al., 2021). As a result, it remains relatively stable, whereas other zones can simultaneously transform into erosion zones with varying degrees of intensity after different erosion levels, leading to scattered cellular state changes and added uncertainties. Consequently, its interaction with other erosion areas is more complex, resulting in lower simulation accuracy.

In addition to the factors considered in the model, there may be other influences. The accuracy of the model may be affected by root structure, as plants with deeper roots can significantly reduce erosion, even on slopes with minimal vegetation coverage (Feng et al., 2018; Yu et al., 2019). Further investigation into root density and structure as anti-erosion factors could improve the model, particularly in areas with more variable root systems, such as aggregated and random vegetation patterns. Moreover, the Pisha sandstone region exhibits complex soil dynamics, influenced by the composition of sand and silt, which vary in their resistance to erosion. Incorporating soil composition parameters, such as clay content or organic matter, may enhance the accuracy of simulations for areas with high erosion intensity (Rodrigo-Comino et al., 2018; Gong et al., 2023). In conclusion, although the MCE-CA-Markov model successfully simulates erosion trends for different slope types, addressing the aforementioned factors could improve the accuracy of predictions for high-erosion intensity areas and provide a more detailed understanding of soil erosion dynamics under varying environmental conditions. Future research could integrate these factors to provide a more comprehensive erosion simulation framework, applicable to complex landscapes such as the Pisha sandstone region.

4.3 Effects of vegetation patch pattern on soil erosion on slope

The patch pattern of vegetation has a significant impact on the soil erosion process on slopes. Different vegetation distribution patterns regulate soil erosion by altering the flow paths of water and the movement of sediments. In this study, soil erosion intensity is lower on slopes with uniformly distributed vegetation patches. This may be due to the changes in the hydrological connectivity of the slope surface. The uniform distribution pattern is more evenly distributed and more dispersed than the aggregated and random distribution patterns. The hydrological connectivity of vegetation in this pattern is the weakest, meaning that the uniform distribution of vegetation fragments the slope more, making it easier for water and sediment flow to be intercepted by vegetation patches (Tang et al., 2021). As a result (Figure 5), the effective space for erosion on the slope is reduced, leading to increased soil accumulation. This results in a higher soil infiltration rate and a significant reduction in runoff and sediment production during the erosion process. This effectively reduces the transport of coarse sediments and obstructs the direct flow paths of water. In contrast, vegetation patches in random distribution are more likely to form irregular flow channels, leading to increased erosion intensity in localized areas. During heavy rainfall, water flow converges between randomly distributed vegetation patches, resulting in uneven distribution of erosion patches and potentially forming localized areas of high erosion intensity (Huang et al., 2017). Compared to the previous two vegetation patterns, aggregated vegetation communities typically consist of larger patches. These larger patches increase water retention time and promote downward water infiltration, thereby reducing erosion rates. Therefore, aggregated vegetation patches effectively trap larger particles, reducing the downslope movement of sediments (Zhao et al., 2020; Liu et al., 2018). Consequently, this characteristic makes the optimized layout of aggregated distribution highly significant for the practical application of soil and water conservation.

Additionally, this study found that after rainfall, the terrain factors on uniformly distributed slopes showed the smallest changes, while the bare slope control surface showed the greatest changes in micro-topographic factors. However, regardless of the vegetation patch pattern, individual plants, clusters, or patches of vegetation on the upslope direction will form raised soil mounds that intercept soil. Due to the different spatial distribution patterns of plants, there will still be soil deposition, leading to significant variations in micro-topographic changes on the slope. Minor variations on the slope, such as differences in gradient and aspect, influence the convergence and divergence of water flow, thereby altering the role of vegetation in blocking or guiding water flow (Tuo et al., 2023). Particularly on slopes facing south or southwest, where there is sufficient sunlight, vegetation grows more effectively, and soil erosion is relatively minimal.

5 Conclusion

This study focuses on three typical vegetation patch patterns (uniform, aggregated, and random distribution) on slopes and bare slope control surfaces in the Baojia Gou watershed of the Pisha sandstone region. The CA-Markov model was used to simulate the dynamic characteristics of soil erosion conditions on different slopes in 2023, exploring the transfer patterns of soil erosion intensity types on the side slopes under different vegetation patterns, and simulating the spatial evolution of soil erosion intensity types. The results show that: (1) Different vegetation distributions lead to different erosion intensity patterns. In the uniformly distributed, aggregated, and bare control slopes, the erosion intensity is predominantly within the mild erosion area. However, on the side slopes with random distribution, the soil

erosion intensity shifts from the mild erosion area to slight erosion area. (2) Rainfall is a key driving factor for soil erosion, influencing runoff and sediment yield. The erosion dynamics are the result of the combined effects of vegetation patch patterns, slope gradient, micro-topography, and slope aspect. The CA-Markov model achieved high simulation accuracy, with Kappa coefficients for different vegetation patterns ranging from 65.24% to 75.88%. The spatial layout of the simulated soil erosion intensity maps for different side slopes closely matched the actual soil erosion intensity maps, demonstrating the model's effectiveness in simulating the soil erosion processes on vegetated slopes. This study provides new insights into the dynamic interactions between vegetation patterns and slope soil erosion, emphasizing the value of optimizing vegetation management to mitigate erosion risks. Future research may improve the model by integrating other influencing factors (e.g., soil mechanical composition, vegetation root density) to enhance simulation accuracy and the practical relevance of soil and water conservation efforts.

Data availability statement

The original contributions presented in the study are included in the article/supplementary material, further inquiries can be directed to the corresponding author.

Author contributions

YS: Conceptualization, Visualization, Writing–original draft. SZ: Investigation, Supervision, Writing–review and editing. LL: Methodology, Writing–review and editing. ZC: Investigation, Writing–review and editing. YZ: Software, Writing–review and editing.

Funding

The author(s) declare that financial support was received for the research, authorship, and/or publication of this article. This study was funded by the Inner Mongolia Autonomous Region Science and Technology Major Project "Study on the Spatial Pattern System of Forest and Grass in Inner Mongolia Based on the Carrying Capacity of Water and Soil Resources" (2024JBGS0021) and the National Natural Science Foundation of China "Pisha Sandstone Slope Erosion Spatio-temporal Variation and Vegetation Patch Pattern Evolution Mutual Feedback Mechanism" (42267049).

Conflict of interest

The authors declare that the research was conducted in the absence of any commercial or financial relationships that could be construed as a potential conflict of interest.

Generative AI statement

The author(s) declare that no Generative AI was used in the creation of this manuscript.

Publisher's note

References

Aguejdad, R. (2021). The influence of the calibration interval on simulating non-stationary urban growth dynamic using CA-markov model. *Remote Sensing13* 13 (3), 468. doi:10.3390/rs13030468

BriniImen, A., Dimitrios, D., and Kalaitzidis, C. (2021). Linking soil erosion modeling to landscape patterns and geomorphometry: an application in crete, Greece. *GreeceApplied Sci.* 11 (12), 5684. doi:10.3390/app11125684

Cai, L. Y., and Wang, M. (2020). Effect of the thematic resolution of land use data onurbanexpansion simulations using the CA-Markov model. *Arabian J. Geosciences* 13 (23), 1250. doi:10.1007/s12517-020-06248-z

Chase Clement, G. (1992). Fluvial landsculpting and the fractal dimension of topography. *Geomorphology* 5 (1-2), 39–57. doi:10.1016/0169-555x(92)90057-u

Chen, F., 2006 Landscape dynamics analysis in the process of vegetation restoration in Gulang oasis-desert ecotone.

Crompton, O. V., and Thompson, S. E. (2020). Sensitivity of dryland vegetation patterns to storm characteristics. *Ecohydrology* 2269. doi:10.1002/eco.2269

D'Ambrosio, D., Di Gregorio, S., Gabriele, S., and Gaudio, R. (2001). A Cellular Automata model for soilerosion by water. *Phys. Chem. Earth, Part B Hydrology, Oceans andAtmosphere* 26 (1), 33–39. doi:10.1016/s1464-1909(01)85011-5

Eigentler, L., and Sherratt, J. A. (2020). An integrodifference model for vegetation patterns in semi-arid environments with seasonality. *J. Math. Biol.* 81 (3), 875–904. doi:10.1007/s00285-020-01530-w

Elias, O., and Schindler, F. (2015). Momentum and mean reversion in regional housing markets: evidence from variance ratio tests. *Int. J. Strategic Prop.* 19 (3), 220–234. doi:10.3846/1648715x.2015.1031854

Fazlolah, A. M., Bubak, S., Marjan, M., Salmanmahiny, A., and Mirkarimi, S. H. (2018). Evaluation of the relationship between soil erosion and landscape metrics across Gorgan Watershed in northern Iran. *Environ. Monit. Assess.* 190 (11), 643. doi:10.1007/s10661-018-7040-5

Feng, T., Wei, W., Chen, L., Rodrigo-Comino, J., Die, C., Feng, X., et al. (2018). Assessment of the impact of different vegetation patterns on soil erosion processes on semiarid loess slopes. *Earth Surf. Process. Landforms* 43, 1860–1870. doi:10.1002/esp.4361

Gong, Y., Yu, H., Tian, P., Guo, W., Chen, L., and Shen, D. (2023). Field experiments on quantifying the contributions of Coreopsis canopies and roots to controlling runoff and erosion on steep loess slopes. *J. Mt. Sci.* 20, 1402–1423. doi:10.1007/s11629-022-7775-x

Grazhdani, S., and Shumka, S. (2007). An approach to mapping soil erosion by water with application to Albania. *Desalination* 213, 263–272. doi:10.1016/j.desal.2006.03.612

He, B., He, L., and Wang, R. (2014). Dynamic simulation of soil erosion on hedgerow slope based on CA-Markov model. *J. Nanchang Inst. Technol.* 33, 5–10.

Huang, Q., Huang, J., Yang, X., Ren, L., Tang, C., and Zhao, L. (2017). Evaluating the scale effect of soil erosion using landscape pattern metrics and information entropy: a case study in the Danjiangkou reservoir area, China. *Sustainability* 9 (7), 1243. doi:10.3390/su9071243

Ji, X., Thompson, A., Lin, J. S., Jiang, F. S., Li, S. X., Yu, M. M., et al. (2019). Simulating and assessing the evolution of collapsing gullies based on cellular automata-Markov and landscape pattern metrics: a case study in Southern China. *J. Soils Sediments* 19 (7), 3044–3055. doi:10.1007/s11368-019-02281-y

Liu, J., Gao, G., Wang, S., Jiao, L., Wu, X., and Fu, B. (2018). The effects of vegetation on runoff and soil loss: multidimensional structure analysis and scale characteristics. *J. Geogr. Sci.* 28, 59–78. doi:10.1007/s11442-018-1459-z

Liu, R., Xu, F., Zhang, P., Yu, W., and Men, C. (2016). Identifying non-point source critical source areas based on multi-factors at a basin scale with SWAT. *J. Hydrology* 533, 379–388. doi:10.1016/j.jhydrol.2015.12.024

Liu, X., and Zhang, D. (2015). Temporal-spatial analyses of collapsed gully erosion based on three-dimensional laser scanning. *Trans. Chin. Soc. Agric. Eng.* 31, 204–211. doi:10.3969/j.issn.1002-6819.2015.04.029

Ma, L., Yang, X., and Wu, Z. (2003). Simulation of spatial evolution of soil erosion under different land use models. *Soil water conservation Bull.* 1, 49–51. doi:10.13961/j.cnki.stbctb.2003.01.013

Mohamed, M., Zouagui, A., and Fenjiro, I. (2021). A review of soil erosion modelingby R/USLE in Morocco: achievements and limits. *E3S Web Conf.* 234, 00067. doi:10.1051/e3sconf/202123400067

Nikolaos, E., Evdoxia, L., and Emmanouil, P. (2020). Inherent relationship of the USLE, RUSLE topographic factor algorithms and its impact on soil erosion modelling. *Hydrological Sci. J.* 65 (11), 1879–1893. doi:10.1080/02626667.2020.1784423

Nurlina, Kadir, S., Kurnain, A., Ilham, W., and Ridwan, I. (2022). Analysis of soil erosion and its relationships with land use/cover in Tabunio watershed. *IOP Conf. Ser. Earth Environ. Sci.* 976 (1), 012027. doi:10.1088/1755-1315/976/1/012027

Pajouhesh, M., Gharahi, N., Iranmanesh, M., and Cornelis, W. M. (2020). Effects of vegetation pattern and of biochar and powdery soil amendments on soil loss by wind in a semi-arid region. *Soil Use Manag.* 36, 704–713. doi:10.1111/sum.12630

Porto, P., Bacchi, M., Preiti, G., Romeo, M., and Monti, M. (2022). Combining plot measurements and a calibrated RUSLE model to investigate recent changes in soil erosion in upland areas in Southern Italy. *J. Soils Sediments* 22, 1010–1022. doi:10.1007/s11368-021-03119-2

Qun, C., Yi, J. X., and Wu, Y. L. (2019). Cellular automaton simulation of vehicles in the contraflow left-turn lane at signalized intersections. *IET Intell. Transp. Syst.* 13 (7). doi:10.1049/iet-its.2018.5451

Rodrigo-Comino, J., Taguas, E. V., Seeger, M., and Ries, J. B. (2018). Quantification of soil and water losses in an extensive olive orchard catchment in Southern Spain. *J. Hydrology* 556, 749–758. doi:10.1016/j.jhydrol.2017.12.014

Sun, G. Y., and Deng, W. S. (2015). "Dynamic simulation of land use temporal and spatial evolution based on CA-markov," in Proceedings of 2015 International Conference on Computer Science and Environmental Engineering(CSEE 2015), 1174–1183.

Tang, C., Liu, Y., Li, Z., Guo, L., Xu, A., and Zhao, J. (2021). Effectiveness of vegetation cover pattern on regulating soil erosion and runoff generation in red soil environment, southern China. *Ecol. Indic.* 129, 107956. doi:10.1016/j.ecolind.2021.107956

Tuo, D., Lu, Q., Wu, B., Li, Q., Yao, B., Cheng, L., et al. (2023). Effects of wind–water erosion and topographic factor on soil properties in the loess hilly region of China. *Plants* 12 (13), 2568. doi:10.3390/plants12132568

Wan, L. H., Li, S. H., Chen, Y., He, Z., and Shi, Y. L. (2022). Application of deep learningin LandUse classification for soil erosion using remote sensing. *Front. Eart h Sci.* 10. doi:10.3389/feart.2022.849531

Xiang, J., Thompson, A., Lin, J., Jiang, F., Yu, M., et al. (2019). Simulating and assessing the evolution of collapsing gullies based on cellular automata-Markov and landscape pattern metrics: a case study in Southern China. *J. Soils Sediments* 19 (7), 3044–3055. doi:10.1007/s11368-019-02281-y

Yeh, S. H., Wang, C. A., and Yu, H. C. (2006). Simulation of soil erosion and nutrient impact using an integrated system dynamics model in a watershed in Taiwan. *Environ. Model. & Softw.* 21, 937–948. doi:10.1016/j.envsoft.2005.04.005

Yi, B., Song, L., Qian, Q. Z., and Wei, Z. (2021). Study on dynamic change of land use in QingzhenCity based on GIS technology and CA-markov model. *E3S Web Conf.* 271, 02017. doi:10.1051/e3sconf/202127102017

Yu, Y., Wei, W., Chen, L., Feng, T., and Daryanto, S. (2019). Quantifying the effects of precipitation, vegetation, and land preparation techniques on runoff and soil erosion in a Loess watershed of China. *Sci. total Environ.* 652, 755–764. doi:10.1016/j.scitotenv.2018.10.255

Yuan, L., Chang, C., and Zhang, Q. (2008). Study on erosion and sediment yield model of small watershed based on cellular automata. *Soil water conservation Bull.* 2, 85–89. doi:10.13961/j.cnki.stbctb.2008.02.030

Zhang, B., Hu, S. G., Wang, H. J., and Zeng, H. R. (2023). A size-adaptive strategy to characterize spatially heterogeneous neighborhood effects in cellular automata simulation of urban growth. *Landsc. Urban Plan.* 229, 104604. doi:10.1016/j.landurbplan.2022.104604

Zhang, L., Antoinette, L., and Lacey, S. (1996). Modeling approaches to the prediction of soil erosion in catchments. *Environ. Softw.* 11 (1-3), 123–133. doi:10.1016/S0266-9838(96)00023-8

Zhang, S. H., Fan, W., Li, Y. Q., and Yi, Y. (2017). The influence of changes in land use and landscape patterns on soil erosion in a watershed. *Sci. Total Environ.* 574, 34–45. doi:10.1016/j.scitotenv.2016.09.024

Zhang, Z., Hu, B. Q., Jiang, W. G., and Qiu, H. H. (2021). Identification and scenario prediction of degree of wetland damage in Guangxi based on the CA-Markov model. *Ecol. Indic.* 127, 107764. doi:10.1016/j.ecolind.2021.107764

Zhao, J., Feng, X., Deng, L., Yang, Y., Zhao, Z., Zhao, P., et al. (2020). Quantifying the effects of vegetation restorations on the soil erosion export and nutrient loss on the Loess Plateau. *Front. plant Sci.* 11, 573126. doi:10.3389/fpls.2020.573126

Zhao, Y. H., Fang, S., Wang, X. F., and Huang, X. (2013). Analysis of landscape pattern based on the CA-markov model. *J. Appl. Sci.* 13 (10), 1889–1894. doi:10.3923/jas.2013.1889.1894

frontiers | Frontiers in Environmental Science

TYPE Original Research
PUBLISHED 03 January 2025
DOI 10.3389/fenvs.2024.1511449

OPEN ACCESS

EDITED BY
Xudong Peng,
Guizhou University, China

REVIEWED BY
Mehmet Ali Çullu,
Harran University, Türkiye
Youjin Yan,
Nanjing Forestry University, China
Fengling Gan,
Chongqing Normal University, China

*CORRESPONDENCE
Hongsong Chen,
hbchs@isa.ac.cn

RECEIVED 15 October 2024
ACCEPTED 19 November 2024
PUBLISHED 03 January 2025

CITATION
Duan X, Fu Z, Deng Y and Chen H (2025) Characteristics of water distribution and preferential flow processes and nutrient response on dolomite slopes in the southwestern karst region.
Front. Environ. Sci. 12:1511449.
doi: 10.3389/fenvs.2024.1511449

Characteristics of water distribution and preferential flow processes and nutrient response on dolomite slopes in the southwestern karst region

Xiaoqian Duan[1,2,3], Zhiyong Fu[1,2], Yusong Deng[1,2] and Hongsong Chen[1,2]*

[1]Key Laboratory of Agro-ecological Processes in Subtropical Region, Institute of Subtropical Agriculture, Chinese Academy of Sciences, Changsha, China, [2]Huanjiang Observation and Research Station for Karst Ecosystems, Chinese Academy of Sciences, Huanjiang, China, [3]Guangxi Key Laboratory of Agro-Environment and Agro-Product Safety, College of Agriculture, Guangxi University, Nanning, China

Understanding the characteristics of the soil water content and preferential flow is critical for a thorough comprehension of soil nutrient loss in Karst slopes/ecosystems. We monitored the soil water content and soil temperature at 0–20, 20–40, and 40–60 cm depths on a typical Karst dolomite slope at a high frequency to determine the water distribution characteristics and confirm the occurrence of preferential flow from 2018 to 2021. The soil properties and nutrients in different soil layers during the rainy and dry seasons were determined along the slope (from upper to lower slope positions, with a total of 9 sampling sites). The results revealed that the saturated hydraulic conductivity of the soil at the upper slope position was significantly ($p < 0.05$) greater than that at the middle and lower slope positions. The soil water content at the down slope position was greater than that at the middle and upper slope positions, further more, coupling monitoring of the soil water content and temperature revealed obvious preferential flow in the Karst dolomite slope. In addition to the spatial variability in the water content, the soil nutrients exhibited regular spatial variations. The dissolved organic carbon (DOC), dissolved organic nitrogen (DON), total nitrogen (TN), total phosphorus (TP) and total potassium (TK) contents were the lowest at the upper slope position and the highest at the down slope position, whereas the difference in nutrients between the rainy and dry seasons was the greatest at the upper slope position. Our results demonstrated that the patterns of the soil water content and surface nutrient loss are consistent along the Karst dolomite slope and are related to the occurrence of preferential flow. Furthermore, the results suggested that, compared with those in previous studies, which focused only on soil properties in the Karst regions of Southwest China, the variation in the soil water content and occurrence of preferential flow may be more important than previously assumed.

KEYWORDS

water distribution, preferential flow, nutrient loss, Karst region, dynamic monitoring

1 Introduction

Karst landforms constitute one of the main types of landforms worldwide, accounting for approximately 12% of the Earth's land area, and occur primarily in the Mediterranean Sea area, Eastern Europe, the Middle East, Southeast Asia, Southeast America and the Caribbean region (Peng and Wang, 2012; Lu et al., 2014; Hartmann et al., 2015). Owing to notable development and severe soil erosion, the soil in Karst regions is thin and scattered (Herman et al., 2012; Li et al., 2019; Liu et al., 2020; Zhang et al., 2021).

Notably, total nitrogen (TN) and total phosphorus (TP) in soil are the major limiting nutrients of ecosystem productivity and play key roles in ecosystem restoration or succession (Zhang et al., 2015; Wen et al., 2016). The ecological problem of soil nutrient degradation in Karst regions has attracted the attention of many researchers (Turrión et al., 2009; Albaladejo et al., 2012). Li et al. (2017) studied the impacts of agricultural abandonment on soil C and N contents and reported that the soil C and N contents increased following agricultural abandonment. Moreover, the significant effects of the lithology and land cover type on soil nutrients have been reported in a few studies (Kooijman et al., 2005; Karchegani et al., 2012; Hoffmann et al., 2014; Rossel et al., 2014). In addition, relevant studies have noted that water is the main driving force of soil erosion, as well as the carrier and driving force of nutrient loss (Peng and Wang, 2012). In the absence of significant differences in the lithology, human factors, vegetation coverage, and other conditions, soil erosion may be the main factor leading to nutrient depletion in Karst regions.

At present, studies on the impact of soil erosion on nutrient migration on Karst slopes have focused mostly on surface water movement. Song et al. (2017) reported that runoff erosion directly affects the process of soil nutrient depletion, especially under heavy rainfall conditions, and that an excessive water input can cause a reduction in the soil nutrient content. Wang et al. (2016) analyzed the impact of runoff on soil nutrients on Karst slopes. Yao et al. (2021) studied the effects of rainfall intensity and underground fracture gaps on nutrient loss in karstic sloping farmland and reported that the effect of underground cavities on the loss of sediment nutrients was greater than that of runoff. Owing to the chemical and physical weathering on Karst slopes, the weathering degree of bedrock is high, macropores are obviously developed, the water holding capacity of the soil layer is low, and the permeability is high. Previous research has shown that the surface runoff coefficient on Karst slopes is less than 5% and that almost all of the rainfall infiltrates (Chen et al., 2012; Fu et al., 2015). Fissures and sinkholes distributed on Karst slopes are important water and nutrient leakage channels, and surface water and soil easily seep into the ground along holes (cracks), resulting in notable nutrient loss (Jiang et al., 2014). In contrast to surface runoff, subsurface flow is the primary mechanism of soil nutrient loss in Karst areas. Subsurface flow determines the infiltration and redistribution of precipitation in soil and affects the soil water content in different soil layers. Further more, due to the presence of cracks, they affect soil water distribution, facilitate rapid infiltration of water, and may lead to more frequent occurrence of preferential flow during water infiltration during rainfall (Sheng et al., 2009; Hardie et al., 2011). The subsurface flow that bypasses part of the soil matrix through macropores and does not follow Darcy's law is referred to as preferential flow (Clothier et al., 2008). Soil preferential flow is not an individual phenomenon. Moreover, this process is common at various spatial scales (from pores to watersheds) and time scales (from 10 s to 10 years) and can occur in soils with different textures and structures (Nimmo, 2012; Liu et al., 2005). The existence of preferential flow enhances the infiltration depth and infiltration area, accelerates the downward movement of water, and provides a preferential flow path for water infiltration. Water is the main carrier of soil nutrients, and the content of soil nutrients is affected by water content changes (Korkanc and Dorum, 2019), preferential flow may accelerate the loss of surface soil nutrients during rainfall (Hopp and McDonnell, 2009). In summary, preferential flow significantly affects soil nutrient levels, which can promote or inhibit the ability of soil to filter nutrients, thereby enhancing or harming the functionality of ecosystems (Clothier et al., 2008; Wei et al., 2024). Therefore, it is essential to account for the characteristics of preferential flow in Karst soil and understand the relationship between preferential flow and slope water distribution characteristics in slopes, which is conducive to elucidating the impact of preferential flow on soil nutrient loss.

The geological structure and soil characteristics in Karst areas are unique, leading to differences in the water infiltration process compared with those in other regions, and preferential flow may occur more frequently. Although the importance of preferential flow in the process of soil nutrient loss in Karst areas has been recognized, research on the development status of preferential flow in Karst slope soils is lacking, whereas research on the impact of preferential flow on soil nutrients has also been relatively slow. Notably, methodological and technical difficulties are encountered in studying the developmental characteristics of preferential flow on Karst slopes and its impact on nutrient distribution. Previous studies on preferential flow changes have usually been performed via tracer and staining methods. Different methods present distinct advantages and focuses, and it is currently difficult to unify them. In addition, onsite measurement methods are destructive, with limited experimental samples and a lack of monitoring and analysis of preferential flow under natural rainfall conditions (Gerke et al., 2015; Hencher, 2010; Allaire et al., 2009). Therefore, evaluating the impact of preferential flow in soil on nutrient loss within those soils is difficult. Obviously, studying preferential flow on Karst slopes via appropriate methods is important for distinguishing whether preferential flow in soil on Karst slopes has developed and for determining its impact on the distribution of soil nutrients within those slopes. With improvements in experimental and numerical research methods, preferential flow has been analyzed through synergistic observations of the soil water content and temperature (Li et al., 2014; Gharabaghi et al., 2015; An et al., 2017). In alignment with previous studies, this study aimed to analyze preferential flow on Karst slopes through long–term high–frequency monitoring of the soil water content and temperature at different slope positions.

The Karst region in southwestern China is one of the three major areas with concentrated Karst distributions in the world (Jiang et al., 2014; Hu et al., 2021). Dolomite [$CaMg(CO_3)^2$] is a widely distributed carbonate rock in this region with favorable porosity and permeability. Therefore, it is realistic to choose a Karst dolomite slope in this region to analyze the impact of preferential flow on soil nutrient loss. The main objectives of this study were to (1) explore

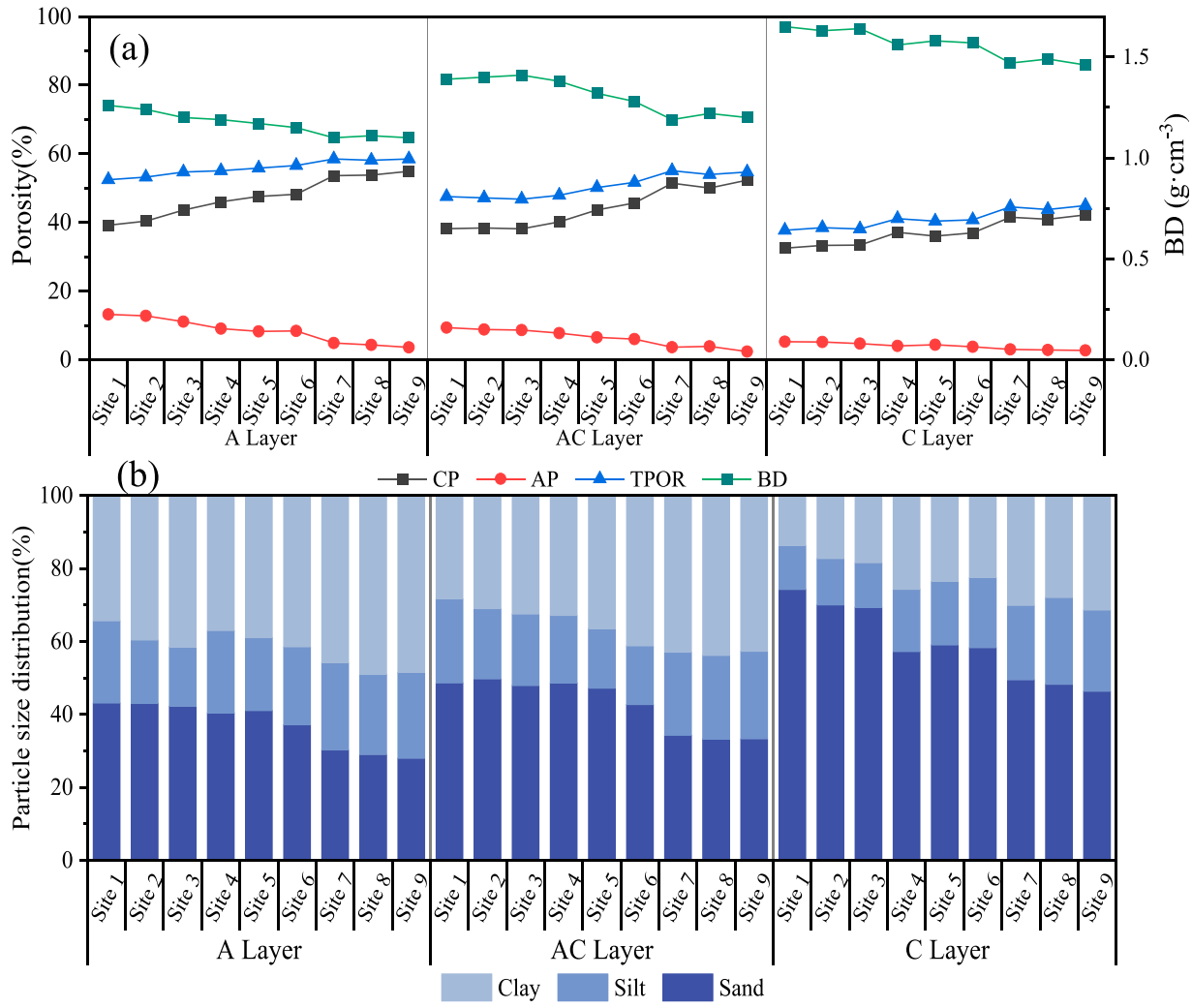

FIGURE 1
The soil physical properties of various layers in different sites: **(A)** Bulk density (BD) and total porosity (TPOR), capillary porosity (CP) and non-capillary porosity (AP); **(B)** Soil mechanical composition.

the characteristics of preferential flow on Karst slopes under natural rainfall conditions and its relationship with water distribution on those slopes and (2) analyze the characteristics of nutrient loss on Karst slopes and its potential relationship with preferential flow. The results could provide useful information on the conditions under which the spatial characteristics of nutrient loss on Karst slopes are beneficial for the restoration and management of degraded slopes. This study offers a theoretical basis for the prevention and control of rocky desertification and for ecological governance.

2 Materials and methods

2.1 Study area and sample collection

The experimental site is located in the Mulian Comprehensive Experimental Demonstration Zone of Ecosystem Observation of the Chinese Academy of Sciences, Huanjiang County, Guangxi Autonomous Region (24°43′59″–24°44′49″N, 108°18′57″–108°19′58″E). It is a typical Karst landscape unit (Figure A1). This county features a subtropical monsoon climate, with an average annual temperature of 19.9°C. The annual precipitation reaches 1,389.1 mm, with abundant rainfall but an uneven seasonal distribution. The rainy season (April to September) accounts for more than 70% of the annual rainfall, and the greatest amount occurs from June to July. The dry season lasts from October to March of the following year.

The soil in the study area is derived from dolomite residues, the main types of clay minerals are illite (2:1 non expansive clay mineral), montmorillonite (2:1 expansive clay mineral), and kaolinite (1:1non expansive clay mineral), with montmorillonite having a higher content. Except for the mountaintop, the research area is almost continuously covered by shallow soil. The thickness of the soil layer gradually increases downwards along the slope, and the degree of soil development gradually increases. Along the slope direction, clay particles mainly gather at the down slope, while gravel is concentrated on the upper slope. Meanwhile, the soil organic matter content gradually increases from the upper to the down of

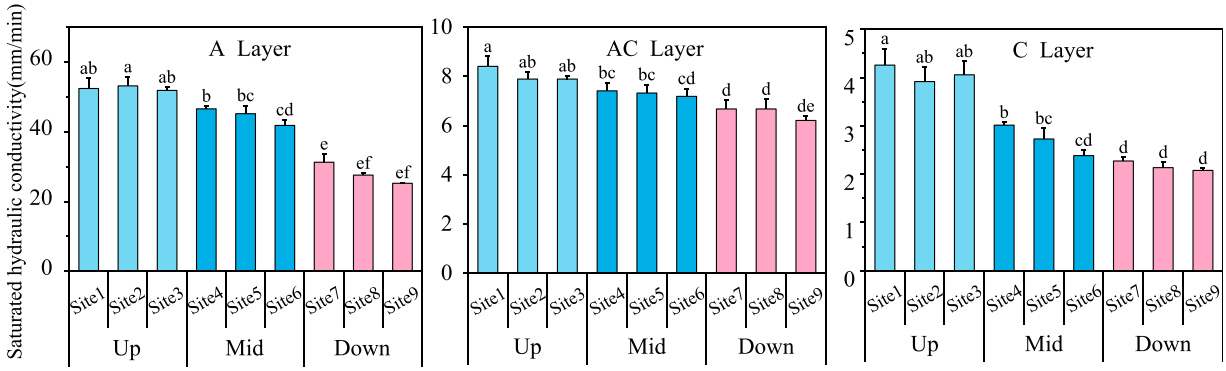

FIGURE 2
Vertical variation of saturated hydraulic conductivity of soil profiles at different slope positions. Different uppercase and lowercase indicated significant differences at 0.05 level between different slope positions.

TABLE 1 Test for saturated hydraulic conductivity of different slope sites (upper slope, middle slope and lower slope) in the test Karst slope different soil layer (A layer, AC layer and C layer).

Soil layer	Slope position	*t*	Df	Sig
A Layer	Upper - Middle	4.318	16	0.001
	Upper - Lower	16.513	16	0.000
	Middle - Lower	7.107	16	0.000
AC Layer	Upper - Middle	4.754	16	0.000
	Upper - Lower	8.447	16	0.000
	Middle - Lower	4.798	16	0.000
C Layer	Upper - Middle	4.984	16	0.000
	Upper - Lower	17.682	16	0.000
	Middle - Lower	3.771	16	0.002

slope, the soil organic matter content was significantly higher at the down slope (26.96 ± 1.53b) than for the upper slope (22.06 ± 1.84a) and middle-slopes (23.58 ± 1.23a). To eliminate the impact of vegetation on the erosion process, we conducted experiments on slopes where the vegetation and species diversity levels were not significant, and where the main vegetation types included herbs and shrubs. To clarify the physical properties of different soil layers in the vertical profile of the study slope, soil samples were collected in the exact same location from the surface to the deep soil layer in the vertical profile according to the geomorphological characteristics of the dolomite slope. A total of nine sampling points were established along the slope direction in the upper slope (sites 1, 2, and 3), middle slope (sites 4, 5, and 6), and down slope (sites 7, 8, and 9) sections, with two profiles arranged for each sampling point as duplicates. The soil layers on the dolomite slope at the test site were further divided into three layers according to their color and texture (from top to bottom): the A layer, AC layer and C layer. The "A" layer is black surface layer. "AC" is a yellow illuvial horizon and "C" is a white dolomite strongly weathered layer. To clarify the physical properties and nutrient contents in the different soil layers within the vertical profile of the Karst dolomite slope, soil samples were collected from the surface layer to the deep soil layer along the vertical profile according to the abovementioned soil layer division. We collected undisturbed soil samples from these layers with a ring knife to quantify the soil bulk density (BD) and saturated hydraulic conductivity (K_s). Disturbed soil samples were used to determine the soil mechanical composition and soil nutrients, with samples for soil nutrient measurement collected at the same sites in March 2022 and October 2022.

2.2 Soil sample analysis

The soil bulk density (BD) and porosity were determined via the ring knife method (Cerda and Doerr, 2010), The soil mechanical composition was analyzed by the pipette method, and the samples were classified in terms of their sand (0.05–2 mm), silt (0.002–0.05 mm) and clay (<0.002 mm) compositions on the basis of the American standard classification system (Duan et al., 2021). The basic conditions of the soil samples are shown in Figure 1.

The total nitrogen (TN) content was analyzed via the semimicro-Kjeldahl-flow injection method (HGCF-200, China), the total phosphorus (TP) content was determined via NaOH fusion-molybdenum-antimony anticolor development-UV spectrophotometry (UV-2600, China), and the total potassium (TK) content was obtained via the NaOH melting atomic absorption flame photometry method (AA320CRT, China) (Bao, 2000). Dissolved organic carbon and dissolved organic nitrogen (DOC and DON, respectively) levels were analyzed via extraction with 0.5 M K_2SO_4 (Xiao et al., 2020). The constant-head method was used to measure the soil saturation hydraulic conductivity, K_s (mm/min), which can be calculated as follows:

$$K_s = \frac{10QL}{A\Delta HT}$$

where K_s (mm/min) is the saturated hydraulic conductivity, Q (mL) is the outflow within time t, L (cm) is the linear distance of the water flow path, A (cm^2) is the water flow cross-sectional area, ΔH (cm) is the total head difference between the beginning and end of the seepage path, and T (min) is the outflow time.

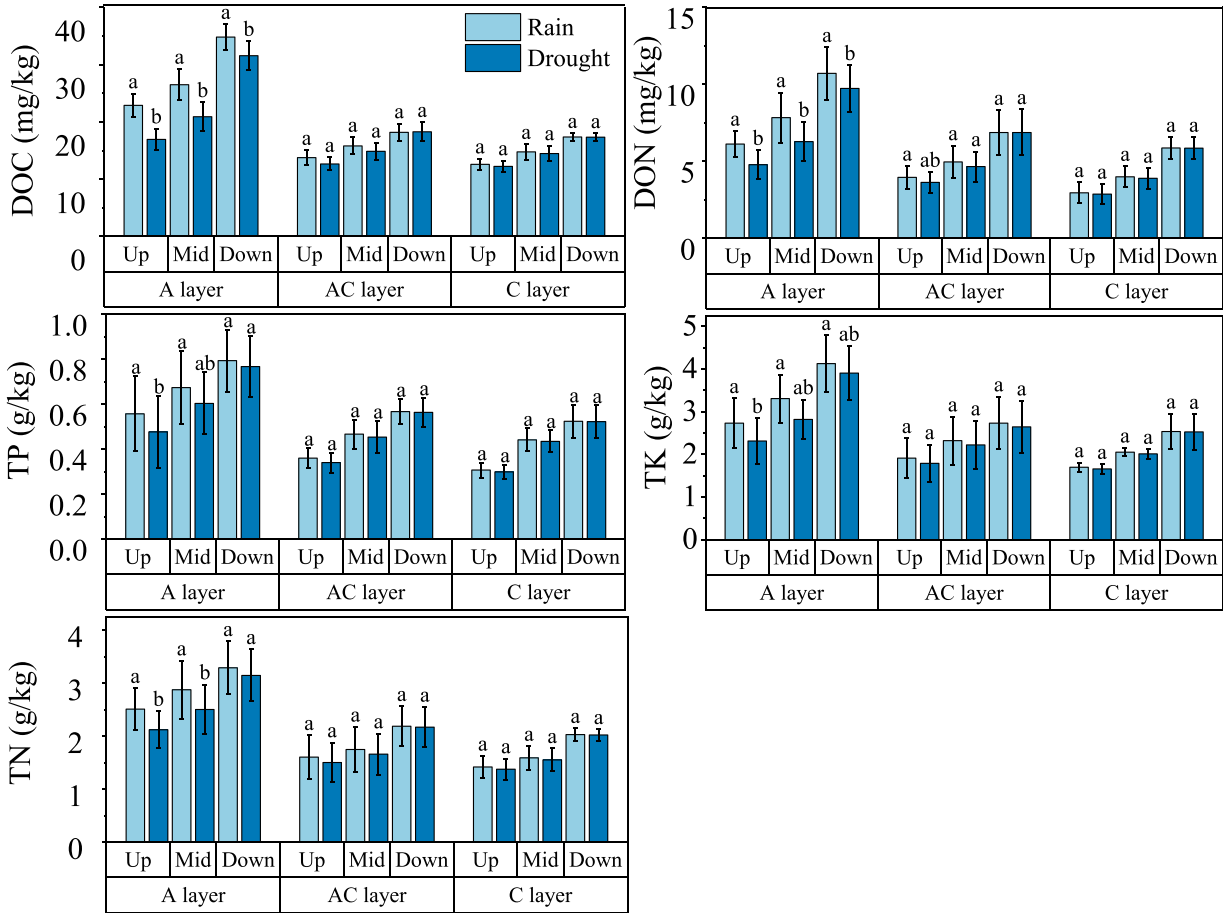

FIGURE 3
Rainy and dry season variations of soil nutrient content in different slopes and soil horizons on karst dolomite slopes.

2.3 Monitoring of the soil water content on a karst slope

To obtain the change in the soil water content on the test Karst slope, three soil water monitoring sites were established at three slope sites (upper, middle, and down slope sites). One soil moisture sensor (Hydra II) was installed horizontally to obtain the soil profiles at depths of 0–20 cm on the upper slope, and three soil moisture sensors were installed horizontally to obtain the soil profiles at depths of 0–20 cm, 20–40 cm, and 40–60 cm at the middle and down slope sites. The sensors were calibrated before installation. Rainfall and air temperature data were obtained from meteorological stations within the Mulian catchment. The soil water contents at all the sites were recorded at 30–min intervals beginning in January 2018.

2.4 Data processes

The statistical analyses were performed via the SPSS 21.0 for Windows statistical software package. Additionally, the tests included the normality test, homogeneity test of variance, *t*-test (significance: 0.05), and one-way analysis of variance (ANOVA) of the soil properties among the different soil layers and sites. Correlation analysis was performed, and related charts were constructed via Origin 21 software.

3 Results and analysis

3.1 Soil physical properties and K_s distributions along the slope

As shown in Figure 1, the clay content (particle size<0.002 mm) among the slope positions (sites 1–9) gradually increased from the upper to down slope positions, with the lowest clay content at site 1 and the highest at site 9 for the same soil layer. In addition, the change in the soil BD gradually decreased from the upper to lower slope positions with increasing slope. The lowest BD at site 9 was 1.10 g/cm^3, and the maximum BD at site 1 was 1.26 g/cm^3. This difference may be due to the higher content of coarse particles at the upper slope position than at the down slope position. The aeration porosity (>0.015 mm) at the upper slope position was obviously greater than those at the middle and down slope positions, and the value ranged from 3.59% to 13.23% from sites 1 to 9. Although the total porosity at the down slope position was high, the aeration porosity was lower than that at the upper slope position. A comparison of the same slope sites in the different soil layers

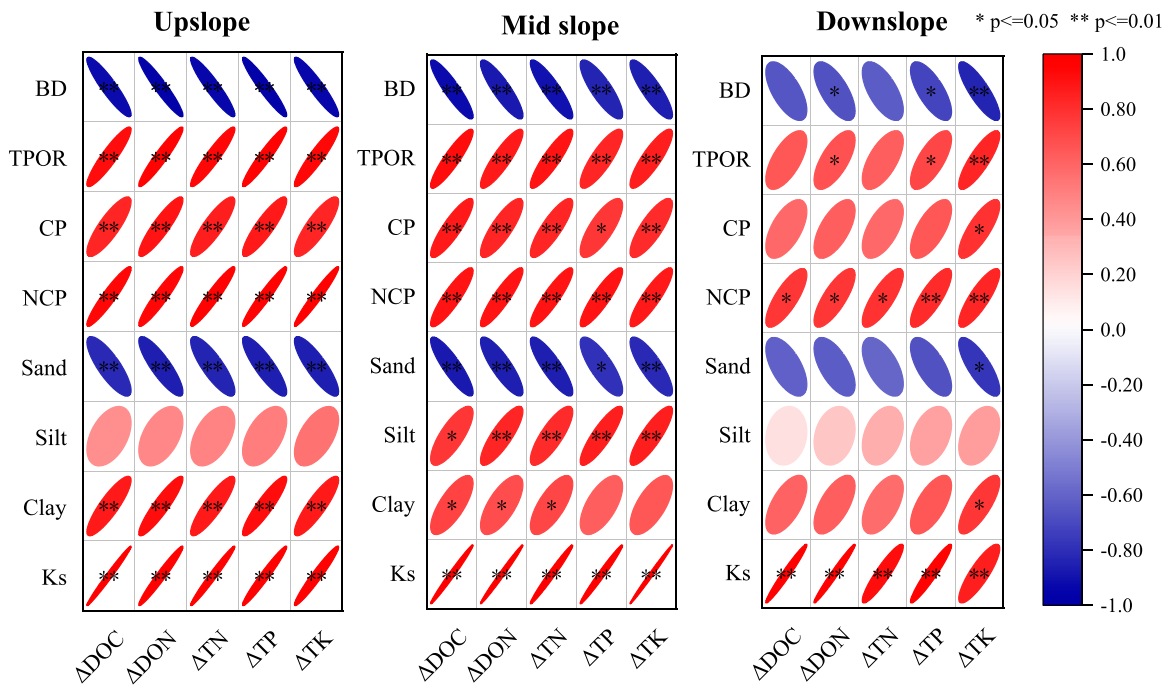

FIGURE 4
Correlation analysis between soil nutrient content variation and soil properties at different slope locations on karst dolomite slopes.

revealed that the sand content (particle size range 0.05–2 mm) and BD significantly increased and that the soil aeration porosity gradually decreased from the A layer to the C layer.

Figure 2 shows that the K_s of the dolomite slope exhibited significant spatial heterogeneity. The K_s decreased gradually from sites 1 to 9, and the K_s of the soil at the down slope position was significantly lower than that at the upper and middle slope positions ($p < 0.05$). Moreover, the difference in the K_s between the different test sites at the same slope position was not significant. The difference in K_s among the different slope positions was greatest in layer A. For layer A, the average K_s at site 1 was 52.34 mm/min, whereas that at site 9 was 25.24 mm/min. At the same slope position, the K_s values of the different soil layers also significantly differed, and the K_s values of the A layer were significantly higher than those of the AC and C layers. As indicated in Table 1, the differences in K_s among the down, middle and upper slope positions in the A, AC and C layers were significant ($p < 0.05$). In summary, the K_s values of Karst dolomite slopes exhibit consistent spatial variability.

3.2 Variation characteristics of nutrients at different sites on the karst slope during the rainy and dry seasons

As shown in Figure 3, the DOC, DON, TN, TP and TK contents along the slope during the rainy and dry seasons were the lowest at the upper slope position and the highest at the down slope position. In addition, the difference in soil nutrients between the rainy and dry seasons gradually decreased from the upper slope position to down slope position. The soil nutrient levels at each site were lower during the rainy season than during the dry season. Notably, soluble nutrients in the soil were lost after the rainy season. This phenomenon was most evident at the upper slope position, and the decrease in soil nutrients at the upper slope position was greater than that at the middle and down slope positions after the rainy season. In the vertical profile, the soil DOC, DON, TN, TP, and TK contents gradually decreased with increasing soil layer depth. Notably, these values were highest in the A layer and lowest in the C layer. In addition, the analysis of nutrient changes at different soil depths during the rainy and dry seasons revealed that the loss of soil nutrients after the rainy season mainly occurred in the A layer. The loss of nutrients in the A layer was greater than that in the AC and C layers after the rainy season, and the DOC, DON, TN, TP, and TK contents in the A layer at the upper slope position significantly differed between the rainy and dry seasons ($p < 0.05$). Compared with those before the rainy season, the soil nutrient levels in each layer basically decreased, but the nutrient levels in the deep layers (AC and C layers) at the down slope position slightly increased. Thus, after the rainy season, the DOC, DON, TN, TP, and TK migrated under the influence of water infiltration, resulting in a significant decrease in nutrients in the topsoil layer.

The correlations between the changes in soil nutrients and the basic properties during the rainy and dry seasons are shown in Figure 4. The results revealed that the correlations between the soil nutrient changes and soil properties were consistent across the upper, middle and down slope positions, indicating that the losses of soil DOC, DON, TN, TP, and TK were consistent. Further analysis of the correlations between the changes in soil nutrients and soil properties revealed a significant positive correlation between the changes in soil nutrients and K_s at the three slope positions ($p < 0.01$).

10.3389/fenvs.2024.1511449

TABLE 2 Dynamic variation characteristics of rainfall during 2018–2021.

Time	Precipitation (mm)	Rainfall duration (h)	Maximum 30 min rainfall intensity ($mm \cdot h^{-1}$)	Maximum 60 min rainfall intensity ($mm \cdot h^{-1}$)	Rainfall event frequency (n)
2018–1	43.4	167.4	3.6	3.0	7
2018–2	9.4	35.0	10	5.2	3
2018–3	160.8	115.2	42.8	26.4	8
2018–4	86.4	65.9	47.2	20.8	8
2018–5	152.8	145.5	33.6	22.6	13
2018–6	175.8	139.5	41.2	23.4	14
2018–7	159.6	190.9	69.6	41.6	13
2018–8	173.8	134.4	29.6	19.6	19
2018–9	228.0	149.9	27.2	16.2	8
2018–10	83.4	188.6	15.2	8.2	9
2018–11	45.0	118.2	11.2	5.8	7
2018–12	7.0	17.6	5.6	3.4	6
2019–1	0.4	0.98	0.4	0.4	1
2019–2	78.0	183.0	11.6	6.8	4
2019–3	81.8	234.1	14.0	7.4	9
2019–4	40.8	23.2	26.0	14.2	5
2019–5	153.4	157.3	44.8	26.4	9
2019–6	253.4	161.9	65.6	40.8	15
2019–7	314.2	223.4	56.0	30.2	11
2019–8	46.4	69.6	13.6	7.8	10
2019–9	77.2	71.8	51.6	29.2	6
2019–10	72.2	93.3	22.4	11.4	8
2019–11	26.6	65.4	16.4	10.2	6
2019–12	12.4	93.5	3.2	1.6	6
2020–1	50.4	145.8	5.6	2.8	9
2020–2	65.0	206.4	18.4	11.2	6
2020–3	201.4	217.1	58.8	29.6	11
2020–4	116.6	128.8	19.2	11.4	7
2020–5	124.4	79.6	46.0	25.2	9
2020–6	432.0	169.2	51.2	52.4	14
2020–7	131.6	129.6	19.2	13.8	8
2020–8	190.2	189.2	72.8	45.6	18
2020–9	740.4	277.2	81.6	77.6	10
2020–10	7.4	24.4	6.0	3.2	5
2020–11	1.2	13.4	0.2	0.2	3
2020–12	3.6	23.2	0.8	0.4	5
2021–1	5.2	55.6	0.8	0.6	5
2021–2	50.6	80.1	9.2	7.6	4
2021–3	57.2	208.0	6.4	5.0	9

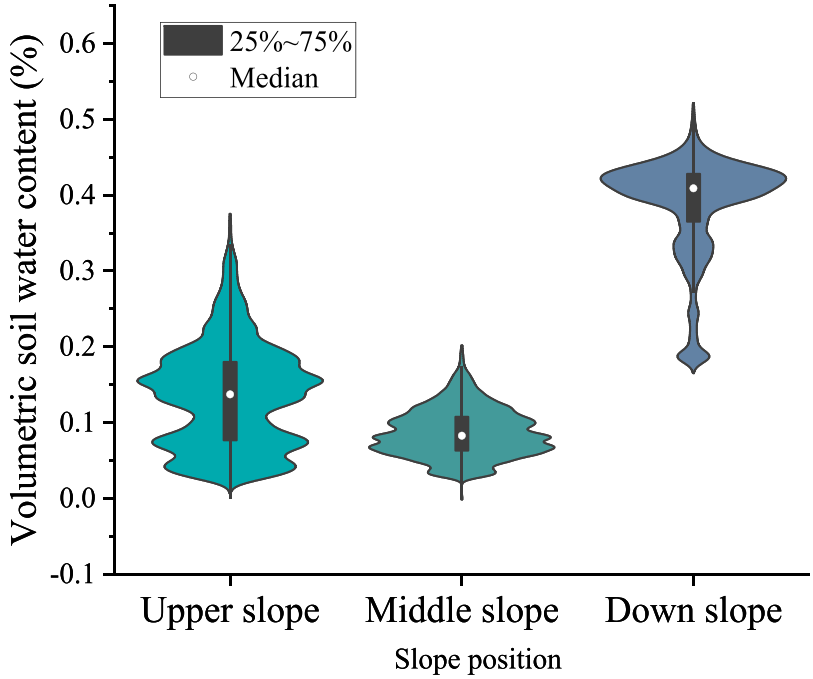

FIGURE 5
Descriptive statistics of soil water content on the different slope positions during the observation period.

Further analysis of the correlation between the soil nutrient change rate and basic soil properties revealed that the change in soil nutrients at the three slope positions was significantly positively correlated with K_s ($p < 0.01$) and significantly positively correlated ($p < 0.05$ or $p < 0.01$) with the noncapillary porosity (NCP). In addition, there was a significant negative correlation ($p < 0.01$) between the changes in soil nutrients and BD at the upper and middle slope positions. Therefore, soil nutrient loss is related to soil properties, especially NCP and K_s.

3.3 Monitoring results for the soil water content in the karst test slope

As indicated in Table 3, the rainy and dry seasons are very distinct in the Karst dolomite area. The rainfall amount in December 2018 was only 7.0 mm, but in September, it reached 228.0 mm. Similar variation patterns were also observed in 2019, 2020, and 2021. The minimum rainfall during the monitoring period was 0.4 mm (January 2019), and the maximum rainfall was 740.4 mm (September 2020). Due to the significant difference in nutrients between the rainy and dry seasons, mainly concentrated in the surface layer, the dynamic trend of soil moisture content in the surface layer (0–20 cm) of different slope positions was analyzed (Figures 5, 6). As shown in Figure 5, during the monitoring period from 2018 to 2021, the average soil water contents at the upper, middle and down slope positions were 0.14, 0.09 and 0.39 cm^3/cm^3, respectively. Notably, the soil water content gradually increased from the upper to down slope positions in general, and the down slope position presented a higher soil water content than that at the upper and middle slope positions. Additionally, the coefficient of variation (CV) of the soil water content at the different slope positions was analyzed during the monitoring period. The CV is the ratio of the standard deviation to the average value, which reflects the degree of statistical dispersion of the sample values. The CV values of the soil water content at the upper, middle and down slope positions were 50.23%, 36.76% and 17.49%, respectively. The CV of the soil water content was greater at the upper slope position than at the middle and down slope positions, indicating that the fluctuation in the soil water content at the upper slope position was the greatest.

Furthermore, as shown in Figure 6, the variation characteristics of the soil water content and the response to rainfall at the three slope positions were basically consistent. The soil water content is generally high during rainfall, and the maximum soil water contents at the upper, middle and down slope positions are 0.38, 0.43 and 0.57 cm^3/cm^3, respectively. The maximum soil water content occurs during rainfall. Moreover, the difference in the soil water content between the upper and middle slope positions was small, whereas the difference between the upper and down slope positions was notable. In general, the characteristics of the soil water content on the Karst dolomite slope during the monitoring period were as follows: down slope > middle slope > upper slope. In addition, the variation trends in the soil water content and CV were opposite. That is, the soil water content at the upper slope was low, with a relatively large variation range and a relatively dispersed distribution. In contrast, the soil water content at the down slope position was high, with a small variation range and a relatively concentrated distribution, and the response to rainfall was not as obvious as that at the upper slope position.

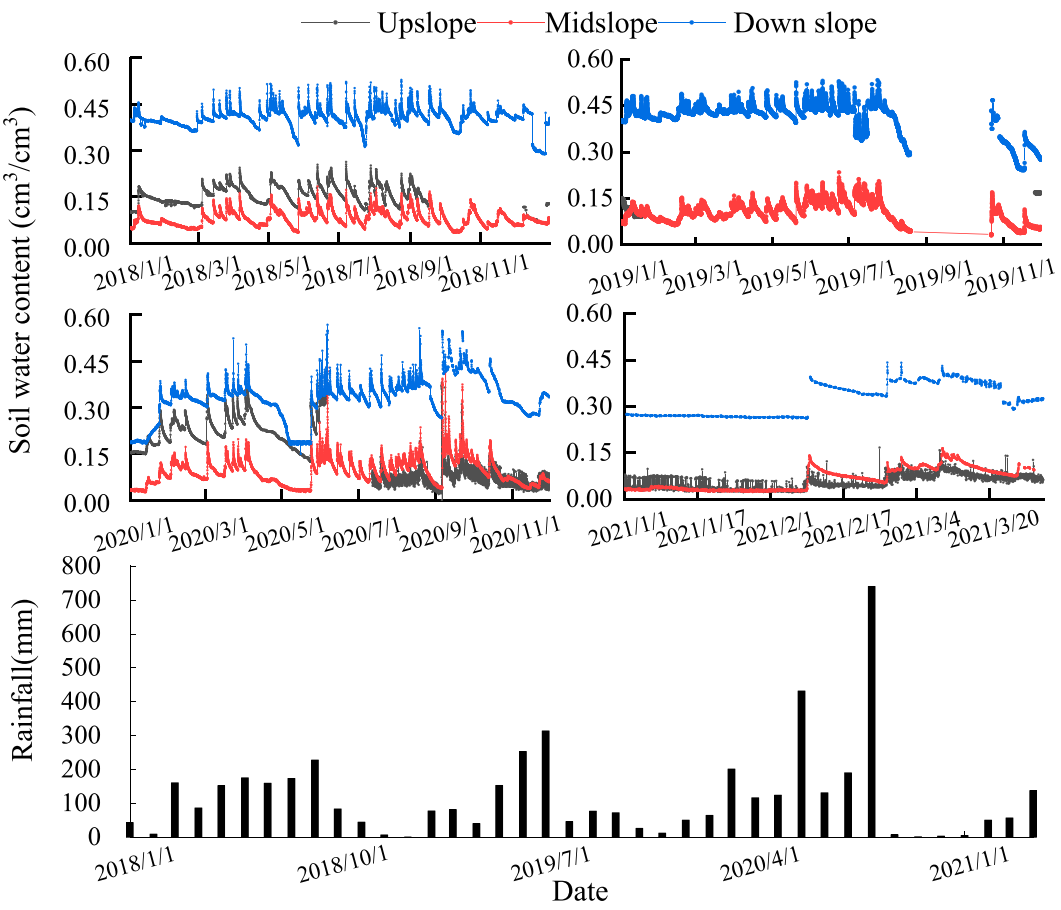

FIGURE 6
Temporal variation of daily average soil water content on the different slope positions during the observation period.

3.4 Characteristics of the moisture and temperature changes in the preferential and substrate flow processes on karst slopes

The changes in soil water and temperature during the monitoring period when typical preferential and matrix flow processes occurred in the slope are shown in Figures 7, 8, respectively. Figure 7 shows that the soil water content gradually increased from depths of 0–20 cm, 40–60 cm and 20–40 cm. During preferential flow, water directly infiltrated from the surface to depths of 40–60 cm, and the deep soil water content changed rapidly. Moreover, temperature analysis revealed that because the air temperature (20.9°C) was lower than the topsoil temperature (25.8°C and 24.7°C) and heat exchange between rainwater and soil was greater, resulting in the topsoil temperature gradually decreasing with increasing rainfall. The 20–40 cm layer exhibited soil matrix flow, and because the soil temperature at 0–20 cm was greater than that at 20–40 cm and 40–60 cm, the soil temperature at 20–40 cm first increased but then decreased. The preferential flow caused the soil temperature at depths of 40–60 cm to decrease prior to the other layers. Moreover, during the infiltration process, the rainwater temperature increased due to the heat exchange with the high-temperature soil, resulting in the soil temperature at depths of 40–60 cm gradually rising later.

The changes in the soil water content and temperature during matrix flow differed from those during preferential flow (Figure 8). In particular, with rainfall infiltration, the soil water content at depths of 0–20 cm, 20–40 cm and 40–60 cm increased in turn. During rainfall, the temperature within the 0–20 cm soil layer gradually decreased because the rain temperature was lower than the surface soil temperature. However, due to the difference in temperature among the three soil layers, the soil temperature at 0–20 cm was greater than that of the deeper soil, so water replacement occurred with rainfall infiltration. That is, before the rainfall arrives, the water in the surface soil infiltrates into the deeper soil, causing the soil temperature to rise at the depth at 40–60 cm, however, when the rainfall arrives, the temperature begins to decrease.

4 Discussion

4.1 Characteristics and mechanisms for water distribution in slopes

During the monitoring period, the soil water content in the Karst slope varied among different slope positions under the same climatic conditions, as shown in Figures 5, 6. The soil water content

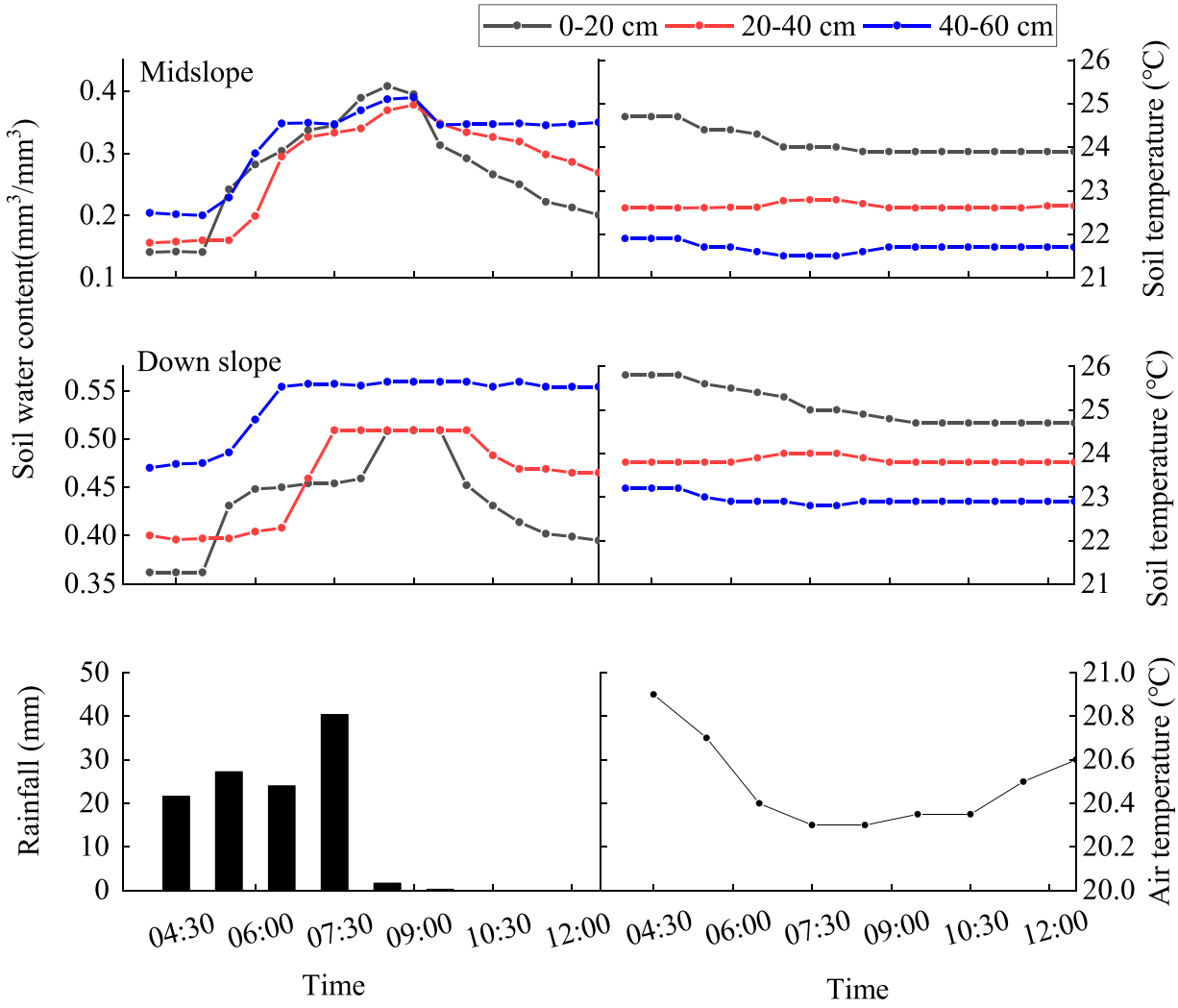

FIGURE 7
Trends of the soil water content and temperature during preferential flow.

at the down slope position was significantly greater than that at the middle and upper slope positions. The CV of the soil water content was the lowest at the down slope position, which was the opposite of the trend in the soil water content. Cui and Zhi (2018) noted that the main controlling factors affecting soil hydrological processes and water distributions differ at different regional scales. On a small scale, when there are no significant differences in the slope topography or vegetation, factors including the soil BD, texture, and cracks, more greatly impact soil hydrological processes.

We consider that the low soil water content at the upper slope position during the monitoring period may be related to the large number of aeration pores and the high K_s of the soil at that position. The distribution of pores in the Karst slope is evident, and the content of aeration pores is high at the upper slope position, which notably affects the process of soil water infiltration (Hincapie and Germann, 2009). Zhang et al. (2014) noted that soil with more aeration pores and a denser macropore distribution exhibited greater soil connectivity and greater K_s. This may be the main reason why the K_s at the upper slope position is significantly ($p < 0.05$) greater than that at the middle and down slope positions (Figure 2; Table 2). In addition, soil with more aeration pores can provide favorable infiltration channels for surface water (Sheng et al., 2009; Krisnanto et al., 2016). Therefore, preferential flow occurs easily in the surface soil later because soil water content is less concentrated in that soil layer, the depth of the wetting front is significantly greater than that in soil with fewer aeration pores, and the subsurface flow process is fast, so preferential flow easily occurs (Liu et al., 2005; Abaci and Papanicolaou, 2009).

An analysis of the monitoring results of the soil water content revealed that preferential flow occurs on Karst slopes during rainfall (Figure 7). We speculate that the frequency of soil preferential flow varies among the different slope positions and that the frequency of soil preferential flow at the down slope position is lower than that at the middle and upper slope positions. This may be due to the significant difference in the soil K_s among the different slope positions, as shown in Figure 2 and Table 2.

The soil at the upper slope position exhibits a higher water permeability than that at the down slope position, and the K_s is

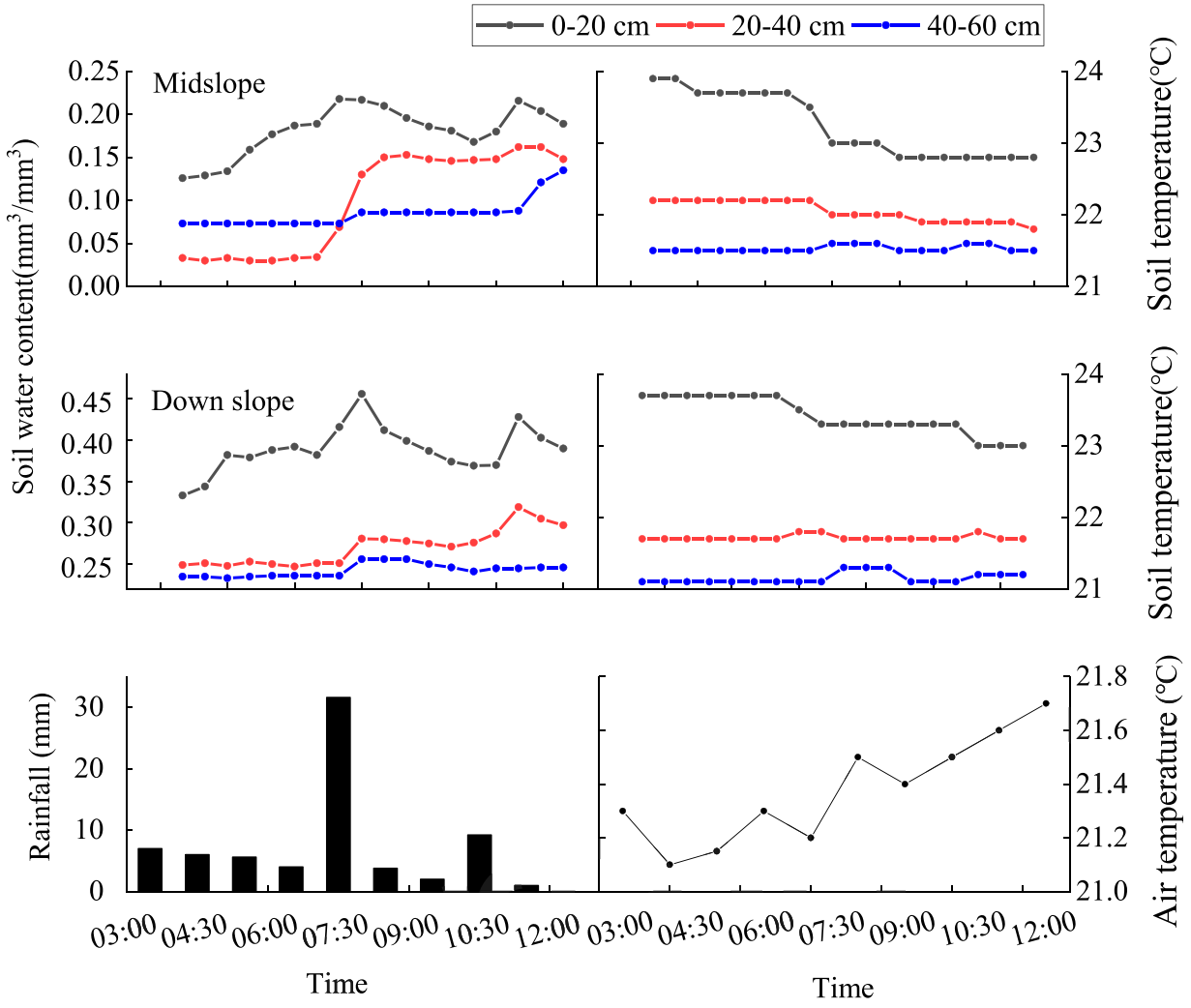

FIGURE 8
Trends of the soil water content and temperature during typical substrate flow.

significantly greater than that at the down slope position. Therefore, the resistance of the soil water content on the down slope in the process of infiltration is high, and resulting in a lower possibility of preferential flow at the down slope position. In addition, when the soil water content at the lower slope position is the highest, but the CV is the lowest, as shown in Figures 5, 6. Bodner et al. (2013) pointed out that the frequency of preferential flow is lower for soils with high water content and low CV values, and the transport capacity of soil water is lower, which is consistent with our view. Moreover, the close relationship between the occurrence frequency of preferential flow and the soil water content has also been widely recognized. The main principle is that water easily infiltrates soil with a high frequency of preferential flow, resulting in a low soil water content in the surface layer (Greve et al., 2010; Hardie et al., 2011; Tao et al., 2017; Wei et al., 2024).

In addition to the porosity and K_s, the difference in the soil mechanical composition affects the frequency of preferential flow (Hincapie and Germann, 2009; Beven and Germann, 2013). As shown in Figure 1, the soil mechanical composition at the different slope positions on the Karst slope exhibits obvious spatial variability, and the soil sand content at the upper slope position is significantly greater than that at the down slope position. Tao et al. (2020) noted that on granite Benggang slopes, an increase in the sand content promotes the formation and development of preferential soil flow, and the amount of preferential flow in the sand layer is three times greater than that of matrix flow. This is consistent with the analysis of preferential flow and texture in this study. The occurrence frequency of preferential flow at the upper slope position with a higher sand content is greater than that at the down slope position with a lower sand content. The reason for this phenomenon may be that the specific surface area of sand particles is smaller than that of clay particles, and the adsorption capacity for soil water content is low. Therefore, under the same porosity, water is more likely to be discharged from pores in soils with higher sand contents (Carbajal-Morón

et al., 2017), which improves the soil water infiltration capacity, and thus the degree of preferential flow is greater.

4.2 Characteristics and influencing factors of soil nutrient loss in karst dolomite slopes

We found that the soil DOC, DON, TN, TP, and TK contents in the dolomite Karst slope exhibited obvious spatial heterogeneity. Along the slope direction, the soil nutrient content gradually increased from the upper to down slope positions. In addition, the degree of nutrient loss at the different slope positions varied, and the difference in soil nutrients between the rainy and dry seasons gradually decreased at the nine test points from the upper to down slope positions. Along the vertical profile direction, the DOC, DON, TN, TP, and TK contents in the A layer during the rainy and dry seasons significantly differed, whereas the nutrient contents in the AC and C layers slightly changed (the difference was not significant). As shown in Figure 4, the soil aeration porosity and K_s significantly affected the changes in soil nutrients during the rainy and dry seasons. From the upper to down slope positions, the soil sand content, aeration pore content and K_s gradually decreased, and the loss of soil nutrients between the rainy and dry seasons was low. The significant effects of the lithology and soil properties on the loss of soil nutrients have been reported in a few studies (Albaladejo et al., 2012; Hoffmann et al., 2014; Rossel et al., 2014; Turrión et al., 2009). Teixeira and Misra (2005) noted that the magnitude of the soil nutrient loss was affected by the distribution of macropores. In addition to the soil properties, this difference may be related to subsurface flow. Soil physical properties and lithology affect the soil nutrient loss by influencing the distribution and development of subsurface flow.

Soil water–nutrient seepage is the primary mechanism of soil and water loss in Karst areas (Perakis and Hedin, 2002), and soil nutrients migrate mainly through hydrodynamic forces, which are closely related to water infiltration (Fu et al., 2016; Dai et al., 2017). Combined with Figures 3, 5 the trends in nutrient loss are consistent with the variation characteristics of the CV of the soil water content, with a high CV of the soil water content associated with an increase in the migration rate of soil nutrients. These findings indicate that soil water infiltration due to rainfall is the most direct factor influencing soil nutrient loss on Karst slopes.

Moreover, owing to the pronounced development of surface Karst features and the dense distribution of underground fissures in the Karst area of Southwest China, there is obvious underground seepage in this area (Zhang et al., 2011; Yuan et al., 2012). The results of this study also revealed a preferential flow phenomenon on the Karst slope (Figure 7). We considered that the existence of preferential flow further caused differences in nutrient loss along the slope direction. Preferential flow is an important component connecting the aboveground and underground systems in Karst areas and provides seepage and storage spaces for soil, water, and nutrients. Preferential flow can lead to water displacement, and some of the collected upper soil water moves to the deeper soil to replace the original water (Ma et al., 2016). Soil nutrients, especially DOC and DON, are active components of soil nitrogen and exhibit notable mobility, which can be lost by runoff or leaching with water transport (Perakis and Hedin, 2002; Teixeira and Misra, 2005). Combined with the theory of water replacement, these findings indicate that soluble nutrients may directly reach the deep layer via preferential flow channels. Soil water infiltration at the upper slope position progressed rapidly, and preferential flow frequently occurred, resulting in underdeveloped slope surface runoff, which could easily result in a reduction in the nutrient content in the soil through subsurface flow during rainfall. The rapid infiltration of soil water at the upper slope position and frequent preferential flow contribute to the rapid infiltration of surface water into deep layers, resulting in underdeveloped slope surface runoff and soil nutrient loss during rainfall. This finding is similar to the results of Yan et al. (2019), who reported that fissures with poor connectivity have better soil nutrient and fertility conditions. With decreasing slope position, the soil type on Karst dolomite slopes transitions from lithologic and shallow soils to Alfisols (Meng et al., 2022). The high clay content of Alfisols at the down slope position and the low frequency of preferential flow are helpful for maintaining the relative stability of nutrient levels. The existence of preferential flow easily leads to the direct downward migration of nutrients without interactions with upper soil organisms, which notably impacts the regional nutrient distribution (Allaire et al., 2009). The rate of nutrient loss at the upper slope position was greater than that at the down slope position, indicating that the preferential flow area at the upper slope position was the main zone of rapid soil nutrient loss.

In addition, the variation in TP between the rainy and dry seasons was the lowest among all soil nutrients. This may be due to the intense transformation reaction of phosphorus in soil and the high ability of the soil to adsorb and retain phosphorus, which makes it difficult to transport phosphorus in the soil. In conclusion, preferential flow in Karst dolomite rock leads to nutrient migration, resulting in significant differences in soil surface nutrient changes between the rainy and dry seasons at different slope positions.

5 Conclusion

The K_s of the Karst dolomite slope exhibited clear heterogeneity along the slope, the K_s at the upper slope position is significantly ($p < 0.05$) greater than that at the middle and down slope positions. Owing to the low hydraulic conductivity at the down slope position, the soil water content was greater than that at the middle and upper slope positions. Coupling monitoring of the soil water content and temperature revealed obvious preferential flow on the Karst dolomite slope, and the water content and temperature changes in the soil layer with preferential flow occurred earlier than those in the other soil layers without preferential flow. The patterns of the soil water content and surface nutrient loss on the Karst dolomite slope are consistent across the various positions and are related to the occurrence of preferential flow. There are significant differences in the changes between the different slope positions during the rainy and dry seasons. The average water content at the lower slope

position is the highest, and the CV values of the soil water content and nutrient loss are the lowest. Our results demonstrate that the preferential flow area at the upper slope position is the main zone of soil nutrient loss. Therefore, in Karst areas with rocky desertification and ecological management, we should first analyze the occurrence of preferential flow in surface Karst zones and then explore nutrient migration mechanism. Moreover, soil and water conservation measures should be implemented based on the preferential flow and nutrient characteristics of different slope positions. Seal off on the upper and middle slopes to avoid human disturbance, while coverage and no tillage measures should be carried out on the down slope to reduce nutrient loss.

Data availability statement

The original contributions presented in the study are included in the article/supplementary material, further inquiries can be directed to the corresponding authors.

Author contributions

XD: Conceptualization, Data curation, Formal Analysis, Investigation, Methodology, Validation, Visualization, Writing–original draft, Writing–review and editing. ZF: Data curation, Methodology, Project administration, Software, Writing–review and editing. YD: Conceptualization, Investigation, Project administration, Software, Supervision, Writing–original draft. HC: Conceptualization, Data curation, Funding acquisition, Project administration, Resources, Supervision, Validation, Writing–review and editing.

Funding

The author(s) declare that financial support was received for the research, authorship, and/or publication of this article. We thank the financial support for the research provided by the National Natural Science Foundation of China (No. 41930866), the Guangxi Key Research and Development Program, China (No. AB22035058) and the National Key Research and Development Program of China (No. 2023YFD1902801).

Conflict of interest

The authors declare that the research was conducted in the absence of any commercial or financial relationships that could be construed as a potential conflict of interest.

Generative AI statement

The author(s) declare that no Generative AI was used in the creation of this manuscript.

Publisher's note

References

Abaci, O., and Papanicolaou, A. T. (2009). Long-term effects of management practices on water-driven soil erosion in an intense agricultural sub-watershed: monitoring and modelling. *Hydrol. Process.* 23 (19), 2818–2837. doi:10.1002/hyp.7380

Albaladejo, J., Ortiz, R., Garcia-Franco, N., Navarro, A. R., Almagro, M., Pintado, J. G., et al. (2012). Land use and climate change impacts on soil organic carbon stocks in semi-arid Spain. *J. Soils Sediments* 13 (2), 265–277. doi:10.1007/s11368-012-0617-7

Allaire, S. E., Roulier, S., and Cessna, A. j. (2009). Quantifying preferential flow in soils: a review of different techniques. *J. Hydrology* 378 (1–2), 179–204. doi:10.1016/j.jhydrol.2009.08.013

An, N., Hemmati, S., and Cui, Y. J. (2017). Numerical analysis of soil volumetric water content and temperature variations in an embankment due to soil-atmosphere interaction. *Comput. Geotechnics* 83, 40–51. doi:10.1016/j.compgeo.2016.10.010

Bao, S. D. (2000). *Soil and agricultural chemistry analysis*. 3rd ed. Beijing: China Agriculture Publishing House, 263–270.

Beven, K., and Germann, P. (2013). Macropores and water flow in soils revisited. *Water Resour. Res.* 49 (6), 3071–3092. doi:10.1002/wrcr.20156

Bodner, G., Scholl, P., and Kaul, H. P. (2013). Field quantification of wetting-drying cycles to predict temporal changes of soil pore size distribution. *Soil Tillage Res.* 133, 1–9. doi:10.1016/j.still.2013.05.006

Carbajal-Morón, N. A., Manzano, M. G., and Mata-González, R. (2017). Soil hydrology and vegetation as impacted by goat grazing in Vertisols and Regosols in semi-arid shrublands of northern Mexico. *Rangel. J.* 39 (4), 363–373. doi:10.1071/RJ17061

Cerda, A., and Doerr, S. H. (2010). The effect of ant mounds on overland flow and soilerodibility following a wildfire in eastern Spain. *Ecohydrology* 3 (4), 392–401. doi:10.1002/eco.147

Chen, H. S., Liu, J. W., Zhang, W., and Wang, K. L. (2012). Soil hydraulic properties on the steep karst hillslopes in northwest guangxi, China. *Environ. Earth Sci.* 66 (1), 371–379. doi:10.1007/s12665-011-1246-y

Clothier, B. E., Green, S. R., and Deurer, M. (2008). Preferential flow and transport in soil: progress and prognosis. *Eur. J. Soil Sci.* 59, 2–13. doi:10.1111/j.1365-2389.2007.00991.x

Cui, G., and Zhu, J. (2018). Prediction of unsaturated flow and water backfill during infiltration in layered soils. *J. Hydrology* 557, 509–521. doi:10.1016/j.jhydrol.2017.12.050

Dai, Q. H., Peng, X. D., Yang, Z., and Zhao, L. S. (2017). Runoff and erosion processes on bare slopes in the karst rocky desertification area. *CATENA* 152, 218–226. doi:10.1016/j.catena.2017.01.013

Duan, X. Q., Deng, Y. S., Tao, Y., He, Y. B., Lin, L. R., and Chen, J. Z. (2021). The soil configuration on granite residuals affects benggang erosion by altering the soil water regime on the slope. *Int. Soil Water Conservation Res.* 9 (3), 419–432. doi:10.1016/j.iswcr.2021.03.003

Fu, Z. Y., Chen, H. S., Xu, Q. X., Jia, J., Wang, S., and Wang, K. L. (2016). Role of epikarst in near-surface hydrological processes in a soil mantled subtropical dolomite karst slope: implications of field rainfall simulation experiments. *Hydrol. Process.* 30 (5), 795–811. doi:10.1002/hyp.10650

Fu, Z. Y., Chen, H. S., Zhang, W., Xu, Q. X., Wang, S., and Wang, K. L. (2015). Subsurface flow in a soil-mantled subtropical dolomite karst slope: a field rainfall simulation study. *Geomorphology* 250, 1–14. doi:10.1016/j.geomorph.2015.08.012

Gerke, K. M., Sidle, R. C., and Mallants, D. (2015). Preferential flow mechanisms identified from staining experiments in forested hillslopes. *Hydrol. Process.* 29 (21), 4562–4578. doi:10.1002/hyp.10468

Gharabaghi, B., Safadoust, A., Mahboubi, A. A., Mosaddeghi, M. R., Unc, A., Ahrens, B., et al. (2015). Temperature effect on the transport of bromide and *E. coli* NAR in saturated soils. *J. Hydrology* 522, 418–427. doi:10.1016/j.jhydrol.2015.01.003

Greve, A., Andersen, M. S., and Acworth, R. I. (2010). Investigations of soil cracking and preferential flow in a weighing lysimeter filled with cracking clay soil. *J. Hydrology* 393 (1–2), 105–113. doi:10.1016/j.jhydrol.2010.03.007

Hardie, M. A., Cotching, W. E., Doyle, R. B., Holz, G., Lisson, S., and Mattern, K. (2011). Effect of antecedent soil moisture on preferential flow in a texture-contrast soil. *J. Hydrology* 398 (3–4), 191–201. doi:10.1016/j.jhydrol.2010.12.008

Hartmann, A., Goldscheider, N., Wagener, T., Lange, M., and Weiler, M. (2015). Karst water resources in a changing world: review of hydrological modeling approaches. *Rev. Geophys.* 52 (3), 218–242. doi:10.1002/2013RG000443

Hencher, S. R. (2010). Preferential flow paths through soil and rock and their association with landslides. *Hydrol. Process.* 24 (12), 1610–1630. doi:10.1002/hyp.7721

Herman, E. K., Toran, L., and William, W. B. (2012). Clastic sediment transport and storage in fluviokarst aquifers: an essential component of karst hydrogeology. *Carbonates Evaporites* 27 (3–4), 211–241. doi:10.1007/s13146-012-0112-7

Hincapie, I., and Germann, P. F. (2009). Impact of initial and boundary conditions on preferential flow. *J. Contam. Hydrology* 104 (1–4), 67–73. doi:10.1016/j.jconhyd.2008.10.001

Hoffmann, U., Hoffmann, T., Jurasinski, G., Glatzel, S., and Kuhn, N. J. (2014). Assessing the spatial variability of soil organic carbon stocks in an alpine setting (Grindelwald, Swiss Alps). *Geoderma* 232–234, 270–283. doi:10.1016/j.geoderma.2014.04.038

Hopp, L., and McDonnell, J. J. (2009). Connectivity at the hillslope scale: identifying interactions between storm size, bedrock permeability, slope angle and soil depth. *J. Hydrology* 376 (3–4), 378–391. doi:10.1016/j.jhydrol.2009.07.047

Hu, P. L., Zhao, Y., Xiao, D., Xu, Z. H., Zhang, W., Xiao, J., et al. (2021). Dynamics of soil nitrogen availability following vegetation restoration along a climatic gradient of a subtropical karst region in China. *J. Soils Sediments* 21, 2167–2178. doi:10.1007/s11368-021-02915-0

Jiang, Z. C., Lian, Y. Q., and Qin, X. Q. (2014). Rocky desertification in Southwest China:impacts, causes, and restoration. *Earth-Science Rev.* 132, 1–12. doi:10.1016/j.earscirev.2014.01.005

Karchegani, P. M., Ayoubi, S., Mosaddeghi, M. R., and Honarjoo, N. (2012). Soil organic carbon pools in particle-size fractions as affected by slope gradient and land use change in hilly regions, western Iran. *J. Mt. Sci.* 9, 87–95. doi:10.1007/s11629-012-2211-2

Kooijman, A. M., Jongejans, J., and Sevink, J. (2005). Parent material effects on Mediterranean woodland ecosystems in NE Spain. *Catena* 59 (1), 55–68. doi:10.1016/j.catena.2004.05.004

Korkanc, S. Y., and Dorum, G. C. (2019). The nutrient and carbon losses of soils from different land cover systems under simulated rainfall conditions. *CATENA* 172, 203–211. doi:10.1016/j.catena.2018.08.033

Krisnanto, S., Rahardjo, H., Fredlund, D. G., and Leong, E. C. (2016). Water content of soil matrix during lateral water flow through cracked soil. *Eng. Geol.* 210, 168–179. doi:10.1016/j.enggeo.2016.06.012

Li, D. J., Wen, L., Yang, L. Q., Luo, P., Xiao, K. C., Chen, H., et al. (2017). Dynamics of soil organic carbon and nitrogen following agricultural abandonment in a karst region. *J. Geophys. Res. Biogeosciences* 122 (1), 230–242. doi:10.1002/2016JG003683

Li, X. W., Jin, M. G., Huang, J. O., and Yuan, J. J. (2014). The soil–water flow system beneath a cotton field in arid North-west China, serviced by mulched drip irrigation using brackish water. *Hydrogeology J.* 23, 35–46. doi:10.1007/s10040-014-1210-5

Li, Z. W., Xu, X. L., Zhu, J. X., Xu, C. H., and Wang, K. L. (2019). Effects of lithology and geomorphology on sediment yield in karst mountainous catchments. *Geomorphology* 343, 119–128. doi:10.1016/j.geomorph.2019.07.001

Liu, H. H., Zhang, R., and Bodvarsson, G. S. (2005). An active region model for capturing fractal flow patterns in unsaturated soils: model development. *J. Contam. Hydrology* 80, 18–30. doi:10.1016/j.jconhyd.2005.07.002

Liu, Y., Chen, J., Zhang, X. J., Li, Q. Y., Du, Y., Liu, J. C., et al. (2020). Herbaceous community species composition and productivity are affected by soil depth and funnel effect in a simulated karst experiment. *Glob. Ecol. Conservation* 22, e01033. doi:10.1016/j.gecco.2020.e01033

Lu, X. Q., Toda, H., Ding, F. J., Fang, S. Z., Yang, W. X., and Xu, H. G. (2014). Effect of vegetation types on chemical and biological properties of soils of karst ecosystems. *Eur. J. Soil Biol.* 61, 49–57. doi:10.1016/j.ejsobi.2013.12.007

Ma, Y. Y., Qu, L. Q., Wang, W., Yang, X. S., and Lei, T. W. (2016). Measuring soil water content through volume/mass replacement using a constant volume container. *Geoderma* 271, 42–49. doi:10.1016/j.geoderma.2016.02.003

Meng, Q. M., Wang, S., Fu, Z. Y., Deng, Y. S., and Chen, H. S. (2022). Soil types determine vegetation communities along a toposequence in a dolomite peak-cluster depression catchment. *Plant Soil* 475, 5–22. doi:10.1007/s11104-022-05308-5

Nimmo, J. R. (2012). Preferential flow occurs in unsaturated conditions. *Hydrol. Process.* 26, 786–789. doi:10.1002/hyp.8380

Peng, T., and Wang, S. J. (2012). Effects of land use, land cover and rainfall regimes on the surface runoff and soil loss on karst slopes in southwest China. *CATENA* 90, 53–62. doi:10.1016/j.catena.2011.11.001

Perakis, S. S., and Hedin, L. O. (2002). Nitrogen loss from unpolluted South American forests mainly via dissolved organic compounds. *Nature* 415, 416–419. doi:10.1038/415416a

Rossel, R. A. V., Webster, R., Bui, E. N., and Baldock, J. A. (2014). Baseline map of organic carbon in Australian soil to support national carbon accounting and monitoring under climate change. *Glob. Change Biol.* 20 (9), 2953–2970. doi:10.1111/gcb.12569

Sheng, F., Wang, K., Zhang, R. D., and Liu, H. H. (2009). Characterizing soil preferential flow using iodine-starch staining experiments and the active region model. *J. Hydrology* 367 (1–2), 115–124. doi:10.1016/j.jhydrol.2009.01.003

Song, X. W., Gao, Y., Green, S. M., Dungait, J. A. J., Peng, T., Quine, T. A., et al. (2017). Nitrogen loss from Karst area in China in recent 50 years: an *in-situ* simulated rainfall experiment's assessment. *Ecol. Evol.* 7 (23), 10131–10142. doi:10.1002/ece3.3502

Tao, Y., He, Y. B., Duan, X. Q., Zou, Z. Q., Lin, L. R., and Chen, J. Z. (2017). Preferential flows and soil moistures on a Benggang slope: determined by the water and temperature co-monitoring. *J. Hydrology* 553, 678–690. doi:10.1016/j.jhydrol.2017.08.029

Tao, Y., Zou, Z. Q., Guo, L. H., Yang, B. L., Lin, L., Lin, H., et al. (2020). Linking soil macropores, subsurface flow and its hydrodynamic characteristics to the development of benggang erosion. *J. Hydrology* 586, 124829. doi:10.1016/j.jhydrol.2020.124829

Teixeira, P. C., and Misra, R. K. (2005). Measurement and prediction of nitrogen loss by simulated erosion events on cultivated forest soils of contrasting structure. *Soil Tillage Res.* 83 (2), 204–217. doi:10.1016/j.still.2004.07.014

Turrión, M.-B., Schneider, K., and Gallardo, J. F. (2009). Carbon accumulation in umbrisols under Quercus pyrenaica forests: effects of bedrock and annual precipitation. *CATENA* 79 (1), 1–8. doi:10.1016/j.catena.2009.04.004

Wang, D. J., Shen, Y. X., Huang, J., and Li, Y. H. (2016). Rock outcrops redistribute water to nearby soil patches in karst landscapes. *Environ. Sci. Pollut. Res.* 23 (9), 8610–8616. doi:10.1007/s11356-016-6091-9

Wei, H., Yang, Y. F., Wang, J. Y., Meng, Q. M., and Deng, Y. S. (2024). A comparison of preferential flow characteristics and influencing factors between two soils developed in the karst region of Southwest China. *Soil Tillage Res.* 241, 106132. doi:10.1016/j.still.2024.106132

Wen, L., Li, D. J., Yang, L. Q., Luo, P., Chen, H., Xiao, K. C., et al. (2016). Rapid recuperation of soil nitrogen following agricultural abandonment in a karst area, southwest China. *Biogeochemistry* 129, 341–354. doi:10.1007/s10533-016-0235-3

Xiao, D., Tan, Y. J., Liu, X., Yang, R., Zhang, W., He, X. Y., et al. (2020). Responses of soil diazotrophs to legume species and density in a karst grassland, southwest China. *Agric. Ecosyst. and Environ.* 288, 106707. doi:10.1016/j.agee.2019.106707

Yan, Y. J., Dai, Q. H., Jin, L., and Wang, X. D. (2019). Geometric morphology and soil properties of shallow karst fissures in an area of karst rocky desertification in SW China. *CATENA* 174, 48–58. doi:10.1016/j.catena.2018.10.042

Yao, Y. W., Dai, Q. H., Gan, Y. X., Gao, R. X., Yan, Y. J., and Wang, Y. H. (2021). Effects of rainfall intensity and underground hole (fracture) gap on nutrient loss in karst sloping farmland. *Sci. Agric. Sin.* 54 (1), 140–151. doi:10.3864/j.issn.0578-1752.2021.01.010

Yuan, H., Hu, N., Huang, Y. X., Zhang, Y. Z., He, X. Y., and Xie, H. X. (2012). Study on the response of soil nutrient content to soil loss in karst sloping land of southwest China. *Meteorological Environ. Res.* 3 (3–4), 46–52. doi:10.13989/j.cnki.0517-6611.2012.12.150

Zhang, J., Chen, H. S., Fu, Z. Y., and Wang, K. L. (2021). Effects of vegetation restoration on soil properties along an elevation gradient in the karst region of southwest China. *Agric. Ecosyst. and Environ.* 320, 107572. doi:10.1016/j.agee.2021.107572

Zhang, W., Zhao, J., Pan, F., Li, D., Chen, H., and Wang, K. (2015). Changes in nitrogen and phosphorus limitation during secondary succession in a karst region in southwest China. *Plant Soil* 391, 77–91. doi:10.1007/s11104-015-2406-8

Zhang, X. B., Bai, X. Y., and He, X. B. (2011). Soil creeping in the weathering crust of carbonate rocks and underground soil losses in the karst mountain areas of southwest China. *Carbonates Evaporites* 26 (2), 149–153. doi:10.1007/s13146-011-0043-8

Zhang, Z. B., Zhou, H., Zhao, Q. G., Lin, H., and Peng, X. (2014). Characteristics of cracks in two paddy soils and their impacts on preferential flow. *Geoderma* 228–229, 114–121. doi:10.1016/j.geoderma.2013.07.026

Appendix

To better describe and more clearly show the sampling sites for karst slope, we added the photographs of actual peak-cluster depression karst landscape, and marked the sampling sites of slope shown in Figure A1.

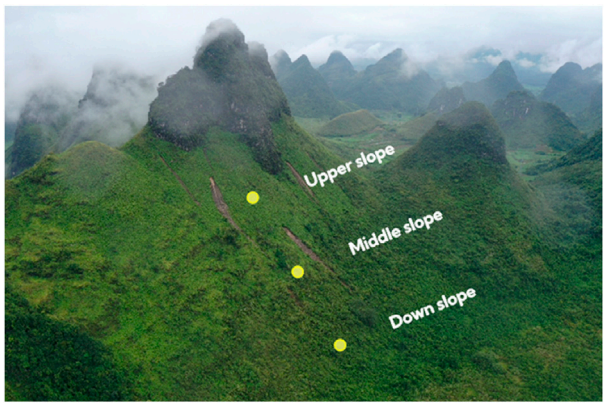

FIGURE A1
The photographs of actual peak-cluster depression karst landscape in Mulian catchment in Huanjiang county, Guangxi, China.

frontiers | Frontiers in Environmental Science

TYPE Original Research
PUBLISHED 24 April 2025
DOI 10.3389/fenvs.2025.1580149

OPEN ACCESS

EDITED BY
Xudong Peng,
Guizhou University, China

REVIEWED BY
Bingbing Zhu,
Shaanxi Normal University, China
Nan ShenChinese Academy of Sciences (CAS), China

*CORRESPONDENCE
Peng Li,
lipeng74@163.com

RECEIVED 20 February 2025
ACCEPTED 08 April 2025
PUBLISHED 24 April 2025

CITATION
Zhang N, Xia Z, Li P, Chen Q, Ke G, Yue F, Xu Y and Wang T (2025) The impact of rainfall and slope on hillslope runoff and erosion depending on machine learning.
Front. Environ. Sci. 13:1580149.
doi: 10.3389/fenvs.2025.1580149

The impact of rainfall and slope on hillslope runoff and erosion depending on machine learning

Naichang Zhang[1], Zhaohui Xia[1], Peng Li[2]*, Qitao Chen[2], Ganggang Ke[2], Fan Yue[1,3], Yaotao Xu[2] and Tian Wang[2]

[1]Power China Northwest Engineering Corporation Limited, Xi'an, China, [2]State Key Laboratory of Eco-Hydraulics in Northwest Arid Region of China, Xi'an University of Technology, Xi'an, China, [3]Shaanxi Union Research Center of University and Enterprise for River and Lake Ecosystems Protection and Restoration, Xi'an, China

Introduction: Soil erosion is a critical issue faced by many regions around the world, especially in the purple soil hilly areas. Rainfall and slope, as major driving factors of soil erosion, pose a significant challenge in quantifying their impact on hillslope runoff and sediment yield. While existing studies have revealed the effects of rainfall intensity and slope on soil erosion, a comprehensive analysis of the interactions between different rainfall types and slope is still lacking. To address this gap, this study, based on machine learning methods, explores the effects of rainfall type, rainfall amount, maximum 30-min rainfall intensity (I30), and slope on hillslope runoff depth (H) and erosion-induced sediment yield (S), and unveils the interactions among these factors.

Methods: The K-means clustering algorithm was used to classify 43 rainfall events into three types: A-type, B-type, and C-type. A-type is characterized by long duration, large rainfall amounts, and moderate intensity; B-type by short duration, small rainfall amounts, and high intensity; and C-type is intermediate between A-type and B-type. The Random Forest (RF) algorithm was employed to assess the impacts of these factors on runoff and sediment yield, along with a feature importance analysis.

Results: The results show that rainfall amount has the most significant impact on runoff and sediment yield. Under different rainfall types, the ranking of the effects of rainfall amount and I30 on H and S is as follows: rainfall amount (C>A>B), I30 (A>B>C). The impact of slope follows a trend of first increasing and then decreasing, with varying degrees of influence on H and S depending on the rainfall type.

Discussion: The novelty of this study lies in combining machine learning techniques to systematically evaluate, for the first time, the interactions between rainfall type and slope and their impact on hillslope runoff and sediment yield in purple soil hilly areas. This research not only provides a theoretical basis for soil erosion control but also offers scientific support for the precise prediction and management of soil conservation measures in purple soil regions.

KEYWORDS

purple soil, random forest, clustering algorithm, slope scale, soil erosion

1 Introduction

Purple soil was formed from purple rocks of the Jurassic and Cretaceous periods (Xiao et al., 2024), and is widely distributed in the middle and lower reaches of the Yangtze River in China (Zhang et al., 2004). It is rich in mineral nutrients, making it an important agricultural natural resource in the region (Chen et al., 2024). Purple soil is the main soil type in the sloping farmland of the Sichuan Basin, characterized by thin soil layers, low permeability, high hydrophobicity, and susceptibility to weathering (Zhang et al., 2023). Additionally, purple soil has low resistance to soil erosion, leading to severe soil erosion and nutrient loss in the area (Chu et al., 2020). Sediment deposition reduces reservoir storage capacity and increases the risk of flooding. Additionally, nutrient transfer leads to eutrophication of water bodies in the upper and middle reaches of the Yangtze River, exacerbating regional water environmental pressures (Gao et al., 2023; Xiao et al., 2024).

Slope is one of the primary contributors to hydraulic erosion, dynamic transport, and sediment transfer (Sun et al., 2022; Yan et al., 2024), and surface runoff plays a decisive role in the soil erosion process (Admas et al., 2022). Surface runoff is the driving force and carrier for sediment, nitrogen and phosphorus transport (Tapas et al., 2024), which on one hand leads to substantial loss of topsoil, and on the other, causes the loss of soluble and readily available nutrients during vegetation growth (Jia et al., 2007), reducing soil fertility. The purple soil distribution area receives abundant rainfall year-round, and most of the sloping farmlands in this region have steep slopes (≥10°), which causes severe soil and water loss. Yan et al. (2023) quantified the effects of five different crop types and rainfall conditions on slope runoff and soil erosion, and the results indicated that rainfall and runoff characteristics have a greater impact on runoff depth and soil loss rate than crop coverage. Chen et al. (2022) evaluated the impact of slope on runoff and sediment yield based on simulated rainfall methods and terrain models, revealing that slope gradient has a significant effect on both runoff and sediment yield. Therefore, rainfall and slope are two key factors influencing the soil erosion process in purple soil distribution areas. Based on a study of microtopographic dynamics in response to erosion processes on cultivated slopes in China's Shaanxi Loess Region, Rao et al. (2024) revealed critical findings: Erosion and deposition predominantly occurred in the middle-lower slope segments, with 70% of the slope surface exhibiting elevation fluctuations below 10 mm, while topographic alterations reached 25 mm in remaining areas. Investigations on purple soil slopes demonstrated that soil profile thickness significantly modulates hydrological processes. The soil's elevated clay fraction and permeability, combined with effective crop canopy coverage during rainy seasons, synergistically suppressed surface runoff generation (Liu et al., 2024). Notably, vegetation systems exert dual mechanisms in soil-water conservation: Canopy architecture enhances rainfall interception and dissipates raindrop kinetic energy, while root networks optimize soil porosity (particularly non-capillary pore development), thereby improving infiltration capacity, attenuating flow intensity, and intercepting sediment transport (Zhang et al., 2025).

For a long time, scholars have studied the mechanisms of runoff and sediment yield on purple soil slopes by adopting methods such as field monitoring, laboratory experiments, or a combination of both (Wang et al., 2024). Ma et al. (2017) analyzed the effects of different rain types on runoff and sediment yield on sloping farmland with different gradients, and the results showed that short-duration, high-intensity rainfall is the main type responsible for soil erosion. Sun et al. (2018) analyzed the impact of different rainfall intensities on runoff and sediment yield on purple soil slopes, pointing out that rainfall intensity and slope runoff were significantly positively correlated. Han et al. (2021) assessed the impact of slope gradient and rainfall intensity on runoff and sediment yield, and the results showed that, under the same rainfall intensity, the reduction in runoff decreases as slope increases, while soil erosion rates increase with steeper slopes.

Rainfall intensity and slope are key factors influencing soil erosion on hillslopes. The characteristics of rainfall, variations in slope, and their interactions play a decisive role in runoff, erosion, and sediment transport processes. While previous studies have explored the individual effects of rainfall intensity and slope on soil erosion, most have not thoroughly examined the complex interactions between rainfall type and slope, particularly under different rainfall types, where the impact of slope on runoff and sediment yield remains unclear. Furthermore, machine learning algorithms have been proven to be highly effective in spatial modeling analysis (Ahmed et al., 2024), yet their application in assessing the impact of soil erosion factors on soil erosion remains scarce. As such, existing research has yet to provide an effective framework for uncovering the specific mechanisms of the interaction between rainfall and slope in hillslope soil erosion, limiting our comprehensive understanding of the erosion process. At the same time, although machine learning methods can offer high prediction accuracy, especially in "black-box" systems, they lack transparent explanations of the model outcomes, making it difficult for researchers to understand the contribution of each predictor variable to the model output. Explaining model results is crucial for enhancing the model's credibility and applicability (Abdollahi et al., 2024).

To fill this research gap, this study employs machine learning methods, combining the K-means clustering algorithm for rainfall type classification and the Random Forest (RF) algorithm to assess the effects of rainfall and slope on hillslope runoff and sediment yield. We propose that machine learning-based analytical methods can effectively reveal the interactions between rainfall type and slope, providing more precise scientific support for soil erosion control in purple soil hilly areas. This study aims to provide scientific data to support soil erosion control under different rainfall types and slope conditions, ultimately offering more targeted management measures for regional soil conservation.

2 Materials and methods

2.1 Research area

The Wanan small watershed is located in Wanan Village, Yunxi Township, Yanting County, Sichuan Province (Figure 1A), with a total area of about 12.36 km^2, situated in the fourth tributary area of the Jialing River in the central Sichuan hilly region (Liu et al., 2022). The region has a mid-subtropical humid monsoon climate (Li et al., 2020), with an average annual temperature of 17.3°C, an annual precipitation of 836 mm, an annual evaporation of 604 mm, and an annual sunshine duration of 1,104 h (Chen et al., 2024). The main soil types include calcaric regosols, cumulic anthrosols, and calcaric

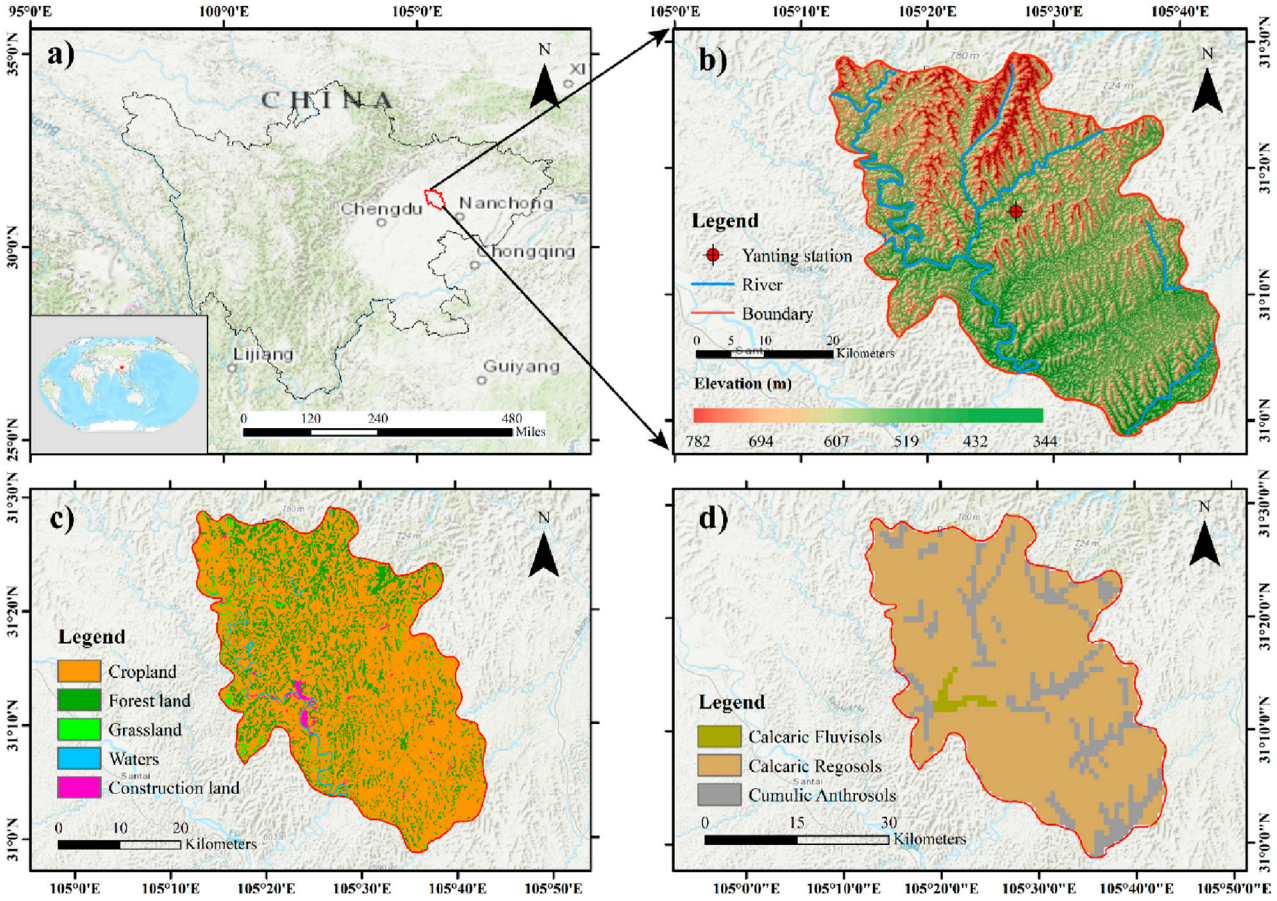

FIGURE 1
Map of the geographical location of the study area, **(a)** The location of the Wan'an small watershed in Sichuan Province, China; **(b)** The location of Yanting Hydrological Station in the Wan'an small watershed and the elevation map of the Wan'an small watershed; **(c)** The land cover map of Wan'an small watershed; **(d)** The soil type map of the Wan'an small watershed.

fluvisols (Figure 1D). The soil profile typically extends to depths of 20–70 cm, with exceptional cases demonstrating thickness exceeding 100 cm in localized areas. Particle size analysis revealed a granulometric composition dominated by silt (86.91%), followed by clay (11.56%) and sand (1.51%). The pedochemical characteristics showed alkaline conditions (mean pH 8.2), moderate organic matter content (20.12 g kg^{-1}), and favorable water retention properties with field capacity measured at 28.3%. Land use is mainly composed of cropland and forestland (Figure 1C). The primary crops are corn, wheat (Li et al., 2020). The main tree species are alder and cypress, which are gradually succeeded by pure cypress stands (Chen et al., 2024).

2.2 Data source

The data for this study were obtained from the Wanan Small Watershed Comprehensive Observation Station in Yanting County, Sichuan Province (Figure 2), covering meteorological and hydrological measurements from 2015 to 2019, including key indicators such as rainfall, runoff, and sediment yield. The Yanting Station established runoff plots with different slope gradients of 6.5°, 10°, 15°, 20°, and 25°. All runoff plots used a crop rotation system of winter wheat and summer maize to simulate local agricultural practices. In terms of cultivation management, sowing and fertilization followed traditional local practices, and no additional irrigation or fertilization was applied during the crop sowing period. Each runoff plot consists of three subplots, each with an area of 20 m × 5 m. To ensure the hydrological independence of the runoff systems, the plots are enclosed by concrete embankments to prevent lateral leakage. Additionally, in accordance with the structural characteristics of purple soil, a 60 cm thick concrete layer is poured at the lower end of the soil profile to simulate an impermeable interface between the soil and underlying rock. The backfilled soil follows the natural stratification of the original soil profile. At the base of each subplot, a collection trough is installed, and runoff from the trough is directed through a drainage pipe into a connected runoff pool for the collection of both runoff and sediment. The outlets and collection pools are kept fully independent to maintain hydrological independence. Furthermore, the plots are designed with varying slopes and soil types to simulate the spatial variability of soil and terrain in real-world conditions, enabling an in-depth investigation of the effects of these factors on slope runoff and erosion. The soil type, soil depth, farming practices, and fertilization methods were generally consistent across all runoff plots (Table 1). In total, 43 rainfall events with precipitation, runoff, and sediment during 2015–2019 were recorded.

FIGURE 2
Runoff plot, in which wheat is planted.

TABLE 1 2015–2019 overview of runoff plot.

Plot number	Slope/°	Slope length/m	Slope width/m	Soil type	Soil thickness/m	Soil conservation measure	Crops	Plant density/hm^2
1, 2, 3	6.5	20	5	Purple soil	50	Crop rotation	Wheat	22,770
							Corn	500
4, 5, 6	10	20	5	Purple soil	50	Crop rotation	Wheat	22,770
							Corn	500
7, 8, 9	15	20	5	Purple soil	50	Crop rotation	Wheat	22,770
							Corn	500
10, 11, 12	20	20	5	Purple soil	50	Crop rotation	Wheat	22,770
							Corn	500
13, 4, 15	25	20	5	Purple soil	50	Crop rotation	Wheat	22,770
							Corn	500

2.3 Methods

2.3.1 Clustering algorithm

The K-means clustering algorithm is a hard clustering algorithm under unsupervised learning (Mondal et al., 2016), which measures data object similarity using Euclidean distance, assuming that the smaller the distance, the greater the similarity (Guan et al., 2024). Before clustering, the number of clusters k is pre-set, and k initial cluster objects are then randomly selected from the dataset, with each representing the mean or center of a cluster. The remaining objects are then calculated based on their distances from all cluster centers and assigned to the nearest cluster, after which the mean of all clusters is recalculated as the new cluster center. This process is repeated until the cluster centers no longer change. The sum of squared errors is as follows (Guan et al., 2024):

$$E = \sum_{i=1}^{k} \sum_{x \in C_i} |x - \bar{x}_i|^2 \quad (1)$$

Here, E represents the sum of squared errors within the cluster, and $\bar{x}_i$ represents the mean value of the cluster C_i. The clustering result should ensure that the data objects within the same cluster are as close as possible, while the data objects in different clusters are as distant as possible. This study used the R language for data analysis

and applied unsupervised machine learning clustering algorithms to perform clustering analysis on 43 rainfall events.

2.3.2 Mann-Kendall rank order correlation trend test

H.B. Mann and M.G. Kendall introduced the Mann-Kendall test, commonly referred to as the M-K test (Mann, 1945; Kendall, 1948). Due to its robustness in handling extreme values, the Mann-Kendall test is widely adopted in hydrological studies (Chen and Grasby, 2009; Liu et al., 2021). In the MK test, the statistical variable S is:

$$S = \sum_{k=1}^{n-1} \sum_{j=k=1}^{n} Sgn(x_j - x_k) \tag{2}$$

where x_j and x_k are the values of the tested factor in years k and j, respectively; n is the year of the study series.

When n ≥ 10, the statistical variable S follows a normal distribution with variance Var(S):

$$Var(s) = n(n-1)(2n+5)/18 \tag{3}$$

The standardized statistic Z is calculated by the following equation:

$$Z = \begin{cases} \frac{S-1}{\sqrt{Var(S)}} & S > 0 \\ 0 & S = 0 \\ \frac{S+1}{\sqrt{Var(S)}} & S < 0 \end{cases} \tag{4}$$

If the value of Z is greater than 0, the time series shows an upward trend; if the value of Z is less than 0, the time series shows a downward trend. Meanwhile, the significance of the upward or downward trend is categorized into three categories according to the ab-solute value of the statistic Z value: when |Z| > 1.65, i.e., P < 0.05; when |Z| > 1.96, i.e., P < 0.01; and when |Z| > 2.58, i.e., P < 0.001.

2.3.3 Random forest algorithm

Random Forest is an ensemble learning method that improves model accuracy and robustness by constructing multiple decision trees (Breiman, 2001). Each tree is generated using the Bootstrap Sampling method, which involves randomly selecting samples from the original dataset with replacement (Li et al., 2024). This means that each tree is trained on a different sub-set of samples, reducing the risk of model overfitting. During training, Random Forest us-es the Bootstrap Sampling method to generate training sets for each decision tree, and the unselected samples are referred to as Out Of Bag (OOB) data (Nie et al., 2022). OOB data is used to assess model error, providing an unbiased estimate of the model's generalization ability.

Random Forest provides a method to evaluate feature importance. By calculating the contribution of each feature to the classification performance of the decision tree ensemble, its importance in the model is quantified. The Feature Importance Measures (FIM) represent the contribution of each feature, and the Out Of Bag (OOB) Error Rate is used as an evaluation metric to more accurately reflect the feature's impact on the overall model (Zhao et al., 2022). The indicator function is defined as (Zhao et al., 2022):

$$I(x, y) = \begin{cases} 1, x = y \\ 0, x \neq y \end{cases} \tag{5}$$

The $FIM_{km}^{(OOB)}$ of the mth feature F_m in the k-th tree is represented as (Zhao et al., 2022):

$$FIM_{km}^{(OOB)} = \frac{\sum_{p=1}^{n_0^k} I\left(Y_p, Y_p^k\right)}{n_0^k} - \frac{\sum_{p=1}^{n_0^k} I\left(Y_p, Y_{p,\pi_m}^k\right)}{n_0^k} \tag{6}$$

Here, n_0^k is the number of observation samples for the k-th tree; Y_p is the true classification label for the p-th sample. Y_p^k is the predicted classification result for the p-th observation of the OOB data by the k-th tree before the random permutation of F_m. Y_{p,π_m}^k is the classification result of the k-th decision tree for the p-th sample after the random permutation of F_m, during which the k-th decision tree needs to be retrained after permuting F_m. When feature F_m does not appear in the k-th tree, $FIM_{km}^{(OOB)} = 0$. The importance score of feature F_m in the entire random forest is defined as (Zhao et al., 2022):

$$FIM_{km}^{(OOB)} = \frac{\sum_{k=1}^{K} FIM_{km}^{(OOB)}}{K\sigma} \tag{7}$$

Here, K represents the number of decision trees in the random forest; σ is the standard deviation of the $FIM_{km}^{(OOB)}$. The importance score $FIM_{km}^{(OOB)}$ of feature F_m represents its contribution to classification accuracy. The feature importance score is evaluated by calculating the mean and standard deviation of the Out Of Bag (OOB) error rate, which reflects each feature's contribution to model performance. The number of decision trees is dynamically adjusted based on the training results, with the number of split nodes set to 3. The calculations were conducted using R programming.

2.3.4 Model performance evaluation

To assess the predictive capability of the model, this study employed various evaluation metrics, including Mean Absolute Error (MAE), Root Mean Square Error (RMSE), and Nash-Sutcliffe Efficiency (NSE). Among them, smaller MAE and RMSE values indicate lower prediction errors and higher accuracy, while a NSE value closer to 1 suggests a higher degree of agreement between the predicted and observed values, reflecting a stronger predictive ability of the model. The formulas are as follows:

$$MAE = \frac{1}{n} \sum_{i=1}^{n} |y_{o,i} - y_{s,i}| \tag{8}$$

$$NSE = 1 - \frac{\sum_{i=1}^{n} \left(y_{o,i} - y_{s,i}\right)^2}{\sum_{i=1}^{n} \left(y_{o,i} - \overline{y_o}\right)^2} \tag{9}$$

$$RMSE = \sqrt{\frac{1}{n} \sum_{i=1}^{n} \left(y_{o,i} - y_{s,i}\right)^2} \tag{10}$$

where $y_{o,i}$ and $y_{s,i}$ represent the observed and predicted values, respectively; n represents the total number of samples; and i indicates the i sample, ranging from 1 to n.

2.3.5 Statistical analysis

In this study, the Random Forest (RF) algorithm was implemented using the random Forest package in the R software environment. A regression tree-based RF approach was chosen, as

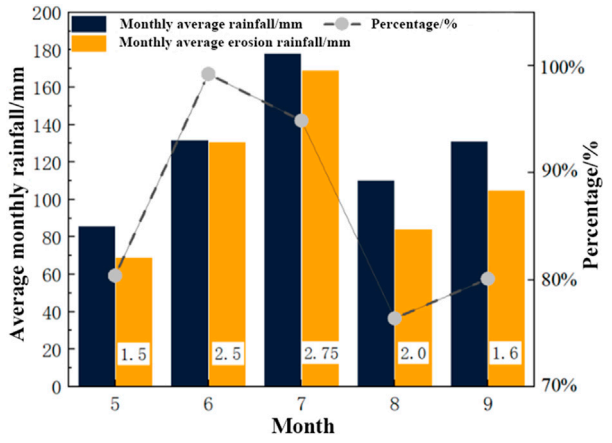

FIGURE 3
Statistics of erosive rainfall in months with frequent rainfall from 2015 to 2019.

the objective was to predict continuous variables, specifically runoff depth and sediment yield, rather than to address classification problems. In the Random Forest model, each decision tree independently generates a prediction, and the final result is obtained by averaging the predictions of all trees. This ensemble technique effectively reduces the risk of overfitting and enhances the overall predictive accuracy of the model. To prevent overfitting or underfitting, 5-fold cross-validation was used in this study to evaluate the model's performance. Graphical outputs were generated using Origin 2021.

3 Results

3.1 Determination and classification of erosive rainfall

3.1.1 Determination of erosive rainfall

A total of 43 erosive rainfall events (>12.7 mm) were selected during the 2015–2019 study period (Yang et al., 2025). Erosive rainfall mainly occurred from May to September each year (Figure 3), with average monthly occurrences of 1.5, 2.5, 2.75, 2, and 1.6 events, respectively. The average annual erosive rainfall was 493 mm, accounting for 57.57% of the average annual total rainfall of 856 mm. Erosive rainfall in the study area was mainly concentrated in the rainy season.

3.1.2 Classification and characteristics of erosive rainfall types

The K-means clustering algorithm was used to perform cluster analysis on 43 erosive rainfall events, and the results were evaluated using a discriminant clustering method. In the analysis, rainfall amount (P), rainfall duration (D), and maximum 30-min rainfall intensity (I30) were selected as rainfall characteristic indicators. The study results categorized these 43 rainfall events into three rainfall types.

The scatter plots of the clustering functions for the three rainfall types are concentrated in different regions (Figure 4). The significance test value of the clustering function for Type B rainfall is $P < 0.05$, indicating that the group centroids of this type show significant differences, with clear clustering boundaries. Type B and Type C rainfall show greater dispersion along function 2 and function 1, while Type A rainfall is more concentrated. Type C rainfall shows the most significant variation in rainfall characteristics, while Type B has strong independent characteristics, and Type A is relatively stable in its rainfall features.

Table 2 shows the clustering results of the 43 rainfall events. The results show that the distribution of rainfall types is as follows: Type A accounts for 8.84%, Type B accounts for 68.7% (the main type), and Type C accounts for 37.2%. Type A rainfall has the longest average duration (46.29 h), the highest average rainfall amount (94.38 mm), and the lowest average maximum 30-min rainfall intensity (19.48 mm/h). Its individual event erosion intensity (S) ranges from 0.092 to 0.882 t/hm^2, and the runoff depth (H) ranges from 1.99 to 21.61 mm. Type B rainfall has the shortest average duration (0.65 h), the lowest average rainfall amount (37.94 mm), and the highest average maximum 30-min rainfall intensity (39.01 mm/h). Its individual event erosion intensity (S) ranges from 0.0095 to 0.361 t/hm^2, and the runoff depth (H) ranges from 0.782 to 4.846 mm. The Type C rainfall pattern exhibited intermediate characteristics between Type A and Type B, with mean values of rainfall duration (26.28 h), maximum 30-min intensity (24.78 mm/h), and total precipitation (63.08 mm) falling between those of the two established rainfall types.

3.2 The relationship between rainfall characteristic indicators and runoff depth, erosion and sediment yield

3.2.1 Importance analysis of rainfall factors on runoff depth and erosion sediment yield

The clustering results identified three rainfall patterns: A, B, and C. Combined with the data from the 15 selected runoff plots, a total of 645 data points were obtained. This data will be consolidated according to different slopes (6.5°, 10°, 15°, 20°, and 25°) and used as input for the Random Forest model, with 75% randomly selected as the training set and 25% as the testing set.

We predicted runoff depth and sediment yield under different slope conditions and assessed the model's performance accordingly (Table 3). At a 6.5° slope, the model's prediction of runoff depth was less than ideal, with a Nash-Sutcliffe Efficiency (NSE) of only 0.58. However, under other slope conditions, the model demonstrated high accuracy in predicting both runoff depth and sediment yield, with NSE values exceeding 0.75.

Based on the model we developed, the feature importance scores from the Random Forest model were used in this study to identify the contributions of various rainfall factors and slope conditions to runoff depth and sediment yield. Rainfall characteristics are the main driving factors of runoff and erosion (Dos Santos et al., 2017). In this study, five rainfall factors were selected: rainfall duration (D), rainfall amount (P), maximum 30-min rainfall intensity (I30), average rainfall intensity (Im), and rainfall erosivity (F). Additionally, two compound rainfall factors were considered: the product of rainfall amount and average rainfall intensity (PIm), and the product of rainfall amount and maximum 30-min rainfall

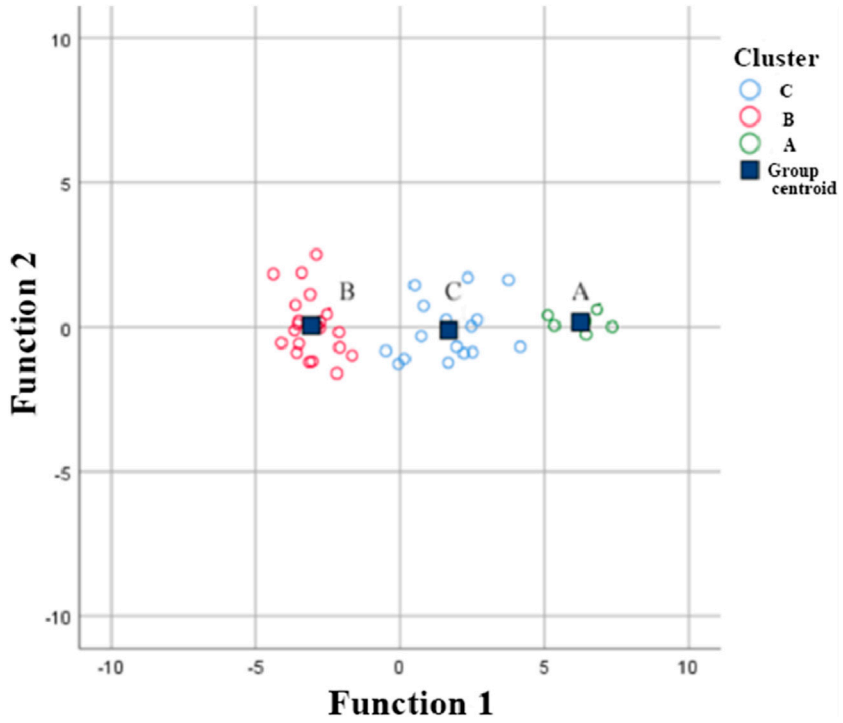

FIGURE 4
Scatter plot of erosive rainfall discrimination classification.

TABLE 2 Rainfall characteristics of different types of rain.

Type of rainfall	Number of events	Characteristic indexes						
			I30/mm/h	P/mm	D/h	Im/mm/h	S/t/hm^2	H/mm
A	6	Mean	19.48	94.38	46.30	3.10	0.55	17.65
		V_{25}	5.60	42.50	39.42	1.20	0.09	1.98
		V_{75}	38.4	185.8	52.12	4.70	0.88	21.61
B	21	Mean	39.01	37.94	0.65	6.90	0.24	6.51
		V_{25}	7.20	14.80	1.00	4.60	0.01	0.78
		V_{75}	89.50	102.00	11.00	8.00	0.36	4.85
C	16	Mean	24.78	63.08	26.28	1.90	0.27	2.69
		V_{25}	1.20	17.40	16.83	1.40	0.01	0.61
		V_{75}	64.9	185.8	35.67	2.80	0.08	2.59

Note: V25 and V75 represent the 25% quantile value and 75% quantile value respectively; I30, P, D, Im, S and H represent the maximum 30 min rainfall intensity, rainfall, duration, average rainfall intensity, runoff depth, and soil loss.

intensity (PI30), to comprehensively analyze the impact of rainfall on soil erosion. The importance of each factor on runoff depth (H) and sediment yield (S) was evaluated using the Random Forest (RF) algorithm (Zhu et al., 2020). For runoff generation, the number of decision trees for each slope was 380, 200, 400, 250, and 600; for sediment production, the number of decision trees for each slope was 500, 800, 400, 460, and 500. The number of split nodes for all models was set to 3.

As shown in Figure 5, PI30 has the highest importance for runoff generation, reaching a maximum of 40.85% at a slope of 5°, with P accounting for a large proportion, while I30 is less important and D has the lowest impact on runoff generation (2%). P has the greatest impact on sediment yield, reaching 41.87% at a slope of 20°. The importance of Im and I30 for sediment yield is as low as 5% and 3%, respectively, at their lowest. It can be concluded that P is the primary factor

TABLE 3 Prediction evaluation of random forest model for hillslope runoff depth and sediment yield under different rainfall patterns.

Predictor variables	Slope classification	MAE	NSE	RMSE
Runoff depth	6.5°	3.69	0.58	5.27
	10°	1.23	0.94	1.17
	15°	0.7	0.82	1.32
	20°	1.21	0.99	2.06
	25°	0.91	0.87	2.13
Sediment yield	6.5°	0.11	0.76	0.22
	10°	0.15	0.92	0.25
	15°	0.11	0.81	0.29
	20°	0.15	0.91	0.24
	25°	0.21	0.87	0.23

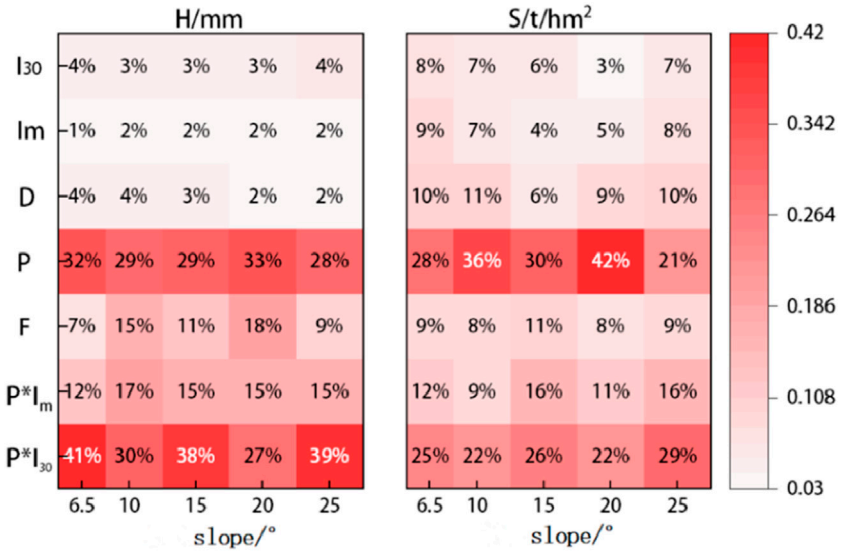

FIGURE 5
Rainfall factor to H, S importance score.

affecting runoff and sediment yield on slopes, and Type A rainfall with high rainfall and low intensity has the greatest erosive impact on corn slopes, which is consistent with previous findings.

3.2.2 The influence of rainfall on slope runoff depth and erosion sediment yield

The Random Forest calculation results show that P has a significant influence on H and S. Under different rainfall types, the effect of P on H and S shows a linear increasing trend (Figure 6). Linear fitting results indicate that the slope of H with increasing P is 0.23, 0.22, and 0.33 for Type A, B, and C rainfalls, respectively, while the slope of S with increasing P is 0.08, 0.04, and 0.1, respectively. The results indicate that the erosive effect of rainfall on purple soil slopes varies across the three rainfall types. Based on the overall trend and fitting results, the order is Type C > Type A > Type B.

3.2.3 The impact of maximum 30 min rainfall intensity on slope runoff depth and erosion sediment yield

As shown in Figure 7, there is a clear correlation between I30 and H, S. As I30 increases, a breakpoint is observed in the relationship for all three rainfall types. Before I30 reaches 17.3 mm/h and 23.4 mm/h, H and S increase slowly with I30, and the slope of the fitted line is close to zero. After I30 exceeds 17.3 mm/h and 23.4 mm/h, H and S increase rapidly, with a noticeable rise in the slope of the fitted line. To further confirm these critical points of I30, the Mann-Kendall test was used to evaluate the significance of the changes in slope. This test is particularly useful for detecting monotonic trends and was applied here to assess whether the slopes of H and S with increasing I30 are significantly different across the three rainfall types. The Mann-Kendall test identified the

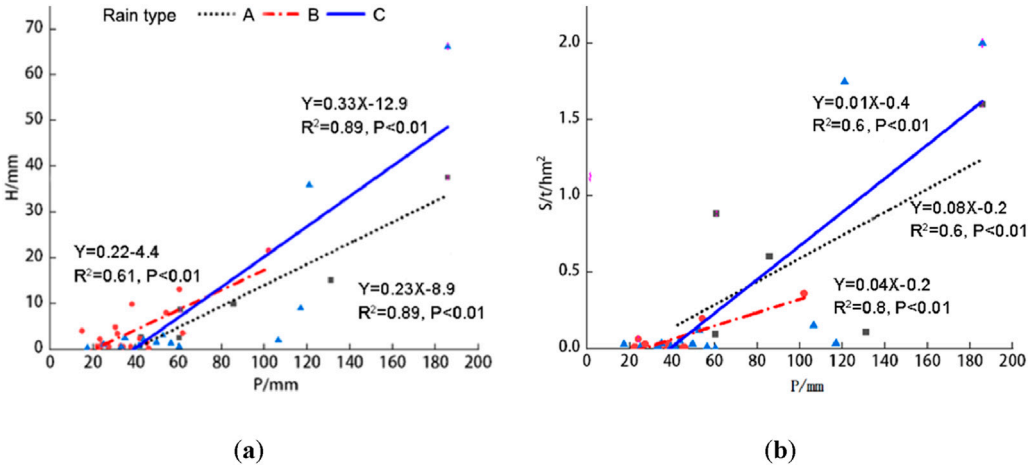

FIGURE 6
The relationship between P and H and S, **(a)** The impact of rainfall on slope runoff for different types of rainfall; **(b)** The effect of rainfall of different rainfall types on slope erosion and sediment yield.

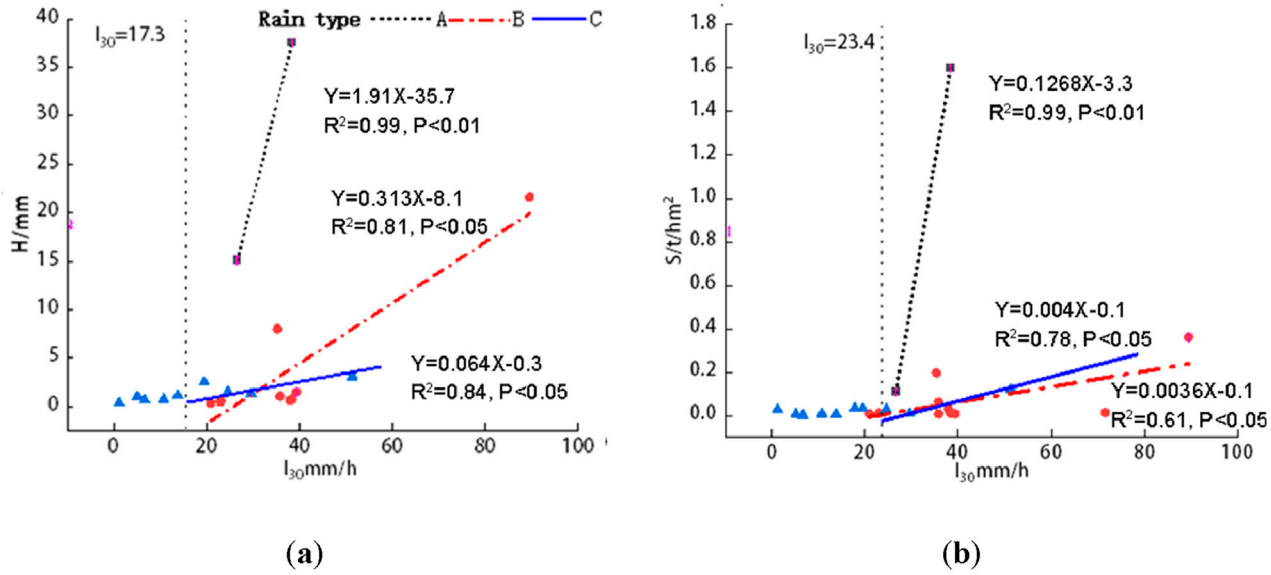

FIGURE 7
The relationship between I30 and H and S, **(a)** The effect of maximum 30 minute rainfall intensity on slope runoff depth under different rainfall types; **(b)** The effect of maximum 30 minute rainfall intensity on slope erosion and sediment yield under different rainfall types.

intersection points for runoff and sediment yield at 17.3 mm/h and 23.4 mm/h, respectively. Furthermore, to evaluate whether the slopes were significantly different, the confidence intervals for the slopes of H and S with increasing I30 for each rainfall type were compared. The slopes of H with increasing I30 for Type A, B, and C rainfall were 1.91, 0.32, and 0.064 mm, respectively, while the slopes of S with increasing I30 were 0.13, 0.036, and 0.004 t/km^2, respectively. If the confidence intervals for two slopes did not overlap, it was concluded that the slopes were significantly different. Based on this analysis, the impact of I30 on runoff and sediment yield follows the order: Type A > Type B > Type C.

3.3 The impact of rainfall and slope on runoff and sediment production on slope surfaces

3.3.1 The influence of different rainfall types on slope runoff and sediment yield

Slope has a significant effect on soil erosion on purple soil slopes (Yang et al., 2023). The relation-ship between runoff depth, sediment yield, slope, and rainfall in the study area is shown in Figure 8.

With changes in slope, the variation pattern of runoff depth on the slopes of runoff plots shows certain differences. Under Type A rainfall, H increases with the slope initially, reaches a peak at a slope

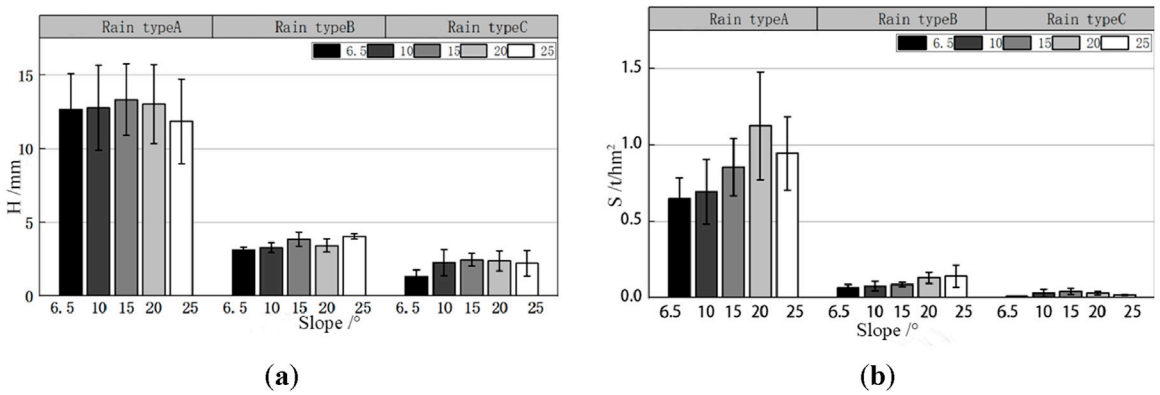

FIGURE 8
Characteristics of H and S under different rain patterns and slopes, **(a)** The influence of different rainfall patterns on slope runoff depth at different slopes; **(b)** The impact of different rainfall patterns on slope erosion and sediment yield at different slopes.

of 15°, and then gradually decreases, forming a convex shape. Under Type B rainfall, H peaks at 15°, then decreases, and rises back to the peak at 25°. Based on Figure 9, this occurs because, under low rainfall, the influence of slope and rainfall on runoff generation is similar, causing fluctuations in runoff at 25°. Under the influence of Type C rainfall, the trend of H increasing with slope is similar to that under Type A rainfall, peaking at 15° with an increase of 8.57%, and then gradually decreasing.

The variation pattern of S with slope differs under each rainfall type, but overall, it shows an initial increase followed by a decrease as the slope increases. Under Type A rainfall, S increases with the slope and reaches a peak at 20°. Under Type B rainfall, S continues to increase with the slope, reaching its maximum at 25°. Under Type C rainfall, the erosion amount peaks at a slope of 15°, with an increase of 37.95%, and then gradually decreases, forming a convex shape.

3.3.2 The influence of slope and important rainfall factors on slope runoff depth and erosion sediment yield

As shown in Figure 9, when rainfall is between 45.1 and 54.2 mm, the impact of rainfall on runoff generation increases significantly, with the maximum growth rate reaching 97.8%, and the influence of slope on runoff also increases simultaneously. When rainfall is between 54.2 and 102 mm, the influence of rainfall begins to decrease, while the influence of slope on runoff increases rapidly and reaches its maximum. At 100–185.8 mm, the effects of both rainfall and slope on runoff generation begin to decrease. When I30 is between 20.95 and 71.62, the impact of I30 and slope on runoff generation is minimal, but beyond this range, the influence increases significantly, with the maximum growth rates reaching 136.52% and 1498.14%, respectively. The larger the I30, the greater the impact of slope on sediment yield.

When rainfall is between 17.4 and 52.7 mm, the impact of rainfall and slope on sediment yield is relatively small. Between 52.7 and 54.2 mm, the impact of slope on sediment yield starts to increase and continues to rise, becoming significant when rainfall reaches 102 mm, and peaking at 185.5 mm. When the I30 value exceeds the critical threshold, the impact of slope on sediment yield is considerable in the range of 17.7–51.4. When I30 reaches 89.5, the effect of slope on sediment yield decreases significantly, while the effect of I30 on sediment yield increases substantially.

4 Discussion

The main goal of this research is to utilize machine learning methods to investigate the effects of different rainfall types and slope conditions on hillslope runoff and sediment yield. By employing techniques such as the K-means clustering algorithm for rainfall classification and the Random Forest algorithm for impact assessment, this study aims to provide a comprehensive analysis of how rainfall characteristics and slope interact to in-fluence soil erosion processes in purple soil hilly areas. This approach not only addresses existing gaps in the literature regarding the complex interactions between these factors but also offers valuable insights for effective soil erosion control and management strategies.

According to this study, Type A rainfall is characterized by low frequency, long duration, high rainfall amount, and low rainfall intensity. Despite the low intensity, its large rainfall amount and extended duration result in higher soil erosion intensity. Type B rainfall, with high frequency, short duration, small rainfall amount, and high intensity, has a moderate erosion effect on soil and should be a priority for soil and water conservation measures. Type C rainfall has a duration and rainfall amount between those of Type A and Type B, and its impact on soil erosion is the smallest. The erosion capacity of these rainfall events is ranked as: Type A > Type B ≥ Type C. This result emphasizes that there are differences in the impact of different types of rainfall on soil erosion. From this perspective, rainfall is an important factor in predicting or indicating the degree of soil erosion in the research area. Other previous studies have also confirmed that rainfall plays a crucial role in the process of soil erosion (Berndtsson and Larson, 1987; Dunne et al., 1991; Fang et al., 2012).

It is noteworthy that the sediment yield caused by B rainfall type is at a moderate level, but as the main rainfall type in the study area, characterized by short-duration heavy rainfall, its impact on soil

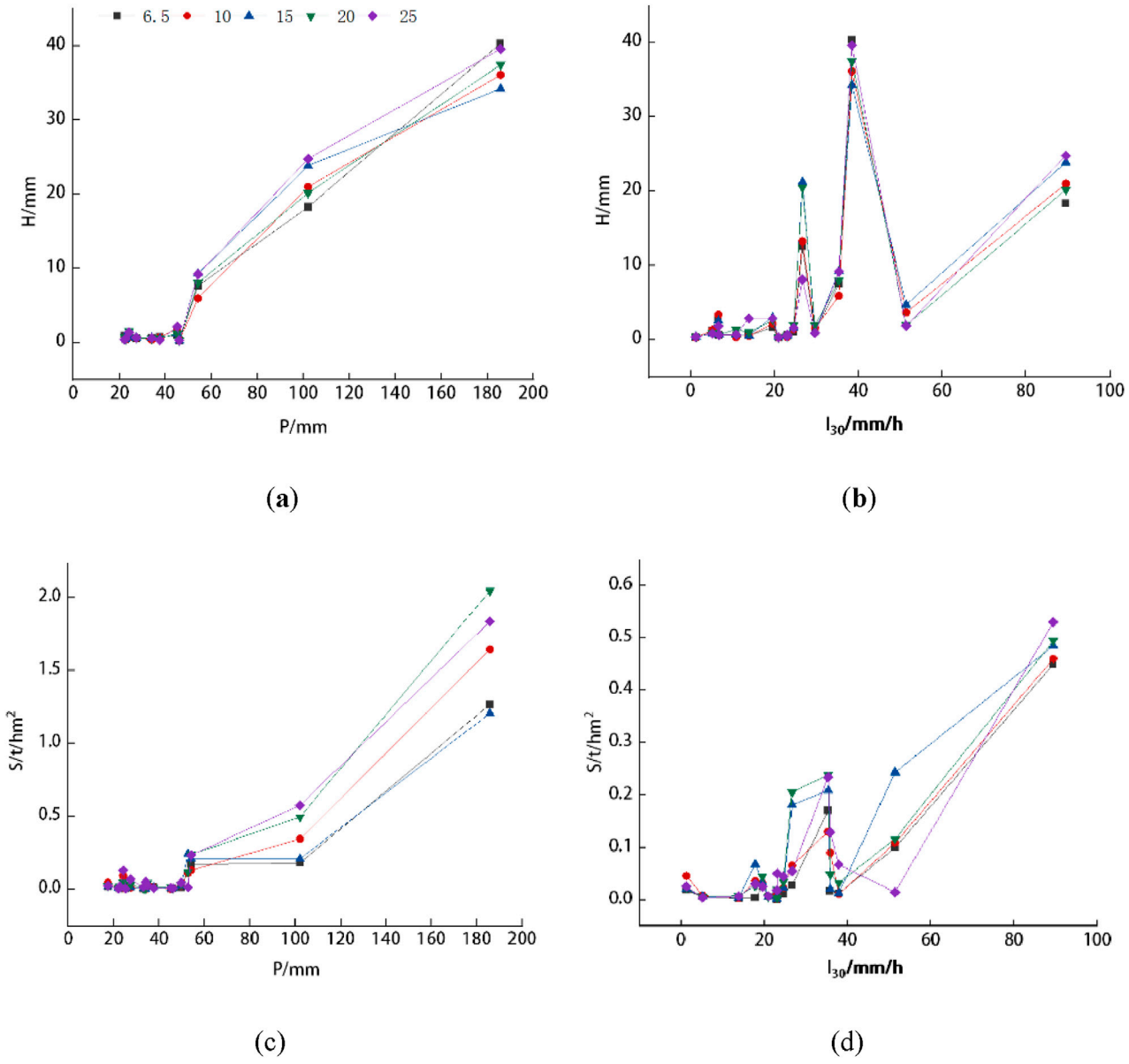

FIGURE 9
Under different slope changes, **(a)** The effect of rainfall on slope runoff depth; **(b)** The effect of maximum 30 minute rainfall intensity on slope runoff depth; **(c)** The effect of rainfall on slope sediment yield; **(d)** The effect of maximum 30 minute rainfall intensity on slope sediment yield.

erosion cannot be underestimated. Previous studies have shown that rainfall intensity is closely related to soil erosion. Cao et al. (Cao et al., 2020) have pointed out that rainfall intensity has a significant impact on surface soil erosion. During the interaction process between rainfall and the soil surface, high-intensity rainfall facilitates the formation of surface crusting and sealing, which can reduce infiltration and increase surface runoff (Vandervaere et al., 1997). The development of surface sealing promotes soil erosion because it increases sediment transport by accelerating surface flow (Assouline, 2004). The research results differ from those of the indoor simulated rainfall experiments (Geng et al., 2010). The study found that the canopy of corn plants can effectively buffer the kinetic energy of rainfall, reducing its ability to convert into erosive energy. As a result, rainfall mainly turns into stemflow and throughfall, which have less erosive energy, thereby mitigating soil erosion (Shou et al., 2016). However, the tall stalks of corn plants also have negative effects. Raindrops regain erosive energy at the edges and tips of corn leaves, intensifying splash erosion under the canopy and in-creasing the turbulence of slope runoff (Ma et al., 2015).

The influence of rainfall factors varies across plots with different slopes. For example, as the slope increases from 20° to 25°, the influence of P on runoff and sediment yield de-creases to 28.47% and 21.32%, while PI30 increases to 39.23% and 29.48%. The main reason is that the rainfall-receiving area of the 25° slope decreases, reducing the amount of rainfall on the slope, which causes the influence of I30 and Im on runoff to increase rap-idly. This result is consistent with the study by Chen et al. (2022), which found that

under fixed conditions of terrain height and rainfall intensity, the total amount of slope runoff continuously decreases with an increase in slope gradient.

Overall, rainfall amount and compound rainfall factors have a significant impact on runoff and sediment yield, consistent with the statistical analysis results of other scholars on the relationship between rainfall characteristics and sediment yield (Foster et al., 1982; Zhang et al., 2021). As the slope increases, the importance of I30, average rainfall intensity, and duration decreases, but their importance gradually increases again beyond 20°. In general, most factors show significant changes in importance around a slope of 20°, indicating the presence of a critical slope at approximately 20° (Hu and Jin, 1999).

The importance of slope for runoff generation under each rainfall type is ranked as follows: Type B > Type C > Type A. For sediment yield, the effect of slope change is ranked as Type C > Type A > Type B across the three rainfall types. Under different rainfall types, H reaches its peak at a slope of 15°, while sediment yield peaks between 20° and 25°, de-pending on the rainfall type. This may be related to the critical slope in the erosion process (Jin, 1995). Figure 8 confirms that slope significantly influences runoff generation across the three rainfall types, and the peak runoff depth at corresponding slopes further validates the existence of a critical slope effect. The influence of slope on runoff generation first in-creases and then decreases with increasing rainfall, while it increases with I30 after reaching the critical values. The impact of slope on sediment yield also shows a trend of first increasing and then decreasing with rising I30, which is similar to the conclusion of Geng et al. (2010). The influence gradually increases as rainfall increases.

Although this study effectively analyzes the impact of rainfall and slope on surface runoff and sediment transport, we also recognize that erosive rainfall and sediment transport are complex processes influenced by multiple interacting factors, including soil properties, land use, vegetation cover, and other climatic variables. Therefore, this study simplifies erosive rainfall into three types (Type A, Type B, and Type C rainfall), without considering the potential interactions between these factors or the broader climatic context. For example, soil permeability, soil moisture content, and land use patterns can all significantly affect surface runoff and sediment processes, yet these factors were not individually considered in this study. Although we effectively classified rainfall types using the K-means clustering algorithm, the simplicity of this method may not have captured the complex nonlinear relationships between rainfall variables, especially the interactions between rainfall amount, duration, and intensity. Thus, the K-means clustering method may, in some cases, limit the accuracy of rainfall type classification. To improve classification accuracy, future research could consider using more advanced clustering methods, such as spectral clustering or deep learning models, which are better equipped to capture nonlinear relationships and patterns within rainfall data. Finally, this study primarily focuses on surface runoff and sediment transport processes in the purple soil hilly region. The applicability of the results and conclusions may be limited in other geographical are-as or under different soil types. Therefore, we recommend that future work incorporate field data from different regions to conduct broader validation and expansion studies, providing more comprehensive soil and water conservation management recommendations.

5 Conclusion

1) In the southwestern purple soil hilly region, erosive rainfall can be classified into three types: Type A (long duration, large rainfall, moderate intensity), Type B (short duration, high intensity, small rainfall), and Type C (moderate duration and rainfall, moderate intensity). Type B rainfall occurs frequently and with high intensity, contributing the most to slope erosion, while Type A rainfall significantly impacts slope erosion, despite its lower frequency. Type C rainfall has a relatively small effect on slope erosion.
2) Rainfall amount is the primary factor affecting slope water and sediment dis-charge, and the composite rainfall factor PI30 plays the most important role in runoff and sediment production. Under different rainfall types, the influence of rainfall amount on runoff depth and sediment discharge is as follows: Type C > Type A > Type B. With in-creasing slope, the impact of rainfall characteristics on water and sediment shows an initial increase followed by a decrease.
3) Slope significantly affects the water and sediment discharge of purple soil slopes. Under different rainfall types, the impact of slope on runoff and sediment varies, but generally shows an increasing-then-decreasing trend. The influence of slope on water and sediment is strongest under Type B rainfall, while the impact on sediment discharge is most significant under Type C rainfall.

Developing a model to explain the complexity and abrupt variations in observed trends remains an important challenge, but the current research has provided substantial insights into the relationship between rainfall characteristics and slope response. While numerous unanswered questions persist in this field, the findings significantly advance our understanding of these complex interactions.

The significance of this study lies in revealing the impact of rainfall and slope on slope water and sediment processes, particularly providing scientific support for soil and water conservation management and ecological protection. The findings can offer decision-making assistance to urban planners, land use managers, and hydrological designers, helping them develop more effective soil and water conservation measures, reduce soil erosion, and promote regional sustainable development.

Data availability statement

The data used in this paper is not publicly accessible at this time, as they are classified as government confidential data. Therefore, the authors do not have the right to disclose them.

Author contributions

NZ: Writing – original draft, Writing – review and editing. ZX: Conceptualization, Supervision, Writing – review and editing. PL: Conceptualization, Funding acquisition, Project administration, Supervision, Writing – review and editing. QC: Supervision,

Writing – review and editing. GK: Writing – review and editing. FY: Writing – review and editing. YX: Visualization, Writing – review and editing. TW: Project administration, Writing – review and editing.

Funding

The author(s) declare that financial support was received for the research and/or publication of this article. This research was supported by the National Natural Science Foundation of China (Grant No. U2243201) and Natural Science Foundations of Shaanxi Province (Grant No. 2023-ZDLSF-65).

Conflict of interest

Authors NZ, ZX, and FY were employed by Power China Northwest Engineering Corporation Limited.

The remaining authors declare that the research was conducted in the absence of any commercial or financial relationships that could be construed as a potential conflict of interest.

Generative AI statement

The author(s) declare that no Generative AI was used in the creation of this manuscript.

Publisher's note

All claims expressed in this article are solely those of the authors and do not necessarily represent those of their affiliated organizations, or those of the publisher, the editors and the reviewers. Any product that may be evaluated in this article, or claim that may be made by its manufacturer, is not guaranteed or endorsed by the publisher.

References

Abdollahi, A., Li, D., Deng, J., and Amini, A. (2024). An explainable artificial-intelligence-aided safety factor prediction of road embankments. *Eng. Appl. Artif. Intell.* 136, 108854. doi:10.1016/j.engappai.2024.108854

Admas, B. F., Gashaw, T., Adem, A. A., Worqlul, A. W., Dile, Y. T., and Molla, E. (2022). Identification of soil erosion hot-spot areas for prioritization of conservation measures using the swat model in ribb watershed, Ethiopia. *Resour. Env. Sustain.* 8, 100059. doi:10.1016/j.resenv.2022.100059

Ahmed, I. A., Talukdar, S., Baig, M. R. I., Shahfahad, M., Ramana, G. V., and Rahman, A. (2024). Quantifying soil erosion and influential factors in guwahati's urban watershed using statistical analysis, machine and deep learning. *Remote Sens. Appl.* 33, 101088. doi:10.1016/j.rsase.2023.101088

Assouline, S. (2004). Rainfall-induced soil surface sealing: a critical review of observations, conceptual models, and solutions. *Vadose Zone J.* 3 (2), 570–591. doi:10.2136/vzj2004.0570

Berndtsson, R., and Larson, M. (1987). Spatial variability of infiltration in a semi-arid environment. *J. Hydrol.* 90 (1), 117–133. doi:10.1016/0022-1694(87)90175-2

Breiman, L. (2001). Random forests. *Mach. Learn.* 45, 5–32. doi:10.1023/a:1010933404324

Cao, L., Wang, S., Peng, T., Cheng, Q., Zhang, L., Zhang, Z., et al. (2020). Monitoring of suspended sediment load and transport in an agroforestry watershed on a karst plateau, southwest China. *Agric. Ecosyst. & Environ.* 299, 106976. doi:10.1016/j.agee.2020.106976

Chen, Q., Wang, T., Li, Z., Zhang, J., Li, P., and Li, B. (2024). Research on water and sand prediction model of purple soil slope based on machine learning. *Acta Pedol. Sin.* 61 (02), 424–433. doi:10.11766/trxb202207020361

Chen, T., Shu, J., Han, L., Tian, G., Yang, G., and Lv, J. (2022). Modeling the effects of topography and slope gradient of an artificially formed slope on runoff, sediment yield, water and soil loss of sandy soil. *Catena* 212, 106060. doi:10.1016/j.catena.2022.106060

Chen, Z., and Grasby, S. E. (2009). Impact of decadal and century-scale oscillations on hydroclimate trend analyses. *J. Hydrol.* 365 (1-2), 122–133. doi:10.1016/j.jhydrol.2008.11.031

Chu, L., Sun, T., Wang, T., Li, Z., and Cai, C. (2020). Temporal and spatial heterogeneity of soil erosion and a quantitative analysis of its determinants in the three gorges reservoir area, China. *Int. J. Env. Res. Pub. He.* 17 (22), 8486. doi:10.3390/ijerph17228486

Dos Santos, J. C. N., de Andrade, E. M., Medeiros, P. H. A., Guerreiro, M. J. S., and de Queiroz Palácio, H. A. (2017). Effect of rainfall characteristics on runoff and water erosion for different land uses in a tropical semiarid region. *Water Resour. Manag.* 31 (1), 173–185. doi:10.1007/s11269-016-1517-1

Dunne, T., Zhang, W., and Aubry, B. F. (1991). Effects of rainfall, vegetation, and microtopography on infiltration and runoff. *Water Resour. Res.* 27 (9), 2271–2285. doi:10.1029/91WR01585

Fang, N., Shi, Z., Li, L., Guo, Z., Liu, Q., and Ai, L. (2012). The effects of rainfall regimes and land use changes on runoff and soil loss in a small mountainous watershed. *Catena* 99, 1–8. doi:10.1016/j.catena.2012.07.004

Foster, G. R., Lombardi, F., and Moldenhauer, W. C. (1982). Evaluation of rainfall-runoff erosivity factors for individual storms. *T. Asabe* 25 (1), 124–129. doi:10.13031/2013.33490

Gao, J., Shi, C., Yang, J., Yue, H., Liu, Y., and Chen, B. (2023). Analysis of spatiotemporal heterogeneity and influencing factors of soil erosion in a typical erosion zone of the southern red soil region, China. *Ecol. Indic.* 154, 110590. doi:10.1016/j.ecolind.2023.110590

Geng, X., Zhen, F., and Liu, L. (2010). Effect of rainfall intensity and slope gradient on soil erosion process on purple soil hill slopes. *J. Sediment. Res.* (06), 48–53. doi:10.16239/j.cnki.0468-155x.2010.06.012

Guan, Z., Yin, Y., Zhang, X., and Chen, Y. (2024). Estimating flash flood disaster susceptibility based on K-means clusterinoand ensemble learning approaches. *J. Appl. Sci.* 42 (03), 388–404. doi:10.3969/j.issn.0255-8297.2024.03.002

Han, D., Deng, J., Gu, C., Mu, X., Gao, P., and Gao, J. (2021). Effect of shrub-grass vegetation coverage and slope gradient on runoff and sediment yield under simulated rainfall. *Int. J. Sediment. Res.* 36 (1), 29–37. doi:10.1016/j.ijsrc.2020.05.004

Hu, S., and Jin, C. (1999). The oretical analysis and experimental studyon the critical slope of erosion. *Acta Geogr. Sin.* (04), 61–70. doi:10.11821/xb199904007

Jia, H., Lei, A., Lei, J., Ye, M., and Zhao, J. (2007). Effects of hydrological processes on nitrogen loss in purple soil. *Water Resour. Manag.* 89 (1), 89–97. doi:10.1016/j.agwat.2006.12.013

Jin, C. (1995). A theoretical study on critical erosion slope gradient. *Acta Geogr. Sin.* (03), 234–239. doi:10.11821/xb199503005

Kendall, M. G. (1948). Rank correlation methods. *J. Ins. Actuaries*. 75 (1), 140–141. doi:10.1017/S0020268100013019

Li, H., Ren, B., Zhou, M., Ma, J., Jiang, N., and Wang, Y. (2020). The process of runoff and sediment production of precipitation of small watersheds in hilly area. *Soil Water Conserv. Chn.* (03), 40–43. doi:10.14123/j.cnki.swcc.2020.0064

Li, J., Liu, J., Wang, Z., Feng, Q., Meng, F., Wang, H., et al. (2024). Refined mapping and spatiotemporal evolution analysis of winter wheat in the Yellow River Delta using sentinel-2 and the random forest algorithm. *J. Agr. Resour. Env.*, 1–15. doi:10.13254/j.jare.2024.0107

Liu, G., Wu, X., Zhao, L., Wu, T., Hu, G., Li, R., et al. (2021). Soil water content in permafrost regions exhibited smaller interannual changes than non-permafrost regions during 1986–2016 on the qinghai-Tibetan plateau. *Catena* 207, 105668. doi:10.1016/j.catena.2021.105668

Liu, H., Zhang, J., Chen, S., Dong, Y., Tian, J., and Lin, C. (2024). Effect of soil thickness on crop production and nitrogen loss in sloping land. *Agric. Water Manag.* 304, 109080. doi:10.1016/j.agwat.2024.109080

Liu, Z., Mo, S., Li, B., and Jiang, K. (2022). Erosion and sediment transport characteristics of different flood types in the typical small watershed in hilly region of cen-tral sichuan. *Soil Water Conserv. chn.* (11), 48–52. doi:10.14123/j.cnki.swcc.2022.0273

Ma, B., Li, Z., Ma, P., and Wu, F. (2015). Effects of maize plants on the redistribution of water under simulated rainfall conditions. *Acta Ecol. Sin.* 35 (02), 497–507. doi:10.5846/stxb201303240505

Ma, X., Zhen, J., Wang, W., Chen, X., Qin, W., Dan, Z., et al. (2017). Characteristics of the runoff and sediment yield of sloping farmland in the purple soil area under different rainfall patterns. *J. Soil Water Conserv.* 31 (02), 17–21. doi:10.13870/j.cnki.stbcxb.2017.02.004

Mann, H. B. (1945). Nonparametric tests against trend. *Econ. J. Econ. Soc.* 13 (3), 245–259. doi:10.2307/1907187

Mondal, A., Ghosh, S., and Ghosh, A. (2016). Robust global and local fuzzy energy based active contour for image segmentation. *Appl. Soft Comput.* 47, 191–215. doi:10.1016/j.asoc.2016.05.026

Nie, X., Chen, H., Niu, Z., Zhang, L., Liu, W., Xing, S., et al. (2022). Digital SOC mapping in croplands using agricultural activity factors derived from time-series data in western fujian. *Int. J. Geog. Inf. Sci.* 24 (09), 1835–1852. doi:10.12082/dqxxkx.2022.220015

Rao, W., Zhang, Q., Qian, Z., Liu, J., and Zhao, G. (2024). Microtopographic response of tilled loess slopes during stages of water erosion development. *Catena* 245, 108309. doi:10.1016/j.catena.2024.108309

Shou, W., Musa, A., Liu, Z., Qian, J., Niu, C., and Guo, Y. (2016). Rainfall partitioning characteristics of three typical sand-fixing shrubs in horqin sand land, north-eastern China. *Hydrol. Res.* 48 (2), 571–583. doi:10.2166/nh.2016.177

Sun, L., Cha, X., Huang, S., Li, S., Chen, S., Bai, Y., et al. (2018). Effects of different rainfall intensity on the slope erosion process in purple soil. *J. Soil Water Conserv.* 32 (05), 18–23. doi:10.13870/j.cnki.stbcxb.2018.05.003

Sun, L., Zhang, B., Yin, Z., Guo, H., Siddique, K. H. M., Wu, S., et al. (2022). Assessing the performance of conservation measures for controlling slope runoff and erosion using field scouring experiments. *Agr. Water manage.* 259, 107212. doi:10.1016/j.agwat.2021.107212

Tapas, M. R., Etheridge, R., Tran, T., Finlay, C. G., Peralta, A. L., Bell, N., et al. (2024). A methodological framework for assessing sea level rise impacts on nitrate loading in coastal agricultural watersheds using swat+: a case study of the tar-pamlico river basin, North Carolina, USA. *Sci. Total Environ.* 951, 175523. doi:10.1016/j.scitotenv.2024.175523

Vandervaere, J. P., Peugeot, C., Vauclin, M., Angulo Jaramillo, R., and Lebel, T. (1997). Estimating hydraulic conductivity of crusted soils using disc infiltrometers and minitensiometers. *J. Hydrol.* 188-189, 203–223. doi:10.1016/S0022-1694(96)03160-5

Wang, X., Chen, W., Huang, G., Tong, S., Xu, X., Nie, Y., et al. (2024). Characteristics of runoff and nitrogen, phosphorus, and carbon loss in sloping cultivated lands in the typical hilly mountainous region of the Upper Yangtze River Basin. *J. Env. Eng. Technol.* 14 (5), 1589–1598. doi:10.12153/i.issn.1674-991X.20230920

Xiao, H., Xiang, R., Yan, R., Xia, Z., Guo, P., Gao, F., et al. (2024). Evaluating the influences hedgerow on soil erosion and nitrogen loss of purple soil sloping farmland under simulated rainfall. *Ecol. Indic.* 158, 111438. doi:10.1016/j.ecolind.2023.111438

Yan, Y., Hu, Z., Wang, L., Jiang, J., Dai, Q., Gan, F., et al. (2024). Impact of extreme rainfall events on soil erosion on karst slopes: a study of hydrodynamic mechanisms. *J. Hydrol.* 638, 131532. doi:10.1016/j.jhydrol.2024.131532

Yan, Y., Jiang, Y., Guo, M., Zhang, X., Chen, Y., and Xu, J. (2023). Effects of grain-forage crop type and natural rainfall regime on sloped runoff and soil erosion in the mollisols region of northeast China. *Catena* 222, 106888. doi:10.1016/j.catena.2022.106888

Yang, F., Wang, N., Zheng, Z., Li, T., He, S., Zhang, X., et al. (2023). Effects of microtopography change driven by seepage and slope gradients on hillslope erosion of purple soil. *Catena* 231, 107353. doi:10.1016/j.catena.2023.107353

Yang, Q., Xu, X., Tang, Q., and Jia, G. (2025). The spatiotemporal variations of global rainfall erosivity and erosive rainfall event based on half-hourly satellite rainfall data. *Catena* 252, 108831. doi:10.1016/j.catena.2025.108831

Zhang, J., Wang, J., Cheng, X., and Chen, J. (2021). Effects of rainfall on slope runoff and sediment yield under different crop measures in the jiangzi river minor watershed. *J. Soil Water Conserv.* 35 (02), 8–14. doi:10.13870/j.cnki.stbcxb.2021.02.002

Zhang, L., Gao, F., Liu, D., Wang, L., Xiang, R., Ye, C., et al. (2023). Estimating sheet erosion on purple soil hillslope treated with polyacrylamide (pam) in the three gorges reservoir area. *J. Hydrol-Reg. Stud.* 49, 101510. doi:10.1016/j.ejrh.2023.101510

Zhang, X., He, X., Wen, A., Walling, D. E., Feng, M., and Zou, X. (2004). Study on the dual isotope method of 137Cs and 210Pb for sediment sources in small watersheds in the hilly area of central Sichuan. *Chn. Sci. Bull.* 49 (15), 1537–1541. doi:10.1360/csb2004-49-15-1537

Zhang, X., Zhang, S., Zhang, F., Li, H., Shi, J., and Chen, J. (2025). Quantifying the effects of the soil erosion factors on water-eroded slopes. *Catena* 249, 108678. doi:10.1016/j.catena.2024.108678

Zhao, Q., Ye, C., and Lu, Y. (2022). A micro-motion feature lmportance evaluation algorithm based on random forest. *Mod. Def. Technol.* 50 (04), 124–131. doi:10.3969/j.issn.1009-086x.2022.04.014

Zhu, Q., Guo, J., Guo, X., Han, Y., Liu, S., Chen, L., et al. (2020). Research on influencing factors of soil erosion based on random forest algorithm-A case study in upper reaches of ganjiang river basin. *Bull. Soil Water Conserv.* 40 (02), 59–68. doi:10.13961/j.cnki.stbctb.2020.02.009

frontiers | Frontiers in Environmental Science

TYPE Original Research
PUBLISHED 02 May 2025
DOI 10.3389/fenvs.2025.1495923

OPEN ACCESS

EDITED BY
Qiang Li,
University of Houston–Downtown,
United States

REVIEWED BY
Susanta Das,
University of Florida, United States
Zhijia Gu,
Xinyang Normal University, China

*CORRESPONDENCE
Woldeyes Debebe,
wolde.debe@gmail.com

RECEIVED 13 September 2024
ACCEPTED 17 April 2025
PUBLISHED 02 May 2025

CITATION
Debebe W, Yirgu T and Debele M (2025) Assessing soil erosion potential for prioritization of land risk area in the Sala watershed of Ari zone, South Ethiopia.
Front. Environ. Sci. 13:1495923.
doi: 10.3389/fenvs.2025.1495923

Assessing soil erosion potential for prioritization of land risk area in the Sala watershed of Ari zone, South Ethiopia

Woldeyes Debebe*, Teshome Yirgu and Mulugeta Debele

Department of Geography and Environmental Studies, Arba Minch University, Arba Minch, Ethiopia

Soil erosion has led to land degradation, which affects the environmental and economic sustainability of agricultural land systems. This study aims to assess the annual soil loss potential to prioritize land risk areas in the Sala watershed for conservation planning. Soil sampling and topographic data were the primary sources of data. The secondary sources were satellite imagery and meteorological data. The Revised Universal Soil Loss Equation (RUSLE) model, integrated with GIS and remote sensing (RS) techniques, was used to formulate optimal soil erosion management plans and assess erosion hotspot areas in the study area. The results showed that the distribution of annual soil loss ranged from 1 to 1,875 t/ha/year, and the mean annual soil loss was 312.6 t/ha/year. The findings also revealed that the watershed was classified as having low soil erosion rates (1–162 t ha/year) (31.91%), moderate soil erosion rates (162–405 t ha/year) (39.67%), high soil erosion rates (405–805 t/ha/year) (20.78%), and very high soil erosion rates (800–1875 t/ha/year) (7.64%). 28.42% of the watershed was classified as having high to very high erosion severity, primarily found on steeper slopes and in areas with inappropriate land use practices. In the Sala watershed, soil and water conservation measures have important implications for improving soil fertility and productivity. Thus, effective land management planning should be implemented to achieve sustainable agricultural land use in the study watershed area.

KEYWORDS

soil erosion, RUSLE, land risk, prioritization, Sala watershed

1 Introduction

Soil erosion is currently a significant environmental and economic concern worldwide (Benavidez et al., 2018; Chuenchum et al., 2019; Pimentel and Burgess, 2013; Ozsahin et al., 2018), endangering freshwater, land, and marine environments (Borrelli et al., 2020). It is one of the environmental problems that hinder the implementation of the first (No poverty) and second (Zero hunger) Sustainable Development Goals by the year 2030 due to declining soil fertility (Moisa et al., 2022). Globally, one-third of agricultural soils are being affected by soil degradation (Hurni and Meyer, 2002), of which water and wind erosion account for 56% and 28% of the observed damage, respectively (Blanco-Canqui and Lal, 2008; Gelagay and Minale, 2016). Assessment of tectonic evolution and fluvial system anomalies in water streams and river basins is crucial for understanding the landscape changes (Ghosh and Kundu, 2025). Soil erosion negatively impacts agricultural production, water resource quality, and the ecosystem's sustainability (Fayas et al., 2019). The erosion process is

influenced by numerous factors, primarily anthropogenic, such as urbanization and mining, and natural causes, such as flash floods and rainstorms (Koirala et al., 2019; Hategekimana et al., 2020). Natural and man-made factors have the potential to accelerate soil erosion (Alexandridis et al., 2015), but it is clear that human activity is the primary cause of soil erosion, accounting for 60%–80% of all soil erosion and degradation (McNeill, 2001). In addition to soil degradation, other difficulties caused by soil erosion include removal of soil nutrients, a decline of crop yields, reduction of soil fertility, and contamination of surface and groundwater supplies by fertilizer nutrients, sediment, and insecticide residues (Hategekimana et al., 2020).

Soil erosion not only decreases soil quality in the detachment area (on-site effect) but also causes significant sediment-related problems in the sedimentation area (off-site effect) (Liu et al., 2020; Mekonnen et al., 2015), with an assessed 15 to 30 billion tons of yearly sediment taken by the world's water erosion to reservoirs and lakes (Thomas et al., 2018b). A recent estimation of land degradation due to soil erosion costs shows that the global economic impact is highly uncertain, from 40 to 490 billion US$, and varies from country to country (Nkonya et al., 2016), with an estimated 24 billion tons of highly productive soil being lost from croplands worldwide (Kassaye and Abay, 2019). In agricultural areas, soil erosion is 10–100 times faster than soil formation (Amundson et al., 2015) and affects 10 million hectares of arable land each year (Gachene et al., 2020). Soil loss resulting from erosion is a universal issue that affects agricultural production and natural resources (Ighodaro et al., 2013; Koirala et al., 2019). The acceleration of soil erosion occurs due to human activities such as intensive agriculture, poor land management, deforestation, and cultivation on steep slopes (Molla, 2017; Alemu and Melesse, 2020; Jayasekara and Kadupitiya, 2018). Additionally, soil erosion is proportional to population growth, overuse of natural resources, degraded land, and poor water management plans (Reichmann et al., 2013; Ozsahin et al., 2018; Deb et al., 2019). Food insecurity, poverty, and unsustainability of land productivity are the results of the factors of soil erosion (Adimassu et al., 2014; Yesuph and Dagnew, 2019).

A recent application to the African continent estimates the annual loss of crop yield to be about 280 million tonnes (Wolka et al., 2018). Over 40% of the extra food required to meet the growing food demands by 2025 will have to come from intensified rain-fed farming in the sub-Saharan Africa region (Bekele, 2021). Especially in East Africa, where Ethiopia shows the highest erosion rates (Gessesse et al., 2015; Lanckriet et al., 2014). The annual rate of soil loss (over 1.5 billion tons) in the nation is much greater than the rate of soil formation on an annual basis (1.5 million tons) (Tamene et al., 2006) with an associated cost of close to one billion Ethiopian birrs each year (Alemu, 2005; Bekele et al., 2019). Sheet and rill erosion mainly affected the highlands of Ethiopia (Gashaw et al., 2019; Yesuph and Dagnew, 2019), with annual soil losses of 200–300 t/ha/year (Gelagay and Minale, 2016). Soil erosion degrades agricultural land by removing nutrient-rich topsoil, increasing runoff from increasingly impermeable subsoils, and reducing the amount of water available to plants (Ettazarini and Mustapha, 2017; Ganasri and Ramesh, 2016). 50% of the country's agricultural area and 88% of its population remain negatively affected by soil loss and resulting sedimentation (Sonneveld et al., 2011). The annual productive capacity in Ethiopia's highlands is decreasing by 2.2% (Tesfahunegn et al., 2014). This threatens agricultural production and productivity (Mihara et al., 2005), ecosystem degradation, increased sedimentation, and increased flood risk (Chuenchum et al., 2019; Pham et al., 2018). Additionally, soil erosion continues to cost the country $1 billion annually and affects 50% of the country's arable land and 88% of its population (Bekele et al., 2019). Because smallholder farmers in the area primarily rely on the land for their livelihood, the resultant severe soil degradation in Ethiopia's highlands has threatened both current and future generations' food security by resulting in lower yields or higher input costs (Teferi et al., 2016). The sustainability of Ethiopian agricultural production is seriously threatened by soil erosion, depletion of organic matter, and soil nutrient removal (Haile, 2012; Elias, 2017; Gelagay and Minale, 2016).

The estimation of human and natural factors is crucial to grasp the individual impact of the factors and establish the decisive watershed for proper management and conservation measures to be planned to mitigate erosion (Ganasri and Ramesh, 2016). Productive land and adequate water availability are crucial for sustainable development and increased food production in those countries whose livelihoods are based on agriculture. Due to this, numerous methods are available for quantifying soil erosion to sustain land and water productivity. Scientists have developed different models, ranging from physical-based models to empirical models, to study soil erosion at various spatiotemporal scales (Karydas et al., 2014). The RUSLE model is developed as an empirical model representing the main factors controlling soil erosion processes, namely climate (rainfall erosivity), soil characteristics (soil erodibility), topography (slope length and slope steepness), cropping and cover management, and conservation practice factors (Abdo HG., 2022; Okenmuo and Ewemoje, 2023; Richi, 2025; Renard, 1997). However, the RUSLE model is the most frequently applied model for predicting the long-term average annual soil loss rate due to raindrop, sheet, and rill erosion, but not from gully and channel erosion (Koirala et al., 2019; Molla and Sisheber, 2017; Renard, 1997; Taye et al., 2018).

Numerous studies have been conducted in Ethiopia that have quantified the potential for soil erosion and identified areas at risk of erosion at various watershed levels by integrating the revised universal soil loss equation (RUSLE) with geographic information systems (GIS) and remote sensing techniques (Belayneh et al., 2019; Gashaw et al., 2018; Moisa et al., 2021; Negash et al., 2021; Mohammed et al., 2022; Tessema et al., 2020; Haregeweyn et al., 2017; Hurni et al., 2015), which is effective in quantifying the magnitude of the issue. As a result, soil loss values in Ethiopia vary significantly due to differences in measurement scales, applied methods, variations in climate, land use, and soil types. Due to the severity and consequences of soil erosion, research was conducted on different watersheds in Ethiopia; however, it did not include the current study area. Thus, no study has been done on the quantification of soil loss potential prioritization risk analysis in the study of the Sala watershed area. A prerequisite of soil conservation is the reversal of land desertion and the enhancement of the agricultural production, the provision of food sanctuary, and sustainability, thereby requiring identification

of critical erosion-prone areas. Therefore, the spatial assessment of soil erosion risks is a fundamental approach to natural resource management and planning in river basins (Ansari et al., 2024).

In the Sala watershed, rill and sheet erosion resulting from unsustainable land use and land management practices, steep slopes, rugged topography, climate change (erosive rainfall), and other anthropogenic activities are the main causal factors. The severity and impacts of soil erosion are leading to the formation of gully erosion, siltation, and sedimentation, which are intensively increasing and causing loss of agricultural productivity due to the depletion of soil fertility and productivity in the current study area. Soil loss carries productive topsoil off-site, leading to decreased soil fertility and crop productivity in the study watershed area. Though soil erosion leading to soil loss is a natural phenomenon, intricately dependent on natural factors such as rainfall intensity, duration and amount, slope gradients and length, soil texture, soil organic matter and soil hydraulic properties, anthropogenic factors such as tillage and soil covers could control it in managed cropping systems (Ochoa-Tocachi et al., 2016; Zhang et al., 2017).

Assessment and mapping of soil erosion rates in a watershed is vital for the identification of critical hotspot areas for a targeted implementation of appropriate land management and rehabilitation measures (Aneseyee et al., 2020; Ganasri and Ramesh, 2016). It is argued that identifying and prioritizing soil erosion risk-prone areas by using the RUSLE model is essential for implementing appropriate soil and water conservation measures for sustainable land use (Azimi et al., 2019). Accordingly, the RUSLE model was combined with GIS and remote sensing techniques to estimate and prioritize spatial soil erosion risk areas in the study watershed. Hence, the present study aimed to estimate the potential mean annual soil loss for prioritization of land risk areas using the RUSLE model in the Sala watershed of the Ari Zone in South Ethiopia. The results of this assessment represent an important basis for decision-makers in improving the performance of soil erosion protection measures and implementing mitigation strategies to prevent the acceleration of erosion in high and very high-risk areas.

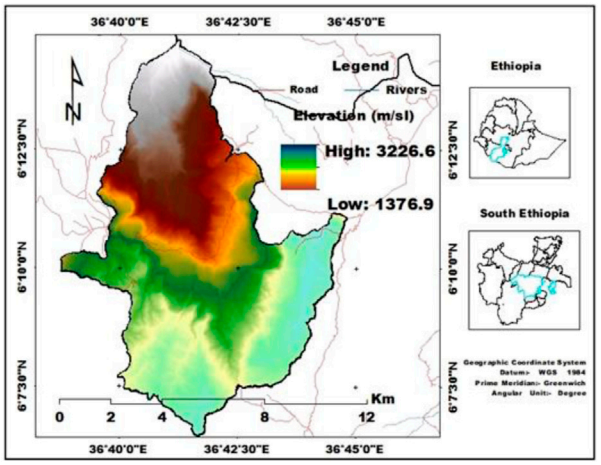

FIGURE 1
Location map of the study area.

The watershed study had a total population of about 39,646, of which 21,024 (53.03%) were female and 18,622 (46.97%) were male. Mixed farming is the main source of income for the communities. Cattle, donkeys, goats, sheep, and mules are the most common livestock productions in the watershed. Some of the dominant seasonal and perennial crops grown in the watershed are *teff* (*Eragrostis tef*), sorghum (*Sorghum bicolor*), banana (*Musa mesta*), potato (*Solanum tuberosum*), taro (*Colocasia esculenta*), cassava (*Manihot esculenta*), barley (*Hordeum vulgare*), wheat (*Triticum vulgare*), bean (*Phaseolus vulgaris*), and others. In the study, crops such as korerima (Aframomum corrorima or Ethiopian cardamom) and coffee (Coffea arabica) are also grown in the watershed. Ensete (*Ensete ventricosum*) is one of the major perennial crops in the study area. It is used as a main staple food crop for the communities in the Sala watershed.

2 Materials and methods

2.1 Study area

The study was conducted in the Sala watershed of North Ari woreda in the Ari Zone, South Ethiopia. The study area is found between 6°7′30° and 6°12′30 N latitude and 36°40′0° and 36°45′0 E longitude. It covers a total area of 7,919.71 ha (ha). An elevation range of 1,391–3,210 m above sea level (Figure 1). The study area is located 585 km south of Addis Ababa. The topography of the study area is characterized by a flat to steep hillside landscape. Most of the study areas are under high mountains with very steep slopes. In the area, Orthic Acrisols (a very deep, well-drained, dark brown clay soil) are the predominant soil type. Average monthly temperatures range from 11°C to 22°C. The mean annual rainfall of the watershed ranges from 753.95–1,552.53 mm per year. The least amount of rainfall occurs during the summer (*Bega*) season, which is from December to February. The dominant rainy season is the Winter (*Kiremt*), which runs from June to August. Acacia abyssinica, Cordia africana, Hagenia abyssinica (also called Koso in Amharic), and bamboo (also called *kerka*) were the indigenous trees found in the study watershed.

2.2 Data sources and methods of acquisition

The RUSLE model variables are estimated from various sources. This method evaluates the influence of climate, soil, topography, and land use factors on soil erosion (Mete and Bayram, 2024). Both primary and secondary data were used for the RUSLE parameters of the study watershed. Soil sampling and topographic data were the sources of primary data. The secondary source was generated from satellite imagery and meteorological data. The rainfall erosivity factor (R-factor) was derived from annual rainfall data for 15 years (2006–2021) obtained from the Ethiopian National Meteorological Agency. Slope length and slope gradient factor (LS-factor) were determined using a digital elevation model (DEM) from a 1: 50,000 scale topographic map with 30 m contour lines of varying heights. The Landsat image was used for the conservation practices (P-factor) and crop management (C-factor).

The soil erodibility factor (K-factor) was determined from field-estimated organic matter, texture, structure, and permeability of the soil of the study area. Three random strata were selected from the watershed elevation, and the major adjacent land use types in each stratum were identified across elevation gradients, of which four

were at the top (cultivated land, grazing land, shrubland, and forest land), three in the middle (cultivated land, grazing land, and forest land), and three at lower altitudes (cultivated land, grazing land, and shrubland), with one depth and three replicates per sample field (4 × 3 × 3 × 3 elevations × 1 depth × 3 replicates). Soil samples were collected at three elevations: upper (2,500–3,210), middle (1,900–2,500), and lower (1,391–1900), followed by identifying land use types across elevation gradients. A total of 30 composite soil samples were collected from different current land use types and altitudinal gradients using a zigzag sampling technique at a constant depth of 0–20 cm from upland (12), midland (9), and lowland (9) to calculate the soil erodibility factor (K-factor).

2.3 Determination of the RUSLE model factors

Scientists have developed several methods to estimate soil erosion through experimental, statistical, and physical methods (Beck et al., 2018; Fredj et al., 2024; Wischmeier and Smith, 1965; Williams, 1975; Renard, 1997). RUSLE is an empirical predictive model used to estimate average annual soil loss. The RUSLE model is a widely used, low-cost, non-data-intensive predictive model for agricultural and forestry watersheds (Renard, 1997). This model for estimating soil erosion from sheets and rills has been developed (Yesuph and Dagnew, 2019; Kulimushi et al., 2021a; Kulimushi et al., 2021b) to prioritize areas at risk of soil erosion (Tessema et al., 2020). The RUSLE model was computed using five erosion parameters to calculate the yearly average soil loss in the Sala watershed (Equation (1)) (Renard, 1997):

$$A = R * K * LS * C * P \quad (1)$$

where *A* is the mean annual rate of soil loss tonne/hectare/year (t/ha/y), *R* is the rainfall erosivity factor (MJ mm/ha/hr/year), K is soil-erodibility (t/ha/MJ mm), LS is slope length and slope steepness, C is land-cover management and P is land management factors, respectively.

2.3.1 Rainfall erosivity (R-factor)

The rainfall erosivity factor (R-factor) represents the aggressiveness of rainfall and is related to the amount and rate of runoff that has the potential to cause erosion. Rainfall can remove and transport detached materials in a specific area, and the RUSLE model uses this factor as input in soil loss determination (Hategekimana et al., 2020). The R-factor is strongly influenced by the storm volume, energy, duration and intensity, raindrop shape, precipitation distribution, and subsequent runoff velocity (Farhan and Nawaiseh, 2015; Amellah and Karim, 2021). This factor can be estimated as a function of kinetic energy/raindrops/and their 30-min maximum intensity (*I*30) (Renard, 1997). However, measurements to generate these variables are not available for Ethiopia as a whole. Therefore, the empirical formula developed by (Hurni, 1985b) was applied to estimate the R-factor for the Ethiopian condition, which has been derived from spatial regression analysis (Helldén, 1987) (Equation 3). The R-factor was developed using the average annual precipitation (P) of the

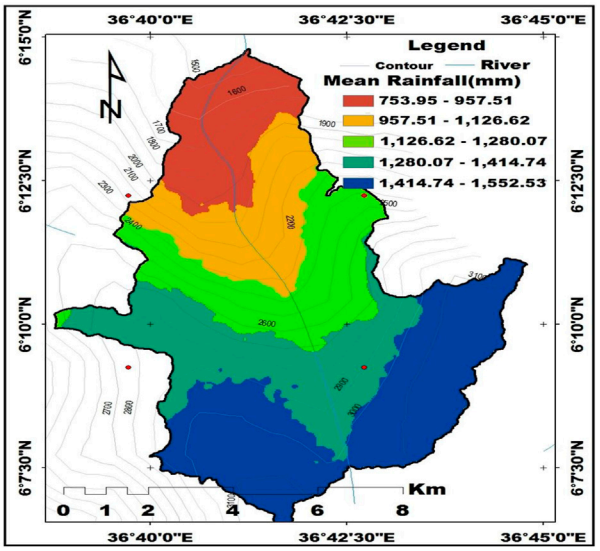

FIGURE 2
R-factor map of the Sala watershed.

precipitation data of five stations from 2006 to 2021 collected by the Ethiopia National Meteorological Agency (Equation 2).

$$R = -8.12 + (0.562^{*}P) \quad (2)$$

where R; is the rainfall erosivity factor in MJ mm ha/h/year, and P is the mean annual rainfall (mm/year).

However, to validate the average rainfall, a standard linear regression equation using DEM was used:

$$Mean\ Rainfall = \alpha + (\beta * DEM) \quad (3)$$

Where α stands for mean rainfall intercept (constant), β The slope coefficients for the predictor (DEM) values of the regression model and DEM for the digital elevation model.

The spatial distribution of the rainfall erosivity factor (R-value) over the study's Sala watershed area is shown in Figure 2. The spatial distribution of different precipitation amounts increases in the mountainous areas of the studied watershed compared to the lowlands, as indicated by the R-factor results of the linear regression model (Table 1; Figure 2). Precipitation and the digital elevation model (DEM) showed a strong correlation (−0.425) (Table 1). Elevation rises by one unit, and precipitation variability is expected to increase by a factor of −0.425 if all other variables stay the same (Table 1). According to Figure 3, the R factor in the study area ranges from 753.95 to 1,552.53 MJ mm/ha/hr/year, with an average value of 1,153.24 MJ mm/ha/hr/year. The results show that the Sala watershed has high rainfall erosivity, which may lead to soil erosion. A higher R-value indicates higher kinetic energy of rainfall and surface runoff, which contributes to higher soil erosion (Balasubramani et al., 2019).

Spatially, the rainfall erosivity distribution was not uniform in the study area due to variations in rainfall shown in Figure 2). The R-value is lower, indicating the low erosivity of rainfall to erode the soil (Asmamaw and Assen, 2019) and low rainfall intensity in the study area (Devatha et al., 2015). The highest elevation in the

TABLE 1 Correlation between rainfall and elevation in the Sala watershed.

		Rainfall	Elevation
Pearson Correlation	Rainfall	1.000	−0.425
	Elevation	−0.425	1.000
Sig. (1-tailed)	Rainfall		0.127
	Elevation	0.127	
N	Rainfall	9	9
	Elevation	9	9

Model	Unstandardized coefficients		Standardized coefficients	t	Sig	95.0% confidence interval for B	
	B	Std. Error	Beta			Lower bound	Upper bound
(Constant)	171.284	9.180		18.658	0.000	149.576	192.991
Elevation	−0.005	0.004	−0.425	−1.242	0.254	−0.015	0.005

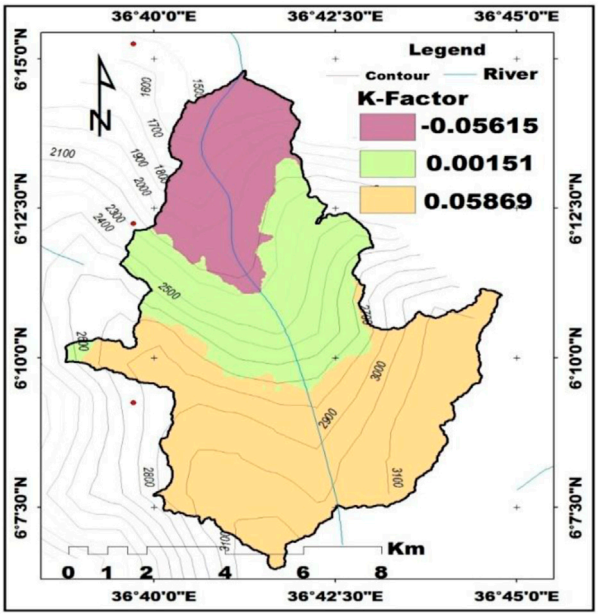

FIGURE 3
K-factor map of the Sala watershed.

southern part of the watershed corresponds to the highest annual rainfall values, while the northern part, which is closest to the outlet, has the lowest rainfall values, as shown in Figure 2. This result is supported by the findings of (Belay et al., 2019), who found a strong relationship between elevation and mean annual precipitation. The major problem of soil loss may occur due to high rainfall as the southern part of the study watershed receives high average annual rainfall (Das et al., 2022). Thus, Figure 2 shows that rainfall-induced erosion rates vary across the watershed.

2.3.2 Soil erodibility (K-factor)

Soil erodibility (K-factor) is the soil's susceptibility to erosion, ease of silt removal, and expected runoff per rainfall contribution (Kayet et al., 2018). K-factor is an assessment of the impact of soil properties on soil loss and the vulnerability of soil to erosion as well as the potential susceptibility of soil to the detachment and transport caused by rainfall and runoff (Alemu and Melesse, 2020; Haile and Fetene, 2012). The influence of soil quality and profile characteristics on soil loss is reflected in the K-factor component (Molla and Sisheber, 2017; Pham et al., 2018; Renard, 1997). Soil texture, organic matter, soil structure, drainage, soil profile depth, and permeability are the primary soil properties that alter the K-factor (Ayalew and Selassie, 2015; Ettazarini et al., 2017; Haregeweyn et al., 2017; Koirala et al., 2019; Molla and Sisheber, 2017; Mohammed et al., 2020; Prasannakumar et al., 2012; Saha, 2018). The K factor was calculated from estimated soil properties, namely texture, organic matter, and structural and permeability (Foster et al., 1981; Panagos et al., 2015). In this study, the K-factor was calculated by the formula of (Equation 4).

$$K = \left(27.66/m^{1.14} * 10^{-8}\ (12 - a)\right) + (0.0043 * (b - 2)) + (0.0033 * (c - 3)) \quad (4)$$

where; m = (silt (%) + very fine sand (%)) (100−clay (%)); a = organic matter (%); b = structure code: (1) very structured or particulate, (2) fairly structured, (3) slightly structured and (4) solid, and c = profile permeability code: (1) rapid, (2) moderate to rapid, (3) moderate, (4) moderate to slow, (5) slow and (6) very slow.

The soil erodibility factor shows the mean long-term soil and soil profile response to the erosive power associated with rainfall and runoff (Millward and Mersey, 1999). The K factor indicates the sensitivity of soil to erosion (Kayet et al., 2018). For soil erodibility estimations, soil type and color methods were adapted from (Hurni, 1985a) as indicated in Table 2). Through laboratory analysis, the study area's soil textures and organic matter values were assessed to estimate the soil erodibility factor (K-value). Figure 3 shows the spatial prediction map of soil K-factor based on Table 2. The results range from −0.056 to 0.058 t/ha/MJ mm, and the average K-factor value is −0.035 t/ha/MJ mm, which is close to 0, indicating low sensitivity to soil erosion (Figure 3). K-value was also negatively correlated with soil permeability (−0.056). These correlations corroborated the general understanding of the soil erodibility vis-à-vis soil texture, organic matter, and permeability (Olaniya et al.,

TABLE 2 Soil properties and their respective K-factor in the Sala watershed.

Soil properties	Upper land	Middle land	Lowland
Silt (%)	14	22.5	22
Very Fine sand (%)	22.9	25.6	28.5
Clay (%)	48.95	37.73	42.7
Organic matter	2.71	3.3	4.68
Structure	3	2	1
Permeability	4	3	2
K-value	−0.056	0.001	0.058

2020). The lowest erodibility was observed in the study area due to the higher organic matter content, which allowed soil fractions to exhibit more excellent aggregate stability (Olaniya et al., 2020). The current findings are in line with earlier research reported on the K-values of tropical soils that range from 0.06 to 0.48 (El-Swaify et al., 1992), and the majority of Ethiopian soils have K-values between 0.05 and 0.6 (FAO–UNDP, 1984).

The lower value of the K factor is associated with the soils having low permeability and low antecedent moisture content. Higher K-values indicate higher erodibility and vulnerability to soil erosion, which could be attributed to low clay and organic matter contents as less aggregation of soil colloids (Bartoli et al., 1992). Soils with good soil structure, high organic matter content, and high permeability are more resistant to erosion. In general, the highest K-value soil is highly affected by erosion and intrinsically susceptible to the erosive force of rainfall, and also intrinsically less resistant to the eroding power of rainfall, whereas the lowest K-value has low soil erodibility and less susceptible to the detaching power of raindrop, and therefore high-resistance to rainfall force (Figure 3).

2.3.3 Slope length and steepness (LS) factor

The LS factor describes the impact of the topographic factors on the rate of soil erosion (Fayas et al., 2019; Wischmeier and Smith, 1978; Haan et al., 1994; Shreevastav et al., 2022; Song et al., 2011). This factor has an impact on the transport capacity of surface runoff (Mandal, 2017; Karna et al., 2021). The steepness gradient affects the flow velocity, whereas the gradient length identifies the distance between the points where erosion begins and the deposition (Renard et al., 1997). The flow velocity on the rate of erosion between the origin and termination of inter-rill processes is influenced by the combined LS factor. The velocity of water flowing over the ground and the slope of the ground surface are dependent parameters (Karna et al., 2021). As slope length increases, soil erosion by water increases due to increased runoff water accumulation. The steeper the slope, the more susceptible it is to soil erosion and *vice versa* (Ostovari et al., 2017; Wang et al., 2020).

The LS factor was initially suggested and determined by direct slope measurements (Renard, 1997); this method was not suitable for studies conducted at the watershed scale. Accordingly, the S-factor is the actual slope divided by the experimental slope (9%), and the L-factor is obtained by dividing the actual horizontal slope length by the experimentally measured slope length of 22.13 m (Arekhi, 2008; Renard, 1997; Wischmeyer and Smith, 1978). Consequently, the topographic factor raster calculator tool in the ArcGIS

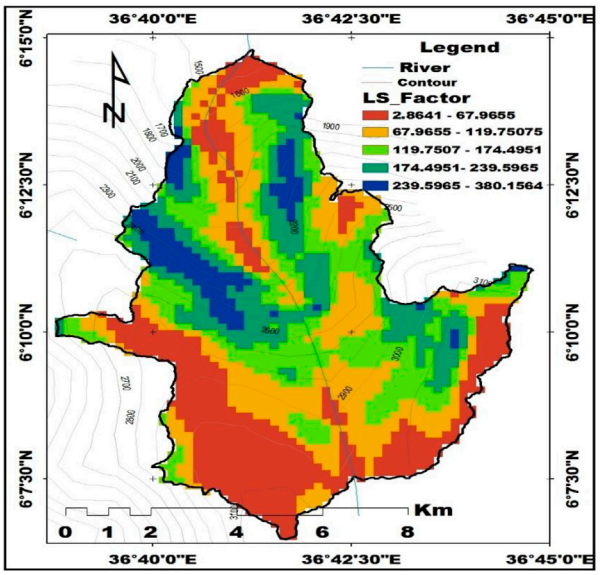

FIGURE 4
LS-factor map of the Sala watershed.

environment was utilized in conjunction with a digital elevation model (DEM) to produce a combined LS factor (Atoma, 2018):

$$L = \left(\frac{\lambda}{22.13}\right)^{m} \quad (5)$$

Where L is the slope length factor, λ is the slope length (m), and m is the slope–length exponent.

$$m = \frac{F}{1 + F'} \quad (6)$$

$$F = \frac{\sin/0.896}{3(\sin)0.8 + 0.56'} \quad (7)$$

Where F = ratio between rill erosion and inter-rill erosion, β = slope angle (^{0}).

In this study, the steepness factor derived from the slope map of the study area was calculated for high-slope (>9%) and low-slope (<9%) lands, as shown below (Mccool et al., 1987; McCool et al., 1997; Renard, 1997):

$$S = 10.8 \times \sin\theta + 0.03, \text{for } \sigma \leq 9\% \quad (8)$$

$$S = 16.8 \times \sin\theta - 0.50, \text{for } \sigma > 9\% \quad (9)$$

Where θ is the slope angle in degrees and σ is the slope gradient in percentage.

The LS factor indicates the impact of topography on the soil erosion process. It is the combined effect of the slope length (L) factor and the slope steepness (S) factor (Figure 4). There is a direct relationship between slope length and erosion rate (Wischmeier and Smith, 1978). As a result, erosion increases as slope length increases. The LS is the ratio of observed soil loss related to the soil loss of a standardized plot (22.13) as indicated in (Schmidt et al., 2019). The LS value is considered to have values between 0.02 and 48 for the Ethiopian condition (Hurni, 1985b), and the study watershed area ranges from 2.86 m at the bottom to 380.15 m at the top (Figure 4). The combined slope LS factor has a greater influence on soil loss in the

southern part of the watershed, whereas the northern and central parts of the watershed also contribute less to soil erosion due to the existing slope (Figure 4). As a result, longer slopes see larger accumulations of runoff from a larger area, which raises flow velocities and causes soil loss to increase with slope. As the watershed is mountainous with a steep slope, it inherits a high slope length factor and consequently high overland flow with high velocity (Das et al., 2020). Thus, as the slope length increases, this leads to high overland flow and increases soil erosion and sediment yield in the study area.

2.3.4 Cropping and cover management (C-factor)

According to (Hategekimana et al., 2020; Renard, 1997) the C-factor shows how vegetation or plant cover and management interventions contribute to soil loss. The ratio of soil loss from a particular vegetated area to the equivalent soil loss from a fallow area with the same rainfall is known as the cover and management factors (Wolka et al., 2015). This establishes how successful crop and soil management strategies are in preventing soil loss. Cover management (C-factor) is used to associate the relative impact of management strategies on conservation plans (Renard, 1997; Fayas et al., 2019). The vegetation cover of the land use class is used to calculate the C-factor value based on land cover management measures (Karna et al., 2021; Zeleke, 2000) states that the dimensionless C-factor value establishes the proportion of soil loss in distinct regions with varying land cover conditions. Four land use/land cover types were identified as cultivated, forest, grazing, and shrublands (Table 3). The Landsat image was used for the classification and mapping of land use/land cover types using Remote Sensing (RS) and Geographic Information Systems (GIS) techniques.

A C-factor map for the study area was made using changes in land use/land cover, which have a significant impact on soil erosion (Kidane et al., 2019). The Sala watershed was classified into four land use/land cover categories, and the C-factor value was assigned (Table 3; Figure 5) for the Ethiopian condition based on the existing literature (Fayas et al., 2019; Olika and Iticha, 2019; Yesuph and Dagnew, 2019; Amsalu and Mengaw, 2014; Girma and Gebre, 2020; Bewket and Teferi, 2009; Wischmeier and Smith, 1978; Hurni, 1985b).

Cover control (C-factor) values in the study watershed range from forest land (0.02) to cultivated land (0.18) (Table 3; Figure 5). The findings demonstrated that from the classified land use/land cover classes, cultivated land predominated (Table 3). The *C* values show that the maximum amount of cultivated land generates high runoff and is vulnerable to erosion, whereas shrub and forest lands receive the lowest values and are resistant to soil erosion and runoff (Table 3; Figure 5). Among the four land use/land cover classes, cultivated land is the most vulnerable, while forest land use is the least vulnerable to soil erosion

TABLE 3 Cropping and cover management C-factor values of the study area.

Land-use and land-cover types	C- factor value
Cultivated land	0.18
Grazing land	0.15
Shrub land	0.05
Forest land	0.02

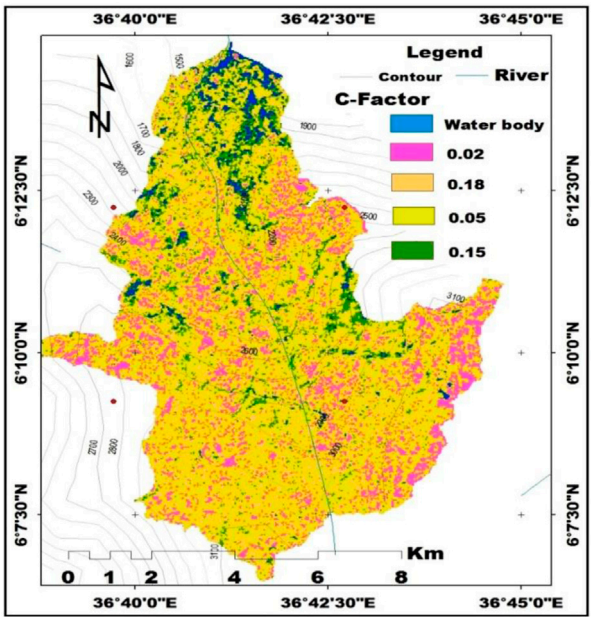

FIGURE 5
C-factor map of the Sala watershed.

(Table 3; Figure 5). Soil is highly eroded, especially when other LULC is converted to cultivated land. The result is in line with the findings of (Negassa et al., 2020). Soil erosion is significantly affected by the land use/land cover conditions of the watershed, according to the present land/land cover analysis findings (Table 3). This conclusion is consistent with prior findings showing that vegetation significantly decreased soil loss and sediment yield (Ebabu et al., 2019; Kidane et al., 2019; Thomas et al., 2018a).

2.3.5 Erosion control practices (P-Factor)

According to (Renard, 1997; Fayas et al., 2019) the erosion control practices factor (P) is also known as the support and conservation practices factor. The support and conservation practices factor (P-factor) measures how conservation practices affect the quantity and rate of soil erosion and runoff (Ayalew and Selassie, 2015; Koirala et al., 2019; Renard, 1997) states that the conservation practice (P-factor) measures the degree to which soil erosion is slowed by support methods such as terracing and contour tillage. On-site, inappropriate physical land management practices were observed. Determining the P-factor is difficult due to the lack of long-term conservation measures and the inconsistent application of conservation practices across the complex and rugged terrain of the study watershed. For these reasons, we computed the P-factor output map using a different estimation method that took into account the type of land use/land cover (Figure 6).

P-factor values varied accordingly, with variations found in the 0.52 to 0.9 range (Table 4; Figure 6). The P-values range from zero (0) to one (1), whereby the values close to zero indicate a good conservation practice and erosion resistance facility, and the values close to one indicate poor conservation practices and no manmade erosion resistance facility (Ganasri and Ramesh, 2016; Olorunfemi et al., 2020; Renard et al., 1997; Wischmeier and Smith, 1978). A value close to forest land (0.52) denotes good conservation practices,

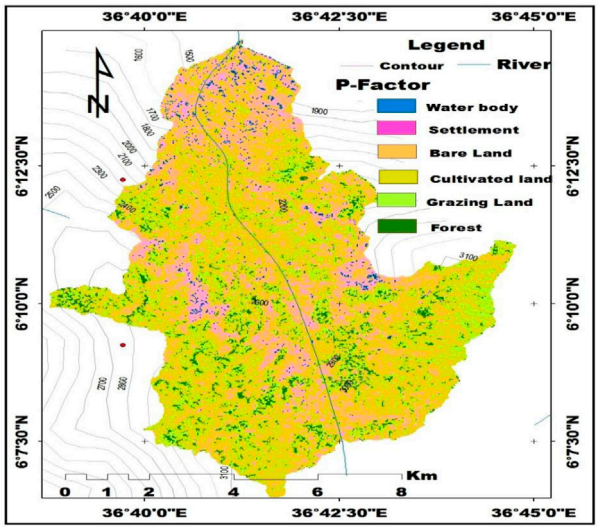

FIGURE 6
P-factor map of the Sala watershed.

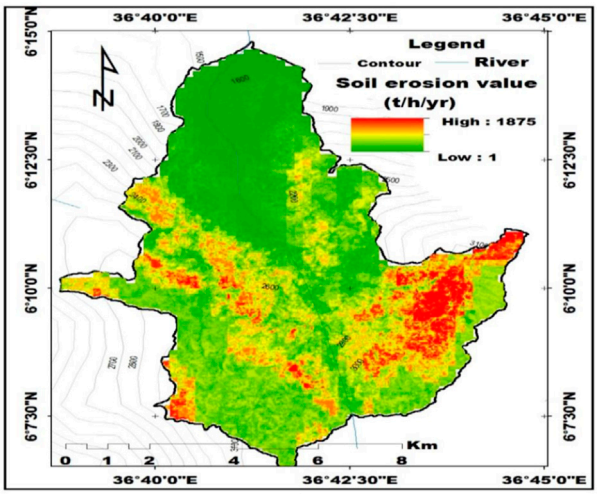

FIGURE 7
Soil risk areas map of the Sala watershed.

TABLE 4 P factor with corresponding LULC type in the Sala watershed.

Land use/land cover	P- value
Waterbody	(-)
Forest	0.52
Cultivated land	0.9
Barren land	0.73
Grazing land	0.62

Source: Olika and Iticha (2019); Fayas et al. (2019); Prasannakumar et al. (2012).

while a value close to cultivated land (0.9) denotes poor conservation practices that need soil and water conservation measures (Table 4). The cultivated and barren lands had a maximum p-factor value, which indicated that they are highly vulnerable to soil erosion due to the weakness of soil conservation practices, whereas forest land is resistant to soil erosion and runoff (Table 4; Figure 6).

3 Results and discussion

3.1 Soil erosion potential assessment for prioritization of land risk areas using the RUSLE model

The potential soil loss in the Sala watershed was calculated by integrating GIS and remote sensing techniques with the RUSLE soil loss parameters (Figure 7). Erosion loss estimation results showed that the annual soil loss rates in the study area range between 1 and 1875 t/ha/year, with a mean annual soil loss of 312.6 t/ha/year (Table 5; Figure 7). The mean annual soil loss was determined by a cell-by-cell analysis of the soil loss surface by multiplying the RUSLE factors. Based on estimated annual soil loss, soil erosion risk areas were classified into four categories ranging from low to very high risk (Table 5), which was adopted, as noted by (Haregeweyn et al., 2017; Woldemariam et al., 2018). According to the findings, 31.91% of the land was categorized as a low-risk area because it had low erosion rates (1–162 t/ha/year). The remaining areas fall into three categories: medium-risk areas (162–405 t/ha/year) (39.67%), high-risk areas (405–205 t/ha/year) (20.78%), and very high-risk areas (800–1875 t/ha/year) (7.64%) (Table 5). The soil erosion rates have led to a decline in soil fertility, water-holding capacity, and crop productivity (Beek et al., 2016; Haregeweyn et al., 2008; Haileslassie et al., 2005). The watershed area with high soil erosion hotspots requires immediate soil and water conservation planning and implementation measures to reduce further soil loss and the development of gullies on those sites.

71.58% of the watershed area is classified as having low to moderate erosion severity (the majority of the study area is the low to medium soil erosion category (Table 5). From the total area of the watershed, 28.42% is grouped under high to very high erosion severity, which needs high soil and water conservation measures (Table 5). The watershed risk map shows that some topographically rugged central locations and most of the southwestern and southeast portions of the watershed are more affected by soil erosion than others (Figure 7). Field observation verified that the high vulnerability of the study watershed to soil erosion is associated with the areas cultivated, barren, and degraded lands with steep slopes. Similar findings were reported (Bekele et al., 2022; Kidane et al., 2019), that the variation in soil erosion rate is due to land use, topography, soil type, and various soil and water management activities. These factors collectively contributed to the decline in soil fertility and crop productivity in the study area. Thus, the developed soil erosion risk map is one of the key inputs to decision-support systems in soil resource management and can have an impact on future land use planning in the study area.

The results of this study regarding the spatial location of soil erosion showed that soil loss classes were high to very high in areas with steep slopes, high drainage density, variation in climate, land use, and soil types, and susceptibility to soil erosion. Soil erosion events result from the spatial integration between the physical geographical factors (topography, precipitation, vegetation cover, and soil properties)

TABLE 5 Soil loss severity classes in the Sala watershed.

Soil loss potential (ton/ha/y)	Soil erosion Risk class	Priority classes	Area	
			Hectare (ha)	(%)
1–162 ton/ha/y	Low	IV	2,527.76	31.91
162–405 ton/ha/y	Moderate	III	3,141.32	39.67
405–800 ton/ha/y	High	II	1,645.12	20.78
800–1875 ton/ha/y	Very High	I	605.51	7.64
	Total Area		7,919.71	

(Khallouf et al., 2021; Abdo and Salloum, 2017; Djoukbala et al., 2019). Moreover, human activities accelerate soil erosion, inferior maintenance measures, agricultural intensification, population growth, urban expansion, and military actions (Mokhtar et al., 2021; Zubkova et al., 2021; Abdo, 2018; Abdo HazemG., 2022). Soil loss tolerance is a valuable criterion for evaluating the potential for production decline and associated economic repercussions, formulating soil erosion control measures, and implementing soil conservation activities (Stefano et al., 2023). As a result, the quantified mean annual soil loss for the entire watershed was 312.6 t/ha/year, which was larger than the tolerable soil loss of 5–11 t/ha/year that was estimated to ensure agricultural and economic sustainability (Morgan, 2009; Renard et al., 1996). Hence, to maintain soil fertility and agricultural productivity, appropriate soil and water conservation measures should be implemented in the study of the Sala watershed, considering areas of topographic differences to prioritize and minimize the risk of soil erosion.

4 Conclusion

Soil erosion is one of the main challenges to agricultural sustainability that affects people's livelihoods due to the sustainable land management practices in the study's Sala watershed. It has huge potential to affect food security by declining agricultural land productivity. In this study, the RUSLE model was used in combination with ground measurements and remote sensing data in a comprehensive spatial assessment of the soil's sensitivity to erosion. The spatial annual soil loss distribution of the watershed ranges from 1 to 1,875 t/ha/year, and the average annual soil loss rate is 312.6 t/ha/year. Based on the assessment of soil erosion severity, 28.42% of the watershed is classified as having high to very high levels of soil erosion, which require special priority and control measures. To prioritize land management options for the study watershed, all RUSLE parameters were integrated to estimate the distribution of soil erosion potential using an erosion risk area map. Thus, based on soil erosion priority levels, integrated soil and water conservation measures should be implemented in the study area to minimize the soil loss risk. Furthermore, estimating soil erosion risk under the spatial and temporal dynamics of different land uses/land covers should be a focus of future research. In addition to this, further studies should be focused on quantifying gullies in the Sala watershed to advance the precision of soil loss and sediment yield estimation.

Data availability statement

The original contributions presented in the study are included in the article/supplementary material, further inquiries can be directed to the corresponding author.

Author contributions

WD: Writing – original draft, Methodology, Formal Analysis, Writing – review and editing. TY: Conceptualization, Methodology, Supervision, Writing – review and editing. MD: Conceptualization, Methodology, Supervision, Writing – review and editing.

Funding

The author(s) declare that no financial support was received for the research and/or publication of this article.

Acknowledgments

The authors thank the farmers who consented to taking a soil sample from their land. The authors express their gratitude for the assistance of the laboratory technicians at the Chemistry Laboratory Center, Arba Minch University, Ethiopia. Additionally, the authors acknowledge the support of the Ethiopian National Meteorology Agency for providing rainfall data.

Conflict of interest

The authors declare that the research was conducted in the absence of any commercial or financial relationships that could be construed as a potential conflict of interest.

Generative AI statement

The author(s) declare that no Generative AI was used in the creation of this manuscript.

Publisher's note

References

Abdo, H., and Salloum, J. (2017). Spatial assessment of soil erosion in Alqerdaha Basin (Syria). *Model. Earth Syst. Environ.* 3 (1), 26. doi:10.1007/s40808-017-0294-z

Abdo, H. G. (2018). Impacts of war in Syria on vegetation dynamics and erosion risks in Safita area, Tartous, Syria. *Reg. Environ. Change* 18 (6), 1707–1719. doi:10.1007/s10113-018-1280-3

Abdo, H. G. (2022a). Assessment of landslide susceptibility zonation using frequency ratio and statistical index: a case study of Al-Fawar Basin, Tartous, Syria. *Int. J. Environ. Sci. Technol.* 19 (4), 2599–2618. doi:10.1007/s13762-021-03322-1

Abdo, H. G. (2022b). Evaluating the potential soil erosion rate based on RUSLE model, GIS, and RS in Khawabi River Basin, Tartous, Syria. *DYSONA-Applied Sci.* 3 (1), 24–32.doi:10.30493/das.2021.311044

Adimassu, Z., Mekonnen, K., Yirga, C., and Kessler, A. (2014). Effect of soil Bunds on runoff, soil and nutrient losses, and crop yield in the central highlands of Ethiopia. *Land Degrad. Dev.* 25 (6), 554–564. doi:10.1002/ldr.2182

Alemu, W. G., and Melesse, A. M. (2020). Impacts of longterm conservation measures on ecosystem services in Northwest Ethiopia. *Int. Soil Water Conservation Res.* 8 (1), 47–55. doi:10.1016/j.iswcr.2019.10.002

Alemu, Z. G. (2005). *Causes of instability in cereal production in Ethiopia*.University of the Free State, Department of Agricultural Economics.

Alexandridis, T. K., Sotiropoulou, A. M., George, B., Karapetsas, N., and Silleos, N. G. (2015). The effects of seasonality in estimating the C-factor of soil erosion studies. *Land Degrad. Dev.* 26 (6), 596–603. doi:10.1002/ldr.2223

Amellah, O., and Karim, el M. (2021). Assessment of soil erosion risk severity using GIS, remote sensing and RUSLE model in Oued Laou Basin (North Morocco). *Soil Sci. Annu.* 72 (3), 1–11. doi:10.37501/soilsa/142530

Amsalu, T., and Mengaw, A. (2014). GIS based soil loss estimation using rusle model: the case of Jabi Tehinan Woreda, ANRS, Ethiopia. *Nat. Resour.* 2014 5. 616–626. doi:10.4236/nr.2014.511054

Amundson, R., Berhe, A. A., Hopmans, J. W., Olson, C., Sztein, A. E., and Sparks, D. L. (2015). Soil science. Soil and human security in the 21st century. *Science* 348 (6235), 1261071. doi:10.1126/science.1261071

Aneseyee, A. B., Elias, E., Soromessa, T., and Feyisa, G. L. (2020). Land use/land cover change effect on soil erosion and sediment delivery in the Winike Watershed, Omo Gibe Basin, Ethiopia. *Sci. Total Environ.* 728, 138776. doi:10.1016/j.scitotenv.2020.138776

Ansari, A., Tayfur, G., and Mohammadi, S. (2024). Assessment of soil erosion and sediment delivery ratio in the Arghandab Catchment, Kandahar province, Afghanistan by using GIS-based RUSLE method. *Geomatics, Nat. Hazards Risk* 15 (1), 2384602. doi:10.1080/19475705.2024.2384602

Arekhi, S. (2008). Evaluating long-term annual sediment yield estimating potential of GIS interfaced MUSLE model on two micro-watersheds. *Pak. J. Biol. Sci.* 11, 270–274. doi:10.3923/pjbs.2008.270.274

Asmamaw, L. B., and Assen, A. M. (2019). Identification of soil erosion hotspot areas for sustainable land management in the Gerado Catchment, north-eastern Ethiopia. *Remote Sens. Appl. Soc. Environ.* 13, 306–317. doi:10.1016/j.rsase.2018.11.010

Atoma, H. (2018). Assessment of soil erosion by rusle model using remote sensing and GIS techniques: a case study of Huluka Watershed, Central Ethiopia. Master's thesis. Addis Ababa (Ethiopia): Addis Ababa University.

Ayalew, G., and Selassie, Y. G. (2015). Soil loss estimation for soil conservation planning using geographic information system in Guang Watershed, Blue Nile Basin. *J. Environ. Earth Sci.* 5 (1), 126–134.

Azimi, S., Reza, M., Bazrafshan, O., Panagopoulos, T., and Sardooi, E. R. (2019). Modeling the impact of climate change and land use change scenarios on soil erosion at the Minab Dam Watershed. *Sustainability* 11 (12), 3353. doi:10.3390/su11123353

Balasubramani, K., Gomathi, M., Bhaskaran, G., and Kumaraswamy, K. (2019). GIS-based spatial multi-criteria approach for characterization and prioritization of micro-watersheds: a case study of semi-arid watershed, South India. *Appl. Geomatics* 11, 289–307. doi:10.1007/s12518-019-00261-y

Bartoli, F., Burtin, G., and Guerif, J. (1992). Influence of organic matter on aggregation in oxisols rich in gibbsite or in goethite. II. Clay dispersion, aggregate strength and water-stability. *Geoderma* 54 (1–4), 259–274. doi:10.1016/0016-7061(92)90108-j

Beck, H. E., Zimmermann, N. E., McVicar, T. R., Vergopolan, N., Berg, A., and Wood, E. F. (2018). Present and future köppen-geiger climate classification maps at 1-km resolution. *Sci. Data* 5 (1), 1–12. doi:10.1038/sdata.2018.214

Beek, C. L. V., Elias, E., Yihenew, G. S., Heesmans, H., Tsegaye, A., Feyisa, H., et al. (2016). Soil nutrient balances under diverse agro-ecological settings in Ethiopia. *Nutrient Cycl. Agroecosyst.* 106, 257–274. doi:10.1007/s10705-016-9803-0

Bekele, B., Muluneh, A., and Wondrade, N. (2019). Geographic information system (GIS) based soil loss estimation using universal soil loss equation model (USLE) for soil conservation planning in Karesa Watershed, Dawuro Zone, and South West Ethiopia. *Int. J. Water Resour. Environ. Eng.* 11 (8), 143–158. doi:10.5897/IJWREE2018.0820

Bekele, D. A., Gella, G. W., and Ejigu, M. A. (2022). Erosion risk assessment: a contribution for conservation priority area identification in the sub-basin of Lake Tana, North-Western Ethiopia. *Int. Soil Water Conservation Res.* 10 (1), 46–61. doi:10.1016/j.iswcr.2021.04.010

Bekele, M. (2021). Geographic information system (GIS) based soil loss estimation using RUSLE model for soil and water conservation planning in Anka_Shashara watershed, southern Ethiopia. *Int. J. Hydrology* 5 (1), 9–27. doi:10.15406/ijh.2021.05.00260

Belay, A. S., Fenta, A. A., Yenehun, A., Nigate, F., Tilahun, S. A., Moges, M. M., et al. (2019). Evaluation and application of multi-source satellite rainfall product CHIRPS to assess spatio-temporal rainfall variability on data-sparse western margins of Ethiopian highlands. *Remote Sens.* 11 (22), 2688. doi:10.3390/rs11222688

Belayneh, M., Yirgu, T., and Tsegaye, D. (2019). Potential soil erosion estimation and area prioritization for better conservation planning in Gumara watershed using RUSLE and GIS techniques. *Environ. Syst. Res.* 8, 20–17. doi:10.1186/s40068-019-0149-x

Benavidez, R., Jackson, B., Maxwell, D., and Norton, K. (2018). A review of the (revised) universal soil loss equation ((R) USLE): with a view to increasing its global applicability and improving soil loss estimates. *Hydrology Earth Syst. Sci.* 22 (11), 6059–6086. doi:10.5194/hess-22-6059-2018

Bewket, W., and Teferi, E. (2009). Assessment of soil erosion hazard and prioritization for treatment at the watershed level: case study in the Chemoga watershed, Blue Nile Basin, Ethiopia. *Land Degrad. Dev.* 20 (6), 609–622. doi:10.1002/ldr.944

Blanco-Canqui, H., and Lal, R. (2008). *Principles of soil conservation and management*. Berlin, Germany: Springer Science and Business Media.

Borrelli, P., Robinson, D. A., Panagos, P., Lugato, E., Yang, J. E., Alewell, C., et al. (2020). Land use and climate change impacts on global soil erosion by water (2015–2070). *Proc. Natl. Acad. Sci. U. S. A.* 117 (36), 21994–22001. doi:10.1073/pnas.2001403117

Chuenchum, P., Xu, M., and Tang, W. (2019). Estimation of soil erosion and sediment yield in the Lancang–Mekong river using the modified revised universal soil loss equation and GIS techniques. *Water* 12 (1), 135. doi:10.3390/w12010135

Das, S., Das, R., Bora, P. K., and Olaniya, M. (2022). Estimation of rainfall erosivity (R) using geo-spatial technique for the state of Tripura, India: a comparative study. *Indian J. Agric. Sci.* 92 (7), 831–835. doi:10.56093/ijas.v92i7.104246

Das, S., Deb, P., Kumar Bora, P., and Katre, P. (2020). Comparison of RUSLE and MMF soil loss models and evaluation of catchment scale best management practices for a mountainous watershed in India. *Sustainability* 13 (1), 232. doi:10.3390/su13010232

Deb, P., Kiem, A. S., and Willgoose, G. (2019). A linked surface water-groundwater modelling approach to more realistically simulate rainfall-runoff non-stationarity in semi-arid regions. *J. Hydrology* 575, 273–291. doi:10.1016/j.jhydrol.2019.05.039

Devatha, C. P., Vaibhav, D., and Renukaprasad, M. S. (2015). Estimation of soil loss using USLE model for Kulhan watershed, Chattisgarh-A case study. *Aquat. Procedia* 4, 1429–1436. doi:10.1016/j.aqpro.2015.02.185

Djoukbala, O., Hasbaia, M., Benselama, O., and Mohamed, M. (2019). Comparison of the erosion prediction models from USLE, MUSLE and RUSLE in a mediterranean watershed, case of Wadi Gazouana (NW of Algeria). *Model. Earth Syst. Environ.* 5 (2), 725–743. doi:10.1007/s40808-018-0562-6

Ebabu, K., Tsunekawa, A., Haregeweyn, N., Adgo, E., Tsegaye Meshesha, D., Aklog, D., et al. (2019). Effects of land use and sustainable land management practices on runoff and soil loss in the upper Blue Nile Basin, Ethiopia. *Sci. Total Environ.* 648, 1462–1475. doi:10.1016/j.scitotenv.2018.08.273

Elias, E. (2017). Characteristics of nitisol profiles as affected by land use type and slope class in some Ethiopian highlands. *Environ. Syst. Res.* 6 (1), 20–15. doi:10.1186/s40068-017-0097-2

El-Swaify, S. A., Zhang, J., Ciesiolka, C. A. A., Palis, R., and Rose, C. W. (1992). Erosion problems and conservation needs of pineapple culture. *I Int. Pineapple Symp.* 334, 227–240. doi:10.17660/actahortic.1993.334.23

Ettazarini, S., El Jakani, M., and Khalid, N. (2017). Assessment of soil loss risk using integrated remote sensing and geographic information system (GIS) techniques in the Argana Basin, Morocco. *Am. J. Innov. Res. Appl. Sci.* 4, 186–194.

Ettazarini, S., and Mustapha, El J. (2017). Assessment of water suitability for irrigation purposes in qalaat Mgouna area, Morocco. *Am. Journ. Innov. Res. Appl. S. C.* 4 (5), 126–135.

FAO–UNDP (1984). *Methodology used in the development of soil loss rate map of the Ethiopian highlands*. Field document 5, Ethiopia (Addis Ababa): FAO/UNDP.

Farhan, Y., and Nawaiseh, S. (2015). Spatial assessment of soil erosion risk using RUSLE and GIS techniques. *Environ. Earth Sci.* 74, 4649–4669. doi:10.1007/s12665-015-4430-7

Fayas, C. M., Abeysingha, N. S., Nirmanee, K. G. S., Samaratunga, D., and Mallawatantri, A. (2019). Soil loss estimation using rusle model to prioritize erosion control in KELANI River Basin in Sri Lanka. *Int. Soil Water Conservation Res.* 7 (2), 130–137. doi:10.1016/j.iswcr.2019.01.003

Foster, G. R., McCool, D. K., Renard, K. G., and Moldenhauer, W. C. (1981). Conversion of the universal soil loss equation to SI metric units. *J. Soil Water Conservation* 36 (6), 355–359. doi:10.1080/00224561.1981.12436140

Fredj, A., Ghernaout, R., Dahmani, S., and Remini, B. (2024). Assessing soil erosion through the implementation of the RUSLE model and geospatial technology in the Isser watershed, Northern Algeria. *Water Supply* 24 (7), 2487–2505. doi:10.2166/ws.2024.154

Gachene, C. K. K., Nyawade, S. O., and Karanja, N. N. (2020). Soil and water conservation: an overview. *Zero Hunger*, 810–823. doi:10.1007/978-3-319-95675-6_91

Ganasri, B. P., and Ramesh, H. (2016). Assessment of soil erosion by RUSLE model using remote sensing and GIS-A case study of Nethravathi Basin. *Geosci. Front.* 7 (6), 953–961. doi:10.1016/j.gsf.2015.10.007

Gashaw, T., Tulu, T., and Argaw, M. (2018). Erosion risk assessment for prioritization of conservation measures in Geleda watershed, Blue Nile Basin, Ethiopia. *Environ. Syst. Res.* 6 (1), 1–14. doi:10.1186/s40068-016-0078-x

Gashaw, T., Tulu, T., Argaw, M., and Worqlul, A. W. (2019). Modeling the impacts of land use–land cover changes on soil erosion and sediment yield in the Andassa watershed, upper Blue Nile Basin, Ethiopia. *Environ. Earth Sci.* 78, 679–722. doi:10.1007/s12665-019-8726-x

Gelagay, H. S., and Minale, A. S. (2016). Soil loss estimation using GIS and remote sensing techniques: a case of Koga Watershed, Northwestern Ethiopia. *Int. Soil Water Conservation Res.* 4 (2), 126–136. doi:10.1016/j.iswcr.2016.01.002

Gessesse, G. D., Mansberger, R., and Klik, A. (2015). Assessment of rill erosion development during erosive storms at Angereb watershed, lake Tana sub-basin in Ethiopia. *J. Mt. Sci.* 12, 49–59. doi:10.1007/s11629-014-3151-9

Ghosh, S., and Kundu, S. (2025). Fluvial anomaly as indicator of tectonically active landscapes: a study in the Darjeeling Sikkim Himalaya, India. *DYSONA-Applied Sci.* 6 (1), 70–85.

Girma, R., and Gebre, E. (2020). Spatial modeling of erosion hotspots using GIS-RUSLE interface in Omo-Gibe river basin, southern Ethiopia: implication for soil and water conservation planning. *Environ. Syst. Res.* 9 (1), 19–14. doi:10.1186/s40068-020-00180-7

Haan, C. T., Barfield, B. J., and Hayes, J. C. (1994). *Design hydrology and sedimentology for small catchments*. Amsterdam, Netherlands: Elsevier.

Haile, G. W., and Fetene, M. (2012). Assessment of soil erosion hazard in Kilie Catchment, East shoa, Ethiopia. *Land Degrad. Dev.* 23 (3), 293–306. doi:10.1002/ldr.1082

Haile, W. (2012). Appraisal of Erythrina Bruci as a source for soil nutrition on Nitisols of South Ethiopia. *Int. J. Agric. Biol.* 14 (3).

Haileslassie, A., Priess, J., Veldkamp, E., Teketay, D., and Lesschen, J. P. (2005). Assessment of soil nutrient depletion and its spatial variability on smallholders' mixed farming systems in Ethiopia using partial versus full nutrient balances. *Agric. Ecosyst. Environ.* 108 (1), 1–16. doi:10.1016/j.agee.2004.12.010

Haregeweyn, N., Poesen, J., Deckers, J., Nyssen, J., Haile, M., Govers, G., et al. (2008). Sediment-bound nutrient export from micro-dam catchments in northern Ethiopia. *Land Degrad. Dev.* 19 (2), 136–152. doi:10.1002/ldr.830

Haregeweyn, N., Tsunekawa, A., Poesen, J., Tsubo, M., Meshesha, D. T., Fenta, A. A., et al. (2017). Comprehensive assessment of soil erosion risk for better land use planning in river basins: case study of the upper Blue Nile River. *Sci. Total Environ.* 574, 95–108. doi:10.1016/j.scitotenv.2016.09.019

Hategekimana, Y., Allam, M., Meng, Q., Nie, Y., and Mohamed, E. (2020). Quantification of soil losses along the coastal protected areas in Kenya. *Land* 9 (5), 137. doi:10.3390/land9050137

Helldén, U. (1987). "An assessment of woody biomass, community forests, land use and soil erosion in Ethiopia," in *A feasibility study on the use of remote sensing and GIS [geographical information system]-analysis for planning purposes in developing countries*. Lund, Sweden: Lund University Press.

Hurni, H. (1985a). An ecosystem approach to soil conservation. *Soil Eros. Conservation* 73, 759–771. Ankeny: Soil Conservation Society of America.

Hurni, H. (1985b). *Erosion-productivity-conservation systems in Ethiopia*. Bromley, Kent, England: Chartwell-Bratt.

Hurni, H., and Meyer, K. (2002). *A world soils agenda: discussing international actions for the sustainable use of soils*. Berne: Geographica Bernensia.

Hurni, K., Zeleke, G., Kassie, M., Tegegne, B., Kassawmar, T., Teferi, E., et al. (2015). *Economics of land degradation (ELD) Ethiopia case study: soil degradation and sustainable land management in the rainfed agricultural areas of Ethiopia: an assessment of the economic implications*. Report for the Economics of Land Degradation Initiative. 94.

Ighodaro, I. D., Lategan, F. S., and Yusuf, S. F. G. (2013). The impact of soil erosion on agricultural potential and performance of Sheshegu community farmers in the Eastern cape of South Africa. *J. Agric. Sci.* 5 (5), 140. doi:10.5539/jas.v5n5p140

Jayasekara, MJPTM, Kadupitiya, H. K., and Vitharana, U. W. A. (2018). Mapping of soil erosion hazard zones of Sri Lanka. *Trop. Agric. Res.* 29, 135. doi:10.4038/tar.v29i2.8284

Karna, B. K., Shrestha, S., and Koirala, H. L. (2021). Geo-information modeling of soil erosion for sustainable agriculture land management in Sambhunath municipality. *J. Geoinformat., Nepal* 20 (1), 47–57. doi:10.3126/njg.v20i1.39478

Karydas, C. G., Panagos, P., and Gitas, I. Z. (2014). A classification of water erosion models according to their geospatial characteristics. *Int. J. Digital Earth* 7 (3), 229–250. doi:10.1080/17538947.2012.671380

Kassaye, G. L., and Abay, G. (2019). Soil degradation extent and dynamics of soil fertility improvement technologies in majete watershed, North Ethiopia. *J. Soil Sci. Environ. Manag.* 10 (3), 39–45. doi:10.5897/jssem2018.0730

Kayet, N., Pathak, K., Chakrabarty, A., and Sahoo, S. (2018). Evaluation of soil loss estimation using the RUSLE model and SCS-CN method in hillslope mining areas. *Int. Soil Water Conservat. Res.* 6 (1), 31–42. doi:10.1016/j.iswcr.2017.11.002

Khallouf, A., Talukdar, S., Harsányi, E., Abdo, H. G., and Mohammed, S. (2021). Risk assessment of soil erosion by using CORINE model in the western part of Syrian Arab Republic. *Agric. Food Secur.* 10, 1–15. doi:10.1186/s40066-021-00295-9

Kidane, M., Bezie, A., Kesete, N., and Tolessa, T. (2019). The impact of land use and land cover (LULC) dynamics on soil erosion and sediment yield in Ethiopia. *Heliyon* 5 (12), e02981. doi:10.1016/j.heliyon.2019.e02981

Koirala, P., Thakuri, S., Joshi, S., and Chauhan, R. (2019). Estimation of soil erosion in Nepal using a RUSLE modeling and geospatial tool. *Geosciences* 9 (4), 147. doi:10.3390/geosciences9040147

Kulimushi, L. C., Choudhari, P., Mubalama, L. K., and Banswe, G. T. (2021a). GIS and remote sensing-based assessment of soil erosion risk using RUSLE model in South-kivu province, eastern, democratic Republic of Congo. *Geomatics, Nat. Hazards Risk* 12 (1), 961–987. doi:10.1080/19475705.2021.1906759

Kulimushi, L. C., Maniragaba, A., Choudhari, P., Ahmed, E., Uwemeye, J., Rushema, E., et al. (2021b). Evaluation of soil erosion and sediment yield spatio-temporal pattern during 1990–2019. *Geomatics, Nat. Hazards Risk* 12 (1), 2676–2707. doi:10.1080/19475705.2021.1973118

Lanckriet, T., Puleo, J. A., Masselink, G., Turner, I. L., Conley, D., Blenkinsopp, C., et al. (2014). Comprehensive field study of swash-zone processes. II: sheet flow sediment concentrations during quasi-steady backwash. *J. Waterw. Port, Coast. Ocean Eng.* 140 (1), 29–42. doi:10.1061/(asce)ww.1943-5460.0000209

Liu, B., Xie, Y., Li, Z., Liang, Y., Zhang, W., Fu, S., et al. (2020). The assessment of soil loss by water erosion in China. *Int. Soil Water Conservation Res.* 8 (4), 430–439. doi:10.1016/j.iswcr.2020.07.002

Mandal, U. K. (2017). Geo-information-based soil erosion modeling for sustainable agriculture development in Khadokhola Watershed, Nepal. *Land Cover Change Its Eco-Environmental Responses Nepal*, 223–241. doi:10.1007/978-981-10-2890-8_10

McCool, D. K., Foster, G. R., and Weesies, G. A. (1997). "Slope length and steepness factors (LS)," in *Predicting soil erosion by water: a guide to conservation planning with the revised universal soil loss equation (RUSLE), 703*. Washington, DC: US Department of Agriculture.

Mccool, D. K., Brown, L. C., Foster, G. R., Mutchler, C. K., and Meyer, L. D. (1987). Revised slope steepness factor for the universal soil loss equation. *Trans. ASAE* 30 (5), 1387–1396. doi:10.13031/2013.30576

McNeill, J. R. (2001). *Something new under the sun: an environmental history of the twentieth-century world (the global century series)*. New York: WW Norton and Company.

Mekonnen, M., Keesstra, S. D., Stroosnijder, L., Baartman, J. E. M., and Maroulis, J. (2015). Soil conservation through sediment trapping: a review. *Land Degrad. Dev.* 26 (6), 544–556. doi:10.1002/ldr.2308

Mete, B., and Bayram, A. (2024). Effects of sediment-storage dams on suspended sediment transport in the Sera Lake Watershed, Northeast Turkey. *Environ. Earth Sci.* 83 (8), 258. doi:10.1007/s12665-024-11572-8

Mihara, M., Yamamoto, N., and Ueno, T. (2005). Application of USLE for the prediction of nutrient losses in soil erosion processes. *Paddy Water Environ.* 3, 111–119. doi:10.1007/s10333-005-0006-6

Millward, A. A., and Mersey, J. E. (1999). Adapting the RUSLE to model soil erosion potential in a mountainous tropical watershed. *Catena* 38 (2), 109–129. doi:10.1016/s0341-8162(99)00067-3

Mohammed, S., Alsafadi, K., Talukdar, S., Kiwan, S., Hennawi, S., Alshihabi, O., et al. (2020). Estimation of soil erosion risk in southern part of Syria by using RUSLE integrating geo informatics approach. *Remote Sens. Appl. Soc. Environ.* 20, 100375. doi:10.1016/j.rsase.2020.100375

Mohammed, S., Gemechu, G. F., Aliyi, M., and Gemechu, T. M. (2022). Prioritizing management options using a risk assessment for soil erosion based on GIS, remote sensing, and RUSLE. In: *A Case Study of Midhagdu Watershed, Eastern Ethiopia*.

Moisa, M. B., Negash, D. A., Merga, B. B., and Gemeda, D. O. (2021). Impact of land-use and land-cover change on soil erosion using the RUSLE model and the geographic information system: a case of Temeji Watershed, Western Ethiopia. *J. Water Clim. Change* 12 (7), 3404–3420. doi:10.2166/wcc.2021.131

Moisa, M. B., Niguse Dejene, I., Merga, B. B., and Gemeda, D. O. (2022). Soil loss estimation and prioritization using geographic information systems and the RUSLE model: a case study of the Anger rRiver sub-basin, western Ethiopia. *J. Water Clim. Change* 13 (3), 1170–1184. doi:10.2166/wcc.2022.433

Mokhtar, A., Jalali, M., He, H., Al-Ansari, N., Ahmed, E., Alsafadi, K., et al. (2021). Estimation of SPEI meteorological drought using machine learning algorithms. *IEEe Access* 9, 65503–65523. doi:10.1109/access.2021.3074305

Molla, H. K. (2017). *The effect of degree of saturation on the results of direct shear tests of C-Φ soil*.

Molla, T., and Sisheber, B. (2017). Estimating soil erosion risk and evaluating erosion control measures for soil conservation planning at Koga watershed in the highlands of Ethiopia. *Solid Earth.* 8 (1), 13–25. doi:10.5194/se-8-13-2017

Morgan, R. P. C. (2009). *Soil erosion and conservation*. National Soil Resources Institute, Cranfield University.

Negash, D. A., Moisa, M. B., Merga, B. B., Sedeta, F., and Gemeda, D. O. (2021). Soil erosion risk assessment for prioritization of sub-watershed: the case of Chogo Watershed, Horo Guduru Wollega, Ethiopia. *Environ. Earth Sci.* 80 (17), 589. doi:10.1007/s12665-021-09901-2

Negassa, M. D., Mallie, D. T., and Gemeda, D. O. (2020). Forest cover change detection using geographic information systems and remote sensing techniques: a spatio-temporal study on Komto protected forest priority area, East Wollega Zone, Ethiopia. *Environ. Syst. Res.* 9, 1–14. doi:10.1186/s40068-020-0163-z

Nkonya, E., Anderson, W., Kato, E., Koo, J., Mirzabaev, A., von Braun, J., et al. (2016). Global cost of land degradation. *Econ. Land Degrad. Improvement–A Glob. Assess. Sustain. Dev.*, 117–165. doi:10.1007/978-3-319-19168-3_6

Ochoa Tocachi, B. F., Buytaert, W., De Bievre, B., Célleri, R., Crespo, P., Villacís, M., et al. (2016). Impacts of land use on the hydrological response of tropical Andean catchments. *Hydrol. Process.* 30 (22), 4074–4089. doi:10.1002/hyp.10980

Okenmuo, F. C., and Ewemoje, T. A. (2023). Estimation of soil water erosion using RUSLE, GIS, and remote sensing in Obibia River watershed, Anambra, Nigeria. *DYSONA-Applied Sci.* 4 (1), 6–14. doi:10.30493/das.2022.349144

Olaniya, M., Kumar Bora, P., Das, S., and Chanu, P. H. (2020). Soil erodibility indices under different land uses in Ri-Bhoi district of Meghalaya (India). *Sci. Rep.* 10 (1), 14986. doi:10.1038/s41598-020-72070-y

Olika, G., and Iticha, B. (2019). Assessment of soil erosion using RUSLE and GIS techniques: a case of Fincha'a watershed, western Ethiopia. *American-Eurasian J. Agric. Environ. Sci.* 19 (1), 31–36.

Olorunfemi, I. E., Fasinmirin, J. T., Olufayo, A. A., and Komolafe, A. A. (2020). GIS and remote sensing-based analysis of the impacts of land use/land cover change (LULCC) on the environmental sustainability of Ekiti state, southwestern Nigeria. *Environ. Dev. Sustain.* 22, 661–692. doi:10.1007/s10668-018-0214-z

Ostovari, Y., Ghorbani-Dashtaki, S., Bahrami, H.-A., Naderi, M., and Dematte, J. A. M. (2017). Soil loss estimation using RUSLE model, GIS and remote sensing techniques: a case study from the Dembecha watershed, Northwestern Ethiopia. *Geoderma Reg.* 11, 28–36. doi:10.1016/j.geodrs.2017.06.003

Ozsahin, E., Duru, U., and Eroglu, I. (2018). Land use and land cover changes (LULCC), a key to understand soil erosion intensities in the Maritsa Basin. *Water* 10 (3), 335. doi:10.3390/w10030335

Panagos, P., Borrelli, P., Meusburger, K., Alewell, C., Lugato, E., and Montanarella, L. (2015). Estimating the soil erosion cover-management factor at the European scale. *Land Use Policy* 48, 38–50. doi:10.1016/j.landusepol.2015.05.021

Pham, T. G., Degener, J., and Kappas, M. (2018). Integrated universal soil loss equation (USLE) and geographical information system (GIS) for soil erosion estimation in A sap basin: central Vietnam. *Int. Soil Water Conservation Res.* 6 (2), 99–110. doi:10.1016/j.iswcr.2018.01.001

Pimentel, D., and Burgess, M. (2013). Soil erosion threatens food production. *Agriculture* 3 (3), 443–463. doi:10.3390/agriculture3030443

Prasannakumar, V., Vijith, H., Abinod, S., and Geetha, NJGF (2012). Estimation of soil erosion risk within a small mountainous sub-watershed in Kerala, India, using revised universal soil loss equation (RUSLE) and geo-information technology. *Geosci. Front.* 3 (2), 209–215. doi:10.1016/j.gsf.2011.11.003

Reichmann, O., Chen, Y., and Iggy, L. M. (2013). Spatial model assessment of P transport from soils to waterways in an eastern Mediterranean watershed. *Water* 5 (1), 262–279. doi:10.3390/w5010262

Renard, F., Ortoleva, P., and Gratier, J. P. (1997). Pressure solution in sandstones: influence of clays and dependence on temperature and stress. *Tectonophysics* 280 (3–4), 257–266. doi:10.1016/s0040-1951(97)00039-5

Renard, K. G. (1997). "Predicting soil erosion by water: a guide to conservation planning with the revised universal soil loss equation (RUSLE)," in *Agricultural research service*. US Department of Agriculture. doi:10.32747/1997.7598424

Renard, K. G., Foster, G. R., Weesies, G. A., McCool, D. K., and Yoder, D. C. (1996). Predicting soil erosion by water: a guide to conservation planning with the revised universal soil loss equation (RUSLE). *Agric. Handb.* 703, 400. doi:10.21203/rs.3.rs-1877352/v1

Richi, S. M. (2025). Integrated RUSLE-GIS modeling for enhancing soil erosion management in Ghamima River Basin, Syria. *DYSONA-Applied Sci.* 6 (1), 104–112. doi:10.30493/das.2024.479955

Saha, S. (2018). Geo-environmental evaluation for exploring potential soil erosion areas of Jainti River Basin using AHP model, eastern India. *Univers. J. Environ. Res. Technol.* 7 (1) 38–55.

Schmidt, S., Simon, T., and Meusburger, K. (2019). Modification of the RUSLE slope length and steepness factor (LS-Factor) based on rainfall experiments at steep alpine grasslands. *MethodsX* 6, 219–229. doi:10.1016/j.mex.2019.01.004

Shreevastav, B. B., Tiwari, K. R., Mandal, R. A., and Singh, B. (2022). Flood risk modeling in southern Bagmati Corridor, Nepal'(a study from Sarlahi and Rautahat, Nepal). *Prog. Disaster Sci.* 16, 100260. doi:10.1016/j.pdisas.2022.100260

Song, X., Du, L., Kou, C., and Ma, Y. (2011). "Assessment of soil erosion in water source area of the danjiangkou reservoir using USLE and GIS," in Information Computing and Applications: Second International Conference, ICICA 2011, Qinhuangdao, China, October 28–31, 2011. (Springer), 57–64. doi:10.1007/978-3-642-25255-6_8

Sonneveld, B. G. J. S., Keyzer, M. A., and Stroosnijder, L. (2011). Evaluating quantitative and qualitative models: an application for nationwide water erosion assessment in Ethiopia. *Environ. Model. Softw.* 26 (10), 1161–1170. doi:10.1016/j.envsoft.2011.05.002

Stefano, C. D., Nicosia, A., Pampalone, V., and Ferro, V. (2023). Soil loss tolerance in the context of the European green deal. *Heliyon* 9 (1), e12869. doi:10.1016/j.heliyon.2023.e12869

Tamene, L., Park, S. J., Dikau, R., and Vlek, P. L. G. (2006). Analysis of factors determining sediment yield variability in the highlands of northern Ethiopia. *Geomorphology* 76 (1–2), 76–91. doi:10.1016/j.geomorph.2005.10.007

Taye, G., Vanmaercke, M., Poesen, J., Van Wesemael, B., Tesfaye, S., Teka, D., et al. (2018). Determining RUSLE P-and C-factors for stone bunds and trenches in rangeland and cropland, North Ethiopia. *Land Degrad. Dev.* 29 (3), 812–824. doi:10.1002/ldr.2814

Teferi, E., Bewket, W., and Simane, B. (2016). Effects of land use and land cover on selected soil quality indicators in the headwater area of the blue nile basin of Ethiopia. *Environ. Monit. Assess.* 188, 83–12. doi:10.1007/s10661-015-5086-1

Tesfahunegn, G. B., Tamene, L., and Vlek, P. L. G. (2014). Soil erosion prediction using Morgan-Morgan-Finney model in a GIS environment in northern Ethiopia catchment. *Appl. Environ. Soil Sci.* 2014, 1–15. doi:10.1155/2014/468751

Tessema, Y. M., Jasińska, J., Tiki Yadeta, L., Świtoniak, M., Puchałka, R., and Gebregeorgis, E. G. (2020). Soil loss estimation for conservation planning in the Welmel Watershed of the genale Dawa Basin, Ethiopia. *Agronomy* 10 (6), 777. doi:10.3390/agronomy10060777

Thomas, J., Joseph, S., and Thrivikramji, K. P. (2018a). Assessment of soil erosion in a tropical mountain river basin of the southern western Ghats, India using RUSLE and GIS. *Geosci. Front.* 9 (3), 893–906. doi:10.1016/j.gsf.2017.05.011

Thomas, J., Joseph, S., and Thrivikramji, K. P. (2018b). Estimation of soil erosion in a rain shadow river basin in the southern western Ghats, India using RUSLE and transport limited sediment delivery function. *Int. Soil Water Conservation Res.* 6 (2), 111–122. doi:10.1016/j.iswcr.2017.12.001

Wang, Z., Wang, G., Zhang, Y., and Wang, R. (2020). Quantification of the effect of soil erosion factors on soil nutrients at a small watershed in the Loess Plateau, northwest China. *J. Soils Sediments* 20, 745–755. doi:10.1007/s11368-019-02458-5

Williams, J. R. (1975). "Sediment-yield prediction with universal equation using runoff energy factor[1]," in *Present and prospective technology for predicting sediment yield and sources: proceedings of the sediment-yield workshop, USDA sedimentation laboratory, Oxford, Miss* (Washington, DC: Agricultural Research Service, US Department of Agriculture), 244–252.

Wischmeier, W. H., and Smith, D. D. (1965). "Predicting rainfall-erosion losses from cropland East of the rocky mountains: guide for selection of practices for soil and water conservation," in *Agricultural research service*. US Department of Agriculture.

Wischmeier, W. H., and Smith, D. D. (1978). *Predicting rainfall erosion losses: a guide to conservation planning*. Maryland: Department of Agriculture, Science and Education Administration.

Wischmeyer, W. H., and Smith, D. O. (1978). Prediction rainfall erosion loss. *Maryland: USDA, Agric. Handb. No 537*.

Woldemariam, G. W., Derribew Iguala, A., Tekalign, S., and Reddy, R. U. (2018). Spatial modeling of soil erosion risk and its implication for conservation planning: the case of the Gobele watershed, East Hararghe Zone, Ethiopia. *Land* 7 (1), 25. doi:10.3390/land7010025

Wolka, K., Mulder, J., and Biazin, B. (2018). Effects of soil and water conservation techniques on crop yield, runoff and soil loss in sub-saharan Africa: a review. *Agric. Water Manag.* 207, 67–79. doi:10.1016/j.agwat.2018.05.016

Wolka, K., Tadesse, H., Garedew, E., and Yimer, F. (2015). Soil erosion risk assessment in the Chaleleka Wetland Watershed, Central Rift Valley of Ethiopia. *Environ. Syst. Res.* 4 (1), 5–12. doi:10.1186/s40068-015-0030-5

Yesuph, A. Y., and Dagnew, A. B. (2019). Soil erosion mapping and severity analysis based on RUSLE model and local perception in the Beshillo catchment of the Blue Nile Basin, Ethiopia. *Environ. Syst. Res.* 8, 17–21. doi:10.1186/s40068-019-0145-1

Zeleke, G. (2000). Landscape dynamics and soil erosion process modelling in the north-western Ethiopian highlands. *Volume 16 of Geographica Bernensia: African studies series. University of Berne, Institute of Geography*.

Zhang, S., Fan, W., Li, Y., and Yi, Y. (2017). The influence of changes in land use and landscape patterns on soil erosion in a watershed. *Sci. Total Environ.* 574, 34–45. doi:10.1016/j.scitotenv.2016.09.024

Zubkova, M., Giglio, L., Humber, M. L., Hall, J. V., and Ellicott, E. (2021). Conflict and climate: drivers of fire activity in Syria in the twenty-first century. *Earth Interact.* 25 (1), 119–135. doi:10.1175/ei-d-21-0009.1

frontiers | Frontiers in Environmental Science

TYPE Original Research
PUBLISHED 30 May 2025
DOI 10.3389/fenvs.2025.1526066

OPEN ACCESS

EDITED BY
Narsimha Adimalla,
East China University of Technology, China

REVIEWED BY
Velibor Spalevic,
University of Montenegro, Montenegro
Tianyang Li,
Southwest University, China

*CORRESPONDENCE
Jinxin Zhang,
zhang_jin_xin@163.com
Zhen Han,
zhan@gzu.edu.cn

RECEIVED 11 November 2024
ACCEPTED 09 May 2025
PUBLISHED 30 May 2025

CITATION
Zhang J, Zhang D, Zhang B, Zeng S and Han Z (2025) Response of soil erosion to rainfall during different dry periods following drip irrigation. *Front. Environ. Sci.* 13:1526066. doi: 10.3389/fenvs.2025.1526066

Response of soil erosion to rainfall during different dry periods following drip irrigation

Jinxin Zhang[1,2]*, Dongdong Zhang[3], Bin Zhang[3], Shuyuan Zeng[3] and Zhen Han[4]*

[1]Institute of Ecological Conservation and Restoration, Chinese Academy of Forestry/Grassland Research Center, National Forestry and Grassland Administration, Beijing, China, [2]Henan Xiaolangdi Forest Ecosystem National Observation and Research Station, Jiyuan, China, [3]PowerChina Guiyang Engineering Corporation Limited, Guiyang, China, [4]College of Forestry, Guizhou University, Guiyang, China

Drip irrigation, a widely adopted water-saving technique, has received limited attention regarding its indirect effects on soil erosion. This study investigates soil erosion characteristics at varying intervals following drip irrigation using simulated rainfall experiments and an unirrigated control (S0) subjected to identical rainfall simulation procedures. The results showed significant hydrological differences between drip-irrigated and unirrigated treatments. Irrigated soils exhibited reduced runoff (mean reduction = 23.19%; $p < 0.05$) and sediment yield (mean reduction = 24.33%; $p < 0.05$) compared to S0, except for runoff in S24. Erosion mitigation was attributed to enhanced rainwater retention via surface irrigation-formed crusts and desiccation cracks generated during extended drying periods. These results highlight a previously under-characterized interaction between water-saving irrigation practices and soil erosion processes. The temporal evolution of soil surface characteristics following drip irrigation appears to influence hydrological responses during subsequent precipitation events, providing new insights for optimizing irrigation strategies in erosion-prone situations.

KEYWORDS

drip irrigation, soil crusting, desiccation cracks, runoff, sediment

1 Introduction

Drip irrigation is a water-saving irrigation technology that provides precise and highly efficient delivery of water and nutrients to crops (Evans and Zaitchik, 2008; van Donk and Shaver, 2016). It is commonly assumed that drip irrigation does not generate surface runoff, thereby mitigating soil erosion. To a significant extent, this method has addressed the issue of water scarcity for crops in arid and semi-arid regions (Yahyaoui et al., 2016; Zhang et al., 2017). Furthermore, drip irrigation has been employed in various regions to resolve the spatial and temporal imbalances between natural precipitation and crop water requirements (Khan et al., 2008; Beser et al., 2016; Yang et al., 2023). For example, it has been utilized to counteract seasonal droughts in agriculture (Xiao et al., 2008; Singh et al., 2009; Stark et al., 2013) and support vegetation rehabilitation and restoration in degraded lands and extremely arid environments (Li et al., 2015; Al-Ghobari and Dewidar, 2018). As such, drip irrigation offers a valuable means of optimizing the use of agricultural land and water resources (Najafabadi et al., 2023).

Although drip irrigation differs from rainfall in that it avoids generating surface runoff and thus does not directly induce soil erosion, its implementation introduces unique surface

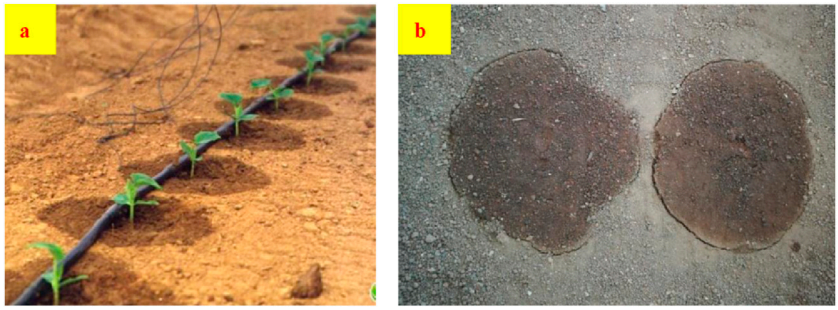

FIGURE 1
Pictures of drip irrigation **(a)** and soil crusts and desiccation cracks **(b)** (note: picture "a" provided by T.W. Lei).

characteristics. During drip irrigation, a wet circular area forms on the surface soil (Figure 1a). Upon drying, this creates physical crusts on the soil surface. Over time, prolonged drying leads to the formation of ring-shaped desiccation cracks surrounding these crusts (Figure 1b). These cracks and crusts may alter the physical properties of the topsoil layer, potentially influencing soil erosion dynamics on slopes during subsequent rainfall events compared to those in untreated slopes (Laker and Nortje, 2019). However, whether these crusts and cracks modify the hydrological response of the soil surface to rainfall-runoff processes and consequently lead to different erosion patterns compared to those in surfaces without drip irrigation remains uncertain. Despite this intriguing possibility, no studies have yet explored this aspect in the existing literature (Chamizo et al., 2012; Hardie and Almajmaie, 2019).

Soil crusts play a significant role in influencing soil erosion. Previous studies have demonstrated that soil crusts reduce water infiltration, increase surface runoff, and decrease sediment yield during rainfall events (Bradford et al., 1987; Wang et al., 2016). Ries and Hirt (2008) highlighted the relationship between rill erosion and soil crusts on fallow lands, attributing this connection to the hydrodynamic forces induced by crust formation. Furthermore, based on research conducted in the Loess Plateau of China, Algayer et al. (2014) emphasized that soil inter-rill erodibility is significantly influenced by the presence of soil crusts. They recommended integrating soil crust characteristics into soil erosion models to enhance the accuracy of erosion predictions. However, the soil crusts examined in these studies were formed under simulated or natural rainfall conditions, leaving a critical gap in understanding crust formation under drip irrigation conditions. The formation mechanisms of crusts under rainfall involve the impact of raindrops on soil particles, which disrupt soil aggregates and reduce soil structure stability (Robinson and Woodun, 2008; Han et al., 2016). In contrast, under drip irrigation, soil particles are not exposed to the erosive force of raindrops, resulting in less disturbance to soil structure. Instead, crust formation under drip irrigation is primarily attributed to the evaporation of soil water (Chamizo et al., 2013; Zhang et al., 2013; Jia et al., 2021). Specifically, the soil within the drip irrigation zone typically retains higher moisture content than the surrounding areas. As the soil water evaporates, the surface layer hardens, leading to the development of circular crusts and desiccation cracks (Figure 1b). These features may exhibit distinct hydrological responses to subsequent rainfall compared to crusts formed under rainfall conditions.

The preceding discussion underscores a notable research gap: the potential impact of circular crusts and desiccation cracks formed after drip irrigation on soil erosion remains unexplored. This study aims to address this gap by conducting rainfall simulation experiments to quantify soil erosion rates at different drying intervals following drip irrigation. The primary objective is to investigate how drip irrigation-formed crusts and cracks influence soil erosion dynamics and provide insights into the broader implications of drip irrigation practices on soil conservation.

2 Materials and methods

2.1 Study area

This study was conducted in the Huaxi district (26°26′18.23″N, 106°39′45.32″E) located in Guizhou province, China. The region exhibits a subtropical humid climate characterized by a mean annual temperature of 14.9°C. The mean annual precipitation is approximately 1,100 mm, which is unevenly distributed throughout the year. Most rainfall occurs between July and September, while the period from April to June often experiences a rainfall shortage during the growing season. Additionally, the study area is part of a karst landscape, where the extensive development of underground river networks results in low groundwater retention capacity at the surface. These climatic and geomorphological characteristics contribute to frequent seasonal drought in the region (Wang et al., 2012). Consequently, the adoption of water-saving drip irrigation technology presents an effective solution to address agricultural water scarcity.

2.2 Soils

The experimental soils were collected from sloping land and classified as yellow soil according to the Chinese soil taxonomy system. According to the World Reference Base for Soil Resources (WRB) classification system, this soil type corresponds to *Xanthic Ferralsols*, characterized as silty clay loam. The soil exhibits a granular structure with a very loose texture, which makes it

TABLE 1 Physical and chemical properties of soil.

Organic matter (%)	Total N (g·kg^{-1})	Total P (g·kg^{-1})	Soil particle size (mm)				
			<0.002	0.002–0.02	0.02–0.2	0.2–2	>2
			%				
9.34	0.351	0.086	38.5	45.5	11.0	5.0	/

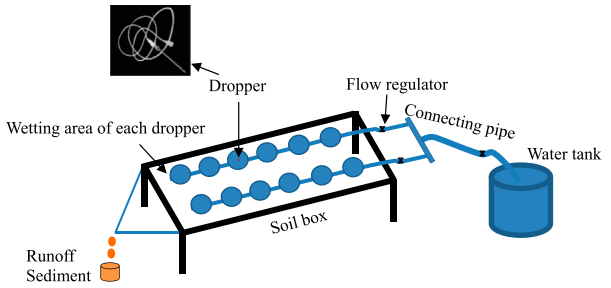

FIGURE 2
Schematic diagram of the drip irrigation simulation system and the experimental soil box.

highly susceptible to erosion. This area experiences significant annual soil loss, leading to severe land degradation and rocky desertification (Wang et al., 2004). The fundamental physicochemical properties of the soil are presented in Table 1.

2.3 Experimental setup and equipment description

2.3.1 Soil box configuration

The experiments were conducted in a controlled rainfall simulation laboratory, and the experimental setup and associated equipment are illustrated in Figure 2. The soil boxes were constructed with dimensions of 1.0 m (length) × 0.5 m (width) × 0.12 m (depth). Since land with a slope greater than 15° accounts for more than 70% of the study area, the soil box surface was sloped at a 15° angle to simulate realistic field conditions. A V-shaped drainage outlet was installed at the downslope end of the box to facilitate the collection of surface runoff and sediment transport. Additionally, eight drainage holes (5 mm in diameter) were positioned at the base of the soil box to allow for free drainage of infiltrating water during rainfall events.

2.3.2 Rainfall simulator

The rainfall simulation apparatus was equipped with two side-spray nozzles, which generated raindrops with a kinetic energy impact rate equivalent to 80% of that observed during natural rainstorms at comparable intensities. This simulator has been extensively used for soil erosion studies across multiple research institutions over several decades, and its detailed specifications have been documented in previous studies (Zhao et al., 2018). Before starting the experiments, the rainfall intensity of the simulator was calibrated to match the target intensity of 90 mm/h, which is commonly used in simulated rainfall experiments to create fast runoff and sediment on the surface. The position of the rainfall simulator was maintained consistently throughout all tests to preserve the uniformity of rainfall conditions.

2.3.3 Drip irrigation simulation apparatus

The drip irrigation system consisted of a water tank, a connecting pipe, and several drippers (Figure 2). For this study, the drippers were replaced with an infusion set to better replicate real-world conditions. During the experiments, needles were vertically inserted into the soil, and water was pumped from the water tank through the connecting pipe. The drip discharge rate was regulated using a flow regulator attached to the connecting pipe. Notably, the process of simulating drip irrigation closely resembled clinical transfusion techniques. In this study, each "wetted circle" was created using 500 mL of water, with a drip discharge rate of approximately 25 mL/min per needle.

2.4 Experiment treatments and procedures

2.4.1 Experiment treatments

To investigate the effects of drip irrigation on soil erosion, this study employed three rainfall treatments applied to soils following drip irrigation: 1) rainfall was applied 24 h after drip irrigation (S24); 2) rainfall was applied 48 h after drip irrigation (S48), and 3) rainfall was applied 72 h after drip irrigation (S72). A surface without prior drip irrigation served as the control measure (S0). Specifically, the S0 treatment was not pre-wetted, thereby preventing the formation of crusts and cracks on the surface prior to conducting the rainfall experiments. This allows for a more accurate comparison with drip irrigation treatments in order to emphasize the effects of drip irrigation on erosion.

2.4.2 Soil preparation

The soil samples were air-dried under ambient conditions in the laboratory and adjusted to maintain a moisture content of approximately 7%. Aggregated soil clods were manually crushed using a spade, and plant residues and gravel were removed using a 5-mm sieve to ensure particle homogeneity. The soil density within the soil boxes was maintained at 1.15 g/cm^3, with a uniform soil depth of 10 cm. After filling the boxes, the soil surface was carefully leveled using a wooden board to ensure consistency across all experimental setups.

2.4.3 Drip irrigation simulation

The drip irrigation simulation apparatus was positioned above the soil boxes, with six dripping devices arranged at intervals of 25 cm × 25 cm across the soil surface. Each device was equipped with a needle inserted into the soil, and a flow regulator was used to maintain a constant water infiltration rate of approximately 25 mL/

10.3389/fenvs.2025.1526066

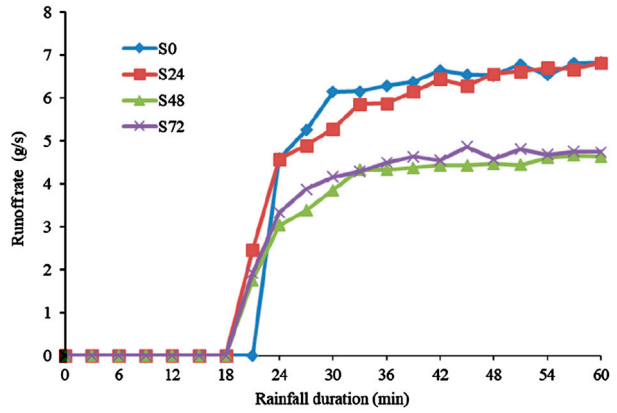

FIGURE 3
Temporal variation in runoff rates under different experimental treatments during a 60-min rainfall event (S0, surface without drip irrigation; S24, rainfall applied 24 h after drip irrigation; S48, rainfall applied 48 h after drip irrigation; S72, rainfall applied 72 h after drip irrigation).

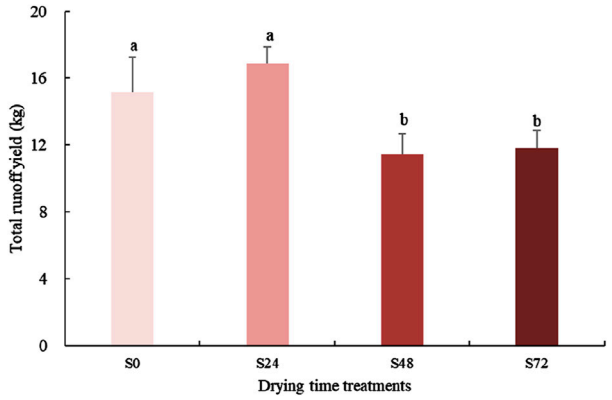

FIGURE 4
Total runoff yields under different experimental treatments during a 60-min rainfall event (S0, surface without drip irrigation; S24, rainfall applied 24 h after drip irrigation; S48, rainfall applied 48 h after drip irrigation; S72, rainfall applied 72 h after drip irrigation; bar represents standard deviation (n = 3); different letters indicate significantly different means based on Fisher's least significant difference *F* test at $p < 0.05$).

min. An amount of 500 mL of water was introduced into each bottle, and the system was allowed to operate until complete infiltration occurred. Following the completion of the drip irrigation simulation, the soil boxes were undisturbed for 24, 48, or 72 h depending on the treatment.

2.4.4 Rainfall simulation and data collection

Rainfall simulations were conducted in a controlled environment for a total rainfall duration of 60 min for all treatments to ensure the attainment of a steady state for runoff measurements. During the rainfall event, surface runoff and sediment were collected at 2-min intervals using 1-L plastic buckets. Immediately following the cessation of rainfall, the weights of the collected samples were recorded. The buckets were then stored at an indoor temperature for approximately 24 h to allow the settling of sediment. After this period, the supernatant water was decanted, and the sediment was transferred to steel cups for further processing.

The sediment samples were oven-dried at 105°C for 8 h to achieve complete desiccation. Once dried, the sediments were weighed to determine their final mass. These data were subsequently used to calculate runoff volume and sediment yield for each treatment.

2.4.5 Statistical analysis

Each experimental trial was repeated three times to ensure the reliability and reproducibility of the results. The differences in runoff and sediment yields among the treatments were statistically analyzed using Fisher's least significant difference (LSD) test to identify significant variations between treatments.

3 Results and discussion

3.1 Surface runoff

The temporal variation in runoff rates across the four rainfall treatments is shown in Figure 3. Compared to that in the S0 treatment, the initial runoff time was delayed by 3–5 min for the S24, S48, and S72 treatments. Analysis of the runoff dynamics revealed minor differences between the S0 and S24 treatments, whereas major discrepancies were observed between the S0 and both the S48 and S72 treatments. For all experimental conditions, the runoff rate achieved a steady state approximately 10 min after the initiation of runoff. The corresponding steady-state runoff rates of the S0, S24, S48, and S72 treatments were 6.64, 6.59, 4.53, and 4.71 g/s, respectively. Notably, the steady-state runoff rates for the S48 and S72 treatments were significantly lower than those observed for the S0 and S24 treatments. These results suggested that the duration of soil drying following drip irrigation significantly influences the soil's hydrological response to subsequent rainfall events. Specifically, longer periods of soil desiccation appear to alter the water infiltration, potentially impacting rainfall-runoff processes.

To further investigate the effect of drip irrigation on rainfall-runoff processes, the total runoff yields were quantified for the four rainfall treatments during a 60-min rainfall event (Figure 4). Significant differences in the total runoff yields were observed among the treatments. The S24 treatment had the greatest total runoff yield (16.88 kg), followed closely by the S0 treatment (15.16 kg). The total runoff yields for the S48 and S72 treatments were notably lower at 11.45 kg and 11.84 kg, respectively. Statistical analysis revealed no significant differences ($p > 0.05$) in the total runoff yields between the S48 and S72 treatments. These patterns observed in the total runoff yields are consistent with the trends in steady-state runoff rates reported in Figure 3, highlighting a strong relationship between soil drying duration and rainfall-runoff dynamics. These findings demonstrate that the timing of rainfall application relative to prior drip irrigation significantly influenced the total runoff yields. The greater total runoff yields observed for the S0 and S24 treatments may reflect differences in soil moisture content and soil crust properties formed by the varying durations of drying following drip irrigation. On the other hand, the lower runoff yields for the S48 and S72 treatments suggest that prolonged soil

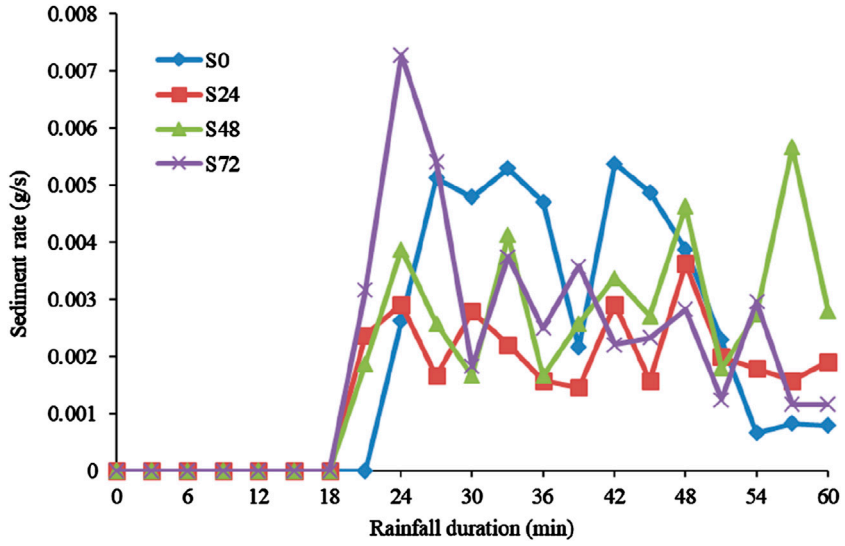

FIGURE 5
Sediment rate curves under different experimental treatments during a 60-min rainfall event (S0, surface without drip irrigation; S24, rainfall applied 24 h after drip irrigation; S48, rainfall applied 48 h after drip irrigation; S72, rainfall applied 72 h after drip irrigation).

desiccation after irrigation altered the soil's hydrological behavior, potentially reducing its runoff-generating capacity during subsequent rainfall events. These results emphasize the importance of considering antecedent soil moisture contents when evaluating hydrological responses to rainfall events in agricultural systems.

The observed results may be attributed to water evaporation from the soil surface following drip irrigation. As illustrated in Figure 1, drip irrigation supplies water directly to crop roots, resulting in localized infiltration within a small circular area around the root zone. Over time, evaporation causes soil moisture loss in the drip-irrigated area, leading to soil hardening and the formation of a physical crust (Wang et al., 2016). Furthermore, as time progresses, desiccation cracks begin to develop around the hardened soil area. These soil changes significantly influence the hydrological response of the entire surface during rainfall-runoff processes. Specifically, after 24 h of drip irrigation, soil moisture has not yet been fully lost, and no desiccation cracks have formed in the drip-irrigated area. Consequently, the soil surface remains relatively intact, facilitating runoff generation during rainfall. This explains the high total runoff yield observed in the S24 treatment. In this case, the initial soil moisture content within the drip-irrigated area is sufficiently high to reduce the average infiltration rate and increase the runoff rate during rainfall events. However, after 48 h of drip irrigation, the soil becomes dry, and a soil crust of moderate intensity forms in the drip-irrigated area. Simultaneously, desiccation cracks begin to develop around the drip-irrigated zone due to soil shrinkage caused by water loss. During rainfall, a significant portion of rainwater infiltrates into the soil through these desiccation cracks, resulting in reduced total runoff. This explains why the total runoff yields for the S48 and S72 treatments are lower than those for the S0 and S24 treatments. These findings align with a previous study on the effects of soil drying on runoff and sediment dynamics on crusted soils (Zhang and Miller, 1993).

On the other hand, many studies have demonstrated that soil crusts can significantly reduce soil infiltration rates, thereby enhancing runoff production (Bradford et al., 1987; Magunda et al., 1997; Wang et al., 2016). Based on these studies, one might expect that the S48 and S72 treatments would exhibit lower runoff yields than the S0 treatment. However, this expectation is not entirely consistent with our observation. We did not consider this a contradiction because soil crusts formed under rainfall conditions are primarily caused by the impact of raindrops, which disperse soil particles to disperse and compact the soil surface, creating a thin and dense layer (Jakab et al., 2013). In contrast, under drip irrigation conditions, soil particles are not subjected to raindrop impact, meaning that the soil structure remains undisturbed. Additionally, the crusts formed by drip irrigation are more easily rehydrated upon subsequent water supplication, allowing for greater infiltration and reduced generation. Therefore, in the case of soils with prolonged drying periods following drip irrigation, the presence of desiccation cracks facilitates increased infiltration and reduces surface runoff during rainfall events. This observation is consistent with the findings reported by Cheng and Cai (2013), who noted that the reduction in infiltration caused by soil crusts is out-weighted by the increase in filtration due to desiccation cracks.

3.2 Sediment

The sediment rates and total sediment yields are critical indicators for evaluating soil erosion dynamics across various experimental treatments. Sediment transport is facilitated by surface runoff, with sediment generation occurring nearly simultaneously with runoff initiation. Unlike the relatively straightforward evolution of the runoff dynamic curves, the sediment production process is more intricate and dynamic. As depicted in Figure 5, the sediment rate exhibits continuous

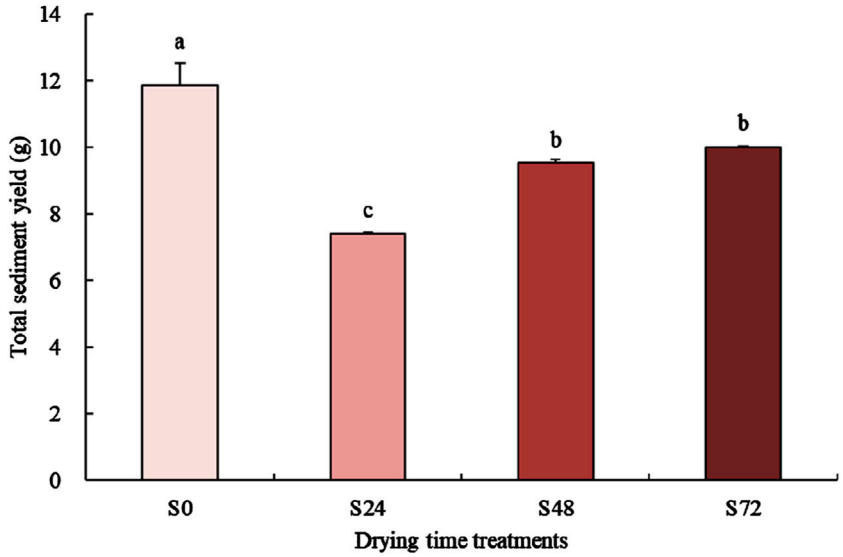

FIGURE 6
Total sediment yields under different experimental treatments during a 60-min rainfall event (S0, surface without drip irrigation; S24, rainfall applied 24 h after drip irrigation; S48, rainfall applied 48 h after drip irrigation; S72, rainfall applied 72 h after drip irrigation; bar represents standard deviation (n = 3); different letters indicate significantly different means based on Fisher's least significant difference *F* test at $p < 0.05$).

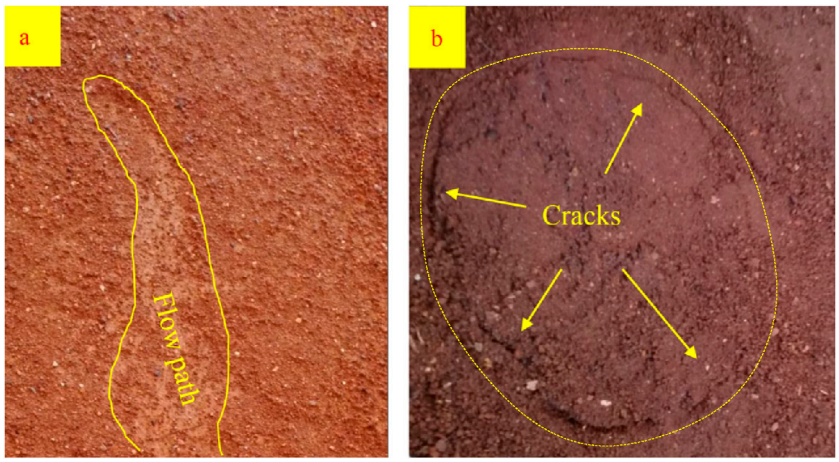

FIGURE 7
Surface change under different experimental treatments during a 60-min rainfall event: **(a)** soil surface without drip irrigation application before rainfall facilitates the production of a flow path; **(b)** soil surface with drip irrigation application before rainfall, and a dotted yellow line showing signs of desiccation cracks.

fluctuations throughout the rainfall period once surface runoff begins, reflecting the complex interplay of hydrological and erosional processes. This phenomenon is primarily due to the nonlinear nature of sediment generation and transport processes (Esteves et al., 2000; Kuhn and Bryan, 2004). In other words, the sediment rate does not necessarily increase with an increase in surface runoff, but it depends on near-surface characteristics such as micro-reliefs (Darboux and Huang, 2005; Zhao et al., 2026). Crusts and cracks in drip-irrigated and unirrigated areas have different responses to water infiltration and rainfall-runoff processes, leading to variations in the anti-erosion ability of the entire surface (Ben-Hur and Lado, 2008; Robinson and Woodun, 2008; Han et al., 2016).

For the S0 treatment, the sediment rate exhibits an initial increase, followed by a subsequent decrease, and ultimately stabilizes after approximately 50 min of rainfall. During this period, a single notable decrease in the sediment rate occurred at approximately the 38-min mark. In contrast, for the other three treatments involving drip irrigation (S24, S48, and S72), the sediment rate experienced multiple fluctuations throughout the rainfall duration, and no clear steady state was observed until the

conclusion of the rainfall event. This discrepancy suggests that the mechanisms governing sediment production differ significantly between soils with drip irrigation-formed crusts and those without such crusts (Kuhn and Bryan, 2004).

As illustrated in Figure 6, the total sediment yields varied considerably among the four treatments. Compared to the S0 treatment, the sediment yields for the S24, S48, and S72 treatments were reduced by 37.59%, 19.71%, and 15.70%, respectively. This reduction can be attributed to the lower surface runoff observed in the S48 and S72 treatments relative to the S0 treatment. Interestingly, despite the S24 treatment having the highest runoff rate among all treatments, it exhibited the lowest sediment yield. This phenomenon can be explained by the presence of a soil crust within the drip irrigation area, which mitigated soil erosion during runoff events, consequently reducing the sediment yield compared to that of the S0 treatment. The elevated sediment yields observed for the S48 and S72 treatments compared to the S24 treatment may be linked to the influence of desiccation cracks on the soil erosion process. Post-rainfall observations revealed the formation of circular rills around the drip irrigation area in these treatments (Figure 7). These rills, characterized by relatively low heights compared to their surroundings, were absent in the S24 treatment. For the S0 treatment, an obvious flow path was formed after rainfall, whereas no such flow paths were observed on the surface of the S48 and S72 treatments due to the impact of the desiccation cracks. This indicates that the presence of desiccation cracks can influence both runoff dynamics and sediment transport pathways, ultimately affecting the total sediment yields.

4 Conclusion

Drip irrigation is a highly effective method for conserving water in agricultural practices. Over the past several years, research into the effects of drip irrigation on soil infiltration and vegetation reconstruction has flourished. However, no study has systematically investigated its impact on soil erosion as it is generally assumed that drip irrigation does not directly contribute to soil erosion. In this study, we conducted a preliminary investigation and concluded that drip irrigation can reduce soil erosion due to the formation of soil crusts and desiccation cracks. Interestingly, if rainfall occurs shortly after drip irrigation, it leads to increased surface runoff. Conversely, after 48 h of drip irrigation, a greater amount of rainwater infiltrates into the soil. These findings highlight the dual role of drip irrigation in both conserving water and influencing soil erosion dynamics, emphasizing the need for further research to provide a deeper understanding of the mechanisms underlying soil erosion in drip-irrigated soils. In this study, only one level of rainfall intensity and slope degree is applied, and the range of rainfall intensity should be expanded in future experiments to make the research results more representative. Furthermore, to better explain the mechanisms between drip irrigation-formed soil crusts and water erosion, it is necessary to quantitatively analyze the physical properties of soil crusts, such as thickness, compaction, and infiltration.

In summary, these findings highlight the complex interplay between soil crust formation, desiccation cracking, and sediment production under varying antecedent soil moisture conditions induced by drip irrigation. The results underscore the importance of considering soil structural changes when evaluating erosion processes in agricultural systems.

Data availability statement

The raw data supporting the conclusions of this article will be made available by the authors, without undue reservation.

Author contributions

JZ: Conceptualization, Data curation, Writing – original draft. DZ: Data curation, Formal analysis, Writing – review and editing. BZ: Data curation, Formal analysis, Methodology, Writing – review and editing. SZ: Formal analysis, Methodology, Writing – review and editing. ZH: Writing – review and editing, Funding acquisition.

Funding

The author(s) declare that financial support was received for the research and/or publication of this article. This study was financially supported by the Fundamental Research Funds for Central Non-profit Research Institutes (CAFYBB2023ZA009-03), the China Power Construction Group Key Technology R&D Program (DJ-ZDXM-2023-07-01), and the Guiyang Science and Technology R&D Program (ZK202348-15).

Conflict of interest

Authors DZ, BZ, and SC were employed by PowerChina Guiyang Engineering Corporation Limited.

The remaining authors declare that the research was conducted in the absence of any commercial or financial relationships that could be construed as a potential conflict of interest.

Generative AI statement

The author(s) declare that no Generative AI was used in the creation of this manuscript.

Publisher's note

References

Algayer, B., Wang, B., Bourennane, H., Zheng, F., Duval, O., Li, G., et al. (2014). Aggregate stability of a crusted soil: differences between crust and sub-crust material, and consequences for interrill erodibility assessment. An example from the Loess Plateau of China. *J. Soil Sci.* 65, 325–335. doi:10.1111/ejss.12134

Al-Ghobari, H. M., and Dewidar, A. Z. (2018). Integrating deficit irrigation into surface and subsurface drip irrigation as a strategy to save water in arid regions. *Agric. Water Manag.* 209, 55–61. doi:10.1016/j.agwat.2018.07.010

Ben-Hur, A., and Lado, M. (2008). Effect of soil wetting conditions on seal formation, runoff, and soil loss in arid and semiarid soils—a review. *Aust. J. Soil Res.* 46, 191–202. doi:10.1071/sr07168

Beser, N., Surek, H., Sahin, S., Kaya, R., Tuna, B., and Cakir, R. (2016). An investigation of various drip irrigation treatments in rice (*Oryza sativa L.*). *Fresenius Environ. Bull.* 25, 3680–3686.

Bradford, J. M., Ferris, J. E., and Remley, P. A. (1987). Interrill soil erosion processes: I. Effect of surface sealing on infiltration, runoff, and soil splash detachment. *Soil Sci. Soc. Am. J.* 51, 1566–1571. doi:10.2136/sssaj1987.03615995005100060029x

Chamizo, S., Cantón, Y., Domingo, F., and Belnap, J. (2013). Evaporative losses from soils covered by physical and different types of biological soil crusts. *Hydrol. Process.* 27, 324–332. doi:10.1002/hyp.8421

Chamizo, S., Cantón, Y., Miralles, I., and Domingo, F. (2012). Biological soil crust development affects physicochemical characteristics of soil surface in semiarid ecosystems. *Soil Biol. and Biochem.* 49, 96–105. doi:10.1016/j.soilbio.2012.02.017

Cheng, Q. J., and Cai, Q. G. (2013). Response of soil surface crusts on soil erosion in loess under simulated rainfalls. *J. Soil Water Conservation* 27, 73–77. (in Chinese with English abstract) doi:10.13870/j.cnki.stbcxb.2013.04.029

Darboux, F., and Huang, C. (2005). Does soil surface roughness increase or decrease water and particle transfers? *Soil Sci. Soc. Am. J.* 69, 748–756. doi:10.2136/sssaj2003.0311

Esteves, M., Faucher, X., Galle, S., and Vauclin, M. (2000). Overland flow and infiltration modelling for small plots during unsteady rain: numerical results versus observed values. *J. Hydrology* 228, 265–282. doi:10.1016/s0022-1694(00)00155-4

Evans, J. P., and Zaitchik, B. F. (2008). Modeling the large-scale water balance impact of different irrigation systems. *Water Resour. Res.* 44, 370–380. doi:10.1029/2007wr006671

Han, Y., Fan, Y., Xin, Z., Wang, L., Cai, Q., and Wang, X. (2016). Effects of wetting rate and simulated rain duration on soil crust formation of red loam. *Environ. Earth Sci.* 75, 149–158. doi:10.1007/s12665-015-4901-x

Hardie, M., and Almajmaie, A. (2019). Measuring and estimating the hydrological properties of a soil crust. *J. Hydrology* 574, 12–22. doi:10.1016/j.jhydrol.2019.04.031

Jakab, G., Németh, T., Csepinszky, B., Madarasz, B., Szalai, Z., and Kertesz, A. (2013). The influence of short term soil sealing and crusting on hydrology and erosion at balaton uplands, Hungary. *Carpathian J. Earth and Environ. Sci.* 8, 147–155. doi:10.1016/j.wasman.2012.12.019

Jia, Q., Shi, H., Li, R., Miao, Q., Feng, Y., Wang, N., et al. (2021). Evaporation of maize crop under mulch film and soil covered drip irrigation: field assessment and modelling on West Liaohe Plain, China. *Agric. Water Manag.* 253, 106894. doi:10.1016/j.agwat.2021.106894

Khan, S., Abbas, A., Gabriel, H. F., Rana, T., and Robinson, D. (2008). Hydrologic and economic evaluation of water-saving options in irrigation systems. *Irrigation and Drainage* 57, 1–14. doi:10.1002/ird.336

Kuhn, N. J., and Bryan, R. B. (2004). Drying, soil surface condition and interrill erosion on two Ontario soils. *Catena* 57, 113–133. doi:10.1016/s0341-8162(03)00242-x

Laker, M. C., and Nortje, G. P. (2019). Review of existing knowledge on soil crusting in South Africa. *Adv. Agron.* 155, 189–242. doi:10.1016/bs.agron.2019.01.002

Li, X. B., Kang, Y. H., Wan, S. Q., Chen, X. L., Chu, L. L., and Xu, J. C. (2015). First and second-year assessments of the rapid reconstruction and re-vegetation method for reclaiming two saline-sodic, coastal soils with drip-irrigation. *Ecol. Eng.* 84, 496–505. doi:10.1016/j.ecoleng.2015.09.004

Magunda, M. K., Larson, W. E., Linden, D. R., and Nater, E. A. (1997). Changes in microrelief and their effects on infiltration and erosion during simulated rainfall. *Soil Technol.* 10, 57–67. doi:10.1016/0933-3630(95)00039-9

Najafabadi, M. A., Nafchi, R. F., Salami, H., Vanani, H. R., and Ostad-Ali-Askari, K. (2023). Effect of different managements with drip irrigation (tape). *Appl. Water Sci.* 13, 37. doi:10.1007/s13201-022-01847-5

Ries, J. B., and Hirt, U. (2008). Permanence of soil surface crusts on abandoned farmland in the Central Ebro Basin/Spain. *Catena* 72, 282–296. doi:10.1016/j.catena.2007.06.001

Robinson, D. A., and Woodun, J. K. (2008). An experimental study of crust development on chalk downland soils and their impact on runoff and erosion. *Eur. J. Soil Science59* 59, 784–798. doi:10.1111/j.1365-2389.2008.01033.x

Singh, R., Kumar, S., Nangare, D. D., and Meena, M. S. (2009). Drip irrigation and black polyethylene mulch influence on growth, yield and water-use efficiency of tomato. *Afr. J. Agric. Res.* 4, 1427–1430.

Stark, J. C., Love, S. L., King, B. A., Marshall, J. M., Bohl, W. H., and salaiz, T. (2013). Potato cultivar response to seasonal drought patterns. *Am. J. Potato Res.* 90, 207–216. doi:10.1007/s12230-012-9285-9

Van Donk, S. J., and Shaver, T. M. (2016). Effects of nitrogen application frequency via subsurface drip irrigation on corn development and grain yield. *J. Plant Nutr.* 39, 1830–1839. doi:10.1080/01904167.2016.1143506

Wang, J., Watts, D. B., Meng, Q., Zhang, Q. F., and Way, T. R. (2016). Influence of surface crusting on infiltration of a Loess Plateau soil. *Soil Sci. Soc. Am. J.* 80, 683–692. doi:10.2136/sssaj2015.08.0291

Wang, M., Wang, X., Huang, W., Zhang, Y., and Ma, J. (2012). Temporal and spatial distribution of seasonal drought in Southwest of China based on relative moisture index. *Trans. CSAE* 28, 85–92. (in Chinese with English abstract) doi:10.3969/j.issn.1002-6819.2012.19.012

Wang, S. J., Liu, Q. M., and Zhang, D. F. (2004). Karst rocky desertification in southwestern China: geomorphology, landuse, impact and rehabilitation. *Land Degrad. and Dev.* 15, 115–121. doi:10.1002/ldr.592

Xiao, X., Zhao, Y. W., and Hu, F. (2008). Comparison of the function of different water-saving rice cultivation systems in the seasonal-drought hilly region of southern China. *J. Sustain. Agric.* 32, 463–482. doi:10.1080/10440040802257462

Yahyaoui, I., Tadeo, F., and Segatto, M. V. (2016). Energy and water management for drip-irrigation of tomatoes in a semi-arid district. *Agric. Water Manag.* 183, 4–15. doi:10.1016/j.agwat.2016.08.003

Yang, P., Wu, L., Cheng, M., Fan, J., Li, S., Wang, H., et al. (2023). Review on drip irrigation: impact on crop yield, quality, and water productivity in China. *Water* 15, 1733. doi:10.3390/w15091733

Zhang, G., Liu, C., Xiao, C., Xie, R., Ming, B., Hou, P., et al. (2017). Optimizing water use efficiency and economic return of super high yield spring maize under drip irrigation and plastic mulching in arid areas of China. *Field Crops Res.* 211, 137–146. doi:10.1016/j.fcr.2017.05.026

Zhang, J. G., Xu, X. W., Lei, J. Q., Li, S. Y., Hill, R. L., and Zhao, Y. (2013). The effects of soil salt crusts on soil evaporation and chemical changes in different ages of Taklimakan Desert Shelterbelts. *J. Soil Sci. Plant Nutr.* 13, 0–1028. doi:10.4067/s0718-95162013005000080

Zhang, X. C., and Miller, W. P. (1993). The effect of drying on runoff and interrill erosion of crusted soils. *Catena Suppl.* 24, 103–144.

Zhao, L. S., Hou, R., Wu, F. Q., and Keesstra, S. (2018). Effect of soil surface roughness on infiltration water, ponding and runoff on tilled soils under rainfall simulation experiments. *Soil and Tillage Res.* 179, 47–53. doi:10.1016/j.still.2018.01.009

Zhao, L. S., Huang, C. H., and Wu, F. Q. (2026). Effect of microrelief on water erosion and their changes during rainfall. *Earth Surf. Process. Landforms* 41, 579–586. doi:10.1002/esp.3844

Frontiers in
Environmental Science

Explores the anthropogenic impact on our natural world

An innovative journal that advances knowledge of the natural world and its intersections with human society. It supports the formulation of policies that lead to a more inhabitable and sustainable world.

Discover the latest Research Topics

See more →

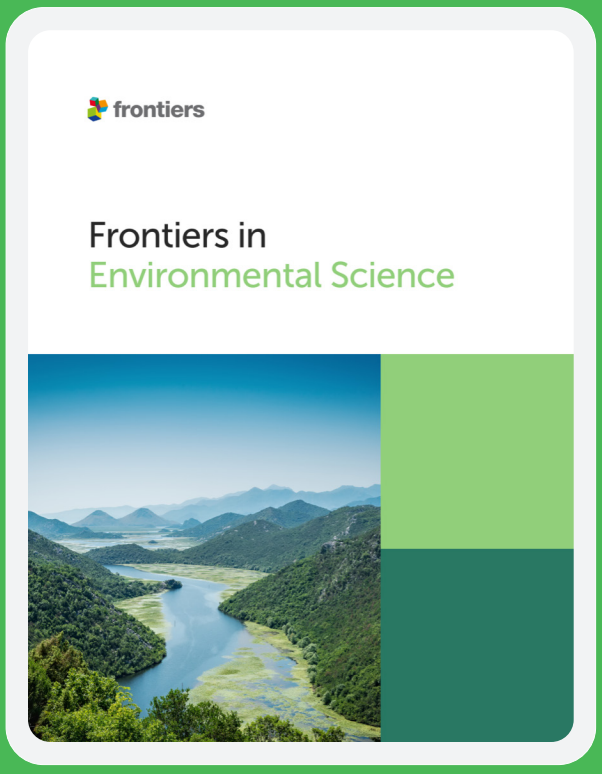

Frontiers

Avenue du Tribunal-Fédéral 34
1005 Lausanne, Switzerland
frontiersin.org

Contact us

+41 (0)21 510 17 00
frontiersin.org/about/contact